



Cellular polypropylene: Optimizing structure, charging  
and energy harvesting conditions

Pavlos Sgardelis

A thesis submitted

in accordance with requirements of  
Newcastle University candidature for the  
Degree of Doctor of Philosophy

School of Engineering

April 2018



## Abstract

Many studies have been conducted in the last decades on Cellular Polypropylene (Cell-PP) films, to be used as a lightweight cheap alternative to expensive conventional piezoelectric materials. There is a limited number of studies considering the non-linear dependence of the piezoelectric properties on the mechanical load applied. This work investigates the influence of morphological and charging parameters on the electromechanical coupling coefficient  $k^{2_{33}}$  within the non-linear region, with the aim to increase it.

Void morphological parameters were extracted out of four types of films, (Treofan GmbH), treated under Gas Diffusion Expansion (GDE). The effect of these parameters to the stiffness were analyzed. Samples were charged with a corona triode and the direct/inverse piezoelectric effect as well as the film ageing were investigated.

The mechanical and piezoelectric responses were obtained simultaneously under compressive tests and the electromechanical coupling coefficient  $k^{2_{33}}$  was derived. The optimum harvesting conditions were also investigated. A 64 runs design of experiments was built and statistical analysis was done on the responses. Finite Element Analysis (FEA) was done on 2D cross-sections of 3D modelled films for comparison of the mechanical response with the real films. A universal method of defining the morphological distributions of Cell-PP films is presented and a high correlation is revealed between the void morphology and the mechanical response. Stiffer materials revealed higher  $k^{2_{33}}$  while further increment is achieved when harvesting within the optimum strain region. With optimum charging, an increment in thermal stability and charge density was achieved, while ageing was reduced and obtained charges were increased.

As indicated by this study, Cell-PP is a high charge/density material able to compete with conventional materials for Energy Harvesting (EH), when charged and used under optimal conditions. Furthermore, EH within the optimum region is a good solution for applications where only small displacements are available.

## Acknowledgements

I would like to thank all the people who have contributed in the creation of this project. I owe my profound gratitude and sincere thanks to my supervisor Dr. Michele Pozzi, Lecturer of Newcastle University, for providing precise guidance, technical contribution, stimulating conversations, counselling and support throughout my career of research. It has been a great pleasure working with him as I have developed professional skills closer to his standards.

I express my gratitude to Newcastle University for the financial support, which without it, this project would not have been possible.

I would like to thank Treofan, Germany, GmbH & Co. KG for providing the samples for this project.

I would like to thank Richie Burnett for his technical contribution and his guidance on health and safety of the corona charger as well as the electronics workshop staff (Paul Watson and Paul Harrison) for their technical support. I also want to thank Ian Douglass for providing help with the high-pressure chamber experiments, Frank Atkinson for producing the PMMA parts and Brian Stoker for manufacturing the corona parts.

Finally, I would like to thank my family and friends which without their patience and moral support this project would not have happened.



# Table of Contents

Chapter 1. Introduction .....	1
1.1 Applications of piezoelectricity .....	1
1.2 Cellular Polypropylene (Cell-PP) .....	2
1.3 Corona charger .....	4
1.4 Research gaps .....	5
1.5 Research questions .....	7
1.6 Thesis outline .....	7
Chapter 2. Background .....	10
2.1 Smart materials .....	10
2.1.1 What are smart materials .....	10
2.1.2 Pyroelectricity .....	10
2.1.3 Thermoelectricity .....	12
2.1.4 Magnetocaloric effect .....	13
2.1.5 Shape memory effect, Superelasticity .....	14
2.1.6 Piezoelectricity .....	15
2.2 Ferro-Electrets .....	17
2.2.1 Electrets .....	17
2.2.2 Cellular Polypropylene (Cell-PP) .....	18
2.3 Functionalizing mechanisms of Cellular Polypropylene .....	20
2.4 Dielectric Resonance spectroscopy (DRS) .....	24
2.4.1 Resonance frequencies .....	24
2.4.2 $k_t^2$ function .....	26
2.5 Charging methods .....	27
2.6 Energy harvesting (EH) .....	30
Chapter 3. Literature Review .....	35
3.1 Piezoelectric Materials .....	35
3.1.1 Single Crystals .....	35
3.1.2 Ceramics .....	36
3.1.3 Polymers .....	37
3.1.4 Composites – Engineered cellular polymers .....	38
3.2. Charging Methods .....	41
3.2.1 Contact charging .....	41
3.2.2 Corona charging .....	41
3.2.3 Other charging techniques .....	46
3.3 Functionalization parameters of cellular electrets .....	46
3.3.1 Void thickness and functionalization Voltage .....	47

3.3.2 Void Pressure .....	50
3.3.3 Temperature .....	51
3.3.4 Permittivity of the material and the gas inside the voids / chamber .....	51
3.3.5 Humidity .....	52
3.3.6 Surface roughness .....	52
3.4 Pre-Functionalization treatments-parameters .....	53
3.5 Non- linearity and viscoelasticity .....	55
3.6 Theoretical models of Cell-PP .....	57
3.7 Energy Harvesting (EH) .....	59
3.7.1 PZT based Energy Harvesting .....	59
3.7.2 Polymer Based Energy Harvesting .....	61
3.7.3 EH Comparison Between PZT and Cell-PP .....	62
Chapter 4. Experimental Methods .....	65
4.1 Corona device .....	65
4.1.1 Design of corona charger .....	65
4.1.2 Health and safety .....	69
4.1.3 Mechanical-electrical characterization .....	72
4.1.4 Constant current calibration .....	73
4.2 Sample pre-functionalization treatment .....	74
4.2.1 Materials .....	74
4.2.2 Gas Diffusion Expansion procedure .....	75
4.2.3 Film morphology .....	75
4.2.4 Stress / Strain - Young's Modulus .....	76
4.3 Sample functionalization procedure .....	77
4.3.1 Grid voltage $V_g$ charging experiments .....	77
4.3.2 Exploring the full space of parameters .....	79
4.3.3 Constant current method .....	82
4.4 Performance characterization .....	83
4.4.1 Static, quasi-static $d_{33}$ .....	83
4.4.2 Inverse piezoelectricity .....	84
4.4.3 Dynamic $d_{33}$ , $C_{33}$ .....	84
4.4.4 Permittivity-capacitance measure .....	87
4.4.5 Impedance analysis .....	88
4.4.6 TSD test .....	89
4.5 Cellular PP model .....	89
4.5.1 Analytical- FEA model .....	90
Chapter 5. Results .....	93

5.1	Corona device performance .....	93
5.1.1	Grid voltage .....	93
5.1.2	Current performance .....	95
5.1.3	Distance $d_g$ , $d_c$ performance.....	96
5.2	Materials .....	99
5.2.1	Gas Diffusion Expansion (GDE) .....	99
5.2.2	Void morphology .....	108
5.3	Static– Quasi static response .....	115
5.3.1	Mechanical response .....	115
5.3.2	Direct piezoelectric response .....	126
5.3.3	Static $k^2_{33}$ .....	137
5.3.4	Creep under static conditions .....	139
5.3.5	Inverse piezoelectric response .....	142
5.3.6	Ageing .....	144
5.3.7	Charge reduction due to overstress .....	149
5.4	Dynamic Response.....	151
5.4.1	Stress relaxation and creep.....	151
5.4.2	Stress rate .....	153
5.4.3	Piezoelectric coefficient $d_{33}$ , stiffness $c_{33}$ .....	158
5.5	Energy harvesting.....	161
5.5.1	Permittivity.....	161
5.5.2	Electromechanical coupling coefficient $k^2_{33}$ .....	162
5.5.3	Power generation .....	166
5.6	Dielectric Resonance Spectroscopy (DRS) .....	171
5.7	Mechanical model.....	172
5.8	Optimum charging method .....	175
5.8.1	Correlation between independent variables .....	175
5.8.2	Relationship between $\Theta_{TSD}$ , and $\Theta$ .....	178
5.8.3	Piezoelectric response .....	180
5.8.4	Sample current, charge density ( $I_{s-Peak}$ , $\rho_s$ ).....	185
5.8.5	Film ageing.....	187
5.8.6	Constant current charging .....	188
Chapter 6. Conclusion .....		191

## Summary of Symbols

a	Thermal expansion coefficient
A	Area
A <sub>air</sub>	Air over polymer ratio (within SEM image)
A <sub>polymer</sub>	Area of polymer within the film (within SEM image)
B	First Paschen Coefficient
c	Elastic stiffness
C <sub>c</sub>	Complex capacitance
D	Electric displacement
d	Piezoelectric coefficient
d <sub>33-peak</sub>	Maximum piezoelectric coupling of the sample
D <sub>avg</sub>	Average peak displacement
dc	Corona tip – sample distance
dcg	Corona tip – grid distance
dg	Grid – sample distance
D <sub>h</sub>	Void height distribution
D <sub>r</sub>	Void aspect ratio distribution
E	Electric Field
E'	Storage modulus
E''	Loss modulus
E <sub>b</sub>	Void critical field
E <sub>cg</sub>	Electric field between the corona tip and the sample
E <sub>g</sub>	Electric field between grid and sample
E <sub>pol-i</sub>	Electric field within the ith polymer layer
E <sub>s</sub>	Charging field
E <sub>vi</sub>	Electric field within the ith void stack
F	Force
f <sub>a</sub>	Antiresonance frequency
F <sub>avg</sub>	Average peak force
f <sub>p</sub>	Parallel frequency
f <sub>s</sub>	Series frequency
G	Second Paschen Coefficient
h	Void thickness
h <sub>p</sub>	Total polymer thickness
h <sub>pi</sub>	Polymer thickness of ith layer

hv	Total void thickness
hvi	Void thickness of ith stack
I	Current
Is	Current flowing through sample
Is-peak	Highest current value during poling
ITSD-peak	Peak charges produced by the sample during TSD
J	Electric current density
K	Boltzman constant
k2	Electromechanical coupling coefficient
l0	Initial thickness of the film
l <sub>exp</sub>	Expanded film thickness
li	Film dimension in direction "i"
Ls	Number of pixels in length (within SEM image)
N	Number of stacks
n	Efficiency
ni	Number of voids within each stack
P	Polarization
p	Pressure
Ps	Switchable polarization
q	Thermal flux
Qs	Charges produced by the sample under a load of 130 kPa
Rload	Load resistor
S	Total entropy
s	Elastic compliance
Se	Electronic entropy
Sm	Magnetic entropy
Sr	Lattice entropy
U	Internal energy
Ud	Dielectric internal energy density
Ue	Elastic internal energy density
Um	Mutual dielectric and elastic energy density
Vav	Potential gained by grid due to migrating charges
Vavg	Average peak voltage
Vc	Corona tip voltage
Vg	Grid voltage
Vg-cal	Sensed grid voltage
Vi	Ionization Potential

$V_p$	Charging potential
$V_s$	Sample surface potential
$W_{in}$	Input power
$W_{out}$	Output power
$W_s$	Number of pixels in width (within SEM image)
$Y$	Young's modulus
$Z$	Impedance
$\alpha$ "alpha"	Seebeck coefficient
$\beta$ "bita"	Dielectric impermeability
$\gamma$ "gama"	Electrical conductivity
$\delta$	Scale parameter of log normal distribution
$\varepsilon$ "epsilon"	Strain
$\zeta_v$ "zita"	Electron-neutral collision cross section
$H$	Enthalpy
$\eta$ "ita"	Inverse piezoelectric strain coefficient
$\theta$	Location parameter of log normal distribution
$\Theta$ "thita"	Temperature
$\Theta_{TSD}$	Temperature where highest peak occurred during TSD
$\Theta_v$	Temperature of neutral atoms
$\kappa$ "kapa"	Permittivity
$\kappa_0$	Permittivity of free space
$\kappa_p$	Permittivity of polymer
$\kappa_v$	Permittivity gas inside the void
$\lambda$ "lamda"	Density
$\lambda_{Cell-PP}$	Density of the film
$\lambda_{exp}$	Density of expanded film
$\lambda_{PP}$	Polypropylene density
$\lambda_{relative}$	Relative density of film over the polypropylene density
$\mu$ "mi"	Shear modulus
$\nu$ "ni"	Poisson's ratio
$\xi$	Ion mobility
$\Pi$	Peltier coefficient
$\rho_g$	Charge density between grid and sample
$\rho_i$ "ro"	Charge density within the ith void stack
$\rho_s$	Obtained charge density after poling
$\rho_{TSD}$	Total Charge density based on TSD
$\sigma$ "sigma"	Stress

$\tau$ “taf”	Phase angle
$u_c$	Speed of corona wind
$u_i$ “epsilon”	Speed of sound in direction $i$
$\varphi$ “fi”	Thermal conductivity
$\psi$ “delta”	Secondary electron emission coefficient
$\omega$	Angular frequency
$\vec{B}$	Magnetic field intensity

## Abbreviations

PZT	Lead Zirconate Titanate
DSLR	Digital Single Lens Reflex
EH	Energy Harvesting
Cell-PP	Cellular Polypropylene
GDE	Gas Diffusion Expansion
FE	Finite Element
GaN	Gallium nitride
MCE	Magnetocaloric Effect
PVDF	Polyvinylidene Fluoride
MCE	Magnetocaloric Effect
DRS	Dielectric Resonance Spectroscopy
TUT’s	Tampere University of Technology
FEP	Fluoroethylenepropylene
PTFE	Polytetrafluoroethylene

# Chapter 1. Introduction

## 1.1 Applications of piezoelectricity

Piezoelectric materials have various applications nowadays. Lead Zirconate Titanate (known as PZT) as well as quartz crystals are broadly used in everyday products. Among them: lighter igniters, crystal oscillators for circuit synchronization to actuators like speakers, optical adjustments in Digital Single Lens Reflex (DSLR) cameras, linear piezoelectric motors as well as applications in the field of micro robotics and sensors (accelerometers, force and pressure sensors etc.) to name some.

Apart from sensors and actuators, piezoelectric materials can be used for Energy Harvesting (EH). Despite the existence of many energy harvesting modules available in the market, piezoelectric harvesters are not used extensively for everyday commercial applications so far.

One of the few applications of urban harvesters are produced by Pavegen. The company develops pavement tile harvesters for urban usage with many projects within UK and Europe as well as overseas.

Smaller scale energy harvesters have also been tested under lab conditions for insole (Luo, Zhu & Beeby, 2015), backpack (Granstrom *et al.*, 2007) and knee joint energy harvesting (Pozzi *et al.*, 2012). Due to the lack of available space, in addition to low output energy density, these devices are only capable of powering small electronic devices, like transmitters, for a short time.

Recently, the council of the European Union, (Brussels, 15/10/2012) decided the gradual reduction of lead by using alternative lead-free materials. Many studies have been done in order to develop such lead-free ceramic devices (Lee & Zhang, 2012; Malič *et al.*, 2015; Rubio-Marcos *et al.*, 2015; Shrouf & Zhang, 2007; Uwiragiye *et al.*, 2017). In addition to lead containment the mechanical properties of ceramic materials (brittle and dense) makes them not the best materials for applications like human EH.

## 1.2 Cellular Polypropylene (Cell-PP)

Polypropylene is a polymer of propylene ( $\text{CH}_2=\text{CHCH}_3$ ). The chemical structure of polypropylene is shown in figure 1.1.

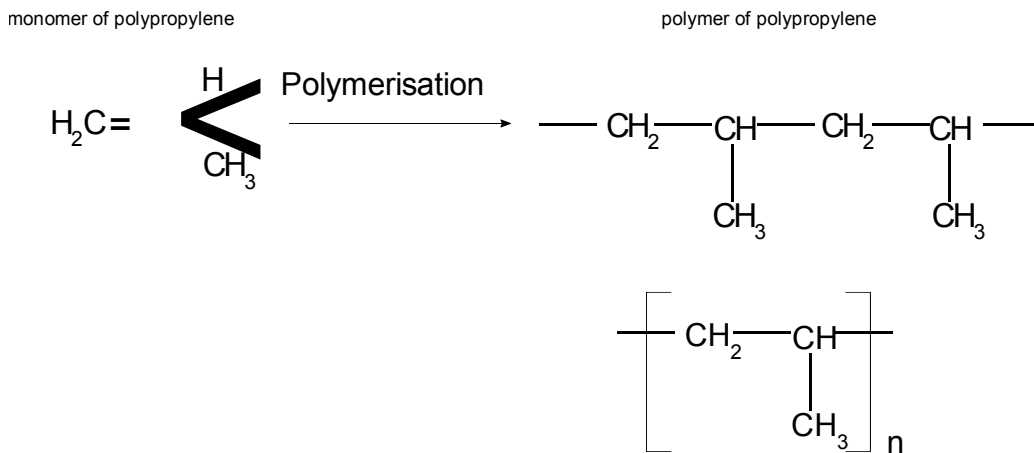


Figure 1.1. Chemical structure of Polypropylene

Polymer materials like Cellular Polypropylene (Cell-PP) and Polyvinylidene Fluoride (PVDF) gained interest, as they are flexible and lightweight. Specifically, Cell-PP shows high piezoelectric properties (over 40 times higher  $d_{33}$  compared to PVDF (Ramadan, Sameoto & Evoy, 2014)), comparable to the conventional materials, while being cheap as it is produced under roll to roll basis. One of the biggest drawbacks of polymers is their lack of charge stability, as they tend to lose their piezoelectric properties under elevated temperatures (Mellinger *et al.*, 2006). This thermal stability, can be increased with some procedures such as chemical modification (An *et al.*, 2009).

The bulk of Cell-PP is not homogeneous. During the manufacturing procedure, bidirectional stretching of Polypropylene /  $\text{CaCO}_3$  nucleating agent mixture results in the formation of micrometer sized voids. The purpose of the  $\text{CaCO}_3$  particles is the initiation of the formation of the above mentioned voids during the stretching procedure. The charging mechanism of Cell-PP is an outcome of micro discharges occurring inside the voids, when the material is placed under high electric field. Charges of opposite polarity are generated and trapped within the border of the voids creating dipoles (Lindner *et al.*, 2002). When under external compressive

mechanical pressure, these charges change their relative position, disturbing the internal field of the bulk. Opposing that field, there is an additional field created between the external layers (Dreyfus & Lewiner, 1976).

One of the main determinants of the charge separation is the thickness of the void (Harris & Mellinger, 2014). The thicker the void, the lower the field that is required for a charge separation to be created and the higher the charge density gained by the end of the charging process. There is a considerable variation in void thickness within Cell-PP films, resulting in voids with different charge densities within the same material, even when they have been charged under the same field. Furthermore, the morphology of the void has a critical role in its stiffness. As an effect, stiffer voids tend to produce fewer charges under moderate strain, compared to more compliant voids, as the relative displacement of their charges is lower. The total response (piezoelectric response of the material), is a combination of the contribution of each void. This introduces a complex response (non-constant charge output) when the material is tested under different mechanical compressions. On top of that, being a polymer, Cell-PP shows creep / stress relaxation (Gaal *et al.*, 2016). This further complicates the piezoelectric / mechanical response of the material.

Morphological aspects like lengths and thicknesses of the material's voids as well as the voids per area can change, when the film undergoes a Gas Diffusion Expansion (GDE) procedure (Tuncer, 2005). Under this procedure, the film is inserted in a high-pressure chamber. The pressure is increased for gas to diffuse inside the voids of the film. Subsequently, the pressure is released from within the chamber as quickly as possible to prevent the gas trapped within the voids from diffusing out. This sudden difference in pressure pushes the borders of the voids apart expanding the film. The stiffness of the material as well as the piezoelectric response, is not monotonically changing with the degree of this expansion. The non-expanded materials, have relatively high stiffness. When expanded, the stiffness decreases up to a point where a minimum is reached. With even higher expansions, the material gets stiffer again. On the contrary, the piezoelectric response under GDE procedure, changes inversely

proportional with stiffness. This results in a broad piezoelectric and mechanical response, depending on the way the GDE procedure is done. For producing sensors or actuators, it is beneficial for the material to have a high piezoelectric response and low stiffness, as this increases the sensitivity. However, for EH applications the stiffness has a key role to the efficiency of the device. In that sense, compliant materials might show low efficiency, as higher mechanical energy input is possibly required to deflect the material in a full mechanical cycle.

The above anomalies imply that the material does not respond linearly with mechanical pressure. During compression, the morphology of the voids changes while the thinnest voids, being the majority inside the material, collapse under moderate strain. This changes the stiffness of the material as the compression increases (Cronin & Ouellet, 2016). Similarly, the piezoelectric response changes according to the displacement of the dipoles, following a non-linear response as well (Hillenbrand' *et al.*, 2002).

The above mechanical properties make Cell-PP a good candidate for a wide range of applications where flexibility and light weight is needed as the GDE procedure provides a wide range of available electrical and mechanical properties to the film.

### **1.3 Corona charger**

As corona triode charging devices are not available commercially, a major task of the project is to design, manufacture and test such a device. The design is based on the updated version of the equipment given by Giacometti et al. (Giacometti, Fedosov & Costa, 1999) although some modifications were made. Building such a device is a complex task due to the very high voltages involved. Extra care needs to be taken for choosing materials able to withstand the high fields to be produced during the poling process. High surface resistivity, dielectric strength, low flammability and humidity absorption are the key properties of the materials surrounding the corona. Furthermore, it is vital for the conductor of the experiments to be safe during the operation of the device. Health and safety precautions were taken for the event of a discharge as well as ozone production.

## 1.4 Research gaps

To this date, there is no experimental work in the literature, on the effect of void morphology to the stiffness of the material. There is also little theoretical work done on this matter. Precise theoretical models are difficult to be implemented, as there is a broad distribution of voids, randomly arranged inside the material. Furthermore, theoretical models done on the effect of void distribution and charging voltage to the piezoelectric performance of the charged material consider the stiffness, as well as the piezoelectric response, constant. This only applies in the narrow, linear region of response of the material, under relatively small compressive strain.

Little work has been done on the electrical and mechanical response of the material in the non-linear region. Both the electrical and mechanical non-linearities might be advantageous for energy harvesting, as the material might show preferable electromechanical response under large strain compared to lower strain. There is also no published work on the piezoelectric response under creep / stress relaxation.

The main aim of this thesis is to find the optimal charging conditions for Cell-PP films, by acknowledging its non-linear behavior and to be used on human based EH. The goal is to devise methods of material processing to maximize the electromechanical coupling coefficient,  $k^2_{33}$ , as the energy conversion efficacy is important for EH (mechanical energy converted into electrical energy in a deformation cycle) and needs to be maximized. The permittivity of the materials should be considered, as it follows the increase in charge density of the voids, and thus the total charge density of the material, during the poling procedure. However, permittivity also has a negative impact to  $k^2_{33}$ , as it appears in the denominator of the electromechanical coupling coefficient, as defined by the IEEE.

Specifically, the harvester should be optimized for harvesting under low frequencies (sub hertz to few hertz), as it is intended to be used for wearable, human based EH. Within this scope, the parameters investigated will refer to the charging conditions and the material

properties / expansion pressure. The parameters describing the poling are temperature ( $\Theta$ ), the corona voltage ( $V_c$ ) and the grid voltage ( $V_g$ ), the current flowing through the sample ( $I_s$ ) as well as the relative distances between the corona and the grid ( $d_{cg}$ ) and the grid to sample ( $d_g$ ). The parameters for the material and expansion pressure are film thickness, stiffness, void structure and number of voids inside the material. To achieve a variation of those pre-functionalization parameters, different materials were used, expanded under different pressures.

Throughout the thesis, the material anomalies such as the non-linearity as well as the viscoelasticity are considered. Different methods for estimation of the electromechanical coupling coefficient  $k^2_{33}$  are used, and comparison is made among them as well as the literature. Finally, the stability of the material is investigated over the different charging and pre-functionalization methods.

## **1.5 Research questions**

The thesis deals with the response of the Cell-PP in both the linear and non-linear region, which depends on the strain the material experiences. In this scope, this work aims to answer the following research questions.

- What is the effect of the void morphology distribution on the mechanical response of the material within the non-linear region?
- What is the relationship between the strain, the stress and the charges under creep and stress relaxation?
- Is stress or strain the appropriate quantity to define the piezoelectric activity of the material within the non-linear region?
- What is the role of the stress rate on the strain and the charge production?
- Which is the best way of validating the mechanical and piezoelectric response of a non-linear viscoelastic material?
- Is Cell-PP energy harvesting in the non-linear region beneficial compared to the linear region?
- What is the role of stiffness for the EH performance?
- Can the charging procedure further enhance the piezoelectric response as well as the charge stability of the material?
- Which are the optimal charging parameters for a better piezoelectric response?

The outcome of the above investigation will be used to find the optimum material properties, as well as the charging parameters for EH purposes. Both the output power density as well as the efficiency of the device will be considered as criteria for the optimum harvester.

## **1.6 Thesis outline**

The first chapter of the thesis is the background (chapter 2). This chapter gives the physical explanation behind smart materials and their effects. A summary of equations is given for each effect, with emphasis on piezoelectricity. The chapter continues with electrets, focusing on the

functionalization mechanism of Cell-PP. Finally, a brief introduction is given for EH.

An extended literature review is given in chapter 3. The first section is a review on piezoelectric materials, with focus on polymers and in particular Cell-PP which is the material used for this project. A brief review of piezoelectric materials and their properties along with a comparison between the PZT and Cell-PP follows. Next, the functionalization mechanism and charging methods of Cell-PP with emphasis on Corona charging are presented. The chapter continues with a broad and analytic description of the functionalization parameters that affect the film piezoelectric properties. The chapter also emphasizes on the pre-functionalization treatment of the film, with GDE procedure being the key pre-functionalization process and thus covering the largest portion. The theoretical models existing in the literature are also critically reviewed in this scope. The literature review chapter gives extra emphasis on the non-linear piezoelectric response and viscoelastic properties of Cell-PP, for their importance in this work. Finally, the energy harvesting applications and capabilities of Cell-PP are explored, based on published work. A comparison over PZT based harvesting devices is made, as it is the most common material used for many applications nowadays.

The methods chapter (chapter 4) has a large portion dedicated to the corona charger device. The materials used as well as the safety features are presented. The chapter continues with the testing methods and the materials.

Chapter 5, is the result-discussion chapter. The results are presented for logical progression, rather than chronologically. The chapter starts with the corona charger performance. The corona device response is presented in accordance to the inputs. The material section presents the differences between four materials, under two different expansion pressures. Extra emphasis is given on the void morphology and distribution. The static and quasi static response of the different materials is also presented, starting with the mechanical response and continuing with the piezoelectric response. The inverse piezoelectric effect is also studied within the non-

linear region. This chapter also investigates the charge reduction due to ageing by considering functionalization and material properties.

The chapter continues with the dynamic response of the material. The effects of creep / stress relaxation as well as the stress rate to the piezoelectric performance are investigated. The dynamic response section finishes with the films being tested for EH. The mechanical Finite Element (FE) model is also presented and compared with the experimental results.

The chapter finishes with the design of experiments data analysis for the charging parameters of the corona charger. The effects of the important factors are presented within this scope.

The thesis ends with a conclusion chapter (chapter 6), where the key findings and limitations are summarized and the future work is presented.

## **Chapter 2. Background**

Since the beginning of mankind, humans used materials to fulfill their needs. The choice of each material was done according to their properties. For example, in ancient times, a flexible type of wood was used for the construction of bows and a stronger, more lightweight type for the arrow. For many centuries, the interest for materials oriented towards their mechanical properties. Once technology emerged, electricity got widely used domestically and other properties of the materials were examined. Thermal and electrical properties started to be of interest and materials that respond to environmental stimuli started being used for a variety of applications. These materials that change their properties in a controllable manner are called “smart materials”.

### **2.1 Smart materials**

#### ***2.1.1 What are smart materials***

Smart materials are materials that respond to environmental changes (external stimuli) like mechanical force, electric or magnetic fields etc. Such materials have been known for many centuries without being used in applications. The last couple of centuries, the field of smart materials gained interest. A big variety of applications, from domestic to medical and aerospace (Giurgiutiu, 2000; Rao, 1999), are nowadays based on smart materials. In many applications, some of these materials are combined to exploit two or more properties. Some properties of these materials are explained below with emphasis given to piezoelectricity due to the aims of this thesis.

#### ***2.1.2 Pyroelectricity***

The first known report of smart materials came from Theophrastus in 314 BC. He described the properties of Lyngourion (a tourmaline crystal) that had the ability to attract bits of wood when heated up. The effect of polarization generated due to temperature increment-decrement is called “Pyroelectricity”. Pyroelectricity exists in a variety of crystals like Gallium

nitride (GaN) (SHUR, BYKHOVSKI & GASKA, 1998) and ceramics PZT (Li, 2004; De Cicco *et al.*, 1999). Artificial pyroelectric materials that produce charge in response to temperature changes were introduced during last century. This response comes from reorientation of the dipoles inside the material due to thermal expansion. It is closely related to Piezoelectricity as the response comes from the deformation (strain) of the material itself (De Cicco *et al.*, 1999; Thakur *et al.*, 2007). There are two effects linked to this response. The primary and the secondary pyroelectric effect.

While in constant electric field  $E$  and stress  $\sigma$ , these two effects are described by

$$\left(\frac{\partial D}{\partial \Theta}\right)_{E,\sigma} = \left(\frac{\partial D}{\partial \Theta}\right)_{E,\varepsilon} + \left(\frac{\partial D}{\partial \varepsilon}\right)_{E,\Theta} \left(\frac{\partial \varepsilon}{\partial \Theta}\right)_{E,\sigma} \quad (2.1)$$

Where  $D$  is the electric displacement,  $\varepsilon$  is the strain and  $\Theta$  the temperature of the material. In this equation,  $\left(\frac{\partial D}{\partial \Theta}\right)_{E,\varepsilon}$  is the primary pyroelectric response and it describes the charges produced after change in polarization due to change in temperature. While in constant stress, the secondary pyroelectric response is described by  $\left(\frac{\partial \varepsilon}{\partial \Theta}\right)_{E,\sigma}$ . Thus, the rate of change of the electric displacement ( $\partial D$ ) due to change of temperature is equal to the direct influence of the change in temperature when in constant strain  $\partial \varepsilon = 0$  plus the indirect influence due to the change in strain imposed by the change in temperature. In other words, the  $\partial D$  is influenced by temperature both directly (primary pyroelectric response) and indirectly (secondary pyroelectric response). It is known that for any ferroelectric material

$$D = P + d\sigma \quad (2.2)$$

Where  $P$  is the polarization term given by

$$P = P_s + \kappa E \quad (2.3)$$

$d$  is the piezoelectric coefficient and  $\kappa$  the permittivity of the material. Using equations (2.1-2.3), the two pyroelectric coefficients that describe the two responses are rearranged as:

$$\text{Primary: } \frac{\partial P_s}{\partial \theta} + E \frac{\partial \varepsilon}{\partial \theta} \quad (2.4)$$

$$\text{Secondary: } \left( \frac{\partial D}{\partial \sigma} \right)_{E, \theta} \left( \frac{\partial \sigma}{\partial \varepsilon} \right)_{E, \theta} \left( \frac{\partial \varepsilon}{\partial \theta} \right)_{E, \sigma} = dca \quad (2.5)$$

where  $c$  is the elastic stiffness of the material and  $a$  the thermal expansion coefficient of the material.

Each pyroelectric material exhibits piezoelectric properties with the exception of crystals belonging to noncentrosymmetric cubic class 432 that their piezoelectric charges cancel out due to the symmetry. This effect is nowadays used in a variety of applications like fire alarms, bolometric infrared sensors and full body scanners (Thakur *et al.*, 2007; Edwards *et al.*, 2012).

### 2.1.3 Thermoelectricity

Thermoelectricity is the effect under which electrical current flows between two dissimilar metals in close circuit, having different temperatures. Thomas Seebeck was the first to observe the thermoelectric effect in 1821. He initially believed that a magnetic field was created out of temperature gradient, but later on found that the magnetic field was created as an outcome of current flow due to the materials potential difference. It was Jean Peltier who later on showed that the material's temperature could be risen or lowered, depending on the direction the current flows. Another thermoelectric effect was found by William Tomson. He suggested that the heat produced or absorbed was proportional to both the current and the temperature gradient, by the Tomson coefficient.

Electrical current density  $J$  and thermal flux  $q$  are known to be coupled functions with equations (2.6) and (2.7) respectively.

$$J = \gamma E - \gamma \alpha \nabla \theta \quad (2.6)$$

$$q = \Pi J - \varphi \nabla \theta \quad (2.7)$$

where  $\gamma$  is the electrical conductivity,  $E$  is the electric field,  $\alpha$  is the Seebeck coefficient,  $\theta$  is the temperature,  $\Pi$  is the Peltier coefficient and  $\varphi$  is the thermal conductivity. In the absence of current density ( $J=0$ ), an

electric field is generated inside the material when a temperature gradient is applied on it (Equation 2.6). Vice versa, when no thermal flux exists ( $q=0$ ), a thermal gradient is developed through the material when an external electric field is applied (Equation 2.7).

In the last decades, thermoelectricity is mainly used for refrigeration or heat engines e.g. Radioisotope thermoelectric generators in aerospace by NASA but with very low efficiency (around 6%) (O'Brien *et al.*, 2008).

### **2.1.4 Magnetocaloric effect**

The Magnetocaloric effect (MCE) was firstly observed by Emil Warburg in 1881. It was found that the temperature of a piece of iron changed when passed through a magnetic field. This effect was later explained by Pierre Weiss in 1917. By applying a magnetic field around a ferromagnetic material results in magnetic orientation of the dipoles in the same direction. The MCE in solid materials results from entropy variations, as the magnetic field is coupled with its spin magnetic moment.

The total entropy  $S$  of a magnetic material at constant pressure is the sum of three entropies. The magnetic entropy  $S_m$  which depends on the magnetic field intensity  $\vec{B}$  and temperature  $\Theta$ , the lattice entropy  $S_r$  and the electronic entropy  $S_e$  which only depends on temperature (partially independent on the magnetic field) (França *et al.*, 2016; Pecharsky *et al.*, 2001).

$$S(\Theta, B) = S_m(\Theta, B) + S_r(\Theta) + S_e(\Theta) \quad (2.8)$$

When the magnetic field around a magnetic solid changes adiabatically by  $\Delta\vec{B}$  at constant  $\Theta$  ( $\Delta\Theta=0$ ),  $S_m$  changes accordingly as it is the only variable depending on the magnetic field. As the process is adiabatic, the total entropy of the material does not change ( $\Delta S = 0$ ). Therefore, the electronic entropy  $S_m$  and the lattice entropy  $S_r$  have to change in order to compensate the changes and fulfil  $\Delta S = \Delta S_m + \Delta S_r + \Delta S_e = 0$

In recent years, this effect is used for environmentally friendly refrigeration in room temperature without using Ozone gas (Romero Gómez *et al.*,

2013). The efficiency of these applications is closely linked to the property of the magnetic material (Oubla *et al.*, 2016).

### **2.1.5 Shape memory effect, Superelasticity**

Thermal shape memory is the effect of restoring a deformed material to its previous shape by heating it, externally or internally, beyond its austenite start temperature. The materials that exhibit this kind of effect are called shape memory alloys and the transformation is called thermoelastic martensitic transformation (Seiner *et al.*, 2016). When the temperature of the material is below the austenite transformation temperature, the material is soft, allowing for deformations. Once heated up again, the material gains its previous shape and higher stiffness. These two phases are called martensite and austenite respectively (Seiner *et al.*, 2016). This effect is used to generate motion for actuators but the speed of their reaction is limited on the speed of heating-cooling phase (Mohd Jani *et al.*, 2014).

Shape memory alloys also exhibit superelasticity (pseudo-elasticity) when the temperature is above the austenitic temperature. At these temperatures, shape memory alloys can revert back to their austenitic phase even when large strains (up to 8%) are applied (Featherstone & Teh, 2006).

Shape memory alloy is mentioned here as it is a smart material. Even though the effect could be indirectly used for energy harvesting, shape memory alloys cannot be directly used for energy harvesting.

### **2.1.6 Triboelectric effect**

Triboelectric effect is the phenomenon of electron exchange between two materials that happens during repeated contact and separation of their surfaces. Triboelectric Nanogenerators (TENGs) utilize this phenomenon to convert mechanical energy to electrical via both electrostatic induction and contact electrification (displacement current, Maxwell's equation). TENGs have been recently investigated as energy harvesters for a variety

of applications like human wearable harvesters (Maharjan *et al.*, 2018), wind energy harvesting (Olsen *et al.*, 2019) and mechanical vibrations (Fu, Ouyang & Davis, 2019).

### **2.1.7 Piezoelectricity**

Piezoelectricity is the generation of electric charges produced by a material, when being under mechanical stress. Similarly, inverse piezoelectricity is the deformation of the material resulting from the application of an electric field upon the material. The word piezoelectricity originates from the Greek word 'πιέζω' (press) and 'ηλεκτρικό' (electric) (Uchino, 2015). Piezoelectricity was first discovered in 1880 by Jacques and Pierre Curie and ever since it became the center of attention for many researchers and developers.

For a ceramic (like PZT) to be piezoelectric, electric dipoles need to be present within it. By default, these dipoles are oriented randomly within the material. This random orientation can change via means of poling. When a high field is applied on the material, the dipoles re-orient themselves parallel to the field rendering the material polarized. When a mechanical stress is applied, the intensity of this polarization within the material changes, as the dipole moments change position with respect to each other. This makes the net field of the bulk material to change from zero, leading to changes on surface charge density.

Despite the high charge stability that most materials have, this dipole moment is reduced when the temperature gets high or even lost when it exceeds the Curie temperature of the material. Nowadays, PZT is the most widely used Piezoelectric material. There are many applications for sensors (sonar, accelerometer etc.) as well as actuators (stacked actuators, speakers etc.), which utilize the piezoelectric and inverse piezoelectric effect respectively (Uchino, 2015; Lee & Zhang, 2012; Gutnik *et al.*, 2012). There are PZT based, commercially available devices with relatively high Curie temperature (typically 300 °C) and high piezoelectric constants of  $d_{31}$ ,  $d_{33}$  and  $d_{15}$ . Furthermore, the electromechanical coupling

coefficients ( $k^2$ ) of PZT is among the highest that can be found in such materials.

In general, piezoelectric materials can be considered closed thermodynamic systems as they do not allow transfer of mass in between the system (themselves) and the surrounding environment. According to IEEE standards on piezoelectric crystals (A.H. Meitzler *et al.*, 1987) linear piezoelectricity can be described by the first law of thermodynamics. As the process is adiabatic (constant entropy  $S$ ), the system can be described by enthalpy  $H$ .

$$H = U - \varepsilon_3 \sigma_3 - D_3 E_3 \quad (2.9)$$

And the piezoelectric coefficient is described as the second derivative

$$d_{33} = - \left( \frac{\partial^2 H}{\partial E_3 \partial \sigma_3} \right) = \left( \frac{\partial D_3}{\partial \sigma_3} \right)_E = \left( \frac{\partial \varepsilon_3}{\partial E_3} \right)_\sigma \quad (2.10)$$

The subscript 3 in equations indicates axis Z which is the thickness (or third) direction. As the samples used in this work are only tested in thickness (or compression) direction, only this mode is reviewed.

The second relation is in constant field  $E$  and describes the piezoelectric effect (output charges per load applied) measured in  $\text{pC N}^{-1}$ . The third relation is in constant stress and describes the inverse piezoelectric effect (output displacement per applied voltage in  $\text{V}^{-1}$ ).

From total derivatives of  $\sigma_3$  and  $D_3$ :

$$d\varepsilon_3 = d\sigma_3 \left( \frac{\partial \varepsilon_3}{\partial \sigma_3} \right)_E + dE_3 \left( \frac{\partial \varepsilon_3}{\partial E_3} \right)_\sigma + dS \left( \frac{\partial \varepsilon_3}{\partial S} \right)_{\sigma, E} \quad (2.11)$$

$$dD_3 = d\sigma_3 \left( \frac{\partial D_3}{\partial \sigma_3} \right)_{\varepsilon_3} + dE_3 \left( \frac{\partial D_3}{\partial E_3} \right)_\sigma + dS \left( \frac{\partial D_3}{\partial S} \right)_{\sigma, \varepsilon_3} \quad (2.12)$$

The elastic compliance  $s_{33}^E$  in constant field is defined as

$$s_{33}^E = \frac{1}{Y_{33}} = \frac{\varepsilon_3}{\sigma_3 - \nu_{33}(\sigma_1 + \sigma_2)} = \left( \frac{\partial \varepsilon_3}{\partial \sigma_3} \right)_{E, S} \quad (2.13)$$

where  $\nu_{33}$  is the Poisson's ration in third direction. Finally, the relative permittivity (dielectric constant) in constant stress is defined as

$$\kappa_3^\sigma = \left( \frac{\partial D_3}{\partial E_3} \right)_\sigma \quad (2.14)$$

By substituting 2.10 and 2.13 to 2.11 we have

$$\varepsilon_3 = s_{33}^E \sigma_3 + d_{33} E_3 \quad (2.15)$$

and by substituting equation (2.10) and (2.14) to (2.12) we have

$$D_3 = d_{33} \sigma_3 + \kappa_3^\sigma E_3 \quad (2.16)$$

The electromechanical response of piezoelectric materials is described by these two (2.15, 2.16) constitutive equations for piezoelectricity. These equations link both the mechanical and electrical properties of a piezoelectric material that shows linear mechanical and electrical response. However, extra care should be taken for materials exhibiting non linearities (most of the ferroelectrets) as stiffness, piezoelectric coefficient and permittivity are not constant. These parameters depend both on the applied excitation signal (frequency and amplitude) and the morphology of the material.

Table 2.1 gives a comparison between the different harvesting techniques with smart materials.

Method	Power Density	Input
Pyroelectricity	14.8 $\mu\text{W cm}^{-2}$ (Wang <i>et al.</i> , 2019)	300 K
Thermoelectricity	260 $\mu\text{W cm}^{-1} \text{K}^{-2}$ (Shimizu <i>et al.</i> , 2019)	300 K
Triboelectricity	118 $\mu\text{W cm}^{-3}$ (Maharjan <i>et al.</i> , 2018)	30 m s <sup>-2</sup>
Piezoelectricity	5.28 $\mu\text{W cm}^{-2}$ (Wu <i>et al.</i> , 2015)	5 N

Table 2.1 Energy harvesting techniques and produced power density.

## 2.2 Ferro-Electrets

### 2.2.1 Electrets

Electrets are dielectric materials that contain a fixed excess of charge either on the surface or inside the material in the form of an oriented dipole or as a space charge. Hence, there are two different types of electrets. Space charge electrets (ionic electrets) are solid polymers whose potential is static due to the excess of charges of one polarity. On the contrary, dipole electrets (also known as Ferroelectrets or Piezoelectrets) are

polymers with encapsulated voids of air inside the bulk of the material. Both of these categories are functionalized when poled under high electric fields. With functionalization, ionic electrets gain charges of one polarity on their surface. The piezoelectric activity of the ferroelectrets is due to micro-discharges occurring within the voids of the film, while being poled. When the external electric field reaches the dielectric strength of the gas inside the voids, positive and negative ions are separated and get embedded within the polymer borders of the voids. These ions form electric dipoles (Xunlin Qiu *et al.*, 2007), rendering the polymer piezoelectric.

### **2.2.2 Cellular Polypropylene (Cell-PP)**

Polymers like Polyvinylidene Fluoride (PVDF) and Cellular Polypropylene (Cell-PP) are non-dense materials whose acoustic impedance is close to that of the air. This further increases their sensitivity over ceramic materials to inputs like vibrations, sound waves etc. (Sborikas & Wegener, 2013; Hillenbrand & Sessler, 2000).

As Cell-PP stiffness in the X and Y axis of the material is 2-3 orders of magnitude higher than the stiffness of Z axis, the material gives negligible deformations in X and Y directions when stress is applied in Z direction. Thus, the material can be considered laterally clamped. This can be inferred by applying Hooke's law which describes that strain in the third direction is caused by a stress in the same direction multiplied by the compliance tensor. For the third direction we have

$$\varepsilon_3 = \frac{\sigma_{33}}{Y_3} - \frac{\sigma_{22}\nu_{23}}{Y_2} - \frac{\sigma_{11}\nu_{13}}{Y_1} \quad (2.17)$$

where  $Y_i$  is the Young's modulus of the material. This suggests that a stress applied in the third direction produces a strain in the same direction but some of the force is dissipated to deform directions 1 and 2 (X and Y). For Cell-PP, the Poisson's ratio in directions  $i=1, 2$  is close to zero and thus the two terms  $\frac{\sigma_{22}\nu_{23}}{Y_2}$  and  $\frac{\sigma_{11}\nu_{13}}{Y_1}$  are considered negligible. Cell-PP is an orthotropic material. Its Young's modulus as well as the Poisson's ratio in third (thickness) direction,  $Y_3$  and  $\nu_{33}$  respectively, are significantly

smaller than the ones in the plane direction (i.e.  $Y_1$ ,  $Y_2$  and  $v_{11}$ ,  $v_{22}$  respectively).

For an orthotropic material, the compliance matrix is given as

$s =$

$$\begin{matrix}
 1/Y_1 & -v_{21}/Y_2 & -v_{31}/Y_3 & 0 & 0 & 0 \\
 -v_{12}/Y_1 & 1/Y_2 & -v_{32}/Y_3 & 0 & 0 & 0 \\
 -v_{13}/Y_1 & -v_{23}/Y_2 & 1/Y_3 & 0 & 0 & 0 \\
 0 & 0 & 0 & 1/\mu_{23} & 0 & 0 \\
 0 & 0 & 0 & 0 & 1/\mu_{31} & 0 \\
 0 & 0 & 0 & 0 & 0 & 1/\mu_{12}
 \end{matrix}$$

where  $\mu_{ij}$  is the shear modulus and  $v_{ij}$  is the Poisson's ratio.

For simplicity, the non-zero components are going to be written as  $x_{ij}$  with  $i$  designating the row and  $j$  the column.  $s =$

$$\begin{matrix}
 x_{11} & x_{12} & x_{13} & 0 & 0 & 0 \\
 x_{21} & x_{22} & x_{23} & 0 & 0 & 0 \\
 x_{31} & x_{32} & x_{33} & 0 & 0 & 0 \\
 0 & 0 & 0 & x_{44} & 0 & 0 \\
 0 & 0 & 0 & 0 & x_{55} & 0 \\
 0 & 0 & 0 & 0 & 0 & x_{66}
 \end{matrix}$$

As  $v_{13}$  and  $v_{23}$  are negligible,  $x_{31}$  and  $x_{32}$  are zero. Due to symmetry,  $v_{31}$  as well as  $v_{32}$  are negligible as well so that  $x_{13}$  and  $x_{23}$  are zero.

So,  $s =$

$$\begin{matrix}
 x_{11} & x_{12} & 0 & 0 & 0 & 0 \\
 x_{21} & x_{22} & 0 & 0 & 0 & 0 \\
 0 & 0 & x_{33} & 0 & 0 & 0 \\
 0 & 0 & 0 & x_{44} & 0 & 0 \\
 0 & 0 & 0 & 0 & x_{55} & 0 \\
 0 & 0 & 0 & 0 & 0 & x_{66}
 \end{matrix}$$

As  $C=S^{-1}$  (Poisson's ratios are negligible), the third element of the stiffness matrix  $c_{33}$  is given as:

$$c_{33} = \frac{1}{x_{33}} = Y_3 \quad (2.18)$$

This means that the total amount of strain in the third direction is only accounted to the stress applied in the same direction. This can be also seen by expressing strain in terms of the stress tensors

$$\varepsilon_3 = \frac{1}{c_{33}}(\sigma_{33} - \nu(\sigma_{11} + \sigma_{22})) \quad (2.19)$$

Cellular polymers are non-homogenous as they have voids with a variety of sizes. These voids are created during the manufacturing process. Cell-PP for example is created by heating and bidirectional stretching of Polypropylene mixed with nucleating agent (typically  $\text{CaCO}_3$ ) (Qaiss *et al.*, 2013).

Once the mixture cools down, the material gets strengthened as the molecules are now oriented and stay that way.

## 2.3 Functionalizing mechanisms of Cellular Polypropylene

Cell-PP owes its piezoelectricity to charges of opposite polarity, trapped inside the upper and lower border of the voids, after ionization of their gas, creating that way dipoles. The Cell-PP piezoelectret, shows almost no piezoelectric activity when charged at fields lower than those of the critical breakdown fields of the voids (Critical field  $E_b$ ). Zhang *et al.* (Pengfeng Zhang *et al.*, 2005) suggests that the piezoelectric coefficient of a specific void increases linearly until the external field  $E_s$  reaches  $2E_b$ . As each void inside the film has different threshold field (smaller voids have higher threshold field than larger voids as shown later on), some of the voids will not reach that field by the end of the charging process, will have no charge density and thus will not contribute to the final  $d_{33}$  value of the material.

Paschen's law is an empirical equation which describes the critical field needed for a breakdown to occur between two parallel plates relative to the pressure of the gas and the distance in-between them. This is

$$E_b(h, p) = \frac{Gp}{\ln\left(\frac{Bph}{\ln(1/\psi)}\right)}, \text{ where } B = \frac{\zeta_v}{K\Theta_v} \text{ and } G = BV_i \quad (2.20)$$

where  $p$  is the pressure of the gas in-between the two plates,  $h$  is the thickness of the gap (maximum void thickness in our case) and  $\Theta_v$  the temperature of the neutral atoms. According to Mellinger (Mellinger, 2011), the highest vertical thickness of the void defines at which potential the first discharge will occur. The properties of the gas also play a key role as  $\zeta_v$  is the electron-neutral collision cross section,  $V_i$  the ionization potential and  $\psi$  the secondary electron emission coefficient. Finally,  $K$  is the Boltzman constant.

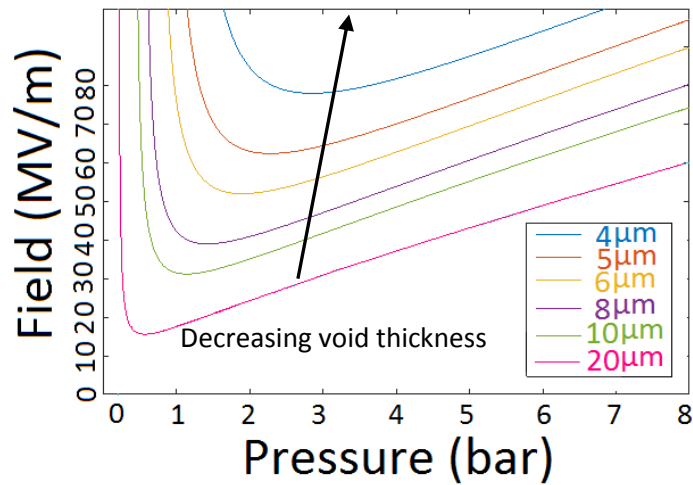


Figure 2.1. Paschen's curve for air for several values of void thickness. Paschen's curve was used to estimate the minimum breakdown field of voids as a function of air pressure for a given void thickness at room temperature.

Figure 2.1 shows the breakdown field for several void thicknesses in relation to the pressure within them. When the pressure is small, Paschen's law is not able to predict the threshold field due to discontinuity. This irregularity of the equation might be due to other phenomena like current tunneling or difficulty of ionization of the gas. Still, Paschen's law can give useful information. It predicts that for every void thickness there is an optimal pressure at which the breakdown occurs using the lowest field. There is a minimum electric field that can be applied at a certain pressure for a given thickness of a void to be charged. For example, a void of 20  $\mu\text{m}$  thickness having a pressure of 1 bar (100 kPa) will experience a

breakdown event (thus gain charge density) at a field of  $18 \text{ MV m}^{-1}$ , while at room temperature (figure 2.1). For a void of  $8 \text{ }\mu\text{m}$  thickness having the same pressure and under the same temperature, a field of  $45 \text{ MV m}^{-1}$  is needed for a breakdown to occur. So, larger voids get charged under lower fields and thus contribute more to the final  $d_{33}$  by the end of the charging process. On the other hand, larger voids experience larger back discharges when the external field  $E_s$  is removed, lowering that way their effective charge density. Explanation of this phenomenon is given later in this chapter.

A. Mellinger and O. Mellinger (Mellinger, 2011), give a good representation on how the material is rendered piezoelectric. Several models for ferroelectret piezoelectricity have been proposed (Sessler, 1999; Hillenbrand & Sessler, 2000; Hillenbrand, Sessler & Zhang, 2005; Harris & Mellinger, 2012; Tuncer, Wegener & Gerhard-Multhaupt, 2005; Paajanen & Va, 2000), by considering the polymer as a combination of alternating layers of polypropylene and voids. A realistic void-thickness distribution can be obtained on the basis of few cross sections of the film. It is assumed that the same distribution applies for the whole sample.

After the void thickness distribution is obtained, the voids can be categorized into  $N$  stacks (groups) composed of  $n_i$  voids each, based on their thickness  $h$  (Hillenbrand & Sessler, 2000). It is assumed that each polymer layer has the same electric field  $E_s$  (Mellinger, 2011). Having this in mind, Kirchhoff's loop rule suggests that, the charging voltage externally applied to the film, should generate an equal potential across it, which can be estimated by (Hillenbrand & Sessler, 2000),

$$V_p = \sum_{i=1}^N n_i h_{vi} E_{vi} + E_{pol-i} \sum_{i=1}^{N+1} n_i h_{pi} \quad (2.21)$$

where  $V_p$  is the externally applied voltage,  $h_{vi}$  is the thickness of the voids in stack "i",  $h_{pi}$  is the thickness of the polymer surrounding each void stack "i",  $E_{pol-i}$  is the electric field within the  $i^{\text{th}}$  polymer layer and  $E_{vi}$  is the electric field build up inside each void stack, due to the externally applied field.

The charge density at each interface can be found by applying Gauss' law. This gives,

$$\rho_i = \kappa_0 (\kappa_p E_p - \kappa_v E_{vi}) \quad (2.22)$$

where  $\kappa_p$  is the relative permittivity of the polymer,  $\kappa_v$  the permittivity of the gas inside the voids and  $\kappa_0$  the vacuum permittivity. When charged, the field inside each void group gets higher based on the following equation derived by equations (2.21) and (2.22),

$$E_{vi} = \frac{\kappa_p \left( V_p + \frac{\sum_{i=1}^N n_i h_{vi} \sigma_i}{\kappa_0} \right)}{\kappa_p h_p + \kappa_v h_v} - \frac{\rho_i}{\kappa_0} \quad (2.23)$$

where  $h_p$  is the total thickness of only the polymer and  $h_v$  the total thickness of the voids added together. Before applying the external field, the charge density  $\rho_i$  in each void stack is assumed to be zero. If the field inside the void is greater than the calculated Paschen breakdown field, micro discharge will occur and the new charge density is found as

$$\rho_{new} = \rho_i + \kappa_0 (E_{vi} - E_{bi}) \quad (2.24)$$

where  $E_{bi}$  is given by equation 2.21. This equation states that the added space charge inside the void, is enough to bring its electric field  $E_{vi}$  back below the threshold when the external electric field  $E_s$  stops from being applied. This phenomenon is called back discharge. More in depth, the dipoles trapped inside the surfaces of the voids, compensate the externally applied field so that  $E_{vi}=E_s$ . When the externally applied field is removed, the field of the void itself is larger than the Paschen breakdown field  $E_b$  and thus, a discharge happens in the opposite direction. The minimum field that the void should have in order for a back discharge to happen is  $2E_b$ . So, even though the larger voids start to gain charge density in lower fields, they experience back discharges at lower fields as well.

When applying a stress on the film, the charge density at its external layers change by  $\frac{\sigma}{\partial h_v}$  where

$$\sigma = -\kappa_0 \kappa_p E_p \quad (2.25)$$

This change is primarily due to the compression of the voided layers, as their Young's Modulus is much lower than the polymer's one, leading to the strain of the polymer layers to be considered negligible for low stresses. The strain to the film due to compression yields

$$\frac{\Delta h_v}{l_3} = \frac{F}{YA} \quad (2.26)$$

where  $F/A$  is the stress on the surface of the sample and  $l_3=h_v+h_p$  is the total thickness of the film as index 3 designates Z direction. After the charging process, the piezoelectric coefficient can be derived by (Hillenbrand & Sessler, 2000; Qiu, Gerhard & Mellinger, 2011)

$$d_{33} = \frac{h_p+h_v(\kappa_p h_p \sum_{i=1}^N n_i \kappa_v h_{vi} \rho_{new})}{c_{33} h_v (\kappa_v h_p + \kappa_p h_v)^2} \quad (2.27)$$

## 2.4 Dielectric Resonance spectroscopy (DRS)

### 2.4.1 Resonance frequencies

The key response parameters of piezoelectrets can be found in various ways. In this section the dielectric resonance spectroscopy method is discussed. It is essentially a frequency sweep response test, driving the piezoelectric material in the inverse piezoelectric effect. Emphasis is going to be given more on the mathematic background and less to the technique itself. The procedure as well as other techniques like static or dynamic measurement of  $d_{33}$  and stress strain measurement are going to be discussed in experimental techniques chapter. Finally, only the thickness response is going to be considered.

The resonance and an anti-resonance frequency of the Cell-PP depend mostly on the dimension of the material. For Cell-PP, these two frequencies fall between some hundreds of kHz to few MHz (Mellinger, 2002) depending on the expansion of the film.

An assumption is made that the material is considered monodimensional. Therefore, any stress applied in the third direction is only generating a strain in the same direction. Care needs to be taken when using this method, as high input signal might result in non-linearities (Sherrit, 2007)

By using  $\sigma$  and  $D$  as independent variables, the derivative of the internal energy per unit volume (keeping all components  $i, j$  (1 to 6) and  $m, n$  (1 to 3) of the tensors for the moment), we have

$$dU = \sigma_i d\varepsilon_i + E_m dD_m + \Theta dS \quad (2.28)$$

leading to

$$\sigma_i = c_{ij}^D \varepsilon_i - \eta_{in} D_n \quad (2.29)$$

and

$$E_m = \beta_{mn}^E D_n - \eta_{mj} K_j \quad (2.30)$$

where  $\eta$  is the inverse piezoelectric strain coefficient and  $\beta$  the dielectric impermeability. From equation (2.29) we have

$$\sigma_3 = c_{ij} \varepsilon_i - (\eta)_{in} D_n$$

$$\sigma_3 = c_{31} \varepsilon_1 + c_{32} \varepsilon_2 + c_{33} \varepsilon_3 + c_{34} \varepsilon_4 + c_{35} \varepsilon_5 + c_{36} \varepsilon_6 - (h)_{in} D_n$$

By derivation, we have

$$\frac{\partial \sigma_3}{\partial z} = c_{31} \frac{\partial \varepsilon_1}{\partial z} + c_{32} \frac{\partial \varepsilon_2}{\partial z} + c_{33} \frac{\partial \varepsilon_3}{\partial z} + c_{34} \frac{\partial \varepsilon_4}{\partial z} + c_{35} \frac{\partial \varepsilon_5}{\partial z} + c_{36} \frac{\partial \varepsilon_6}{\partial z} - (h)_{in} \frac{\partial D_n}{\partial z}$$

By replacing the Voigt notation

$$\begin{aligned} \frac{\partial \sigma_3}{\partial z} = & c_{31} \frac{\partial \varepsilon_{11}}{\partial z} + c_{32} \frac{\partial \varepsilon_{22}}{\partial z} + c_{33} \frac{\partial \varepsilon_{33}}{\partial z} + 2c_{34} \frac{\partial \varepsilon_{13}}{\partial z} + 2c_{35} \frac{\partial \varepsilon_{23}}{\partial z} + 2c_{36} \frac{\partial \varepsilon_{12}}{\partial z} \\ & - (h)_{3n} \frac{\partial D_n}{\partial z} \end{aligned}$$

$$\frac{\partial \varepsilon_{11}}{\partial z} = 0, \quad \frac{\partial \varepsilon_{22}}{\partial z} = 0, \quad \frac{\partial \varepsilon_{12}}{\partial z} = 0 \text{ as they do not refer to } z \text{ direction } \frac{\partial D_n}{\partial z} = 0 \text{ as}$$

there is no space charge in the material and  $\frac{\partial \varepsilon_{13}}{\partial z} = 0, \frac{\partial \varepsilon_{23}}{\partial z} = 0$  as the material is considered laterally clamped.

So,

$$\frac{\partial \sigma_3}{\partial z} = c_{33} \frac{\partial \varepsilon_{33}}{\partial z} = c_{33} \frac{\partial}{\partial z} \left( \frac{\partial^2 l_3}{\partial z} \right) = c_{33} \frac{\partial^2 l_3}{\partial z^2} \quad (2.31)$$

From (2.30) and (2.31) we have

$$\frac{\partial^2 l_3}{\partial t^2} = \frac{c_{33}^D}{\lambda} \frac{\partial^2 l_3}{\partial z^2} \quad (2.32)$$

By applying a harmonic excitation to the thickness direction, (Mellinger, 2003)

$$D_3(z, t) = D_0 e^{i\omega t} \quad (2.33)$$

And by using equation 2.29 and 2.33, equation 2.32 becomes

$$\varepsilon_3 = \frac{n_{33}^2}{c_{33}^D} D_0 \left[ \cos\left(\frac{\omega z}{v_3^D}\right) + \tan\left(\frac{\omega l_3}{2v_3^D}\right) + \sin\left(\frac{\omega z}{v_3^D}\right) \right] e^{i\omega t} \quad (2.34)$$

where  $v_3^D = \sqrt{\frac{c_{33}^D}{\lambda}}$  is the speed of sound traveling in direction 3 (thickness direction).

The Impedance  $Z$  of the sample is given by

$$Z = \frac{V}{I} = \frac{1}{i\omega C_c} \quad (2.35)$$

where  $C_c$  is the complex capacitance. By substituting equations 2.30 and 2.34 to 2.35 we obtain the complex capacitance of the sample with respect to frequency (Mellinger, 2003; Neugschwandtner *et al.*, 2000).

$$C(\omega) = \frac{\kappa_{33}^T A}{l_3} \frac{1}{1 - k_t^2 \frac{\tan(\omega/4f_a)}{\omega/4f_a}} \quad (2.36)$$

where  $l_3$  is the total thickness of the sample,  $k_t^2$  is the electromechanical coupling coefficient in thickness direction for a thin disk sample and  $f_a$  is the anti-resonance frequency given by (Altafim *et al.*, 2010)

$$f_a = \frac{v_3}{2l_3} = \frac{1}{2l_3} \sqrt{\frac{c_{33}^D}{\lambda}} \quad (2.37)$$

By using 2.35 and 2.36 the impedance response with respect to frequency is given by

$$Z(\omega) = \frac{1}{i\omega \kappa_{33}^T A} \left[ 1 - k_t^2 \frac{\tan(\omega/4f_a)}{\omega/4f_a} \right] \quad (2.38)$$

and the electromechanical coupling coefficient is given by

$$k_t^2 = \frac{\pi f_s}{2 f_p} \tan \left[ \frac{\pi f_p - f_s}{2 f_p} \right] \quad (2.39)$$

Where  $f_p$  and  $f_s$  are the parallel and series frequencies, where the real parts of impedance  $Z$  and admittance  $Y$  get maximized respectively.

### 2.4.2 $k_t^2$ function

Re-writing equation (2.39) it is obtained.

$$k_t^2 = \frac{\pi f_s}{2 f_p} \tan \left[ \frac{\pi}{2} \left( 1 - \frac{f_s}{f_p} \right) \right] \quad (2.40)$$

Thus,  $k_t^2$  only depends on the ratio  $\frac{f_s}{f_p}$ .

As the resonance frequency is always lower than the anti-resonance one ( $f_s < f_p$ ) this ratio is always smaller than unity  $\frac{f_s}{f_p} < 1$ . Also,  $k_t^2$  by definition takes values less than unity,  $k_t^2 < 1$ . With these constraints in mind, we obtain the graphic representation shown in figure 2.2.

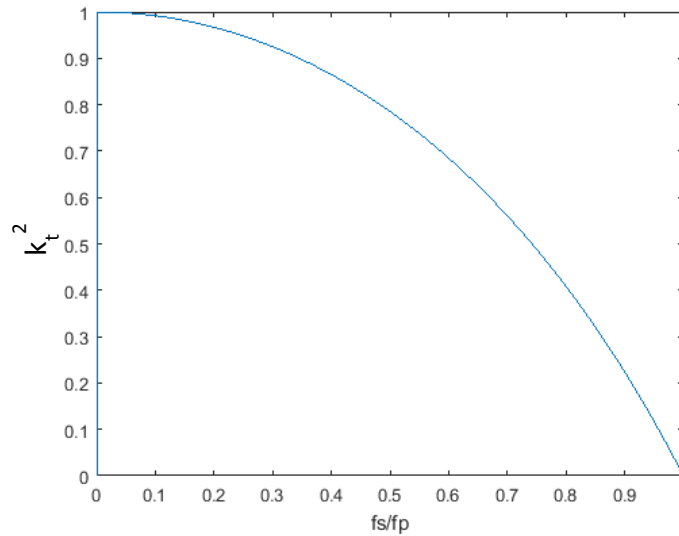


Figure 2.2. Electromechanical coupling coefficient ( $k_t^2$ ) as a function of the resonance to anti-resonance frequency ratio ( $f_s/f_p$ ).  $0 < k_t < 1$  and  $0 < f_s/f_p < 1$

This is to say that as the ratio gets higher, (the resonance frequency increases with respect to the anti-resonance frequency) the electromechanical coupling coefficient decreases.

## 2.5 Charging methods

There are two methods to charge polymer films. Contact charging and corona charging. Contact charging is the simplest way as the principle of this procedure is well known and similar to a capacitor charging. The sample is inserted between two parallel plates. The potential difference between these two plates gets increased, generating a field in between them. That way, dipoles are being created and oriented to the field

direction. Corona charging procedure on the other hand is harder to control as it works by means of electron avalanche. Electron Avalanche occurs when molecules of a gas gets ionized (by losing or gaining an electron) generating ions (Cations or Anions respectively) and free electrons (Intra & Tippayawong, 2009). These particles get accelerated towards or away from the source of the field (the corona tip) depending on the polarity. In negative corona,  $\text{CO}_3^-$  Anions are created and repelled away from the electrode while in positive corona, the positive  $(\text{H}_2\text{O})_n \text{H}^+$  ions travel away from it (Kumara, Serdyuk & Gubanski, 2009). Only a small portion of the gas near the corona tip is taking part to this process as these particles tend to recombine as they lose their kinetic energy away from the tip. With this recombination, a photon is created, helping to maintain the electron avalanche. Corona discharge is widely used by industries for many procedures, like separation of materials and sanitization of water. Many types of devices have been constructed for charging electrets. The most common device is the corona triode introduced by Bernard Gross in the 1970s. It consists of a thin wire set to high voltage, a metallic plate connected to ground where the sample lies and in between, a metallic grid set to the optimal voltage for charging the film. Such a device can measure the charging current as well as the surface potential while charging. The latest improved device can also indirectly control the current flowing through the sample by changing the potential of the metallic grid.

Having a uniform field is a very important aspect while charging films. Especially when it comes for piezoelectrets, as the field created inside a single void depend on the neighbor voids field as well (Mellinger, 2011).

Charging with a corona triode gives many advantages. One of them is the ability to increase linearly the surface potential of the sample  $V(t)$  during charging (Giacometti, Fedosov & Costa, 1999; Mellinger, 2011). While charging, the voltage across the sample can be calculated as

$$V_p(t) = \int_0^{l_3} E_p(x, t) dx \quad (2.41)$$

where  $x$  is the coordinate through the thickness direction and  $E(x, t)$  is the electric field applied across the thickness of the polymer. As the material

gets charged up, its surface potential gets closer to the potential of the grid reducing the current flowing through the sample  $I_s(t)$ . The current density  $j(t)$  is given by (Giacometti & Sinézio Carvalho Campos, 1990),

$$j(t) = \frac{I(t)}{A} = \rho_g(x, t) [\xi E_g(x, t) + v_c] + \frac{\kappa_3 \partial E_g(x, t)}{\partial t} \quad (2.42)$$

where  $v_c$  is the speed of the corona wind,  $\rho_g(x, t)$  is the charge density present between the grid and the sample,  $\xi$  is the ion mobility,  $E_g(x, t)$  is the electric field between the grid and the sample and  $\kappa_3$  the permittivity of air.

When  $j(t)$  is kept constant, the potential difference between the sample surface and the grid  $\Delta V$  is kept constant. Thus, by knowing the voltage of the grid,  $V_g(t)$ , the surface potential can be deduced from the following equation (2.43).

$$V_p(t) = V_g - \Delta V \quad (2.43)$$

The parameter  $\Delta V$  cannot be measured directly but by keeping  $j(t)$  constant,  $\Delta V$  is also kept constant.

When current remains constant, it is also much easier to integrate the total current across the thickness. This results in,

$$j_0 = \frac{C}{A} \frac{dV_p(t)}{dt} + j_c(t) + \frac{(dP(t))}{dt} \quad (2.44)$$

where  $C$  is the sample capacitance given by  $C = \frac{\kappa_3 A}{l_3}$ ,  $l_3$  is the total thickness of the sample,  $j_c(t)$  and  $P(t)$  are set to be the mean values of  $j_c(x, t)$  and  $P(x, t)$  respectively.

In order to find the surface potential of the sample  $V(t)$ , we need to make  $\Delta V = 0$ . For that, experimental data should be collected. By conducting a charging process in constant current mode without a sample, we have  $V_p = V_g$ . The constant current sensed at the other end (underneath the grid) gives a constant current density. This density can be linked with the voltage applied to the grid  $V_{g-cal}$  and thus  $\Delta V$ . This procedure is called current calibration procedure. When charging a sample at the same constant current density, the potential difference  $\Delta V$  between the grid and

the sample is known to be the same as  $V_{g-cal}$  the grid potential used at the current calibration.

Uniformity is also achieved when the current remains constant, as the potential between the grid and the surface of the sample is constant. In other words, the grid has always a higher potential than the sample surface. In case the sample has similar potential to that of the Grid, the charges would drift away from the sample, ruining that way the uniformity. The constant current method is an indirect method (as there is need of experimental data) to measure the surface potential. On the other hand, it is the easiest way of obtaining the surface potential curve while charging.

Charging with a corona device gives many advantages compared to contact charging. The charging process can be done in higher fields in comparison to capacitor-like charging where the maximum field is limited by the thickness of the sample. Current is distributed evenly on the surface of the material owing to the grid electrode. Finally, undesired destructive breakdown events across the sample's thickness are limited to smaller areas, securing the rest of the film. As this equipment is not a commercially available product for this cause, the major drawback is the difficulty of constructing such a device.

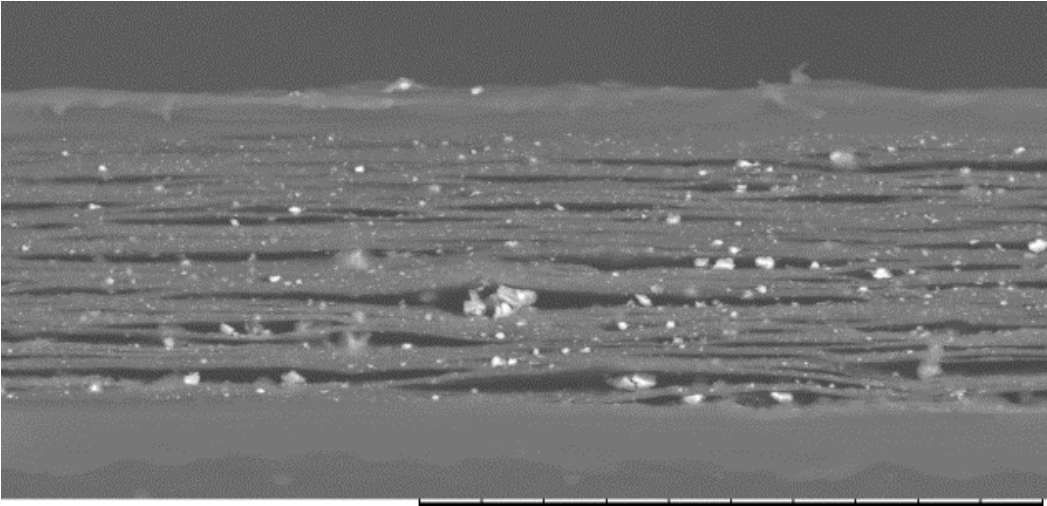
## **2.6 Energy harvesting (EH)**

Among the uses of piezoelectric materials, a recently increased in demand application is energy harvesting (EH). It is the process of converting into electricity the energy available from otherwise untapped sources. This can be, for example, environmental vibrations caused by machinery, temperature gradients around some heat source and any other source of mechanical or vibrational energy. Without EH, this energy is simply wasted. EH has come to prominence in recent years as it is an enabling technology for the Internet of Things (IoT), which the UK Government and the EU Commission are strongly supporting. As the production of battery powered portable devices has been increasing exponentially in the last decades, the problem of autonomy as well as the awareness of environmental issues arises.

Traditionally, vibrational energy harvesters are made of piezoelectric (PZT) ceramics. Despite its large  $d_{33}$  and  $k^2_{33}$  values ( $k^2_{33}$  around 0.5 for third, thickness, direction), this material lacks of physical properties like brittleness and energy to density ratio. As PZT has typical density of around  $7500 \text{ kg m}^{-3}$  its specific energy is in the order of  $4 \text{ J kg}^{-1}$  (for a PZT 5H in  $d_{31}$  mode (Wood, Steltz & Fearing, 2005)). More stretchable materials have come into picture which can solve the above problems. These materials are known as ferroic electrets

In the last 15 years, cellular polymers attracted the researchers' attention. Cellular polymers contain voids, each having the thickness of a few micrometers. As the functionality of the polymer depends on the dipole formed after the breakdown event explained earlier, it is crucial that the charging is handled based on the critical field of the voids. Among ferroelectrets (polymer films exhibiting piezoelectric properties), Cell-PP seems promising for EH. It has been found that with proper treatment and poling, cellular polypropylene shows large piezoelectric activity, with higher  $d_{33}$  coefficient compared to other polymers and comparable to that of PZT (Zhang, Hillenbrand & Sessler, 2004a).

Cell-PP is widely used for packaging and labelling of goods and it is being manufactured in roll to roll basis, having that way a low cost of manufacture. Its large encapsulated cells (Figure 2.3) allow the non-expanded material's density to be around 14 times less than PZT. Due to its light weight, it can have energy density of  $1.2 \text{ J cm}^{-3}$  (Qi, Petersson & Liu, 2014).



NCL7\_6551h0156 2015/03/02 NL D3.9 x1.0k 100 ?m

Figure 2.3. Cross sectional SEM micrograph of a Cell-PP polymer showing the voids. White spots are the  $\text{CaCO}_3$  particles.

The internal energy density of the system (neglecting the thermal term) is given by the sum of the mechanical and electrical work done

$$U = \frac{1}{2}\kappa_3\sigma_3 + \frac{1}{2}D_3E_3 \quad (2.45)$$

By substituting the two constitutive equations (equations 2.15 and 2.16) to 2.45, we have

$$\begin{aligned} U &= \frac{s_{33}^E\sigma_3 + d_{33}E_3}{2}\sigma_3 + \frac{d_{33}\sigma_3 + \kappa_3^\sigma E_3}{2}E_3 \\ &= \frac{s_{33}^E\sigma_3^2}{2} + \frac{d_{33}\sigma_3 E_3}{2} + \frac{d_{33}\sigma_3 E_3}{2} + \frac{\kappa_3^\sigma E_3^2}{2} = \\ \frac{s_{33}^E\sigma_3^2}{2} + d_{33}\sigma_3 E_3 + \frac{\kappa_3^\sigma E_3^2}{2} &= U_e + 2U_m + U_d \end{aligned} \quad (2.46)$$

Where  $U_m$  is the mutual dielectric and elastic energy density,  $U_e$  is the elastic internal energy density and  $U_d$  is the dielectric internal energy density. These three energies are linked together with the electromechanical coupling coefficient  $k$ .

$$k^2 = \frac{U_m^2}{U_e U_d} \quad (2.47)$$

In other words  $k^2$  is the mechanical energy over the total internal stored energy. That gives us

$$k_{33}^2 = \frac{(d_{33}\sigma_3 E_3)^2}{s_{33}^E\sigma_3^2 \kappa_3^\sigma E_3^2} = \frac{d_{33}^2}{\kappa_3^\sigma s_{33}^E} \quad (2.48)$$

There are many procedures for enhancing the piezoelectric coefficient ( $d_{33}$  value) of the polypropylene films. Chemical modification (An *et al.*, 2009) and inflation of the voids via gas GDE processes (Hillenbrand & Sessler, 2000; Zhang, Sessler & Hillenbrand, 2007), are two procedures that contribute to the increment of the  $d_{33}$  constant and the thermal stability of the film. Both procedures though, cause a reduction of the Young's Modulus (Eddiai *et al.*, 2012). This reduction is meaningful for applications like transducers but not particularly useful for EH: the resulting material is simply softer and needs to be squeezed more to achieve about the same energy output. As the need for autonomous-powered, light weight and wireless devices is rising, a few research groups have recently investigated Cell-PP piezoelectric properties for Energy Harvesting, (Zhang, Sessler & Wang, 2014; Pondrom *et al.*, 2014; Anton, Farinholt & Erturk, 2014; Kim, Kim & Kim, 2011). For human-based EH and the development of Body Area Networks, Cell-PP is a good choice, due to its light weight and mechanical flexibility. With a Young Modulus in the order of 1 MPa (compared to 60 GPa of PZT), Cell-PP is compliant enough for applications where minimal reaction forces are desired.

It is also known that charging at optimal pressures, increases the piezoelectric coefficient (Qiu, Mellinger & Gerhard, 2008). Since pressure has a direct impact on the breakdown threshold as well, there is an optimal pressure as Townsend's model of the Paschen breakdown suggests. All of these parameters are analyzed in the next chapter.



## Chapter 3. Literature Review

### 3.1 Piezoelectric Materials

There are many types of solids that exhibit piezoelectricity that are classified into three main categories: single crystals, ceramics and polymers. A brief review of these categories and their piezoelectric properties is presented in this section. It is to be noted from the beginning that some of their properties depend on the excitation frequency, temperature and material composition (in case of composites).

#### 3.1.1 Single Crystals

Naturally occurring quartz crystals, like Silicon dioxide ( $\text{SiO}_2$ ), are being used as resonators for watches and electronics. In the last 50 years, they have been also used for pressure transducers. Some crystals from the perovskite family, like Barium Titanate ( $\text{BaTiO}_3$ ), Strontium Titanate ( $\text{SrTiO}_3$ ) and Lead Titanate ( $\text{PbTiO}_3$ ), are piezoelectric materials and they are used in mixtures to create piezoelectric ceramics. There are also synthetic crystals like Lanthanum Gallium Silicate ( $\text{La}_3\text{Ga}_5\text{SiO}_{14}$ ), Gallium Phosphate ( $\text{GaPO}_4$ ), Lithium niobite ( $\text{LiNbO}_3$ ) and Lithium Tantalate ( $\text{LiTaO}_3$ ). Among them,  $\text{LiNbO}_3$  and  $\text{LiTaO}_3$  have high Curie point temperatures of more than  $1100\text{ }^\circ\text{C}$  and over  $600\text{ }^\circ\text{C}$  respectively. Both are used as a replacement to Quartz with the latter one being superior to naturally formed Quartz as the Silicon atoms are replaced with Gallium and Phosphorus. This change, makes them also better for applications where high temperatures of operation cannot be avoided (Fritze, Schulz & Richter, 2014; Silva, 2014). In terms of piezoelectric properties, a single crystal PMN-PT with Ti / Au- $\text{MnO}_x$  nanocomposite electrodes has a  $d_{33}$  of  $2250\text{ pC/N}^{-1}$  (Chang *et al.*, 2018). PMN-PT also shows high electromechanical coupling coefficient  $k^2_{33}$  of 0.78 (Yamamoto *et al.*, 2013) and high dielectric constant reaching 8000 for the third direction (Cao *et al.*, 2004) depending on the composition.

### 3.1.2 Ceramics

Ceramic piezoelectric materials have been used worldwide as sensors and actuators as they offer high piezoelectric coefficients, especially in thickness direction, ranging from 265 pC N<sup>-1</sup> (Zhang *et al.*, 2006), up to more than 600 pC N<sup>-1</sup> (Liu & Ren, 2009; Wang, Li & Lu, 2011) reaching even 1600 pm V<sup>-1</sup> (Jin *et al.*, 2018) for the case of PZT nanorod arrays. They are cost effective and have high thermal stability as they are able to withstand temperatures ranging from 200 °C for PZT-4 to more than 800 °C for CBN (Turner ... Shrout, 1994). A detailed review for these ceramics is given by (Shinekumar & Dutta, 2015). The most important member of ceramics (in terms of piezoelectricity) is PbTiO<sub>3</sub>, as it is one of the most common piezoelectric member of the PbZr<sub>(x)</sub>Ti<sub>(1-x)</sub>O<sub>3</sub> family (mostly known as PZT, the trade name of one such material). It is a lead based, high density material with high permittivity (values of 3000 have been reported (Liu & Ren, 2009)) and superior piezoelectric properties (piezoelectric coefficients around  $d_{33}=600$  pC N<sup>-1</sup>  $d_{31}=-260$  pC N<sup>-1</sup> and  $d_{15}=730$  pC N<sup>-1</sup> and coupling factors  $k^2_{33}=0.56$ ,  $k^2_{31}=0.15$  and  $k^2_{15}=0.46$  respectively for PZT 5H).

Conventional PZT ceramics contain lead oxide, which is restricted in many countries due to its toxicity. In the last few years, the attention was drawn on the development of lead-free piezoelectric ceramics. There are two main categories of lead free ceramics: perovskites and non-perovskites. Among them, perovskite ceramics are widely studied, as they have better piezoelectric properties compared to the non-perovskite ones (Panda & Sahoo, 2015). Their piezoelectric coefficient and permittivity depends on their grain size (Tan *et al.*, 2015) and the sintering temperature (Malič *et al.*, 2015). Piezoelectric coefficients from 190 pC N<sup>-1</sup> (Bechmann, 1956) to 620 pC N<sup>-1</sup> (Liu & Ren, 2009) have been reported with dielectric constants of even 5000 (in case of the coarse grain Barium Titanate BaTiO<sub>3</sub> ceramic (Arlt, Hennings & de With, 1985)). Furthermore, their electromechanical coupling coefficient can reach values of  $k^2_{33}=0.3$ .

Despite their good piezoelectric properties, the high density of both lead based and lead-free ceramics (depending on lead content ranging from 4250 kg m<sup>-3</sup> in the case of lead-free KNN ceramics (Liu *et al.*, 2015) to >

7500 kg m<sup>-3</sup> for a typical PZT ceramic), their brittleness (that limits the mechanical strain that can be applied on them) and their Young's Modulus (around 50 GPa) makes them weak candidates for applications where cyclic deformation in low frequencies with minimal reaction forces is required (eg. human based EH).

### **3.1.3 Polymers**

In order to address the problems of the ceramic based piezoelectrics, polymeric materials have been studied. Film Ferroelectrets, and among them Cellular Polypropylene (Cell-PP), gained interest in the last decades. Their mechanical properties (lightweight, flexible, acoustic impedance close to that of air (Sborikas & Wegener, 2013) and endurance in high levels of strain), electrical properties (high values of  $d_{33}$ ), as well as their low cost make them a good choice for a variety of applications.

There are two main types of piezoelectric polymers. Bulk polymers like PVDF and voided polymers like Cell-PP. The former appears in various geometric configurations depending on the processing conditions (Ye *et al.*, 2013). Being a polymeric material, PVDF has four times lower density than PZT (around 1800 kg m<sup>-3</sup>) and Young's modulus in the thickness direction ( $c_{33}$ ) in the range of 8-9 GPa. PVDF is often used in  $d_{31}$  mode with typical constant of  $d_{31}=28$  pC N<sup>-1</sup> and electromechanical coupling coefficient of  $k^2_{31}=0.014$  (HARRISON & OUNAIES, 2001). The piezoelectric constant in thickness direction ( $d_{33}$ ) for a single film has a typical value of -30 pC N<sup>-1</sup> (Liu *et al.*, 2015; Kepler & Anderson, 1978) and for shear mode  $d_{15}=-23$  pC N<sup>-1</sup> (Esterly, 2002).

Cellular polymers, are non-homogenous and have enclosed voids with a variety of dimensions. These voids are created during the manufacturing process. Cell-PP for example, developed in 1980s at Tampere University of Technology (TUT), is created by heating up and bidirectional stretching of polypropylene mixed with nucleating agents (CaCO<sub>3</sub>) (Raukola, 1998). Once the mixture cools down, the material gets strengthened as the molecules are now oriented and stay that way. By this procedure, voids of few microns in thickness and hundreds of microns in length are formed

inside the bulk of the material. The average  $d_{33}$  of Cell-PP does not exceed a few hundreds of  $\text{pC N}^{-1}$ , with some exceptions where the reported values of  $d_{33}$  can be 40 times greater than PVDF (up to  $1400 \text{ pC N}^{-1}$  (Zhang, Hillenbrand & Sessler, 2004c) for low excitation frequencies). This enhancement though comes at the cost of stiffness and density, under a certain procedure called gas diffusion expansion (GDE). Without GDE, Cell-PP has a density ranging from  $550 \text{ kg m}^{-3}$  to  $800 \text{ kg m}^{-3}$  depending on the density of the external, non-voided layers and the proportion of  $\text{CaCO}_3$  particles in the mixture, making it three and thirteen times less dense than PVDF and PZT respectively. Finally, the Young's Modulus in thickness direction is typically in the order of few MPa. It can range from  $0.5 \text{ MPa}$  to  $10 \text{ MPa}$  depending on the frequency of excitation, the inflation of the sample and the applied stress. That means that Cell-PP is three orders of magnitude more compliant than PZT. The above properties, makes Cell-PP one of the best candidates in terms of low frequency, high strain energy harvesting and for applications where sensitivity to inputs like vibrations, sound waves etc. is needed. As it is a cheap, lightweight and flexible material, it might be advantageous to be used as a piezoelectric material in applications like wearable energy harvesting or applications where large areas need to be covered.

### **3.1.4 Composites – Engineered cellular polymers**

Composites are materials that combine some of the above-mentioned materials, either from one or two categories. Combining ceramics with polymers is commonly done for ultrasonic transducers (Smith, 1989), where piezoelectric ceramic rods are typically embedded inside a non-piezoelectric polymer. This type of composite is usually referred as “1-3 piezocomposite”. The resultant composite material has low acoustic impedance due to the polymer layer and high electromechanical coupling coefficient resulting from the ceramic part. Nowadays, these composites are commercially available and have  $d_{33}$  ranging from  $60$  to  $160 \text{ pC N}^{-1}$  depending on the composition (Jain *et al.*, 2015; Fang *et al.*, 2015). Another commonly used 1-3 composite material is the PMN-PT. Depending on the composition it can reach coupling coefficients  $k^2_{33}$  of

around 0.79 with Young's modulus of 104 GPa to 170 GPa  $d_{33}$  of 1780 pC N<sup>-1</sup> to 2000 pC N<sup>-1</sup> and density of around 8000 kg m<sup>-3</sup> (Kim *et al.*, 2010; Li *et al.*, 2014; Zhang *et al.*, 2011).

Fouad *et. al* (Belhora *et al.*, 2013) studied an electret / electrostrictive polymer composite for the purpose of energy harvesting producing 84 mW m<sup>-3</sup> of energy density.

Another way of combining two materials into a composite is by combining inorganic particles with the polymer into a uniform dispersion (known as "0-3 piezocomposites"). A detailed procedure is given by K. Prashanthi *et.al* (Prashanthi *et al.*, 2013). The resultant composite is dense in most cases, as the particles used have high density (1380 kg m<sup>-3</sup> in the case of Prashanthi *et. al.* (Prashanthi *et al.*, 2013) and higher when BaTiO<sub>3</sub> nanoparticles are used).

On the other hand, ferroelectret composites and engineered ferroelectrets (engineered in the sense that the shape of the voids is chosen in order to function as Piezoelectrets) have low density, high flexibility and are more compliant than the ceramic based composites. Fluoroethylenepropylene / Polytetrafluoroethylene (FEP / PTFE) films are examples of these composites (Hu & von Seggern, 2006; Zhang *et al.*, 2010; Pisani Altafim *et al.*, 2012b). In this case, non-porous FEP layers are fused with porous, already charged, PTFE layers while under mechanical pressure (Zhang *et al.*, 2010). This way, the cavities are closed and the charges are retained within them.

Finally, engineered cellular polymers are also worth a mention (Qiu, 2010). The only difference with cellular polymers mentioned before is that the void pattern within the film is defined by the manufacturing process. There are techniques that have as an outcome randomly distributed voids inside the film (Saarimäki *et al.*, 2006) but will not be discussed here.

The most common way of achieving control of the microstructure inside the polymer, is by template patterning. X. Zhang *et. al* (Zhang *et al.*, 2012b) were able to manufacture such a structured film out of FEP layers via means of template patterning and fusion bonding process. With this method, quasi-static piezoelectric coefficients of even 3000 pC N<sup>-1</sup> in

thickness direction were reported. Also, samples with very good thermal stability, compared to other polymers (thermally stable at 120°), can reach quasi-static  $d_{33}$  values of 1000 pC N<sup>-1</sup>. This comes again at the cost of stiffness, as the large voids used in their study (60 μm thickness) made the resultant polymer to have a Young's Modulus of 210 kPa.

In another study (Wang *et al.*, 2012), silicon wafer-PDMS composites were manufactured for MEMS transducers (The fabrication process is well described by the study itself (Wang *et al.*, 2012). The authors investigated isolated (sample a) and interconnected (sample b) square voids of 50 μm. In the latter case, the voids are connected with 20 μm wide channels. The resultant piezoelectricity was more than two times higher for sample b. This might be due to the channels themselves acting like voids making the charges residue there after charging. Another parameter taken into consideration for sample b was the coating of the voids with a thin layer of PTFE solution which further increased four times its piezoelectric activity. Another reason why sample b had higher piezoelectric coefficient might be the fact that its functionalization started earlier (keeping in mind that the same external field was applied to both samples). Results about the required poling field were presented by the authors. It was observed that the minimum breakdown field was lower for sample b. It might be the case that the 20 μm channels were the first to reach their breakdown field and thus brought the critical field of the rest of the cavities down. Similar results were presented for Cell-PP by (Harris & Mellinger, 2014) where isolated voids gained less charge density than that predicted for embedded voids inside the material. Another parameter to consider is that the piezoelectric activity was measured under 89 kPa load. This might mean that the material could behave non-linearly. As mentioned by X. Zhang *et. al.* (Zhang *et al.*, 2007) the applied force in respect to the surface area (compressive stress) has a role on  $d_{33}$ . When this ratio gets big, the sample becomes stiffer – denser and the piezoelectric coefficient might get smaller.

Another way of creating engineered polymers is screen printing. Viscous ink is pressed against a patterned stencil. Ink passes through the stencil's open areas creating that way patterns on the substrate. It is reported

(Sborikas *et al.*, 2014) that mixing monomer, photo-initiator and solvent with a specific formulation, a uniform distribution of the voids and void thicknesses could be obtained.

In summary, a cellular polymer piezoelectric material with optimal mechanical properties (low density, high Young's modulus) and high piezoelectric properties (high  $d_{ij}$ ,  $g_{ij}$  and  $k^2_{ij}$ ) can be achieved by controlling as many structure and material parameters as possible while manufacturing the polymer.

## **3.2. Charging Methods**

### **3.2.1 Contact charging**

There are many procedures for charging piezoelectrets. The simplest and easiest method is contact charging. It is essentially a capacitor-like charging where the film has electrodes on both its surfaces and it is inserted between two flat parallel metal plates (Lindner *et al.*, 2002; Mellinger, 2011; Cury Basso *et al.*, 2013). The potential of the plates is increased and electric field is created within the film. The electric field of charging is determined by the sample's thickness. Usually, a constant DC potential is used, with an exception reported by Mellinger (Mellinger, 2011). A  $\pm 6$  kV triangular wave is applied in order to study the increment of charge density inside the voids for each step increment of the potential.

This method has limitations though, as the applied field is limited by the sample's thickness in the sense that higher fields will lead to destructive breakdowns across the film. Once a breakdown (spark) occurs, the charging process cannot continue, as a low dielectric strength path is created for the charges between the two surfaces.

### **3.2.2 Corona charging**

The most widespread technique of charging electrets is via a corona charging equipment. The basic parts of a corona charger are the corona

tip and the grounded plate. In later modifications, a grid is inserted between these two for uniformity of the field.

Many researchers have experimented with corona chargers (Giacometti, 1987; Giacometti & Sinézio Carvalho Campos, 1990; Campos, Giacometti & Oliveira, 1992; Giacometti, Fedosov & Costa, 1999; Molinié, 1999; Bouteffaha *et al.*, 2013; Deng & Adamiak, 1997; Kumara, Serdyuk & Gubanski, 2009; Waller, Iqbal & Safari, 1989; Sahli *et al.*, 2003; Herous *et al.*, 2009). A variety of designs have been built since 1940s when Carlson's invention of an electro-photographic system proved to be a better way of sensitizing a photoconductive plate. The point to plate configuration (Braña *et al.*, 2011) has a major drawback, as the field generated between the wire and the plate is not uniform in any direction. The field has a conic shape and is gradually reducing towards the ground plate. A metal mesh (grid) can be placed between the corona wire and the ground plate, to keep the electric field below it uniform. This design is called "corona triode" and is the most common design found in the literature (Giacometti & Sinézio Carvalho Campos, 1990; Giacometti, 1987; Deng & Adamiak, 1997; Bouteffaha *et al.*, 2013). The charging field is determined by the distance and the potential of the grid.

The importance of the grid to the field uniformity is demonstrated by (Bouteffaha *et al.*, 2013; Giacometti, 1987). The current density is constant near the centre of the sample and decreases near the edge of the grounded plate. A way of testing the sample charge uniformity, is by checking different areas of the charged sample for its piezoelectric activity (Kressmann, 2001).

Another way of increasing field uniformity is to surround the corona tip and the area above the grid by a metal cylinder, which is set to different electric potentials as proposed by (Giacometti & Sinézio Carvalho Campos, 1990).

Another easily controlled parameter that influences the uniformity and shape of the field underneath the grid, is the distance between the grid and the sample (Giacometti, 1987) as well as the charging current (Giacometti & Sinézio Carvalho Campos, 1990). It is found that the field is

more uniform when charging under lower current (Giacometti & Sinézio Carvalho Campos, 1990). Finally, as the distance between the grid and the ground plate decreases, the shape of the field underneath acts upon a more defined area (fades sharply at the edges of the sample) (Bouteffaha *et al.*, 2013). Based on the above, the sample dimensions needs to be considered before the construction of the corona device, as the field affected area is determined by the area that the grid covers.

Charging with many corona points or “saw blade” electrode (Bouteffaha *et al.*, 2013) generates higher current densities compared to a single corona point. The reason is that ions are generated in higher rates as the ionizing plasma area is bigger. This configuration has an effect on the charging time, as the surface of the sample will increase quicker and the charging procedure ends sooner. It is demonstrated by M. Paajanen *et. al.* (Paajanen, Wegener & Gerhard-Multhaupt, 2001a) that there is no improvement in  $d_{33}$  when charging under higher currents.

Another configuration worth mentioning is the ‘third electrode’ point to plate. An electrode surrounds the corona tip and gets either biased to a voltage close to it or grounded (Moon, Chung & Lee, 1994). Both Positive and negative voltages were applied to the corona tip. It was demonstrated that the corona discharge procedure could be controlled more easily by controlling the voltage of the third electrode.

Among various techniques, the corona triode configuration is proved to be better for charging piezoelectrets as it allows the control of more parameters in contrast to contact charge or any other corona configuration (Giacometti, Fedosov & Costa, 1999; Giacometti & Sinézio Carvalho Campos, 1990). The greater advantage though, is the ability of charging at constant current, which introduces charging uniformity and logging or even controlling almost all the crucial parameters for the charging of the ferroelectrets (Giacometti & Sinézio Carvalho Campos, 1990; Giacometti, Fedosov & Costa, 1999; Dias, Marat-Mendes & Giacometti, 1989; Giacometti & DeReggi, 1993; Giacometti, 1987). The potential of the sample can be indirectly inferred by keeping constant the field below the grid (Paajanen, Wegener & Gerhard-Multhaupt, 2001b).

A big draw-back of these devices is that they are not commercially available and building such a device is difficult due to the large voltages involved. Furthermore, it is difficult to control the pressure of the chamber, which seems to increase the piezoelectric coefficient of the film (Paajanen, Wegener & Gerhard-Multhaupt, 2001b; Harris & Mellinger, 2012). Another drawback of corona poling is the induced damage on the surface of the film, demonstrated by R.A. Hill et al. (Hill, Knoesen & Mortazavi, 1994). When this damage propagates, the dielectric strength of the material reduces and a catastrophic breakdown occurs. In order to prevent this, a removable, thin polymer can be placed on the top of the sample as shield. Furthermore, it is beneficial for this thin shield to have low surface roughness, in order to reduce scattering losses (Hill, Knoesen & Mortazavi, 1994).

The whole procedure is based on electron avalanche that occurs when a conductor (the corona tip) is set to high potential. Conductors with small areas, produce larger fields than large area conductors, under the same potential. Thus, the electrode used for the corona tip is usually a thin wire of tens of microns diameter.

The sample is electroded on one side and centred underneath the corona tip, with the electrode facing down. The tip is risen to an electric potential and the field produced is determined by the distance between the corona tip and the ground plate. The current flowing through the sample  $I_s$  is usually monitored with an electrometer during the charging procedure. A probe is attached to the bottom electrode of the sample, connecting the other end to the ground via an electrometer. The charging process ends when the surface potential of the non-electroded side of the sample reaches the equilibrium. This event is designated when the current  $I_s$  becomes zero. By integrating the current, the obtained charge density of the sample can be found. Figure 3.1 shows a negative corona discharge process for a corona triode device. When the field gets high enough, electrons are freed from the molecules of the gas (ionization of gas). These electrons are either accelerated towards the corona tip (positive corona) or away from it (negative corona) depending on whether the potential of the tip is positive or negative. On their way, they hit other

molecules making them lose an electron (electron avalanche). This chain reaction happens close to the corona tip (ionizing plasma region). The formed ions (either cations<sup>+</sup> or anions<sup>-</sup>) continue their way towards the ground but having insufficient energy, they do not cause further ionization (non-ionizing plasma region). Finally, these particles reach the sample (Unipolar region). The particles themselves do not have the energy to penetrate into the bulk material, but they reside on the surface raising this way its surface potential. When that potential increases, the voids inside the polymer experience breakdowns as discussed above.

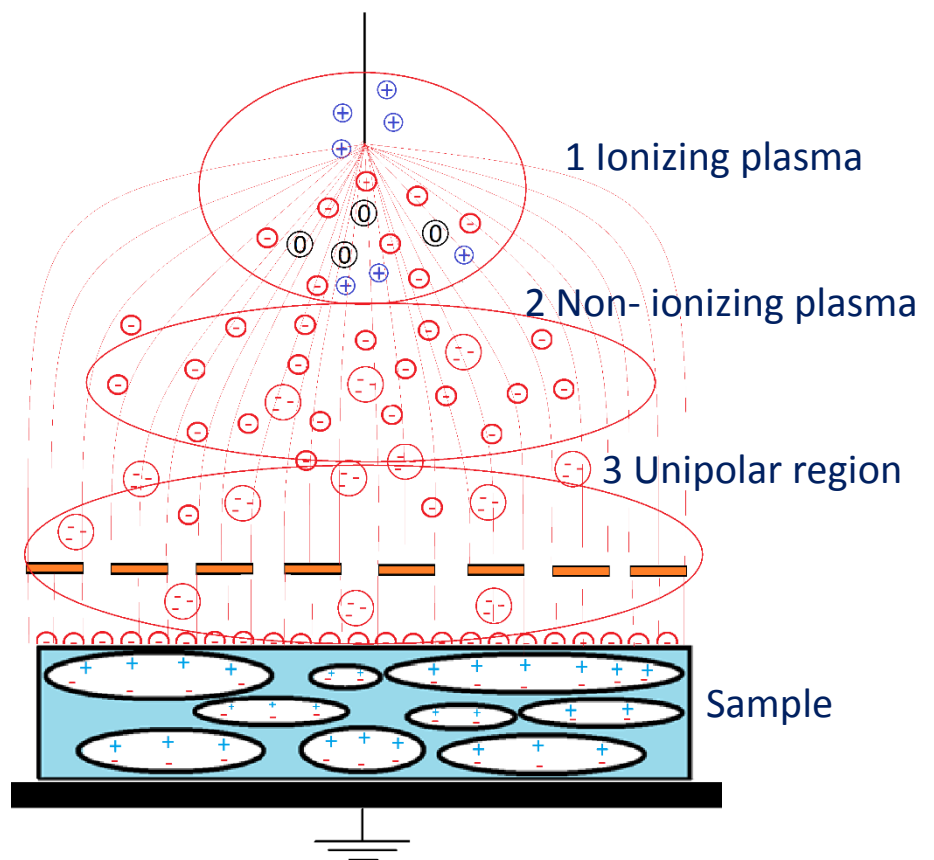


Figure 3.1 Corona discharge process. The process consists of three regions: 1) Ionizing plasma: Electrons are freed from molecules generating electron avalanche 2) Non-ionizing plasma region: Electrons combine to form negative ions 3) Unipolar region: Negative ions continue their way towards the sample

This process is more complex than the contact charging, as it is influenced by environmental parameters like temperature. (Giacometti & Sinézio Carvalho Campos, 1990) demonstrated that the sample current density reduces with temperature. This might be an effect of less ions reaching the

sample, as the high temperature makes them recombine easier. Another significant parameter is the voltage sign of the corona tip. It is found that negative coronas, increase the obtained piezoelectric  $d_{33}$  coefficient compared to positive coronas, under the same field (Qiu *et al.*, 2007a). This might be attributed to more secondary electrons being liberated with negative coronas compared to positive coronas. Finally, negative corona tend to produce more ozone compared to positive corona discharge (Pekárek, 2009).

### **3.2.3 Other charging techniques**

Another technique worth mentioning is electron beam (Glickman *et al.*, 2006; Gross *et al.*, 1987). As this technique is done in low vacuum, the electrons do not collide or recombine with other ions and thus they gain higher kinetic energy, which allows them to penetrate the surface of the material. Recently a soft X-ray charging method was tested on Parylene electrets and showed some significant results of piezoelectric constants of around  $1500 \text{ pC N}^{-1}$  (Feng & Suzuki, 2013; Feng *et al.*, 2012).

### **3.3 Functionalization parameters of cellular electrets**

The final piezoelectric properties of electrets are influenced by various parameters describing either the charging process or the material properties (both mechanical and electrical). For example, Cell-PP shows high piezoelectric coefficient  $d_{33}$ , depending on the inflation by Gas Diffusion Expansion (GDE) procedure (Wegener *et al.*, 2004b; Hillenbrand *et al.*, 2003; Wegener *et al.*, 2004c; Zhang, Hillenbrand & Sessler, 2004a; Wegener *et al.*, 2006; Hillenbrand, Sessler & Zhang, 2005) its inner voided structure (Tuncer, 2005; Wegener *et al.*, 2004a), and the poling parameters (Pengfeng Zhang *et al.*, 2005; Zhukov & von Seggern, 2007b; Mellinger, 2011; Harris & Mellinger, 2014; Paajanen, Wegener & Gerhard-Multhaupt, 2001b; Qiu, Gerhard & Mellinger, 2011). In addition, the thickness of the voids (Mellinger, 2011; Harris & Mellinger, 2014), in combination with the pressure (Qiu, Mellinger & Gerhard, 2008; Harris & Mellinger, 2012), the gas inside them (Paajanen, Wegener & Gerhard-

Mulhaupt, 2001b; Qiu, Mellinger & Gerhard, 2008) and the electric field during charging (Pengfeng Zhang *et al.*, 2005; Mellinger, 2011; Zhukov & von Seggern, 2007b; Qiu *et al.*, 2007a; Altafim *et al.*, 2009a; Sborikas & Wegener, 2013), also affect the final charge density of the voids and the piezoelectric constant  $d_{33}$ . The above parameters can be characterized to two categories: a) environmental or external parameters i.e. parameters of the environment surrounding the sample and b) internal parameters i.e. parameters of the film that are related to the properties of the electret. In some cases, external and internal parameters will affect each other. A short review on the impact of these parameters is given below.

### **3.3.1 Void thickness and functionalization Voltage**

The mechanism behind charging Cell-PP is the creation of dipoles when the charges of opposite polarity get trapped inside the bulk voided part of the material. This happens when the externally applied field is large enough for a Townsend discharge to occur in each individual void. The minimum field needed for this discharge event is called critical field ( $E_b$ ). The critical field in micrometre voids is described by Paschen's law, which was discovered empirically by Friedrich Paschen. The Paschen's curve describes the minimum voltage needed for a discharge to happen between two parallel metal plates. The resultant critical field  $E_b$  is a product of the distance between the two parallel plates and the pressure of the gas existing between them. Furthermore, temperature and gas ionization energy are also considered by Paschen's law, defining the two Paschen's coefficients.

A. Mellinger and O. Mellinger (Mellinger, 2011), compared the theoretically and experimentally obtained  $d_{33}$  after contact charging for a variety of differently expended films under GDE. The void thickness distributions as well as the thickest voids for each film were obtained by SEM images. Based on the thickest void, the critical field was calculated for each film. The actual critical breakdown field was found to be higher than the calculated one in every case. The study also revealed higher obtained  $d_{33}$  than calculated. A possible explanation to this phenomenon is that the

critical field of a void is influenced by neighbour voids that gain charge density earlier. This way, the net field of any void inside the film is disturbed. Later study done on individual, lab-made, voids by S. Harris and A. Mellinger (Harris & Mellinger, 2014), showed an agreement between the theoretical and obtained values of critical field.

The charge density inside an individual void (and as a result its coefficient  $d_{33}$ ) increases linearly with the applied electrical field (Altafim *et al.*, 2009a; Pengfeng Zhang *et al.*, 2005; Mellinger, 2011) when the field is larger than the critical field and up to the equilibrium field where no more charges can be forced inside the material (Pengfeng Zhang *et al.*, 2005; Altafim *et al.*, 2009a). Studies done on Cell-PP, showed that the equilibrium field is about two times the critical field of the void (Pengfeng Zhang *et al.*, 2005).

This equilibrium might be due to the large back discharges occurring under higher fields (Mellinger, 2011). Back discharge is essentially the recombination of the dipoles inside the voids, when the externally applied field is removed.

M. Lindner *et al.* (Lindner *et al.*, 2002) demonstrated that the event of a dielectric barrier discharge inside the film during charging, is accompanied by light emission. This phenomenon, lasts a few ns and can be detected with a photomultiplier. In addition, (Qiu *et al.*, 2007b) showed that the strength of the light emission increases linear with the externally applied field. Studies done to lab-made individual voids, confirmed this linear increment of light emission over electric field (Harris & Mellinger, 2014). The light emission for different void thicknesses is also observed in this study. There is confirmation that thicker voids gain larger charge density than thinner voids, for the same field applied (Harris & Mellinger, 2014).

S. Zhukov and H. von Seggern (Zhukov & von Seggern, 2007a) showed that this light emission takes place only when current is passing through the sample. When the current flowing from the sample becomes zero, the charging process is finished and there are no more dielectric barrier discharges happening.

Voided polymer films like Cell-PP consist of a variety of morphologically different voids inside the bulk of the material. The void thickness

distribution is widespread with voids ranging from less than a micron up to 5 microns for the non-treated material. According to Paschen's law of critical breakdown fields in micrometre voids, the thin voids of the virgin (non-treated) material have high critical breakdown field. They require high charging fields and therefore, the obtained  $d_{33}$  by the end of the charging process is relatively small (Harris & Mellinger, 2012) compared to larger voids charged under the same field. It is advantageous to have large voids inside the material as the critical field of the voids decreases proportional to their thickness. According to Paschen's law, a void of 8  $\mu\text{m}$  thickness has a critical field of  $150 \text{ MV m}^{-1}$ . As the average dielectric strength of a 97  $\mu\text{m}$  Cell-PP sample is around  $100 \text{ MV m}^{-1}$ , it is impossible for voids smaller than 8  $\mu\text{m}$  to get charged before a discharge occurs across the thickness of the material. With a proper GDE, larger voids can be charged under lower fields, avoiding a catastrophic breakdown to occur across the sample as happens when poling under high fields.

There is a variety of morphologically different voids within the film. These voids can range between a few microns to tens of microns in width and length, depending on the expansion of the film. A method of controlling the void thickness distribution before GDE, is blending specific sized additives like solid  $\text{CaCO}_3$  when manufacturing the film (Gilbert-Tremblay, Mighri & Rodrigue, 2012). These particles are mixed with the polymer and therefore the void thickness distribution is controlled by the size of the particles. The void thickness distribution also changes with GDE but this simply leads to an increment of the material thickness and a more spread distribution, thus doesn't entirely control the thickness of the voids. A more detailed review of GDE process is given in sub section 3.4.

A solution to the above problem is given by engineered ferroelectrets made of tubular channels, as discussed in section 3.1, e.g. (Altafim *et al.*, 2009b; Pisani Altafim *et al.*, 2012a, 2012b). The resulting void geometry is controlled by thermal patterning and fusing of polymer films. A big benefit of these 'control pattern' voided films is the control of the film's compliance and the obtained charge density, which is of importance for sensor and energy harvesting projects. Finally, by knowing the shape and number of

voids, theoretical modelling becomes straightforward and the response of the sample is predictable before manufacturing.

### **3.3.2 Void Pressure**

The pressure inside the voids has a significant role to the functionalization of the film (Kim ... Barnard, 2010; Li ... Shung, 2014; Y. Zhang ... Luo, 2011). As demonstrated by H. Scott & A. Mellinger (Harris & Mellinger, 2012), there is an increment of the final  $d_{33}$  of the Cell-PP films by 2.5 times when charging the film under elevated pressures (close to 0.3 Mpa for this case). It was also shown that the pressure increment reduces the back discharges, which mainly happens inside the larger voids. In a similar study of X. Quin and A.Mellinger (Qiu, Gerhard & Mellinger, 2011), it is concluded that there is an optimum pressure up to which the piezoelectric constant rises. It was found that there is a narrow optimum peak of void pressure, around 0.2 MPa. Further increment of pressure, results to reduction of the final  $d_{33}$ . In a similar study (Paajanen, Wegener & Gerhard-Multhaupt, 2001b), elevated pressures of up to 0.5 MPa were applied to the film, having  $N_2$  gas inside their voids. The piezoelectric constant  $d_{33}$  showed no reduction even for values of 0.5 MPa of pressure.

Pressure fits in the empirical equation of Paschen' law and is one of the main parameters that affects the functionalization of the voids. Keeping in mind the wide void thickness distribution, there is not a single optimal pressure for charging all of the voids. It can be concluded that there is a specific optimum pressure for each sample, based on its dominant void thickness of the void thickness distribution and the gas enclosed inside the voids.

Charging at elevated pressures with a corona triode is tricky. There is need of a pressurized chamber that can hold the corona charger. On the other hand, for contact charging is easy to control pressure, as a static mechanical load can be applied on the top of the film.

### **3.3.3 Temperature**

Another parameter that has an influence on the retention of the charges inside the voids is the temperature of the sample while charging (von Seggern, 1981). It is shown by Thermally Stimulated Discharge (TSD) that when charging at elevated temperatures, the thermal stability of cellular PP increases significantly. This increment might be a result of the charges trapped deeper on the borders of the voids as molecular relaxation is taking place. In addition, temperature has an impact on the critical field as the Paschen's Law predicts. Dipoles can be created under lower fields when the temperature is high.

### **3.3.4 Permittivity of the material and the gas inside the voids / chamber**

The permittivity of the material is one of the most important parameters. It is shown that the increment of permittivity has a direct effect to the piezoelectric coefficient of the material (Zhang *et al.*, 2012a).

On the contrary, the electromechanical coupling coefficient  $k_{33}^2$  decreases proportionally to the permittivity of the sample. In general, permittivity is one of the most difficult parameters to control. It is known that the total permittivity of the sample is significantly increased by the charging process itself (Zhang ... Xia, 2007) but the only way of actively increase the permittivity of the material is by creating composites.

In case of corona charging, when the gas inside the charging chamber (Korge, Laan & Paris, 1993) as well as the gas inside the voids is changed (Paajanen, Wegener & Gerhard-Multhaupt, 2001a) the piezoelectric coefficient increases. When gases with large electrical breakdown strength and higher permittivity, like SF<sub>6</sub>, exists inside the chamber, the charging process can be done in higher fields without spark occurring.

M. Paajanen et al (Paajanen, Wegener & Gerhard-Multhaupt, 2001a) showed that changing the air inside the voids to a gas with relatively lower breakdown strength, the piezoelectric activity was maximised. Specifically,

expansion with N<sub>2</sub> gas gave almost 6 times higher piezoelectric coefficients than with SF<sub>6</sub> gas.

In addition, studies show that less back discharges occur inside the voids when the permittivity of the gas is higher. Paschen's law combines the above conditions (void thickness, gas electronegativity, applied field and void pressure) under which a breakdown occurs within a micrometer sized gap. The law suggests that there is a minimum field required for a discharge to occur. It applies to the individual voids inside the polymer (Harris & Mellinger, 2014) and to some extent to the whole polymer (Mellinger, 2011), where discharges in a certain void lowers the critical field of its neighbor voids.

### **3.3.5 Humidity**

Humidity is one of the parameters that has an influence on the sample's surface potential decay after charging as well as the electron avalanche process happening during the corona charging procedure. It is known that when charging with corona devices the air surrounding the surrounding environment should be dry in order to prevent arcing. When in high density values collisions with electrons take place releasing more electrons eventually leading to sparks. Based on studies done (Yovcheva, Mekishev & Marinov, 2004), it is found that the surface potential decays quicker when the film is stored in higher relative humidity after the charging procedure. On the other hand, there are no significant results indicating the influence of relative humidity prior the charging procedure.

### **3.3.6 Surface roughness**

The surface of the Cellular PP sample is not perfectly smooth. Especially after GDE procedure, as the voids gets expanded and the external layers gets repousse-like. As a result, there exists a thin layer of air due to the material roughness which changes the motion of the charges traveling towards the sample (Ono, Nakazawa & Oda, 2004; Sessler, Alquié & Lewiner, 1992). D. Pan et al. (Daosheng Pan *et al.*, 2009) demonstrated

that the obtained  $d_{33}$  of a flat surface sample is increased compared to a rough surface sample. To prevent this decrement, an extra thin polymer layer with smoother surface can be placed on top of the sample (Hill, Knoesen & Mortazavi, 1994). An irregularity (roughness) also exists to the surfaces of the grounded plate (measuring electrode) and the electroded surface of the material. There is a possibility that the contact area between these two surfaces will be smaller due to this irregularity (Ono, Nakazawa & Oda, 2004). A solution to the roughness problem is to apply a material, like silicon oil, between the measuring electrode and the polypropylene sample in order to decrease the limitation of charge movement from the sample's electrode to the measuring electrode (Ono, Nakazawa & Oda, 2004).

### **3.4 Pre-Functionalization treatments-parameters**

The most effective way of increasing the Cell-PP piezoelectric coefficient  $d_{33}$  is by GDE procedure (Wegener *et al.*, 2004c, 2004b; Zhang, Hillenbrand & Sessler, 2004b). It is found that with GDE the thickness of the voids, and as a result the film thickness, increases. The large voids can now gain charge density in lower fields, and a larger piezoelectric constant is achieved by the end of the charging procedure (Zhang, Hillenbrand & Sessler, 2004c; Harris & Mellinger, 2012; Mellinger, 2011; Hillenbrand *et al.*, 2003). Furthermore, studies done on polypropylene ferroelectrets have shown that by a second expansion process, which occurs after the charging and the metallization of the film, the piezoelectric activity could be increased by 40% in some cases (Zhang, Hillenbrand & Sessler, 2004b; Zhang, Sessler & Hillenbrand, 2007). It is worth mentioning here that after a third expansion, the charges are retained inside the film. However, there is a limitation while using this procedure, as there is a point where the over-expanded films tend to have lower piezoelectric coefficients (Tuncer & Wegener, 2004, 2004; Sborikas & Wegener, 2013).

GDE procedure also affects the mechanical properties of the film. Studies have shown that the morphology of the inner voided structure, and

specifically the maximum width to maximum thickness ratio of the voids (aspect ratio), defines the overall stiffness of the material (Tuncer, 2005; Tuncer & Wegener, 2013; Wegener *et al.*, 2004a; Sgardelis & Pozzi, 2017).

Enis Tuncer (Tuncer, 2005) simulated the voided part of the material by a rhomboidal-like mesh structure with the length / thickness ratio of each void being the key for the overall stiffness of the material. Under the GDE treatment the void length to thickness ratio decreases (Tuncer, 2005) and the structure becomes stronger. Non-expanded and little expanded materials show rapid increase of stiffness under compression forces, compared to highly expanded materials, as the voids collapse easily under small stresses due to their weak structure (high length / thickness ratio). This results in compression of the bulk material rather than the air cavities. Greater expansion of the film results in thicker voids, providing room for higher strains on the weak structure, before the voids collapse. However, after a certain point, further expansion results into round voids (Wegener *et al.*, 2004b) and thus to a strong structure and high material stiffness (length / thickness ratio close to unity).

Many studies showed that the relationship of stiffness to relative density is "U" shaped, with a breakpoint of expanded / virgin density ratio of about 0.45 where the stiffness in third direction  $c_{33}$  is minimized (Wegener *et al.*, 2004b, 2006; Hillenbrand, Sessler & Zhang, 2005; Wegener *et al.*, 2004c). Furthermore, GDE temperature effects the final piezoelectric response of the material. The temperature during GDE (or in some cases after GDE) ensures permanent inflation. It is found that there is an optimum temperature of around 85 °C that leads to higher  $d_{33}$  values (Zhang, Hillenbrand & Sessler, 2004c). At lower temperatures, the inflated shape is not consolidated and the voids relax to a lower thickness, whereas higher temperatures damage the structure.

Another method of increasing  $d_{33}$  is by stretching the film during testing. J. Hillenbrand *et al.* (Hillenbrand' *et al.*, 2002) demonstrated that stretched Cell-PP has higher  $d_{33}$  value compared to non-stretched ones. Another study done by D. Pan *et al.* (Daosheng Pan *et al.*, 2009) showed that non-stretched, cross linked polypropylene samples, with round voids have

lower  $d_{33}$  compared to heat-stretched ones. More specifically, 150% stretching ratio normal to the film gave the highest piezoelectric response. Essentially, these methods fall under the same category with GDE, as they provide another way of changing the morphology of the voids.

As explained in a previous section, the mechanism behind the charge production on the external layers of the film is the relative displacement of the dipoles inside the voids as a response to the external compressive stress applied. Thus, materials with high stiffness, have lower piezoelectric coefficient  $d_{33}$ .

GDE is usually desirable, as piezoelectricity is strongly related to the elastic properties of these materials. Thus, minimizing the stiffness and the density is beneficial for many applications, where the film is used as a sensor or a transducer. On the contrary, in applications like energy harvesting low stiffness it is not desirable and thus stiffness needs to be optimized.

Another treatment worth mentioning is the chemical modification of samples. (An *et al.*, 2009) reported the case of Cell-PP treated with  $\text{CH}_2\text{Cl}_2$ , sequentially oxidized with the aid of an oxidizing solution and finally treated in hydrofluoric acid at RT for six hours. The resultant sample was chemically modified not only at the external layers but in depth. This procedure resulted in thermal stability at elevated temperatures but also in a decrease in stiffness.

### **3.5 Non- linearity and viscoelasticity**

It is well known that voided polymer films, including Cell-PP exhibit non linearities in terms of their piezoelectric and mechanical responses (Schwodiauer, Graz & Bauer, 2004; Tuncer & Wegener, 2004; Daosheng Pan *et al.*, 2009; Kressmann, 2001). To account for non-linearity, the effective area of the film, as well as the film thickness under compressive mode should be stated so that the stress and the produced charge density (as far as EH is concerned) can be easily deducted. That way, different experiments can be compared.

As explained in section 3.4, void morphology changes with GDE procedure. Specifically, the void length/thickness ratio decreases proportional to GDE. Likewise, this ratio decreases proportional to the compressive stress applied on the material. Under small compressive stress (no more than few kPa), Cell-PP has a linear stress-strain response (Gaal *et al.*, 2016) (constant  $c_{33}$ ) as well as  $d_{33}$  (Daosheng Pan *et al.*, 2009; Lou, Zhang & Xia, 2012; Hillenbrand *et al.*, 2003). When the compressive stress is high enough (in the orders of tens to hundreds of kPa usually), the piezoelectric response becomes non-linear. (Hillenbrand *et al.*, 2002; Kressmann, 2001; Cronin & Ouellet, 2016). Gaal *et al.* (Gaal *et al.*, 2016) demonstrated that for a continuous stress increment of 3 kPa, the rate of strain decreases. That implies that the material stiffness increases with the applied compressive stress. On the other hand, Reiner (Kressmann, 2001) demonstrated that when in the non-linear region (up to 60 kPa in this case) the stiffness of the Cell-PP sample initially decreases by almost 25% and then increases back up. The same holds for the rate of change of charges ( $d_{33}$ ) over stress in this study. This implies that  $d_{33}$  and/or  $c_{33}$  are not constants but depend on the applied stress (and as a result strain). It is evident that by compressing the material, an inverse response to the GDE procedure is obtained. As a result, in order to obtain this inverse response, the material needs to be inflated so that the obtained density over the initial density ratio is more than 0.45, which is the peak, where the maximum  $d_{33}$  and the minimum  $c_{33}$  occur according to the literature (Wegener *et al.*, 2006; Tuncer & Wegener, 2004; Zhang, Hillenbrand & Sessler, 2004c).

The change of stiffness over the applied stress is not the only non-linearity of Cell-PP. The stress-strain response is different between the loading and unloading sequence (Gaal *et al.*, 2016). The material appears stiffer during the unloading phase, compared to the loading one. A comparison of the charge production between the loading and the unloading sequence has not been explored in the literature. On the top of that, there is no evidence that this difference occurs in the non-linear region only.

Another parameter that can be considered non-linear is the storage and the loss modulus over different frequencies and strains. (Gaal *et al.*, 2016)

showed that storage modulus increases with frequency, following a sigmoid function. On the other hand, loss modulus shows a specific frequency where it is maximum. Both of these phenomena can be attributed to the relaxation of the material.

### **3.6 Theoretical models of Cell-PP**

A number of models for Cell-PP piezoelectricity have been proposed. Finite element method was employed by E. Tuncer et al. in order to compare the numerically calculated response with the analytical expression (Tuncer, Wegener & Gerhard-Multhaupt, 2005). M. Paajanen et al. (Paajanen & Va, 2000) simplifies the film down to two external layers of polypropylene, with a gas layer in-between them. The total gas inside the polymer was estimated based on Scanning Electron Microscope (SEM) cross-sectional images of the film. In this 2D model, the gas layer has an area equal to the estimated sum of all the gas inside the voids. The inverse piezoelectric effect was tested and comparison between the experimental data and the model, reveals agreement for small displacements.

Other models treat the film as alternating layers of polypropylene and gas, based on the thickness of the voids (Paajanen, Lekkala & Valimaki, 2001; Harris & Mellinger, 2012; Hillenbrand & Sessler, 2000; Hillenbrand, Sessler & Zhang, 2005). According to these models, the number of voids is counted on the basis of cross sections of the film and categorised to bins based on their maximum thickness. It is assumed that the same distribution applies for the whole sample. Harris and Mellinger (Harris & Mellinger, 2012) were able to estimate the final charge density of the voids after poling by utilizing the Paschen's law of breakdown field in gases. The final charge density is determined by the void thickness and the pressure of the gas inside each void layer.

In the above-mentioned models, the modulus of elasticity (modulus of axial compression  $c_{33}$ ) is assumed to be constant. These models show agreement with experimental data in the linear part of strain, but do not explore the mechanical properties and the film's piezoelectricity beyond

the linear region. Typically, the stiffness in thickness direction ( $c_{33}$ ) is in the order of MPa but can vary from 0.5 up to 10 MPa depending on the frequency of excitation, the inflation of the sample and the stress applied. This non-linearity is obvious when the film is experiencing high strains.

M. Wegner et al. (Wegener *et al.*, 2006), considered the stiffness change due to expansion. A two-layer sample was modelled and the electromechanical coupling coefficient was derived in terms of relative density and stiffness of the film. The electromechanical coupling coefficient has a “U” shape, when plotted against the relative density. The same shape is also found for the  $d_{33}$  and the  $c_{33}$  as discussed earlier. The  $k_{33}$  is maximized when the relative density is close to 0.46. Based on the same paper, at this relative density, the stiffness is maximized and the  $d_{33}$  is the lowest. This suggests that the stiffness of the material plays a key role for the electromechanical coupling coefficient  $k^2_{33}$ .

The stiffness of the material is not constant and needs to be described in terms of mechanical stress applied to the film as there is a link between the morphological structure of the film and the stiffness, under high strains. P. Sgardelis and M. Pozzi (Sgardelis & Pozzi, 2017) studied the non-linearity of the film, for a variety of morphologically different samples. The rate of change of stiffness  $c_{33}$  obtained by compressive experimental results was plotted over the median void length/thickness ratio obtained by the distribution histogram. The stiffness rate seems to increase in accordance to the increment of the length/thickness ratio. These results were in agreement with the finite element results of 3D modelled films.

Another analytical model was presented by M.R. Haberman and .H. Berthelot (Haberman & Berthelot, 2007). This model described the influence of the material and the voids on the macroscopic piezoelectric performance of the film. The 3D approximation, utilized the constituent material properties as well as the void morphology to determine the effective stiffness, the dielectric permittivity and the piezoelectric coupling coefficients.

### **3.7 Energy Harvesting (EH)**

Wireless sensor networks require to be powered by batteries. Since they need to be autonomous, the batteries should be charged by energy sources like mechanical energy, light or thermal gradients existing in their local environment. The devices that harvest these untapped sources of ambient energies and produce electricity are called energy harvesters. Humans have been harvesting energy for thousands of years. Two basic examples of kinetic energy sources are the wind and the water used in wind and water mills. A relatively new energy to be harvested is solar energy. The first solar cell was created in 1954 by Aleksandr Stoletov. Ever since, solar energy harvesting has been used, especially for powering remote modules in space projects.

Mechanical energy on the other hand, refers to low-level vibrations and matter movements. For an energy harvester, the efficiency of mechanical to electrical conversion is important and needs to be investigated. As mentioned in the introduction section, the electromechanical coupling coefficient  $k^2_{33}$  is an important parameter to be considered as it is the direct measurement of mechanical to electrical energy conversion (and vice versa).

As the harvested sources provide low energy, the efficiency of the harvester is of crucial importance. Some of these harvesters are categorized according to the material and listed below along with the obtained power density and their contributions to our knowledge.

#### **3.7.1 PZT based Energy Harvesting**

J. Cho et al. (Cho *et al.*, 2005) explored the parameters that affect the electromechanical coupling coefficient  $k^2$  on a thin-film PZT membrane. It was found that the tensile residual stress produced during manufacturing, leads to a reduction of the  $k^2$  even by two orders of magnitude. Another parameter found to affect the  $k^2$  was the electrode coverage. The optimum coverage area for the electrode, was found to be 60 % of the surface area. Finally, a DC bias, increased the  $k^2$  by almost two times. The optimum DC bias seems to be changing with the residual stress. For samples with high

residual stresses, higher DC voltages seem to be optimal. Similar results were found by the same group upon testing the theoretical model of such a device (Cho *et al.*, 2005).

C.H. Choi *et al.* (Choi *et al.*, 2013) experimented with the composition of ceramics, aiming to find the optimum mixture that increases the output energy density. High energy output densities of  $231 \text{ kW m}^{-3}$  were achieved under 85 Hz of excitation frequency. The efficiency of conversion was close to  $\eta=0.96$  and  $k_p=0.66$ .

Another high-power harvesting device was developed by M. Zhu (Zhu & Worthington, 2009), based on previous optimized harvesters. The device produced power density of  $370 \text{ W m}^{-3}$  under an acceleration of 0.23 g.

Apart from the studies done on the optimization of the materials used, other studies were focused on the energy extraction optimization from the harvester. M. Pozzi and M. Zhu (Pozzi, 2016; Zhu & Worthington, 2009) explored the frequency up-conversion method by letting a PZT-5H bimorph resonate at its natural frequency upon plucking. This method provides the optimal solution to the problem of dense harvesters working under the low frequencies involved in human energy harvesting.

It is known that PZT ceramics have a linear response throughout their strain region. Despite that, different energy output responses can be obtained by different means of excitation. C. N. Hu *et al.* (Chao-Nan Xu *et al.*, 1998) demonstrated that slow stress produced two orders of magnitude higher output power density than impact stress of the same stress level.

Finally, another human based energy harvesting device was developed, based on both PZT and PVDF based harvesters (Shenck & Paradiso, 2001). The PVDF harvester was placed underneath the front, flexible part of the shoe, while the PZT bimorph harvester was placed under the heel of the shoe. A comparison was made between the two harvesters with the PZT providing 2.5 times more energy than the PVDF. The harvesters could provide enough energy to power up an RFID circuit for wireless data transmission.

### **3.7.2 Polymer Based Energy Harvesting**

A variety of EH applications with polymers have been proposed. N. Wu et al. (Wu *et al.*, 2015) created a Sensor – Harvester for health monitoring and energy harvesting, based on Cell-PP. Heart beats were measured on both the wrist and arm of humans. The harvester produced current peaks of 0.2 nA and 0.3 nA for every heartbeat of a young man, under relaxation and after 5 min exercise respectively. This device was also tested as an EH, under a cyclic compressive stress of 5 Hz, 285 kPa. The harvester produced a peak power of almost 53 mW m<sup>-2</sup>.

In another study, SR Anton et. Al. 2014 (Anton, Farinholt & Erturk, 2014) tested the capability of a commercially available “HS-06 film” harvester. A capacitor is used to store the energy coming out of the sample. In addition, a diode bridge rectifier circuit with a smoothing capacitor was connected to the output of the harvester.

The 1 mF capacitor was charged to 4.67 V within 30 minutes, with the 15.2 X 15.2 cm<sup>2</sup> sample being under harmonic strain excitation of 0.75 at 60 Hz. It is worth mentioning that in real life vibration harvesting, the input signal has many frequencies and differences in the amplitude (more like white noise) i.e. the input is more of energy than power. Many excitation frequencies were used in that study. It was found that the output power increases dramatically with increasing frequency of excitation and for the range between 10 Hz and 30 Hz. The specific sample on the other hand, has a Young’s Modulus of 0.5- 1 GPa.

Another study done on commercially available Cell-PP films (Luo *et al.*, 2015), produced a peak power of 56 mW m<sup>-2</sup> (800W m<sup>-3</sup>) under compressive stress of 16.5 kPa, dissipated on a 1 Gohm resistor. The study also showed that the charging ability obtained by a 10 - layer ferroelectret was 29 times larger than the single layer ferroelectret. The material produced a linear Voltage / Force response from 2 kPa to 16.5 kPa.

L. Mateu and F. Moll (Mateu & Moll, 2006) used a commercially available harvester module and analysed parameters like energy required and magnitude of excitation of human walking, to find the appropriate capacitor

and voltage values for discontinuous load operation. A piezoelectric discharge controller was also used as the importance of controlling the discharge of the piezoelectric element is fairly important.

Another Human based Energy Harvesting application was proposed by J.Granstrom et. al. (Granstrom *et al.*, 2007). In that study, a theoretical model of PVDF piezoelectric straps on a backpack was investigated. The experimental results showed relatively good agreement with the theoretical model with no more than 13% difference between the actual and the calculated output power. It was found that three 28  $\mu\text{m}$  thickness strap can provide an average power of 45.6 mW. Multi straps were tested. It was found that the maximum output power was attained with fewer straps and higher load.

An interesting device was built by Zhan et al. (Zhang, Sessler & Wang, 2014). Fluorinated Ethylene Propylene (FEP) and Polytetrafluoroethylene (PTFE) were pressed together and fusion bonded. Films of 60 to 500  $\mu\text{m}$  were produced and tested under compression mode as harvesters. The device gave a maximum peak power density of 1.2  $\text{mW m}^{-2}$  under 1 kPa, 120 Hz of excitation.

There are few studies on energy harvesting with Cell-PP. Furthermore, most of them focus on the manufacture and testing of a device, rather than the properties of the material. Human energy harvesting requires high performance under sub-Hertz to no more than 2 Hz frequency. It is also known that the input power increases with frequency, leading to higher output power. Finally, apart from the functionalization and pre-functionalization parameters that affect  $d_{33}$ , and eventually  $k^2$ , there are other ways of increasing the piezoelectric performance.

### **3.7.3 EH Comparison Between PZT and Cell-PP**

Ceramic materials like PZT are widely used for EH. There are many applications from railway sensors to human walking energy harvesting. The major drawback of this material is its brittleness and density, making it a poor choice for human based energy harvesting applications where high strain and mechanical flexibility is required. For such an application,

ferroelectric polymers may be advantageous over traditional piezoelectric ceramics (e.g. PZT) in the sense that they fulfil three of the most important requirements. They are light weight, not as limited in mechanical strain as traditional harvesters made of PZT and finally they are suitable for applications where the input energy has low frequency e.g. human movement. As the “flexible electronics” emerges, piezoelectric polymers gain the attention of researchers. Large areas can be covered with films and harvest energy from the whole surface with large mechanical strain capability.

Cellular Polypropylene (Cell-PP) is a good candidate for such applications as it shows strains varying from 0.13 to 0.6 for moderate stress applied, between 100 to 500 kPa (Cronin & Ouellet, 2016). Despite its low electromechanical coupling coefficient  $k^2_{33}$  (typically less than 0.01 (Wegener *et al.*, 2006), well below commercially available PZT harvesters which have  $k^2_{33}=0.36$  and 0.2 for a PZT membrane (Cho *et al.*, 2005)) its density is more than 13 times less. In addition, its roll to roll manufacturing process makes it a cheap material.

One of the biggest problem of any energy harvesting application is the losses in electrical energy from the material to the electrical components. A. Cornogolub *et al.* (Cornogolub, Cottinet & Petit, 2016) investigated two methods of energy transfer done with hybrid harvesters. The first one is a typical, one direction sourcing from the harvester to the load. In the second one the charges produced are returned to the harvester with the aid of a circuit. This method can be used for applications where the current is important.

In conclusion, PZT is 13 times heavier than Cellular polypropylene as well as non-flexible. Stacking piezoelectrets like polypropylene or ferroelectrets like Fluorinated ethylene propylene (FEP) to engineered films might be advantageous for Human EH applications.



## Chapter 4. Experimental Methods

### 4.1 Corona device

#### 4.1.1 Design of corona charger

As explained in the Literature, the poling process of Cell-PP films is a result of Ion accumulation to their surface. That way, the sample surface potential rises and the field across its thickness increases. By increasing the electric potential of the “corona tip” Ions are generated and accelerated towards lower potentials, due to electron avalanche. A metallic grid is placed under the “corona tip” to provide a uniform field for the sample that sits below.

Keeping in mind that the gas inside the chamber is air having a dielectric strength of  $3 \text{ MV m}^{-1}$ , there is a minimum corona tip to grid  $d_{cg}$  and grid to sample  $d_g$  distance that should not be exceeded to prevent discharges. On the contrary, there is a minimum electric field that needs to be present for the creation and maintenance of the electron avalanche. Thus, one of the objectives is to have enough travel distance for the corona tip to the grid, in order to explore a greater range of charging electric fields. The final design is presented in figure 4.1.

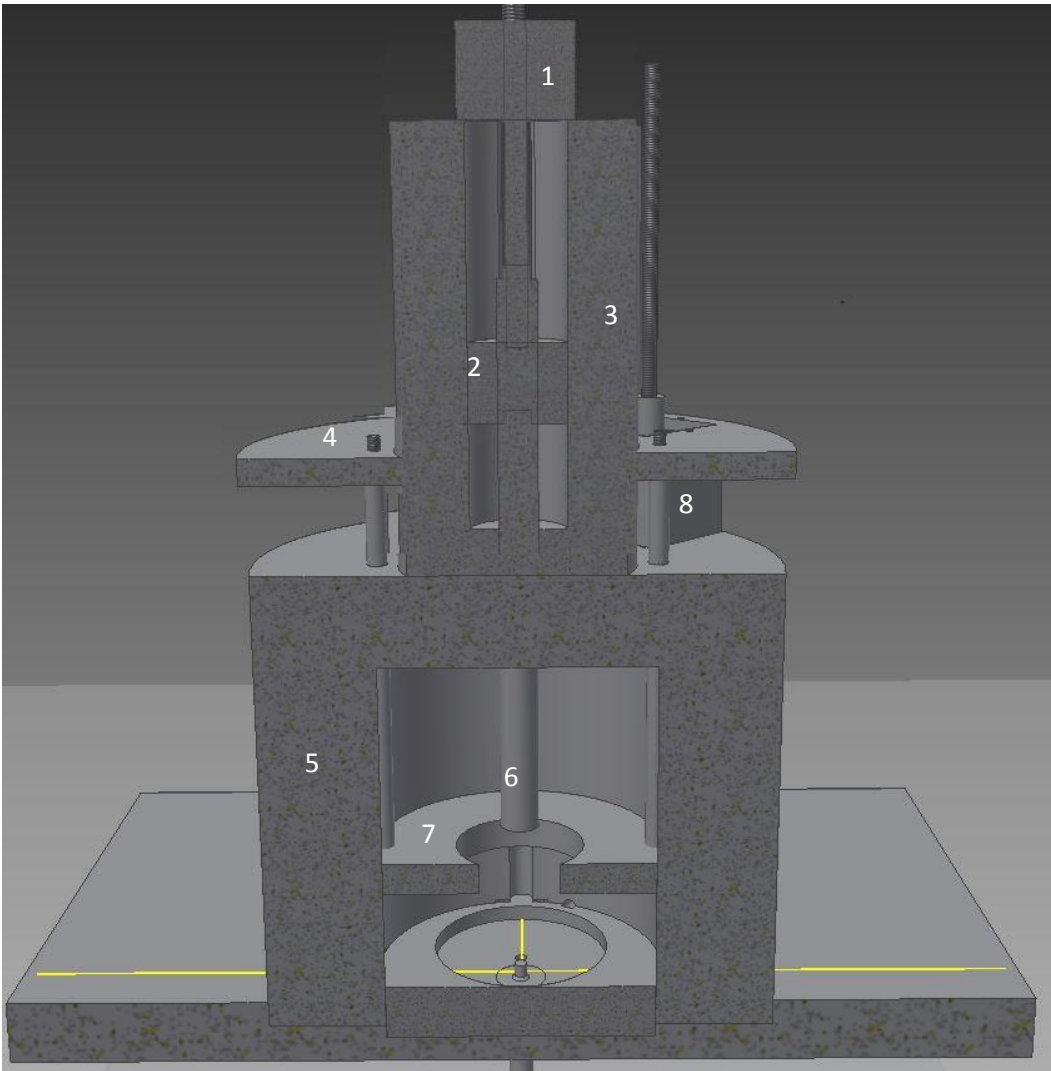


Figure 4.1 Half section view of the final design of the corona chamber. Assembly created with Autodesk Inventor. 1) Non- captive linear stepper motor 2) Piston (acetal) 3) Piston guide cylinder (acetal) 4) Grid guide (acetal) 5) chamber (acetal) 6) Corona holder (acetal) 7) Grid holder (acetal) 8) Captive linear stepper motor.

The corona charger consists of two “live” parts, the corona tip and the grid. A thin 89  $\mu\text{m}$  diameter tungsten wire serves as corona tip. It is 20 mm long and half of it (10 mm) is embedded into an acetal rod ‘6’ having the other 10 mm end of the wire exposed. Tungsten was selected due to its durability under high voltages. The grid needs to be significantly larger than the sample to assure a uniform field. A 50 mm radius stainless steel grid is attached to a circular acetal holder ‘7’. Its opacity is 63% with a wire diameter of 63  $\mu\text{m}$ .

Repeatability is a key parameter to the experiments. As small variations in  $d_g$  and  $d_c$  can dramatically influence the resultant field, a precise way of setting these distances is needed. Linear stepper motors are used for translation of both the corona tip and the grid '1'. The threaded motor shafts that control the displacement of the corona tip and the grid have lengths of 150 mm with pitch of 8 mm and 2 mm respectively. The motor resolution is  $1.8^\circ$  per step equivalent to linear displacements of  $40 \mu\text{m}/\text{step}$  and  $10 \mu\text{m}/\text{step}$  to the corona tip and the grid respectively. The repeatability of the motors was tested with the aid of a calliper and no significant uncertainties were observed. A further increment to the resolution is obtained by 8 micro-steps per steps, leading to resolutions of  $5 \mu\text{m}$  and  $1.25 \mu\text{m}$  respectively. This micro stepping is meaningful for the constant current experiments, as the current flowing through the sample  $I_s(t)$  changes dramatically for small changes of  $d_{cg}$  and  $d_g$ .

The chamber '5' and the guide cylinder '3' are made of Acetal and have a thickness of 45 mm and 27 mm respectively in order to stop the fields from propagating outside the device. Acetal was chosen based on its dielectric strength of  $0.5 \text{ MV m}^{-1}$ . Based on calculations done, the insulating wall of the chamber as well as the guide cylinder can safely withstand 22.5 kV and 13.5 kV of potential difference across them respectively. The Acetal piston '2' is there to prevent high voltage to arc from the corona tip wire to the grounded, non-captive motor rod. A plate '4' acts like a guide by pushing simultaneously two rods attached to the grid holder '7'. The plate is displaced linearly with a captive stepper motor '8'.

As only one High Voltage (HV) Power Supply (PSU) is provided, a way of energising the grid is needed. The HV PSU chosen to supply the corona tip is a Glassman FJ30R4. It can provide 30 kV of electric potential with 0.5% uncertainty and a maximum of 4 mA of current. The current is displayed in the front panel of the device with 1% of uncertainty. The surface potential of the sample is equal to the potential of the grid when the charging process ends. Electric potentials ranging from 6 kV to 9 kV across the sample are commonly used for contact charging. In order to provide such ranges, a voltage divider of HV resistors rated at 2 kV each

was created with total resistances of  $R_1=507\text{ M}\Omega$  and  $R_2= 90\text{ M}\Omega$  (figure 4.2).

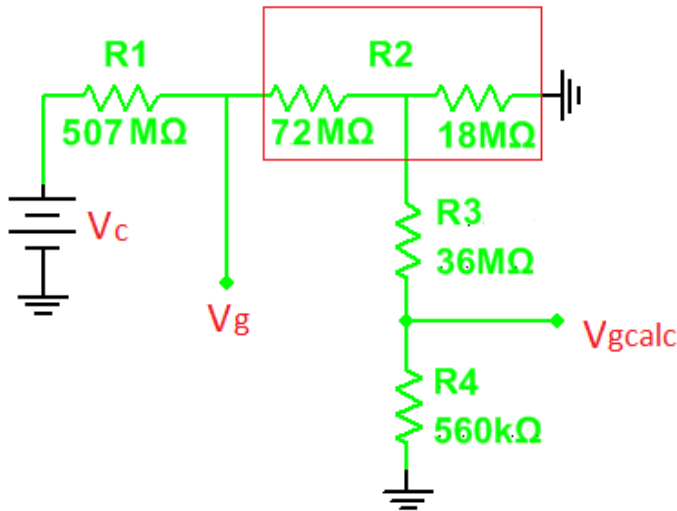


Figure 4.2 High voltage electrical circuit of the corona charger.  $V_c$  = corona tip voltage,  $V_g$  = grid voltage,  $V_{gcalc}$  = Voltage sensing ( $V_{gcalc}<40\text{V}$ )

As a result, the minimum corona tip voltage  $V_c$  to grid voltage  $V_g$  has a ratio of 6.6 so that

$$V_g = \frac{V_c}{6.6} + V_{av} \quad (4.1)$$

where the  $V_{av}$  is the voltage potential gained by the grid due to the migrating charges (further details are provided in chapter 5). When the PSU provides 30 kV to the corona tip, the grid is provided with 4.5 kV. The current flowing through the divider in that case, is significantly lower than the capabilities of the PSU with a maximum value of 50  $\mu\text{A}$ . As  $R_2$  is large enough, there is accumulation of charges that migrate from the corona tip on the grid. This effect rises  $V_g$  to potentials significantly higher than the voltage divider can provide. The resultant potential  $V_g$  depends on  $V_c$ ,  $d_{cg}$  and  $d_g$  as the grid gains or loses charges due to the fields created above and below it. In order to measure this change, another voltage divider is placed in parallel to the final part of the HV resistor  $R_2$  (figure 4.2). The ratio of this division is 460 so that

$$V_{g-calc} = \frac{V_g}{460} \quad (4.2)$$

The corona tip to grid distance  $d_{cg}$  is used to control the grid potential  $V_g$ , as the corona tip voltage  $V_c$  is kept constant throughout the experiments.

#### **4.1.2 Health and safety**

A small section of safety measures implemented in the corona triode is presented below.

A Faraday cage was built to enclose the whole setup of the corona triode. The cage is made of 5 mm thick Polymethyl Methacrylate (PMMA) to prevent any unintentional physical access to the setup by the user during the charging procedure. A perforated steel with 6 mm mesh as well as another net with 25 mm mesh runs the interior of the Faraday cage. Both meshes are electrically connected to ground by many paths. This is to prevent the field from reaching the surrounding environment and to stop any live, loose wire to zap through the PMMA.

Three safety interlocks (two switches and one key switch) are placed in series to the output enable button of the HV PSU. These switches disable operation automatically whenever the enclosure is opened or the key returns to the power off position.

A hard grounding mechanical interlock switch prevents the enclosure from opening unless the power supply and the HV cables are all connected to ground. This way, the user can only have access to the interior of the Faraday cage when the HV PSU is connected to ground. A 'mushroom' emergency button is located close to the device. In case of an emergency, it switches off the power supply to every electronic equipment on the setup bench.

Every low voltage wire coming out of the enclosure, passes through a duplicated voltage-clamp arrangement using Zener diodes in back to back configuration that automatically limit the potential from rising more than 24V above ground. In case of damage, diodes fail in short circuit, rendering the device non-functional but safe. The operation of each of these clamping circuits has been verified by testing at currents in excess of that capable of the HV power supply (figure 4.3).

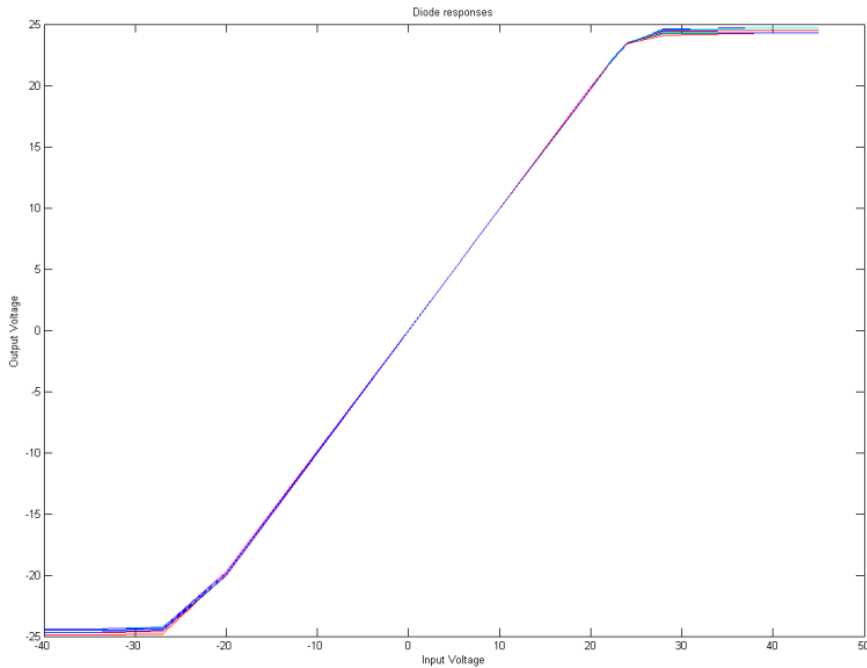


Figure 4.3. Output Voltage obtained from the Voltage clamp circuit in response to the input voltage. The Zener diodes clamp the input output to a maximum of 24 V.

While inside the Faraday cage, these low voltage wires are also covered with an earthed copper screen to prevent the high voltage arcing to them. The final circuit for the motor control is given in figure 4.4.

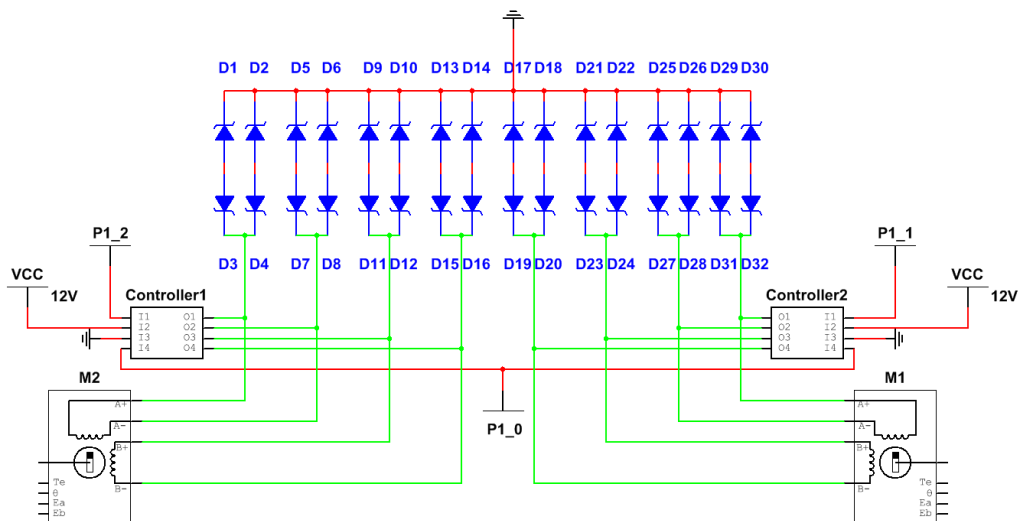


Figure 4.4. Motor safety circuit. Green wires represent wires placed inside the hazardous environment of the Faraday cage. Each of these wires is

connected to a duplicated voltage clump circuit. D1-32 Zener diodes clamp the output down to 24 V (figure 4.3).

Every metallic component inside the cage is electrically grounded via two separate paths and the whole device lies on an aluminum plate, electrically grounded by a supplemental grounding path, permanently connected to earth at the distribution board. Every live HV cable is kept as far as possible from the ground plate to minimise the capacitances created between the wire and the ground. This is done to prevent potential risk of charge accumulation within the wires. In the case of any discharge, high stored energy might exceed the safe limits. Figure 4.5 shows the final design with the safety measures.

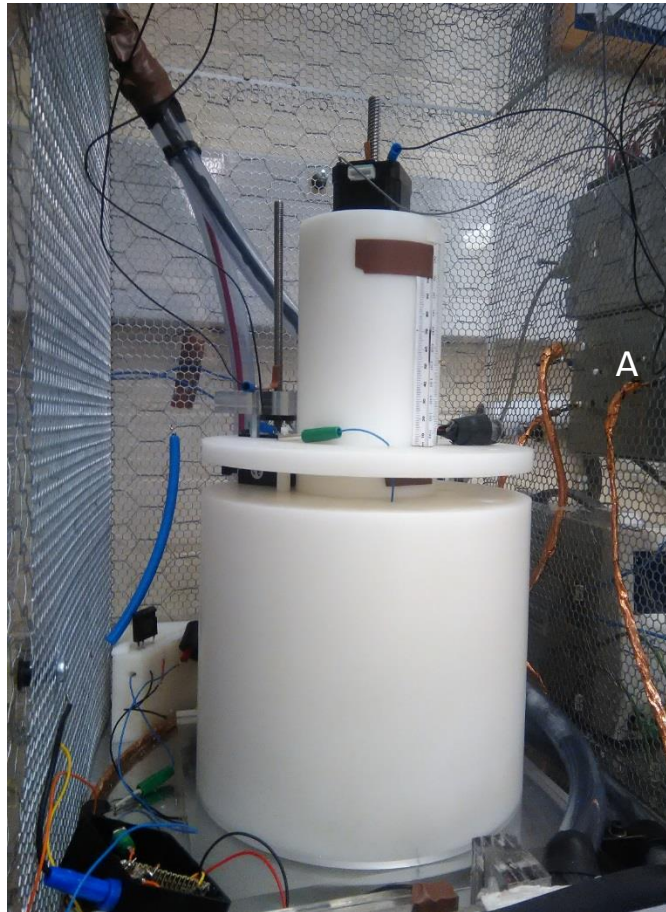


Figure 4.5 Photo of the final design inside the Faraday cage. Copper tape covers every low voltage wire going outside the Faraday cage. The metal box “A” sitting outside the cage is the motor control with all the voltage clamp circuitry.

Finally, the charger was switched on and ozone production was measured after 15 minutes of continuous usage. Ozone strips were placed both inside and outside the corona chamber. European commission states that a person should not be subjected to ozone concentrations exceeding  $120 \mu\text{g m}^{-3}$  for more than 8 hours. Based on the ozone strip placed just outside the chamber, the ozone levels outside the chamber did not exceed  $90 \mu\text{g m}^{-3}$ . The reading was observed after the chamber was opened. The strip inside the chamber indicated that the concentration levels reached  $150 - 210 \mu\text{g m}^{-3}$  but once the chamber opens, the concentration fell quickly to safe levels, eliminating any risk for the user.

#### **4.1.3 Mechanical-electrical characterization**

The corona device permits control of several charging parameters, such as the corona to grid  $d_{cg}$  and grid to sample  $d_g$  distances, which affect the current distribution, current density  $J_s$  of the sample and the two electric fields  $E_{cg}$  and  $E_g$  (fields between the corona tip-grid and grid-sample respectively). The potential of the corona tip is close-loop-controlled by the HV PSU and is set manually by the user with a step of 100 V. Although the HV PSU can supply both positive and negative voltages, in this project only negative corona is tested. Depending on the current flowing through the sample, the time for charging a single 5 mm diameter samples is around 5 to 15 minutes. When  $I_s$  becomes zero, the sample is considered charged and the charging process can be stopped. In reality, a background current always exists due to the corona wind being sensed at all times by the current measuring tip. The experiments in this case end when  $I_s$  becomes constant and has value significantly smaller than the beginning of the poling process.

To investigate how each of the parameters  $d_{cg}$ ,  $d_g$  and  $V_c$  affect  $V_g$  as well as the current density  $I_s$ , a set of calibrations curves were experimentally obtained. For these experiments, no sample was placed on the measuring tip inside the chamber.

For the first set of calibration,  $d_g$  was set to 4 mm above the measuring tip and  $V_c$  was ramped up from 1 kV to 30 kV with a step of 1 kV. The current

$I_s$  and the potential  $V_g$  were measured for each step and for  $d_c$  equal to 21 and 31 mm. For the same experiment, the potential  $V_g$  with respect to  $V_c$  was obtained.

#### 4.1.4 Constant current calibration

For this experiment,  $V_c$  was kept constant at 27 kV and the grid distance was set to  $d_g = 6$  mm. The Corona tip was displaced from 52 mm to 19 mm and the current  $I_s$  was measured. The result is shown in figure 4.6.

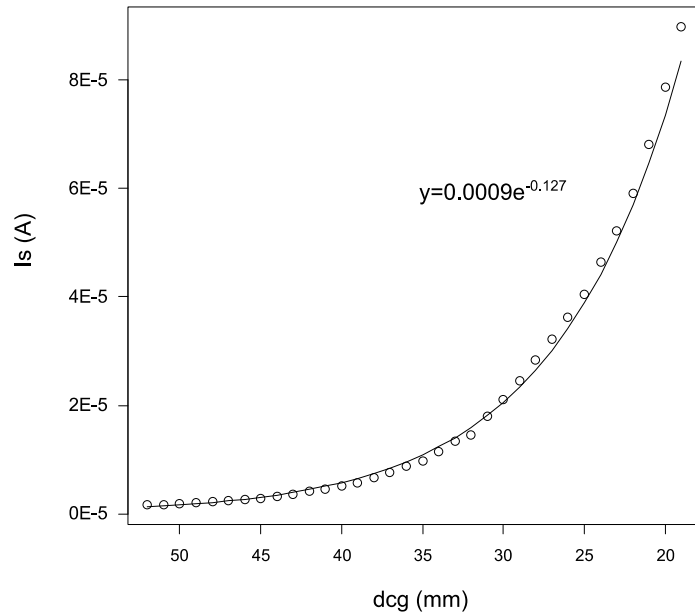


Figure 4.6 Current  $I_s$  over the corona tip to grid distance  $d_{cg}$ . The corona tip was displaced from 52 mm to 19 mm with a step of 1 mm. The exponential curve fitted (formula embedded in the figure) was used for the constant current poling estimation.

This calibration curve fit is used for the constant current calibration. The objective of this experiment is to keep the current  $I_s(t)$  constant throughout the poling procedure. This can be achieved by keeping the potential difference between the grid  $V_g$  and the sample surface  $V_s$  constant. As there is no direct way of measuring  $V_s$  during poling procedure the current is controlled indirectly by the displacement of the corona tip and thus resulting to increment or decrement of the potential difference between the grid and the sample. For each experiment,  $d_g$  and  $V_c$  is kept constant at all time. Data logging of all parameters is done with the aid of Labview. The user sets the desired current density. Firstly, the corona tip is displaced quickly for the current  $I_s$  to reach the desired value. Then, the corona tip to

grid distance  $d_{cg}$  is controlled so that the actual current density is constant and close to the desired one throughout the charging procedure. The charging process stops just before a breakdown occurs. This breakdown can be seen long before it occurs and is designated by a sudden increase of the current  $I_s$ .

## 4.2 Sample pre-functionalization treatment

### 4.2.1 Materials

Two types (families) of Cell-PP, kindly provided by Treofan (Germany) in the form of A4 sheets, were used: the EUH family with nominal density of  $550 \text{ kg m}^{-3}$  and nominal thickness of  $75 \text{ }\mu\text{m}$  and the LRH family with nominal density of  $680 \text{ kg m}^{-3}$ . Three materials from this family are used, with nominal thicknesses of  $60 \text{ }\mu\text{m}$ ,  $70 \text{ }\mu\text{m}$  and  $80 \text{ }\mu\text{m}$ . The code names as well as the nominal thickness and density of these films provided by the manufacturer are presented in figure 4.7

#### WHITE VOIDED

(Density  $0.55 \text{ g/cm}^3$ )

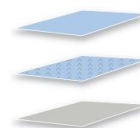
Type	Structure	Nominal thickness ( $\mu\text{m}$ ) (gauge)		Unit weight ( $\text{g/m}^2$ )	Yield ( $\text{m}^2/\text{kg}$ )	Description/ Application
EUH		40	160	22.0	45.5	Treated on both sides; one side glossy, one side matt
		50	200	27.5	36.4	
		60	240	33.0	30.3	
		70	280	38.5	26.0	
		75	300	41.3	24.2	

(Density  $0.68 \text{ g/cm}^3$ )

Type	Structure	Nominal thickness ( $\mu\text{m}$ ) (gauge)		Unit weight ( $\text{g/m}^2$ )	Yield ( $\text{m}^2/\text{kg}$ )	Description/ Application
LRH		70	280	47.6	21.0	Treated on both sides; suitable for large format sheet-fed offset
		80	320	53.3	18.8	

#### SURFACE LAYER OUTSIDE:

Gloss layer, untreated  
Gloss layer, treated  
Metallised layer



#### CORE LAYER:

Transparent layer  
White layer  
Voided layer



#### SURFACE LAYER INSIDE:

Matt layer, low seal, untreated  
Matt layer, untreated  
Matt layer, treated

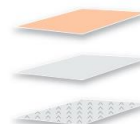


Figure 4.7 Code names and properties of the cellular PP films provided by Treofan (Germany).

The EUH family has one glossy and one matt external surface. The LRH family has both its external surfaces matt. The interior voided layer is the same for all samples as the manufacturer suggests.

#### **4.2.2 Gas Diffusion Expansion procedure**

All Cell-PP samples were inflated with a gas diffusion expansion (GDE) procedure under 2 MPa for 20 minutes and 5 MPa for 20 and 60 minutes. Firstly, the samples were inserted in a balloon filled up with Argon gas, to ensure for gas purity. The balloon was placed inside a high-pressure chamber. The pressure was then increased for gas to diffuse inside the voids. After the time elapsed, the pressure was decreased as quickly as possible (approximately 58 sec and 90 sec exponential decrease for 2 MPa and 5 MPa respectively). As the gas does not have the time to diffuse out of the voids again, this sudden difference of pressure leads to the inflation of the voids. Subsequently, the samples underwent a heat treatment for 10 seconds at 85 °C to make the inflation of the structure permanent. The mechanical stabilization of the inflated structure after heat treatment, is an outcome of the increase in crystallinity, that results to the stiffening of the internal cavities.

#### **4.2.3 Film morphology**

Small strips from different areas from each type were cut using a scalpel in order to be viewed with the Hitachi TM3030 Scanning Electron Microscope (SEM). In total 5 images of their cross sections were taken with an energy of 15 KeV used for higher resolution.

Film morphological parameters were estimated, for every type of sample and every pressure (2 MPa and 5 MPa expanded samples) using a custom-made image processing software. The image processing and classification algorithms were customized for the needs of the project in order to isolate the voids in the image and estimate their dimensions. The image processing program was created in Visual Basic language. It maps the voids of the cross-section images of the samples based on the contrast difference. Extra care is taken for the sensitivity of the program to be in par with the contrast of the image taken. The program reads the resultant source file of the SEM image and finds the size of the image and the magnification. Then, it converts the number of pixels into  $\mu\text{m}$ , based on

the real length to pixel ratio of the image. The outputs of the program are presented below.

The maximum thickness of each void is essentially the longest line of pixels existing in the isolated void within the image. Based on the maximum thickness, the voids are placed into bins. The void thickness distribution  $D_h$  is obtained and the critical field  $E_b$  is then estimated for each stack, based on Paschen's law (equation 2.21). In the same way, the maximum length can also be found for each void. The aspect ratio for each void is calculated as the maximum length over the maximum thickness. By categorizing these aspect ratios found in the film, the void aspect ratio distribution  $D_r$  is obtained. The aspect ratio is further analyzed, as it is directly linked to the stiffness of the material. The area of each void is also calculated. Another parameter extracted is the elongation of each void, calculated as the area of the void over its maximum thickness.

Apart from the void characterization and distributions the materials are also characterized for the total amount of air existing inside the film, which is given by the sum of areas of all voids. The porosity is then defined as the fraction of air inside the film. Finally, other parameters like final expanded thickness  $l$  and void count (voids/mm<sup>2</sup>) are estimated.

#### **4.2.4 Stress / Strain - Young's Modulus**

All of the materials, expanded with GDE under 2 MPa and 5 MPa of pressure, were tested under static compressive mechanical analysis tests, performed with Perkin Elmer 8000 Dynamic Mechanical Analyser (DMA). The test is done on a 5 mm diameter disk, extracted out of each material, using a circular hole drilling plier. Despite the fact that Perkin Elmer 8000 uses a Linear Variable Differential Transformer (LVDT), which is embedded in the device to measure the displacement of the clamp, the real-time displacement data are not available at the output of the instrument. In order to obtain the real time displacement data, the Micro epsilon NCDT 6200 capacitive sensor was used.

The material is inserted between the metal clamps for the compression test. The holder rises the sample against the stationary part of the clamp, up to the point where a preload of 10 kPa is applied. A sinusoidal mechanical dynamic force, with an amplitude of 10 kPa was constantly applied to the sample. The static uniaxial stress was increased from zero to 330 kPa, with steps of 10 kPa. The creep response of the material is also considered in this test. The material was let to relax, for enough time, so that the creep displacement would not affect the resultant strain. The stress strain curve was plotted and the Young's modulus was derived, for each step increment of the static stress. Statistical analysis was done on the  $D_r$  and  $D_h$  distributions, in order to find the relation between the void morphology and the stiffness of the material.

### **4.3 Sample functionalization procedure**

Three sets of experiments with two main functionalization processes were conducted. The first functionalization process requires the inputs  $V_c$ ,  $d_{cg}$  and  $d_g$  to be constant throughout the charging procedure. There are two sets of experiments in this case. The first one is exploring the effect of only the  $V_g$  on the piezoelectric coefficient of the material and is done on all the materials, including expansions of 2 MPa, 5 MPa and non-expanded films. The second one, studies all the three inputs ( $V_c$ ,  $d_{cg}$  and  $d_g$ ), including different temperatures while charging, and is only done to samples expanded under 5 MPa. The second functionalization process is the constant current method. In this case, the voltage of the grid is continuously changing, in order to keep the current  $I_s$  constant.

#### ***4.3.1 Grid voltage $V_g$ charging experiments***

The variable  $V_g$  experiment is done at room temperature and aims to explore the link between the sample potential  $V_s$  (charging stops when  $V_s = V_g$ ) and the piezoelectric response ( $d_{33}$ ) for each material, expanded under pressures of 2 MPa and 5 MPa as well as for non-expanded materials.

Square samples of 15 X 15 mm were prepared for each material. A circular electrode of 5 mm diameter (matching the diameter of the current measuring probe) was made out of silver paint on the centre of the bottom side of the sample. It is crucial that the electroded area sits in the middle of the 15 X 15 mm sample and that the electrode is significantly smaller than the sample size, to avoid current tracking from the top surface to the bottom electrode and eventually to the current ( $I_s$ ) measuring probe. This plays a role equivalent to a guard ring (Giacometti & Sinézio Carvalho Campos, 1990). Once the paint dried out, its surface conductivity was checked with a multimeter.

The sample was inserted in the corona device, so that the electrode was in contact with the current measuring probe. The grid was displaced 4 mm ( $d_g=4$  mm) above the sample and the corona tip voltage was set to 27 kV ( $V_c=27$  kV). Subsequently, the data logging started and the corona tip potential was enabled. The sampling frequency of the current  $I_s$  was set to 10 Hz during the poling process. During charging, the surface potential  $V_s$  of the sample rises and eventually reaches the potential of the grid  $V_g$ . According to the literature, time is not critical for the final  $d_{33}$ , as long as the process is stopped when  $V_s=V_g$ . As there is no means of measuring  $V_s$  directly, this event is designated by the sample current  $I_s$  remaining constant, for a significant amount of time. The final value of  $I_s$  is the constant corona wind  $I_w$  current and is subtracted from each measurement of the current  $I_s$ .

Once the charging procedure is finished, the HV-PSU is switched off, the data logging stops and the sample is taken out of the corona chamber. The second surface gets electroded, and the sample is cut down to the shape of the electrode with the aid of a punch plier (for 5 mm radius samples). Then, the sample is checked for short circuit between the two electrodes.

The corona tip was positioned so that  $d_{cg}= 29, 25, 21, 17$  and  $12$  mm, and the obtained grid potential ( $V_g$ ) was  $6.2, 7.5, 8, 9.1$  and  $11.5$  kV respectively. In total, the experiment was conducted 48 times, to account for the 4 materials, the 3 expansions (including non-expanded materials) and the 4 corona to grid distances.

### **4.3.2 Exploring the full space of parameters**

This experiment is essentially a set of tests where all charging and non-charging parameters of the 4 materials are explored. For this experiment, samples of 20 X 20 mm<sup>2</sup> were extracted from each material. After expansion at 5 MPa for 60 minutes, a 12 X 12 mm<sup>2</sup> electrode was made with silver paint at the centre of the bottom layer of the sample. Bigger samples are used in this experiment to increase the signal / noise ratio, as one of the outputs of the experiment, the current  $I_s$ , increases with the area of the sample. The sample is inserted in the corona chamber and the temperature below the sample is increased until it stabilizes to the desired point. The temperature of the sample was monitored by a thermocouple, which sits below the sample. The thermocouple reading is considered accurate, as the sample is thin enough to acquire the surrounding temperature. The logging starts and the corona tip voltage is enabled. Once  $I_s$  stabilises marking the end of charging, the heating element is switched off and the sample is left to cool down to room temperature while the  $V_c$  is still enabled. Once the sample reaches room temperature, the potential  $V_c$  is disabled, the sample is taken out of the chamber and the second electrode is created as described previously.

A full factorial design of experiments, consisting of five factors (4 materials, 3 corona voltages  $V_c$ , 4 corona to grid distance  $d_{cg}$ , 4 grid to sample distance  $d_g$  and 4 charging temperature  $\Theta$ ) is created in R suite (R core team, 2017). Four of the factors refer to the charging parameters used for the corona charging procedure. The fifth factor refers to the material used for charging and as a result, includes all the morphological parameters (stiffness, distributions etc). An assumption is made that the influence of the charging procedure to the material morphology is negligible. The range of the inputs was selected based on the literature and the capabilities of the device. Table 4.1 gives a synopsis of the factors as well as their levels.

Factors Levels	Corona voltage $V_c$ (kV)	Corona- grid distance $d_{cg}$ (mm)	Grid- sample distance $d_g$ (mm)	Temperature $\Theta$ (°C)	“sample”
1	20	12	4	23	LRH 60
2	25	17	5	60	LRH 70
3	30	22	6	70	LRH 80
4	-	27	7	80	EUH75

Table 4.1 Factors and levels of the design of experiments.

The first level of temperature (23 °C) represents the average room temperature, when the heating element was not used to heat up the sample. The lowest value for corona voltage  $V_c$ , as well as the highest values of  $d_{cg}$  and  $d_g$ , correspond to the lowest potential and fields that can produce and sustain electron avalanche. The full factorial design consists of 768 different experiments. The R function OptFederov of the package AlgDesign (Wheeler, 2014) is used to reduce the total amount of runs to 64 optimal experiments, enough to describe the phenomenon, resulting in 16 experiments per material. The measured quantities (outputs) are divided into two categories. The first category is the corona device outputs that are either measured directly or calculated. The second category is the material outputs that are derived by the performance of the material under a variety of tests, presented in table 4.2 along with their descriptions.

All parameters will be used in order to determine the best charging conditions.

The grid voltage  $V_g$  and the sample field  $E_s$  are given by equations 4.1 and 4.3 respectively.

$$E_s = \frac{V_g}{l_3} \quad (4.3)$$

where  $l_3$  is the film's thickness.  $E_s$  is a composite parameter directly related to  $V_g$ ,  $V_{av}$  and  $V_c$  and the sample thickness.

<u>CORONA</u> <u>PARAMETER</u>	Symbol	Units	Description
Grid Voltage	$V_g$	kV	Average grid voltage during charging
Avalanche Voltage	$V_{av}$	kV	Grid potential gained by migrating charges
Corona-Grid Field	$E_c$	MV $m^{-1}$	Field created between the corona tip and the grid
Sample Field	$E_p$	MV $m^{-1}$	Charging field
<u>MATERIAL PARAMETER</u>			
Sample current peak	$I_{s-peak}$	$\mu A$	Highest current value during poling
Sample charge density	$\rho_s$	$Q m^{-2}$	Obtained charge density after charging
Sample Capacitance	$C_s$	F	Capacitance of the sample measured after charging
Peak piezoelectric performance	$d_{33-peak}$	$pC N^{-1}$	Maximum piezoelectric coupling of the sample
Maximum charges	$Q_s$	nC	Charges produced by the sample under a load of 130 kPa
TSD peak temperature	$\Theta_{TSD}$	$^{\circ}C$	Temperature where highest peak occurred during TSD
TSD peak temperature value	$I_{TSD-peak}$	pC	Peak current produced by the sample during TSD
TSD charge density	$\rho_{TSD}$	$Q m^{-2}$	Total Charge density based on TSD
Ageing	-	%	Reduction of produced charges under 130 kPa

Table 4.2 Measured outputs of the design, their symbol, unit and description.

$E_s$  is considered as a separate input variable, due to its critical role to the charging process, which is well explained in the literature and demonstrated in experiments within this work. The approach is to exclude  $E_s$ 's strong correlation to the response in order to investigate the role of the rest of the factors that are expected to have a smaller influence to most of the output parameters. For this, linear regression models of each output variables with the independent variables were implemented in R suite. The models are of the form:  $\text{response} = E_s + \Theta + d_{cg} + d_g + \text{"sample"}$ , unless otherwise stated. Note that  $\Theta$ ,  $d_{cg}$ ,  $d_g$  and "sample" are treated as factors. The level of rejection of the null hypothesis within this analysis is the 1% ( $P < 0.01$ ).

### **4.3.3 Constant current method**

This experiment is done to explore the effect of poling with constant current to  $d_{33}$ . For this experiment, grid to sample distance  $d_g$  was set to 6 mm. As only one power supply was available, the electric potential of the grid  $V_g$  is indirectly controlled by displacing the corona tip to or away from the grid which is connected to a high voltage (HV) potential divider. When the tip is approaching the grid, more current is injected into the grid, which raises  $V_g$  as charges then need to flow to ground through the large resistance of the divider.

The corona tip is brought to the highest point away from the grid. The user sets the desired current  $I_s$  in Labview. Once the sample is inside the chamber,  $V_c$  is enabled and the corona tip motor displaces with full speed towards the grid. Once the current reaches the desired value, the error to the controller is zeroed and the displacement starts being controlled in close loop by the software. The poling process is stopped before any discharge happens on the sample, or interrupted by the program, if any other limitation of the device is reached (importantly if minimum  $d_{cg}$  distance reached). This is designated by a rapid increment of  $I_s$ , without any increment of the  $V_g$  by the displacement of the corona tip. Since for this experiment  $V_g$  is not constant, the results will be compared to the previous experiment based on the final  $V_g$  obtained.

#### **4.4 Performance characterization**

The experiments described below were done with aim to obtain the key parameters like piezoelectric coefficient, stiffness and permittivity as a function of stress applied. These parameters are needed to calculate the resultant electromechanical coupling coefficient  $k^2$  which is central to this work. Both static and dynamic compression tests were held for this purpose within the linear and the non-linear region of the material.

##### ***4.4.1 Static, quasi-static $d_{33}$***

To assess the static piezoelectric coefficient  $d_{33}$  of the functionalized samples, each sample should be compressed very carefully. Since a small misalignment of a few degrees between the crushing plates would lead to a smaller area of the sample sustaining most of the compression, a custom-made test rig was constructed. It is essentially a rod of 5 mm diameter that has the ability to slide in the vertical direction and compress the sample against another stationary rod with the same diameter. As the signal coming out of the sample is rather small, the exterior of the test rig is covered with an electrically grounded metallic mesh, acting as a Faraday cage for noise reduction. In order to provide a uniform pressure to the whole area of the sample as well as a better conductive continuity, electrically conductive silicone pads were inserted between the metal plates and the sample surfaces. When testing large samples metal plates, having the size of the sample, were inserted between rods and pads to evenly distribute the load. Due to the conductivity of the Silicone pads (around  $4 \text{ k}\Omega \text{ mm}^{-1}$ ), they do not interfere with the measurement of charges and the total resistance between rods and electrodes on the sample is kept sufficiently small. The testing procedure starts with the sample being inserted between the brass rods of the rig. The weight of the upper rod provides a preload of 0.16 N to the sample, assuring contact between the pads and the surface of the material at all time. The sample gets short circuited (using the Zero-CHK of the Keithley 6517b

electrometer) for the excess charges to vanish and subsequently the load is applied. Stresses in the range of 25.5 kPa to 510 kPa for the 5 mm diameter sample and 1.45 kPa to 131 kPa for the 12 X 12mm<sup>2</sup> samples are applied on the sliding rod. The charges from the surface of the sample are measured with Keithley 6517b electrometer. The quasi-static charges were also logged by a program build in Labview. The effect of creep / stress relaxation to the charges over time was logged, under both the loading and unloading sequence.

#### **4.4.2 Inverse piezoelectricity**

The samples were inserted between the custom-made test rig, so that the external electrodes were in contact with the brass rods which in turn were connected to the Glassman HV-PSU. The Micro epsilon NCDT 6200 capacitive sensor module was used to measure the thickness increment that the potential difference caused, with the CS005 measuring probe. Voltage potentials ranging between 50 and 200 V were applied to the film. In order to investigate the inverse piezoelectric effect within the non-linear region, the samples were pre-stressed and allowed to relax, under static loads ranging between 3.5 kPa to 110 kPa. Finally, the direct piezoelectric effect was compared to the inverse piezoelectric effect, within the non-linear region of strains.

#### **4.4.3 Dynamic $d_{33}$ , $c_{33}$**

Two set-ups were used for the dynamic experiments. The first experimental setup utilizes an electrodynamic shaker to provide the dynamic compression acting on the sample. The sample strain, the compressive force acting upon the sample as well as the charges produced, are simultaneously logged with a capacitive displacement sensor, a load cell and an electrometer respectively.

A custom-made compression setup, schematically depicted in figure 4.8, was mounted on the Data Physics V20 shaker. A PMMA platform was designed built and placed on the shaker head, to host the measuring

probe of the Micro epsilon NCDT 6200 capacitive sensor. The CS005 measuring probe, having a range of 500  $\mu\text{m}$ , was securely embedded in the PMMA platform. PMMA spacers provided an offset from the head of the shaker. A load cell is mounted on top of the PMMA spacer, with one end being mechanically unconstrained. A threaded rod goes through the non-constrained side of the load cell, pointing to the centre of the PMMA platform. A PMMA disc is screwed on the thread, with copper tape added on its bottom side to form the target of the capacitive probe.

The sample is sandwiched between two stiff metal plates. An additional thin layer of silver paint is added between the metal plates and the sample surfaces. This extra layer has the same effect as the silicone pads mentioned before, but its thickness can be neglected securing the validity of the strain measurements.

Embedded wires inside the PMMA platform are in electrical contact with the metal plated of the sample. The charges produced by the sample are measured between the embedded wires and the threaded rod. The rod can be lowered to provide preload to the sample sitting below it. The shaker head displacement is opposed by the thread of the load cell. The load cell used, has a range of  $\pm 50\text{N}$ . The charges from the surface of the sample are measured with the aid of Keithley 6517b Electrometer. The sample is inserted in-between the plates and a preload of 0.5 N is applied.

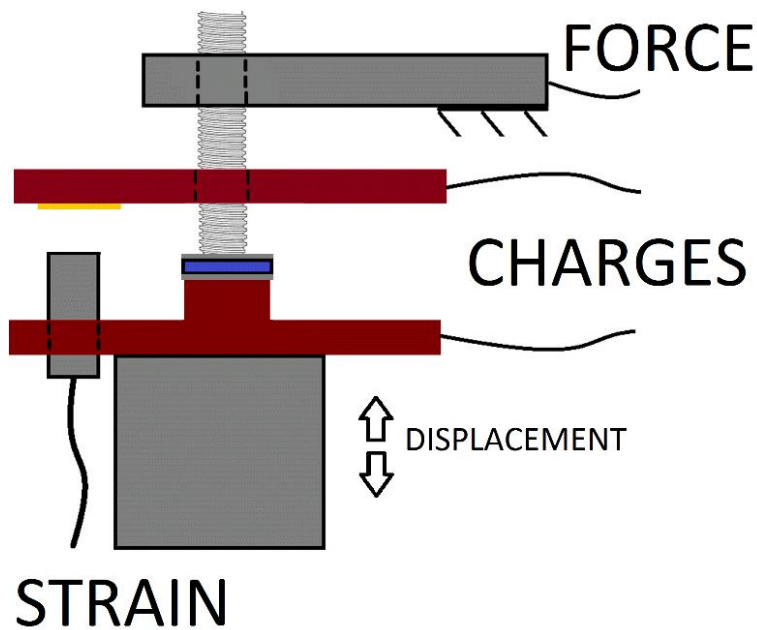


Figure 4.8 Experimental setup for dynamic  $d_{33}$ ,  $c_{33}$  and force measurement. The shaker head displaces in the vertical direction, thereby compressing the sample lying between the clamp. A reaction force is provided by the load cell via the threaded rod. Charge, displacement and applied force are measured in synchrony.

A Sinewave signal is applied to the shaker amplifier, leading to a sinusoidal displacement of its shaft. The force  $F(t)$ , the produced charges  $Q(t)$  and the compressive displacement  $\Delta l(t)$  (defined as the difference between the current and the previous thickness of the sample) are logged and plotted directly with the aid of Labview. Different mechanical excitation frequencies ranging from 0.1 Hz to 1 Hz as well as different preloads are applied to the sample, in order to investigate the stress / strain and the piezoelectric response both in the linear and non-linear region of the material.

The effect of the stress rate to the strain, the stiffness and the charges were also monitored. The EUH 75 material, expanded under 5 MPa was used for these tests. The Shimadzu EZ-SX was used to mechanically compress the sample. The CS005 measuring probe was attached to the end of the Shimadzu moving part to measure the displacement of the head. The applied force was measured by the Shimadzu and the charges generated by the Keithley 6517b Electrometer. As strain is of interest, an additional, thin layer of silver paint was used between the sample and the

metal plates, instead of silicone pads. The sample was placed between the clamps of the machine and a preload of 0.5 N (3.6 kPa) was applied. A variety of stress rates, ranging from 2.5 kPa s<sup>-1</sup> to 300 kPa s<sup>-1</sup> were applied, reaching the final value of 300 kPa of stress. The stress/strain curves were obtained as a function of stress and the stiffness  $c_{33}$  was calculated, for every stress value.

Finally, the creep/stress relaxation of the film was investigated, using the same experimental setup and material. In order to minimize creep / stress relaxation of the material during the loading phase, a high stress rate of 300 kPa s<sup>-1</sup> was chosen. A preload of 3.6 kPa was initially applied, followed by the stress ramp. The compression of the film was stopped at a variety of strains, ranging from 0.04 to 0.18. Once the compression stopped, the stress / creep relaxation was logged, until no more displacement or force change was observed. The data of this test, were used to link the equilibrium applied stress with the equilibrium strain (stress and strain after creep / stress relaxation).

#### **4.4.4 Permittivity-capacitance measure**

Two experiments were done to investigate the permittivity of the material to explore the change in permittivity under different strains. The 12 X 12mm<sup>2</sup> functionalized samples were inserted in the custom-made static test rig, referred in section 4.4.1.

In the first experiment, capacitance was defined as Q/V and the functionalized samples were treated as parallel plate capacitors, having their capacitance (C) given by equation 4.1.

$$C_{33} = \frac{\kappa_{33}A}{l_3} \quad (4.1)$$

Where  $\kappa_{33}$  is the permittivity of the material and A the area of the sample. The samples were charged under a variety of voltage potentials, low enough to assure no poling of the material. In order to investigate the effect of strain, the material was subject to a variety of static preloads, ranging between 1.4 kPa and 250 kPa. As the capacitive displacement sensor could not be used to measure the compressive displacement, the

thickness of the film at equilibrium was provided by the data obtained in section 4.4.2.

Two switches connect the sample with the input voltage source and another two the sample with the output to Keithley 6517b electrometer device, (figure 4.9).

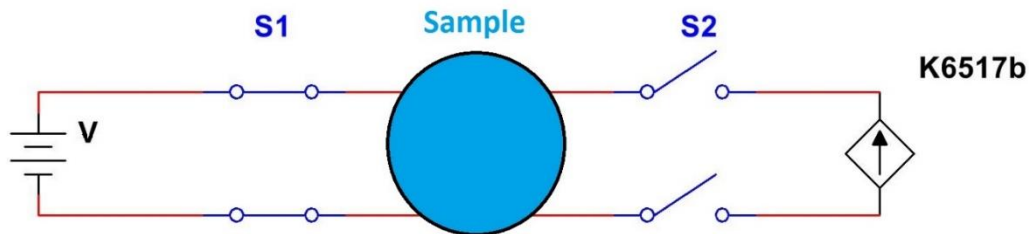


Figure 4.9 Experimental setup of capacitance- permittivity measurement

When closing S1, the sample gets charged, reaching the power supply potential. After the sample is charged, S1 is opened and subsequently S2 is closed, allowing the sample to discharge through the electrometer. The permittivity is found by equation 4.1.

The second experiment uses the same experimental setup and principle, but the capacitance is measured by a network analyser. The Bode 100 network analyser was used to measure the sample's capacitance, while the sample is pre-stressed under a variety of static loads.

#### **4.4.5 Impedance analysis**

For this experiment, an LRH 70 sample, expanded under 5 MPa was used. Gold (Au) electrodes of 70 nm thickness were sputtered on both external layers of the sample. As investigated by (Mellinger, 2003) good electrode conductivity is essential for this test. Bode 100 network analyser was used for obtaining the frequency response of the sample for frequencies between 10 Hz and 40 MHz. Thin wires of 16  $\mu\text{m}$  diameter, to ensure low mechanical inertia, were attached with silver paint to both surfaces of the sample and to the network analyser device. The setup was firstly calibrated without the sample in order to find the inductance of the wires, which is needed for further parameter estimations. As Bode 100 stimulates the sample with a low signal sine wave, the sample is

considered to work under the linear region. All the data obtained with this technique are compared with the data obtained with the previous methods.

#### **4.4.6 TSD test**

Thermally Stimulated Discharge (TSD) tests were conducted to determine the amount of charges embedded inside the bulk of the material, as well as to determine the thermal stability of the samples. This is the last experiment done on the samples, as it is destructive. All the 12 X 12 mm<sup>2</sup> samples, charged under the design explained in section 4.3.2, were tested. Each sample was sandwiched between two metal plates. An additional silver paint layer was used in between the sample surfaces and the metal plates. The sample was inserted in the Perkin Elmer 8000 DMA. A controlled linear temperature sweep of 3 °Cmin<sup>-1</sup> was applied on the sample, from room temperature to 180 °C. As the temperature increases, charges are released from the bulk of the material due to molecular movements. Electrically grounded aluminium screened wires connect the metal plates to the Keithley 6517b electrometer. The produced charges are measured and logged during the temperature increment. Once the temperature reaches 180 °C, the data are saved and the final obtained charge density, is compared to the charge density obtained from the charging procedure.

#### **4.5 Cellular PP model**

Each material family, expanded under 2 MPa and 5 MPa, was digitally recreated in Matlab (Mathworks) as a 3D model. 2D Cross sections of this digital material were imported to Ansys for FEA, where compression tests were held, in order to investigate the mechanical properties of each modelled film.

#### **4.5.1 Analytical- FEA model**

To study the mechanical response of Cellular Polypropylene films, 3D models of the geometry were produced having similar morphological properties with the real films. The morphological properties were obtained from SEM cross sectional images: distribution of void thickness (referred as  $D_h$  distribution), void aspect ratio (referred as  $D_r$  distribution), total thickness  $l_3$  of the film and porosity (voided area / total area) and the inflation of the material was measured between the expanded and uninflated state. As there is a lot of noise at the output of the image processing program, voids with less than  $1 \mu\text{m}^2$  of area were not considered for further analysis.

The 3D geometry of Cell-PP was designed on the basis of analytical Splines. The film is considered to be made of  $N$  layers of polymer. Each layer was defined by two splines parallel to  $X$  axis with the distance between them designating the thickness of the layer. A set of points, equal to the average number of voids observed in the SEM images, were randomly distributed within the 3D space, between the layers, designating the position of each void. In order to mimic the biaxial stretching applied in the manufacture of those films, discs were created in the  $X$ - $Y$  plane of the film with their radius determined by contact with nearest neighboring disks in the same layer. Initially, the film's porosity is zero, as the layers are in contact with each other. Simulation of the pressure-expansion treatment is done by increasing the thickness of each void, so as to achieve the observed aspect ratio (void aspect ratio). During this procedure, the void borders push the Splines, which in turn follow the expansion in the  $Z$  direction depending on the voids, above or below them. The morphological parameters of the modeled material were estimated from 2D cross sections with exactly the same procedure used for the real material.

Log-normal distributions were fitted to both the void thickness ( $D_h$ ) and aspect ratio ( $D_r$ ) empirical distributions for the real and the modelled films. The estimated parameters of the real films were linked to the modelled films parameters. The statistical suite R with the package `fitdistrplus` (Delignette-Muller *et al.*, 2017) were used for statistical analysis. The comparison of two empirical distributions was done with Kolmogorov-

Smirnov test in order to determine whether they come from the same distribution.

The 2D cross sections of the modelled films were fed to Inkscape to generate a suitable surface for importing into ANSYS FEA software. The problem was solved under plane strain approximation. A suitable mesh size was selected and pads were placed on the top and bottom layer to ensure uniform distribution of the compressive load. The geometry was constrained from displacements in any other direction except the direction of the compression. For this analysis, the voids are considered to be closed pore. As a result, the pressure inside them is inversely proportional to their area. The mechanical response was obtained after applying different mechanical loads. The load-deflection curves obtained were compared to the experimental results acquired via Dynamical Mechanical Analyzer (DMA) to validate the model.



## Chapter 5. Results

### 5.1 Corona device performance

#### 5.1.1 Grid voltage

The corona charger was tested for its voltage, field and current response, in the absence of a sample. As the equipment is custom made, the interaction between the components is not known. The corona charger was firstly tested for its interaction between the corona tip  $V_c$  and the grid  $V_g$  voltages as well as the field  $E_{cg}$  created between them. The field  $E_{cg}$  can be estimated by equation 5.1.

$$E_{cg} = \frac{V_c - V_g}{d_{cg}} \quad (5.1)$$

The estimation of the field by equation 5.1 is an approximation of the real field, as  $V_c$  is applied on a thin wire rather than a plate. Still, this approximation is considered a good one for the purpose of this work. Due to the experimental setup, the voltage of the grid ( $V_g$ ) is the result of two contributions. The first ( $V_c / 6.6$ , (equation 5.2)) is the direct potential resulting from the voltage divider (shown in chapter 4, Figure 4.2).

$$V_g = \frac{V_c}{6.6} + V_{av} \quad (5.2)$$

The second is the potential increase gained due to negative ions, repelled from the negative potential corona tip and being accelerated towards the grid, forming a “corona wind”. The total electrical potential of the grid and the component of the potential due to the voltage divider are shown in figure 5.1a.

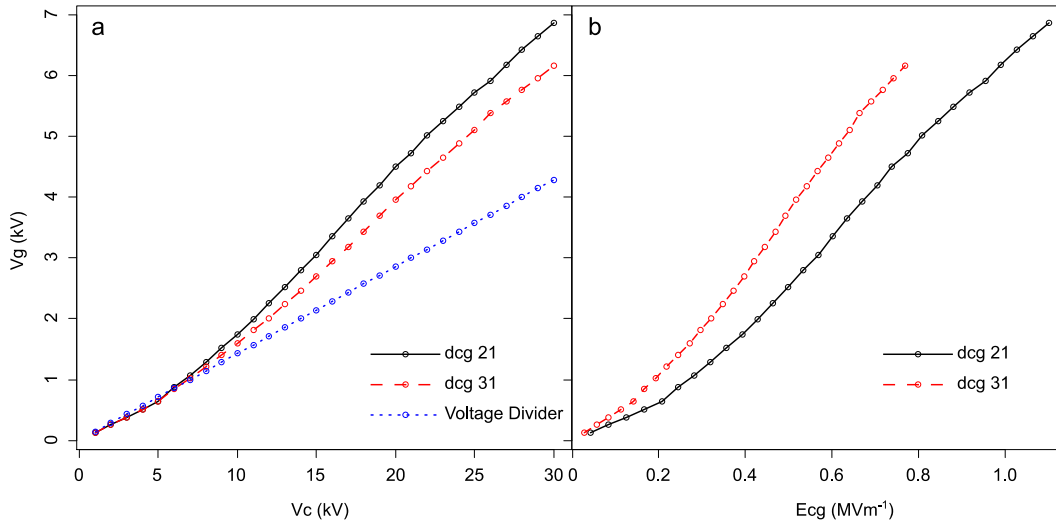


Figure 5.1. Voltage of the grid ( $V_g$ ) over **a)** corona voltage ( $V_c$ ) and **b)** field between the corona tip and the grid ( $E_{cg}$ ), for distances between the corona tip and the grid  $d_{cg}$  of 21 mm and 31 mm. The distance between the grid and the measuring tip ( $d_g$ ) is kept constant at 4 mm. Single run data. The potential of the grid emerging from the voltage divider is also plotted for comparison.

As the data in figure 5.1a suggests, the total potential  $V_g$  is similar for both the 21 mm and 31 mm cases and almost equal to the potential gained by the voltage divider, when the potential of the corona tip ( $V_c$ ) is lower than 5 kV. It is evident that either there is no electron avalanche taking place for  $V_c < 5$  kV or the electron avalanche is weak enough, so that the negative and positive ions recombine before they reach the grid. The latter case can be excluded, as there is no evidence of voltage increment due to the corona wind, even when the distance between the corona tip and the grid is decreased by almost 48% from 31 mm to 21 mm (Figure 5.1 a).

Further investigation on the parameters that influence the electron avalanche can be done by analysis of figure 5.1 b. By comparing  $V_g$  for the 31 mm and the 21 mm  $d_{cg}$  distances, it can be seen that the resultant  $V_g$  for a  $d_{cg}$  of 31 mm is higher for every given field  $E_{cg}$  (figure 5.1 b). On the other hand, figure 5.1a suggests that the obtained  $V_g$  is only moderately dependent on the distance  $d_{cg}$ . As known, the point to plate fields like  $E_{cg}$  (created between the corona tip and the grid) is not constant in the direction of the field. The field gets higher towards the corona tip. This

explains why the voltage  $V_g$  is influenced more by the distance  $d_{cg}$  compared to the voltage  $V_c$ . The same can be concluded for the electron avalanche, as it is the only reason for  $V_g$  increment.

### 5.1.2 Current performance

Under the same experimental conditions, the current  $I_s$  flowing through the grid towards the measuring probe is measured. Keeping in mind that no sample exists between the measuring probe and the grid, the value of the sensed current is higher than that expected during sample charging experiments. Furthermore, the current is a result of ion migration only. Figure 5.2 shows the obtained current  $I_s$  for each value of  $V_g$  obtained by  $V_c$  increment from 0 kV to 30 kV.

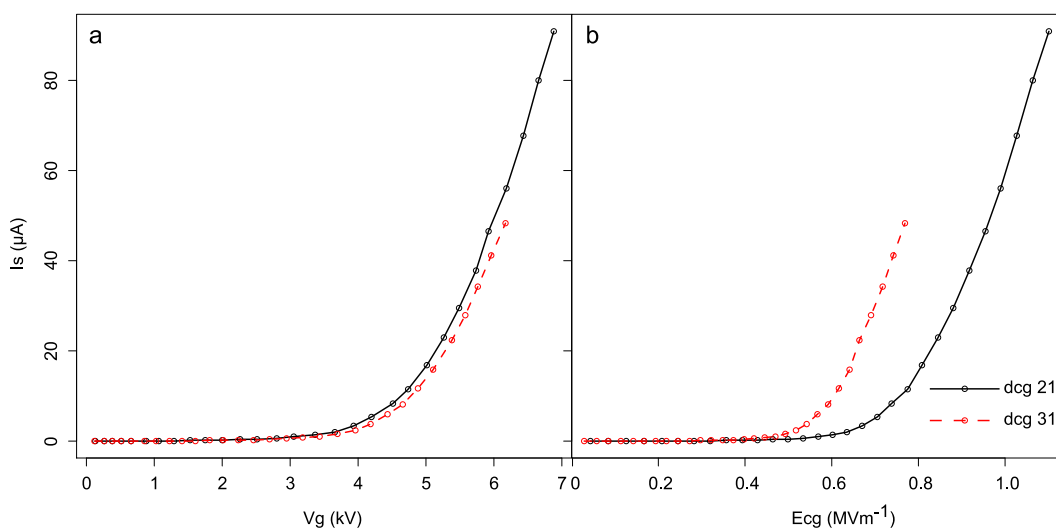


Figure 5.2. Current ( $I_s$ ) flowing through the measuring tip, over **a)** grid voltage ( $V_g$ ) and **b)** field between corona tip and grid ( $E_{cg}$ ), for distances between the corona tip and the grid ( $d_{cg}$ ) of 21 mm and 31 mm. The distance between the grid and the measuring tip is 4mm.

The lack of electron avalanche is again evident in figure 5.2 a. There is no current flowing from the grid to the measuring tip for  $V_g < 0.65$  kV. This observation is in agreement with the lack of current hypothesis made above (figure 5.1) for  $V_c < 5$  kV resulting to a grid potential of  $V_g = 0.75$  kV only due to the HV voltage divider.

Also, for a  $V_g$  potential up to 3 kV, the current sensed by the measuring tip does not exceed 0.74  $\mu\text{A}$ . That means the charges are captured by the

grid and flow through the voltage divider to the ground, rather than the high air gap impedance that the distance  $d_g$  provides. Comparing the two curves obtained for  $d_{cg}$  of 21 mm and 31 mm in figure 5.2 a, and for a  $V_g$  of 6 kV, there is a difference of 15% on the current. This can be attributed to the higher charges obtain, when the field  $E_{cg}$  is higher, as more charges are picked up by the measuring tip per time unit. Finally, despite the higher final value of  $I_s$ , in case of the  $d_{cg}=21$  mm, the measured current per  $E_{cg}$  unit field is lower (figure 5.2). That means that for higher  $d_{cg}$  distances, less charges per unit field are picked by the measuring tip.

### **5.1.3 Distance $d_g$ , $d_c$ performance**

The grid voltage and the current response are both tested for displacements of both the grid ( $d_g$ ) and the corona tip ( $d_c$ ), as well as for  $V_c$  potentials of 20 kV, 25kV and 30 kV. By increasing  $d_g$ , the  $d_{cg}$  is decreased by the same amount, as equation 5.3 shows.

$$d_{cg} = d_c - d_g \quad (5.3)$$

Figure 5.3 shows the responses of grid voltage ( $V_g$ ) and measured current ( $I_s$ ) over  $d_g$  for a variety of  $d_c$  and  $V_c$  values.

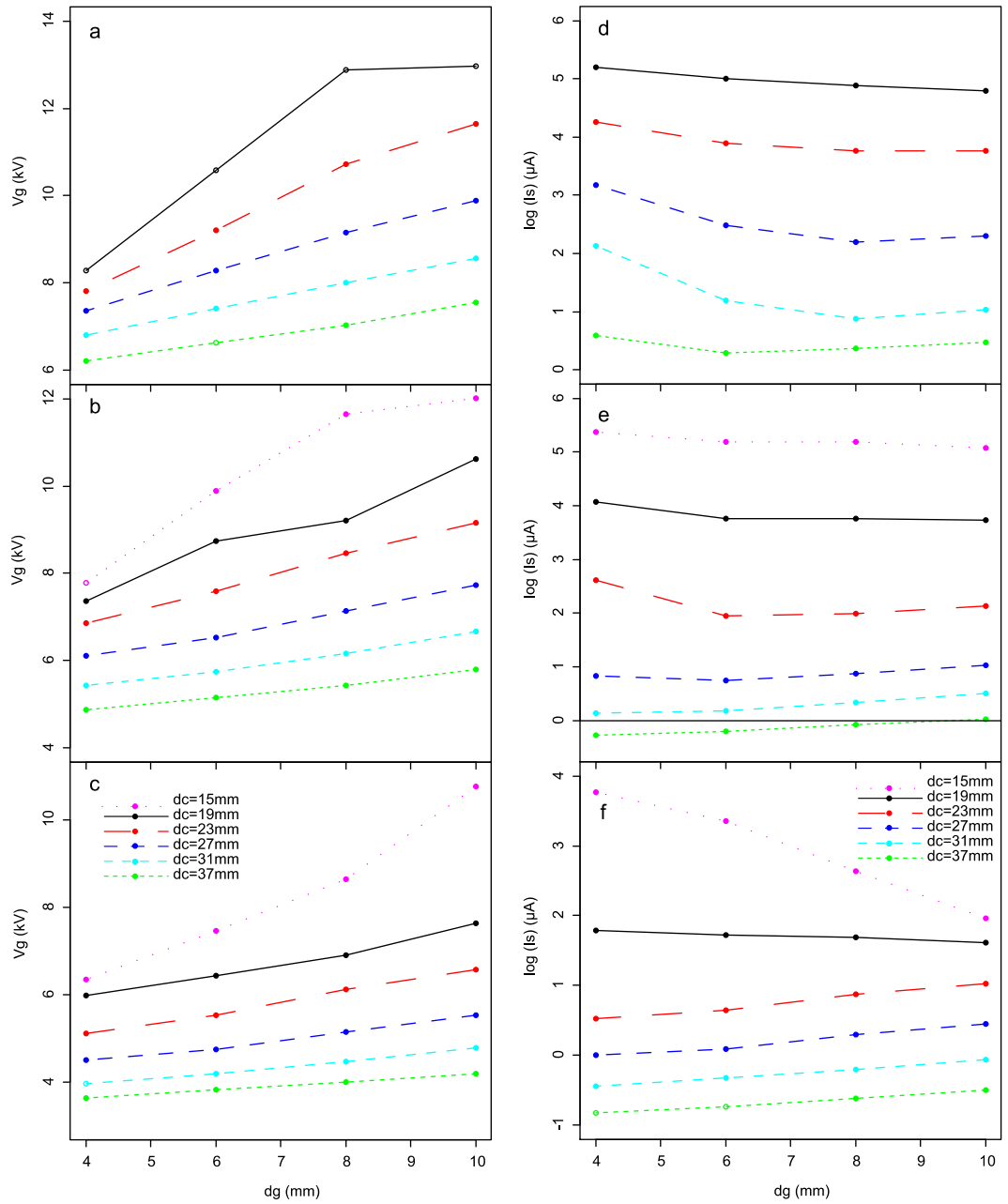


Figure 5.3. Grid voltage  $V_g$  (left side) and measured current  $I_s$  (right side) over  $d_g$  for a variety of  $d_c$  values. Top to bottom:  $V_c = 20$  (a,d),  $V_c = 25$  (b,e) and  $V_c = 30$  kV (c,f).

Referring to the voltage graphs, the voltage of the grid is increasing almost linearly with both  $d_g$  increment and  $d_c$  decrement. This is expected, as both these changes decrease  $d_{cg}$ . The increment slope of  $V_g$  over  $d_g$  also increases proportional to  $V_c$ . The voltage of the grid reaches a saturation around 13 kV as shown for the case of  $V_c = 30$  kV. Values greater than this could not be attained with the existing setup. The equivalent test with  $d_c = 15$  mm and  $V_c$  of 30 kV could not be implemented even for  $d_g = 4$  mm.

The response of the current on the other hand, is not similar to the voltage. For  $V_c$  of 25 kV and 20 kV, increments of  $d_g$  for high  $d_c$  increase the current. This does not apply for lower values of  $d_c$ , where the current reduces with increasing  $d_g$ , even though the voltage of the grid increases. Despite that phenomenon, lowering the corona tip (reducing  $d_c$ ) increases both the current  $I_s$  and the voltage  $V_g$ . This influence is going to be used for the constant current method, explained later.

The corona charger response is summarized in figure 5.4. The influence of both  $V_c$  and  $d_{cg}$  to  $V_g$  and  $I_s$  is presented in a form of meshed 3D graph.

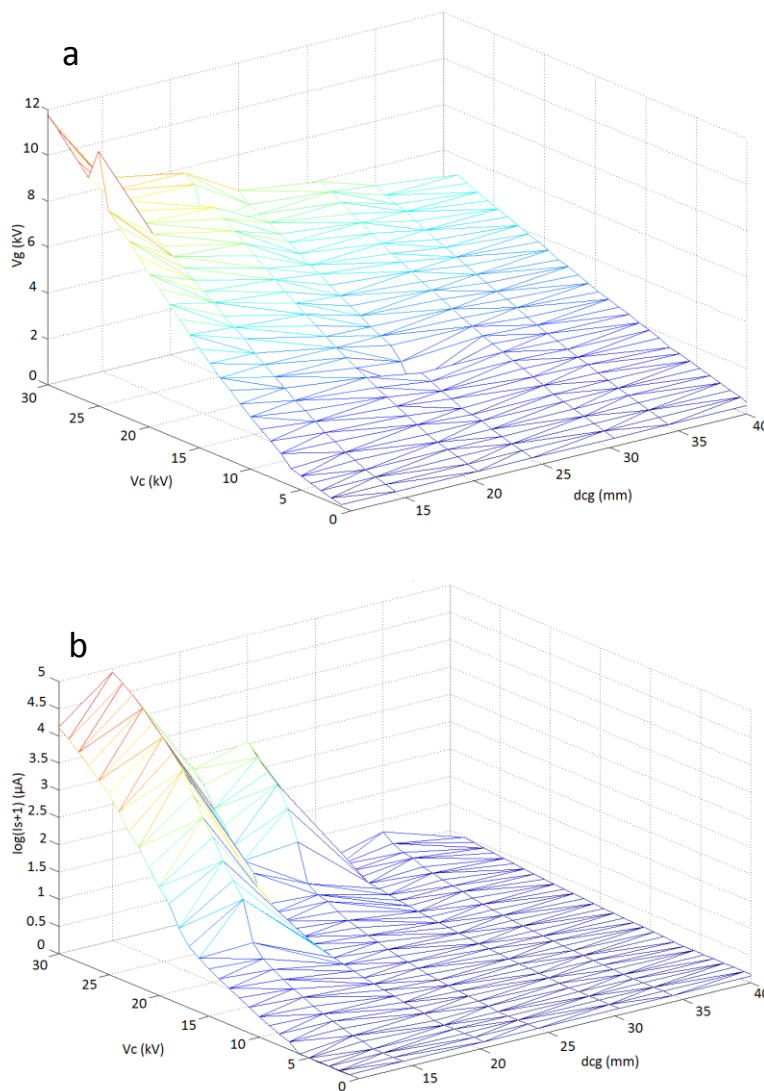


Figure 5.4. Corona charger grid (top) and log of the current response (bottom). Plots combine all explored values of  $d_g$  and  $V_c$ . The logarithm of the current  $I_s$  is given on Z axis (figure 5.4b), as the values span a large range.

Since low constant current charging provides better results in terms of field uniformity, the optimum charging area of operation is initially expected to be within 10 mm to 20 mm for  $d_{cg}$  and 25 kV to 28 kV for  $V_c$ . This hypothesis is going to define the factor levels for the design of experiments presented later in the chapter. The distance  $d_g$  is not considered, as the film charging field is determined only by  $V_g$ , assuming that electron avalanche exists.

## **5.2 Materials**

### ***5.2.1 Gas Diffusion Expansion (GDE)***

The samples underwent a GDE procedure to increase their thickness. As explained in the literature section, the obtained thickness of the material is influenced mostly by how quickly the depressurization part of the process is done. More specifically, the initial rate of decrease of the pressure at the start of the depressurization process is of importance, as it defines the differential pressure between the voids and the environment (pressure chamber). This initial “impact” force, lasts for sub seconds and could not be calculated with the existing setup. An estimation was attempted, by defining it as the difference between the initial pressure and the pressure after 3s called  $\Delta p$ . Quicker depressurizations results in thicker voids. This depressurization of the chamber, for pressures of 2 MPA and 5 MPA, is shown in figure 5.5.

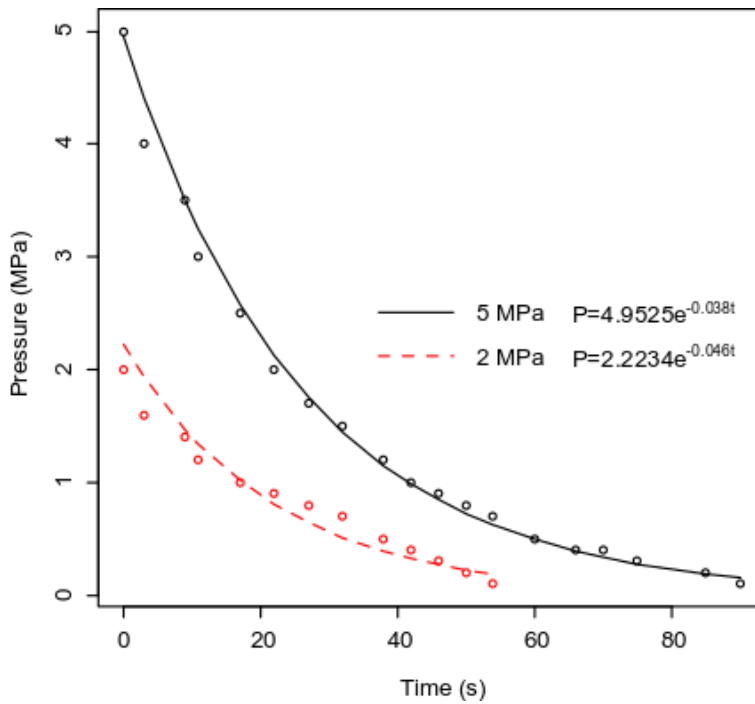


Figure 5.5. Chamber depressurization process for initial pressures of 2 MPa and 5 MPa with the exponential fits of the data. Single run measurements.

The 3s  $\Delta p$  for 5 MPa and 2 MPa initial pressure is 0.4 MPa and 1 MPa respectively (first two points of the graphs) acting against the walls of the voids for each occasion respectively. That translates to a rate of 0.13 MPa s<sup>-1</sup> and 0.33 MPa s<sup>-1</sup> of initial slope. That is a 39% difference in  $\Delta p$  acting against the border of the voids, comparing the two expansions (2 MPa to 5 MPa)

The samples underwent heat treatment at 85 °C for 10 s short after their GDE, for their expanded thickness to become permanent. The obtained thickness of each sample type was measured from cross sectional images, using SEM and analysing with a custom made image processing software. The energy used by the SEM was the highest (15 KeV) for the purpose of obtaining the maximum image resolution. However, polymer degradation occurs when this energy is focused on a small area (i.e. X2000 magnification). The energy density emitted from the machine is high enough to damage the voids progressively after a short period of time. The progressive damage done to the polymer is shown by the cross-section images in Figure 5.6.

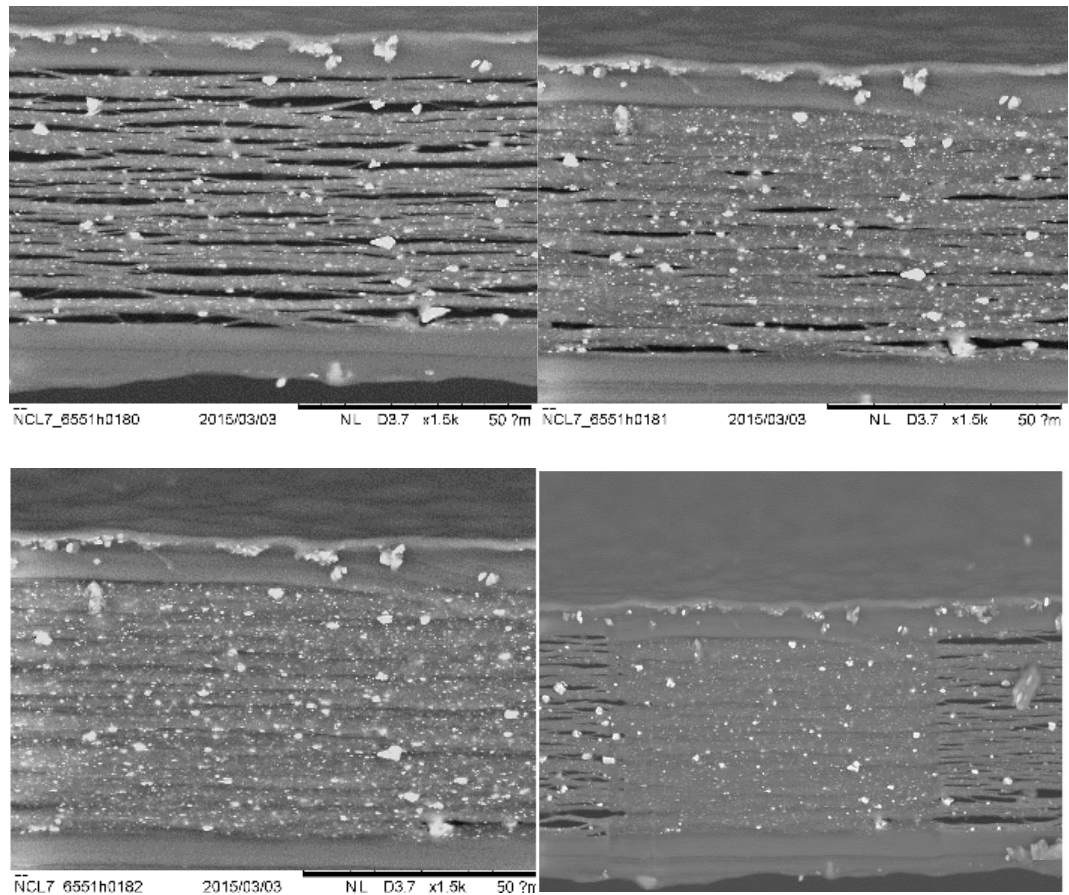


Figure 5.6. The 15 keV beam damages the sample's surface. Image taken after 10 s (top left) , 40s (top right) and 60 s (bottom). The image at the bottom right is showing a wider area of the cross section, with both the damaged and non-damaged areas. The white dots are the  $\text{CaCO}_3$  particles

The TM 3030 SEM has the ability to reduce the beams energy to 5KeV with an expense of the void borders not being as profound due to less contrast between the polymer and the void, leading to higher uncertainties to the void border identification via the image processing software. Thus, for the rest of the images, 15 keV of energy is used and the image is captured as fast as possible.

Any observations made on the films are assumed to hold for the total volume of the sample, as it is assumed that cross sectional images provide a correct representation for the whole material. From the obtained images, one cross section from each material type and expansion is shown in figure 5.7. Non- expanded material cross sections are not included, as these have very few visible voids, leading to meaningless

narrow distributions. However, cross section images were still obtained for the non- expanded materials in order to measure the thickness of each film and compare it with the expanded ones.

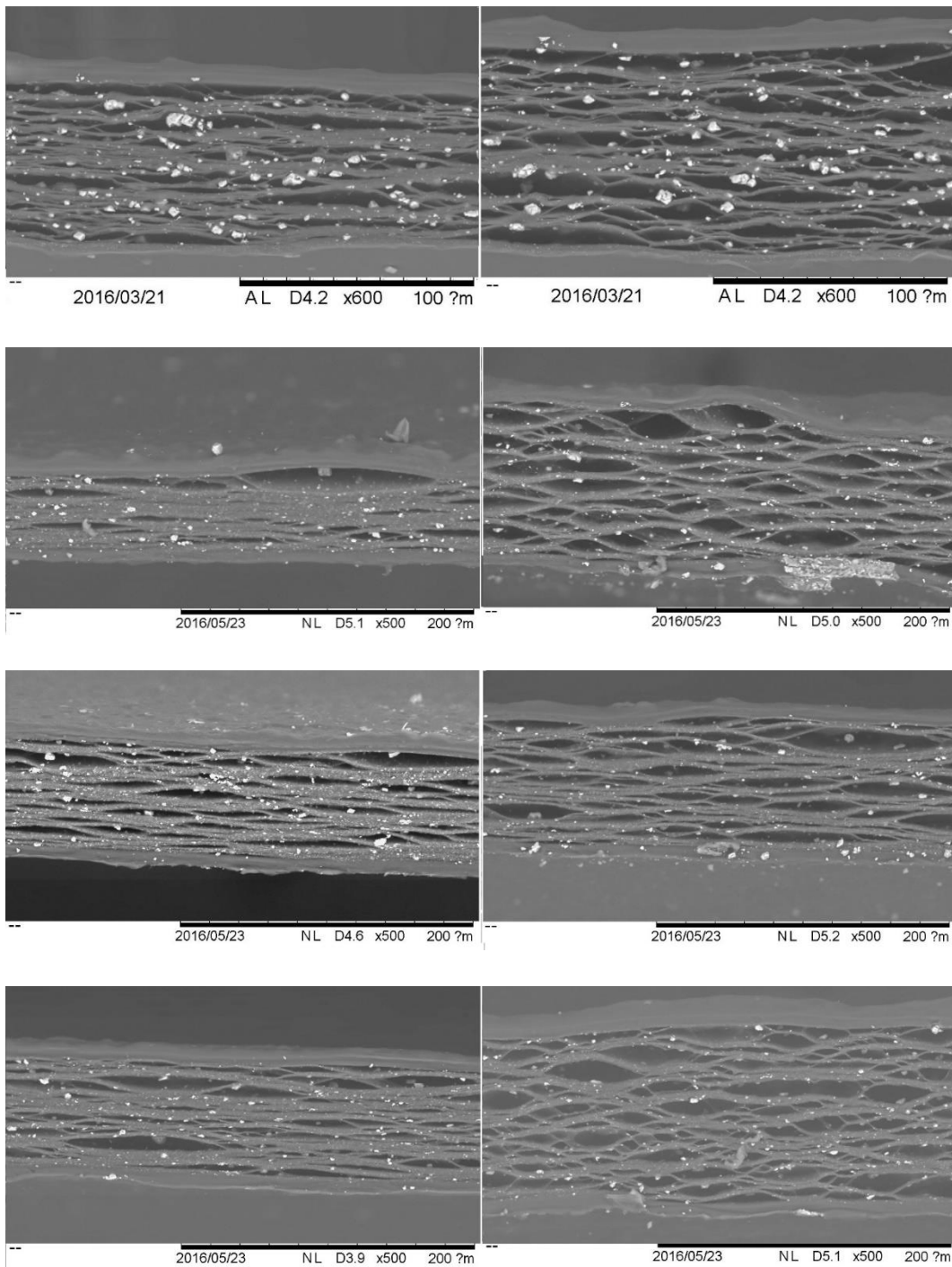


Figure 5.7. Cross sectional images of EUH 75 (first row), LRH 60 (second row), LRH70 (third row) and LRH80 (forth row). Materials expanded with GDE at 2 MPa (left) and 5 MPa (right). Photos taken under 15 keV of energy.

Higher expansions result in more and thicker voids inside the polymer. It is observed from cross sectional images that as the inflation ratio increases, previously not expanded voids gain thickness. This results in higher void density after the high (5 MPa) compared to the lower (2 MPa) expansion, for all materials shown in figure 5.7. The voids emerge due to the separation of polymer layers. This separation of the layers happens mostly where  $\text{CaCO}_3$  particles exist. Each void is expected to have at least one of these particles inside it. When not visual, the particle might be left on the part of the film that got cut away or exist further inside the void or even displaced during the cutting of the cross section. However, some of these particles seen embedded in the polymer material did not form a void around them possibly due to lack of stress.

Based on both the manufacturer data sheet and observations, the difference among the LRH family are only resulting from different non-expanded film thickness (60  $\mu\text{m}$ , 70  $\mu\text{m}$  and 80  $\mu\text{m}$  for the LRH 60 LRH 70 and LRH 80 respectively). On the other hand, a different void morphology can be seen for the EUH 75 (figure 5.7 a), when compared to the rest of the materials. The shape of the EUH 75 voids is irregular and creased, while the shape of voids in the rest of the materials is closer to ellipsoids.

The thickness of LRH 60 expanded under 5 MPa pressure is comparable to the thickness of LRH 80 expanded under the same pressure. The cross sections of the two materials are placed next to each other for comparison in figure 5.8.

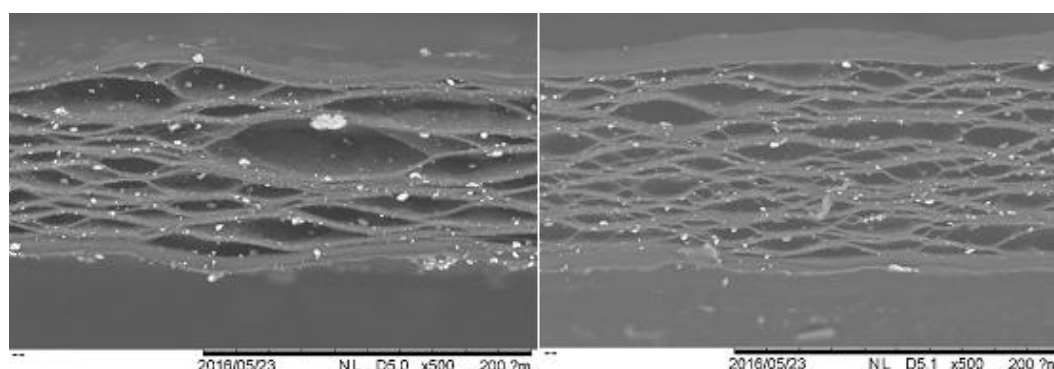


Figure 5.8. Cross sectional images taken with SEM for LRH 60 (left) and LRH 80 (right). Both samples underwent expansion process under 5 MPa pressure.

LRH 60 has significantly less void density than LRH 80, with voids being considerably larger. That means that the air inside the LRH 60 film is divided over a fewer number of voids, resulting in thicker voids. As voids close to the external layers become thicker, the surface roughness of the material increases. This leads to uncertainties in the measurement of the total thickness of the material. The largest uncertainty was found for LRH 60 expanded under 5 MPa. The roughness of the external layer can be seen even by naked eye (figure 5.9).

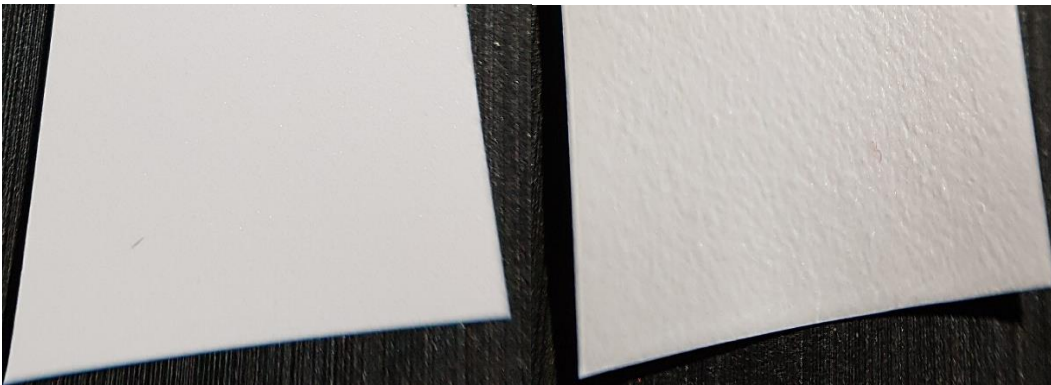


Figure 5.9 Roughness of non-expanded (left) and 5 MPa expanded (right) LRH 60.

Optical profilometry (Alicona 3000 by Optimax) was tested in order to quantitate the surface roughness of the material. The surface roughness could not be measured with such device, as the transparency of the material was very high. No further investigation of the roughness is made, as it is not relevant to this work.

Analysis of 5 cross sections of each material type, reveals the average final thickness obtained (figure 5.10).

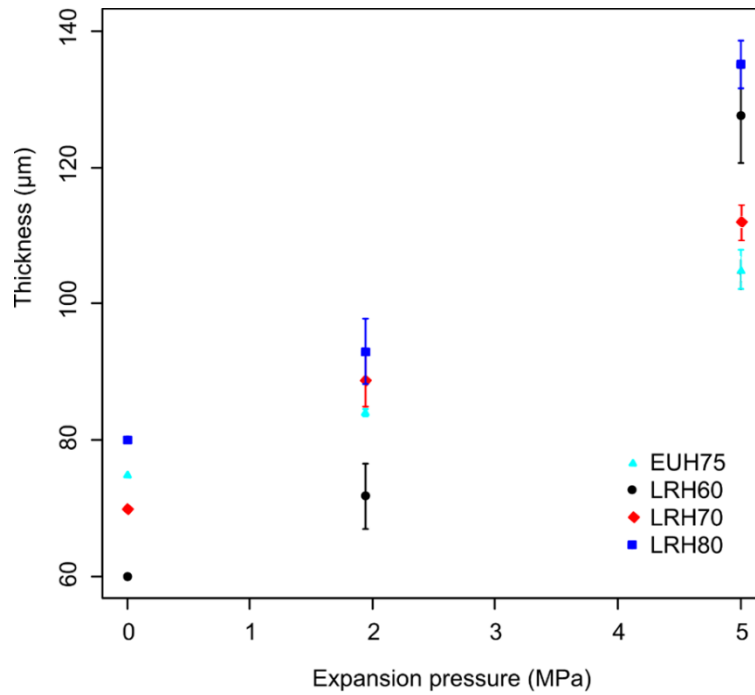


Figure 5.10 Initial non-expanded and final obtained thickness of each film for each material type. The non-expanded materials are presented under a 0 MPa expansion. Each data point is the average of 5 cross sectional images. Error bars represent the standard deviation.

LRH 70 and EUH 75 show almost linear thickness increment for 2 MPa and 5 MPa of expansion (figure 5.10). This might suggest that their inflation process is easier to control. On the other hand, LRH 60 and LRH 80 seem to follow an exponential like thickness increment with expansion. As shown in figure 5.8 and inferred from figure 5.10 the thickness of LRH 60 varies considerably within the same image and as an extend between images, causing a large deviation when measuring it.

The area covered by air over the total area of the voided sample (excluding external layers) can also be estimated from the obtained cross sectional images. The equation used for measuring this ratio is given below (equation 5.4).

$$A_{air} = \frac{\sum(A_{void})}{L_s W_s} \quad (5.4)$$

Where  $L_s$  and  $W_s$  is the number of pixels within the length and the width of the voided part of the image respectively and the  $A_{void}$  is the number of pixels within each void.

Subtracting the area covered by air inside the 2 MPa and 5 MPa expanded materials from the total voided sample area, yields the polymer area of the material  $A_{\text{polymer}}$ . Knowing the polymer area, an estimation of the air existing inside the non-expanded material can be done (by subtracting the polymer area from the total voided sample area of the non-expanded samples) as it could not be accurately measured based on the cross sections. The air coverage area is shown in figure 5.11 as a function of expansion pressure.

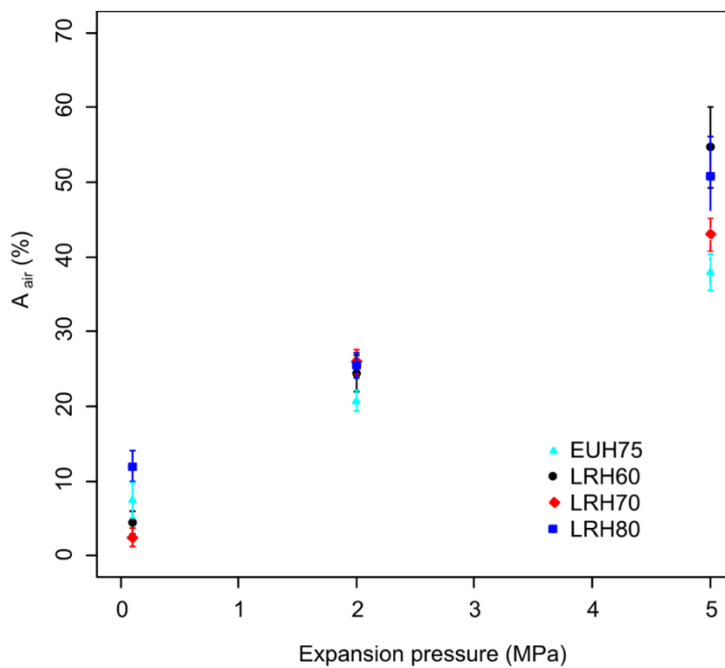


Figure 5.11 Percentage of the voided part (air filled) over expansion pressure of all material types as estimated from cross-sectional images, . Each data point is the average estimate obtained from 5 cross sectional images. Error bars represent the standard deviation.

Subtracting the area of air in the non-expanded material from the area of air in the expanded materials at 2 MPa and 5 MPa respectively, yields the air added to the materials due to expansion. The average ratio of this extra air between the 2 MPa and the 5 MPa is  $0.45 \pm 0.04$  %, that is the 5 MPa samples have higher percentage of air as expected. This could be directly linked to the ratio of  $\Delta p$  (the initial pressure slope of the depressurization process) between 2 MPa and 5 MPa as the relative percentage of air inside the film increases linearly with the initial  $\Delta p$  of the depressurization process. This may only apply to the materials and expansions used within

this work. As reported in the literature, the relative density of the material has a significant influence on the final film stiffness (Wegener *et al.*, 2006; Tuncer & Wegener, 2004). The relative density is defined as the ratio of the film density,  $\lambda_{Cell-PP}$  (the density of air + polypropylene) over the density of the polypropylene  $\lambda_{PP}$  (equation 5.5).

$$\lambda_{rel} = \frac{\lambda_{Cell-PP}}{\lambda_{PP}} \quad (5.5)$$

It is assumed in this point that  $\lambda_{pp}$  is  $946 \text{ kg m}^{-3}$  considering a negligible effect of the  $\text{CaCO}_3$  particles to the density of the material. The densities of the non-expanded materials  $\lambda_{Cell-PP}$  are provided from the manufacturer as  $680 \text{ kg m}^{-3}$  for LRH family and  $550 \text{ kg m}^{-3}$  for EUH family. The density of the expanded material is calculated taking into account that the material is expanded only towards the z axis and that the resultant increment of sample volume is only due to the increased volume of voids. The initial volume is  $V_1 = \text{surface area} \times l_0$ , and the volume after expansion is  $V_2 = \text{surface area} \times l_{exp}$ , where  $l_0$  is the thickness of the non-expanded film and  $l_{exp}$  is the thickness of the expanded film. The film mass is  $m = \lambda_{Cell-PP} \times V_1$  and so the density of the expanded material is  $\lambda_{exp}$  is  $m/V_2 = \lambda_{Cell-PP} \times \text{surface area} \times l_0 / \text{surface area} \times l_{exp}$ . Thus, the density of the expanded material is calculated by equation 5.6

$$\lambda_{exp} = \lambda_{Cell-PP} \frac{l_0}{l_{exp}} \quad (5.6)$$

Where  $l_0$  is the thickness of the non-expanded film and  $l_{exp}$  is the thickness of the expanded film. Once the densities of the expanded materials are found, equation 5.5 is used to find their relative density compared to  $\lambda_{PP}$ . The relative density over the expansion pressure is shown in figure 5.12 for expanded and non-expanded materials.

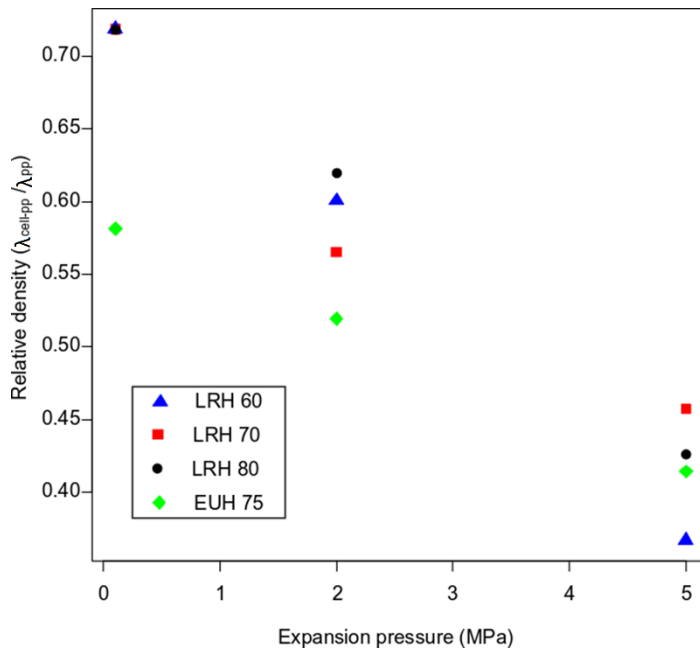


Figure 5.12. Relative density ( $\lambda_{Cell-PP}/\lambda_{PP}$ ) of all material types over expansion pressure. Each data point is the average estimate obtained from 5 cross sectional images.

According to the literature (Wegener *et al.*, 2006; Tuncer & Wegener, 2004), films stiffness drops to the minimum, when expanded to the point where the relative density reaches a value of 0.46. Based on figure 5.12 some of the material types, expanded under 5 MPa of pressure, might be stiffer than when expanded under 2 MPa of pressure, as their 5 MPa relative density is higher than 0.46.

### 5.2.2 Void morphology

The same image processing software was used to measure the maximum thickness and length of each void for each material type and expansion, excluding non-expanded materials. An example of void border identification by the program is shown in figure 5.13.

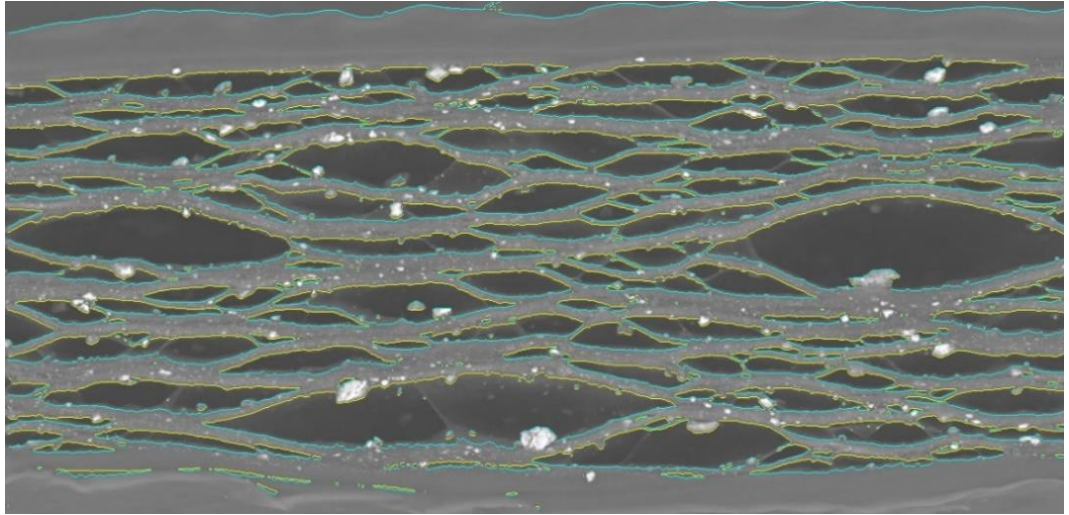


Figure 5.13 Identification of the voids as well as the external layers with the custom-made software. Upper and lower boundary of voids shown in yellow and cyan respectively.

As the contrast varies between images, the user has the ability to vary the contrast threshold, for void and layers identification. This threshold is changed manually, leading to uncertainties in estimation of both the maximum thickness and length of each void. This difference though, was found to be less than 3% under repeated identifications of a specific void.

After all of the images were analyzed, the empirical distributions of void thickness ( $D_h$ ) and aspect ratios ( $D_r$ ) (maximum length/maximum thickness) for all the expanded materials at 2 and 5 MPa were calculated by categorizing similar thickness and length values in stacks. The resultant distributions are shown in figure 5.14.

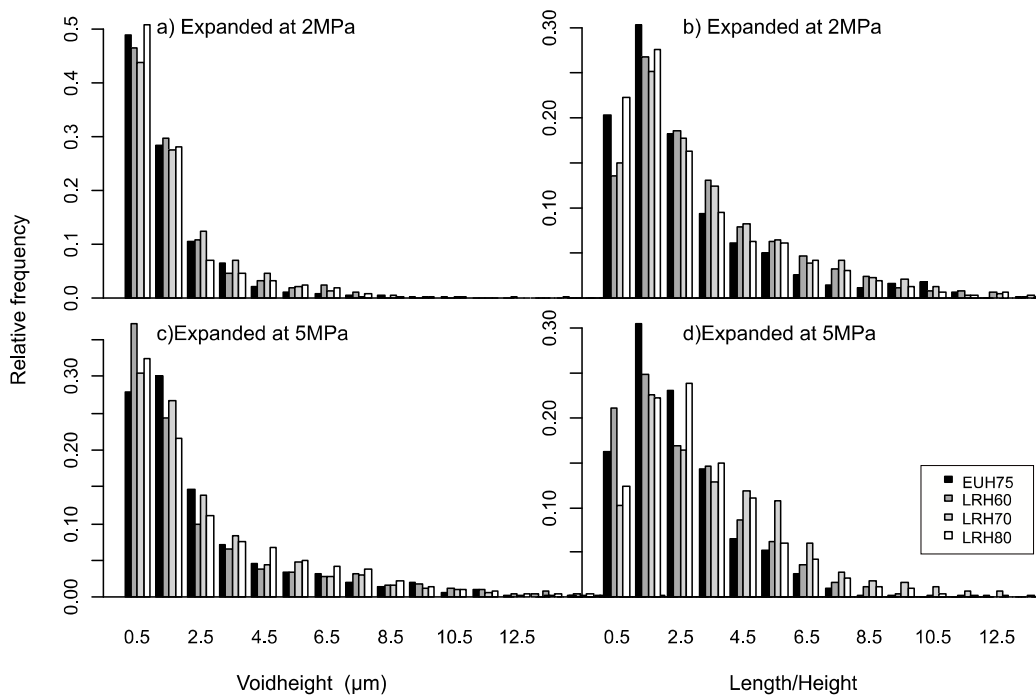


Figure 5.14. Histograms (relative frequencies) for the empirical distribution of void thickness (a, c) and aspect ratio (b, d) based on 5 SEM cross sections of the samples per each material. Polymers expanded under 2 MPa (a, b) and 5 MPa (c, d).

Expanding the samples with 2 MPa pressure, a wider void thickness distribution (Dh) is obtained. Under this expansion, larger voids of up to 15  $\mu\text{m}$  thickness exist in all four materials. By expanding at 5 MPa pressure an even wider distribution is obtained, with a significant number of voids reaching even 20  $\mu\text{m}$  in thickness in all materials. Especially LRH 60 and LRH 80 have a few voids of above 30  $\mu\text{m}$ .

The histograms presented in figure 5.15 are very informative but are difficult to interpret. A simple way of describing these distributions is needed. Log normal distributions were fitted to these data for simplicity and easier manipulation. That way, two variables, location  $\theta$  and scale  $\delta$ , ( $\theta$  and  $\delta$ , from the Greek words “θέση” and “διακύμανση”) defines the peak location and the width (broadness) of each histogram respectively.

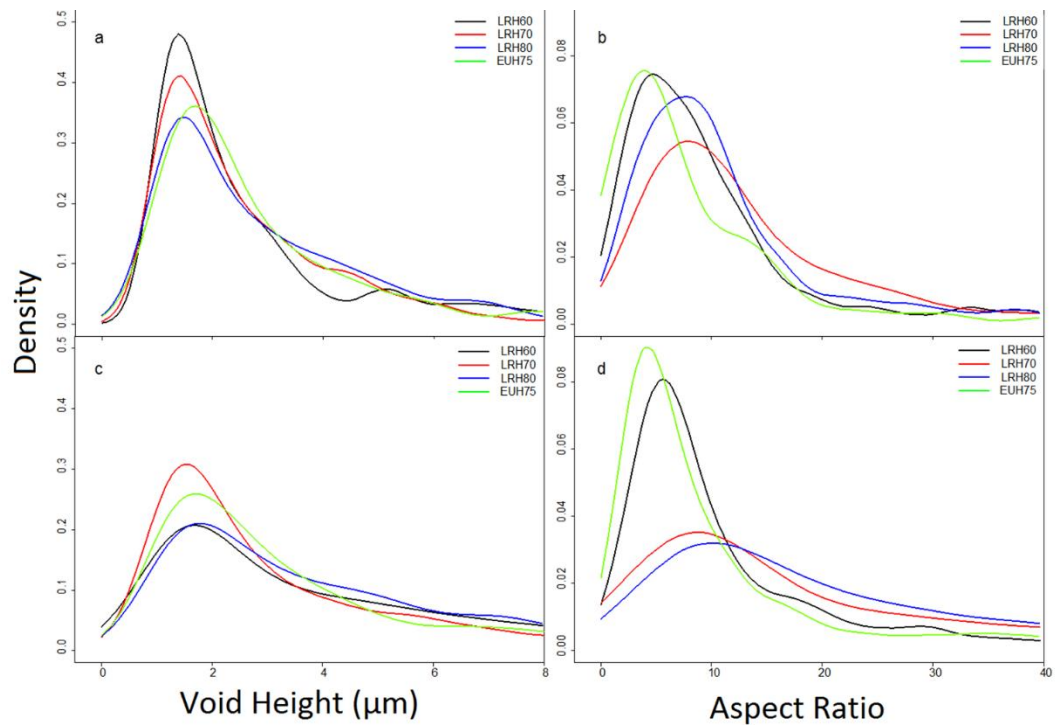


Figure 5.15 Log normal fits on empirical distributions  $D_h$  (left) and  $D_r$  (right) for 2 MPa expansion (top) and 5 MPa expansion (bottom). Density represents the relative frequency of occurrence.

It can be inferred that LRH 60 and EUH 75 expanded under 5 MPa of pressure, share similar narrow  $D_r$  distributions (figure 5.15 d). Within the same figure, similarities can be observed between LRH 70 and LRH 80.

The visual aid of this approach is not the only benefit, as the parametrization of the distributions allows further statistical analysis. Table 5.1 sums up the main parameters of the log-normal distributions fitted to the empirical data.

	Void Thickness ( $\mu\text{m}$ )			Aspect Ratio	
	Material /Parameter	Location ( $\theta$ )	Scale ( $\delta$ )	Location ( $\theta$ )	Scale ( $\delta$ )
2 MPa	EUH 75	0.869	0.580	1.953	1.152
	LRH 60	0.762	0.575	2.083	0.972
	LRH 70	0.790	0.570	2.506	0.9
	LRH 80	0.872	0.600	2.253	0.880
5 MPa	EUH 75	1.065	0.724	2.021	0.956
	LRH 60	1.192	0.785	2.222	0.913
	LRH 70	0.966	0.705	2.790	1.034
	LRH 80	1.192	0.715	2.949	0.926

Table 5.1 The parameters ( $\theta$  Location and  $\delta$  Scale) of the log-normal distribution fitted on the void thickness and aspect ratio empirical data, for 2 MPa and 5 MPa expansions.

For low inflations, there are no major differences between the inferred distributions  $D_h$  and  $D_r$ , among the different materials. In the case of  $D_r$  distributions (figure 5.15b, d) there are differences by material that become more pronounced at the higher 5 MPa expansion (figure 5.15 d). For each material type the location parameter  $\theta$  for  $D_r$  has a bigger value for the higher expanded samples indicating that void lengths increased more than void thickness, following higher inflation. This is more noticeable in the case of LRH 80 and LRH 70, where the scale parameter  $\delta$  also increased after higher inflation (5 MPa). On the contrary, the  $D_r$  distributions of LRH 60 and EUH 75 did not change significantly. Two sample Kolmogorov-Smirnov (KS) tests for EUH75 and LRH60 yield similarities among the 2MPa and 5MPa of inflation with p-values of  $p = 0.316$  and  $p = 0.04$  respectively. Additionally, the  $D_r$  distribution for these two materials gets narrower ( $\delta$  decreased) after high inflation (5MPa in comparison to 2MPa). As  $\theta$  parameter of  $D_h$  distribution suggests, voids of LRH60 under 5 MPa expansion (table 5.1) expanded the most, having a

comparable void thickness distribution to the LRH 80 at the same inflation (KS test p-value = 0.084, both  $\theta$  and  $\delta$  comparable). From the estimated parameters  $\theta$  and  $\delta$ , the mean, median, mode, variance, skewness and kurtosis of the distributions were calculated (based on equations 5.7-5.12) and their statistical differences in terms of expansion factor and/or the material were evaluated (Table 5.2).

$$mean = e^{\theta + \frac{\delta^2}{2}} \quad (5.7)$$

$$median = e^{\theta} \quad (5.8)$$

$$mode = e^{(\theta - \delta^2)} \quad (5.9)$$

$$variance = e^{2\theta + \delta^2} (e^{\delta^2} - 1) \quad (5.10)$$

$$skewness = (e^{\delta^2} + 2)\sqrt{2\pi} \quad (5.11)$$

$$kurtosis = e^{4\delta^2} + 2e^{3\delta^2} + 3e^{2\delta^2} - 6 \quad (5.12)$$

Considering the void thickness distribution, significant increases of almost all parameter values were only due to higher inflation. For the Dr distribution, the only significant differences were found for the location and the mode parameter and were limited to EUH 75 samples having significantly lower values compared to LRH 70 or LRH 80.

Parameter	Void Thickness		Void Aspect Ratio	
	Material	Inflation (MPa)	Material	Inflation
location	ns	5>2 *	LRH70>EUH75	ns
scale	ns	5>2**	ns	ns
mean	ns	5>2*	ns	ns
median	ns	5>2*	ns	ns
mode	ns	ns	LRH80>EUH75	ns
variance	ns	5>2*	ns	ns
skewness	ns	5>2**	ns	ns
kurtosis	ns	5>2*	ns	ns

Table 5.2 Analysis of Variance results for the factors (material or inflation) affecting the parameters of a) void thickness and b) void aspect ratio distribution. ns = no significant effect, \* significant difference, p<0.05 \*\*.

significant difference  $p < 0.01$ . The factor level differences, if significant, are indicated.

It is also evident that materials with higher initial thickness have higher aspect ratios at high inflations ( $\theta$  of  $D_r$ , increases proportional to the nominal thickness of the film, table 5.1). An exception is EUH 75 as its high thickness is due to its thicker external glossy layer. However, more informative is the relation between relative density and the location parameter  $\theta$ , for both the  $D_h$  and  $D_r$  distributions (figure 5.16). Non-expanded materials are not included, as it was difficult to extract meaningful distributions from SEM cross sections.

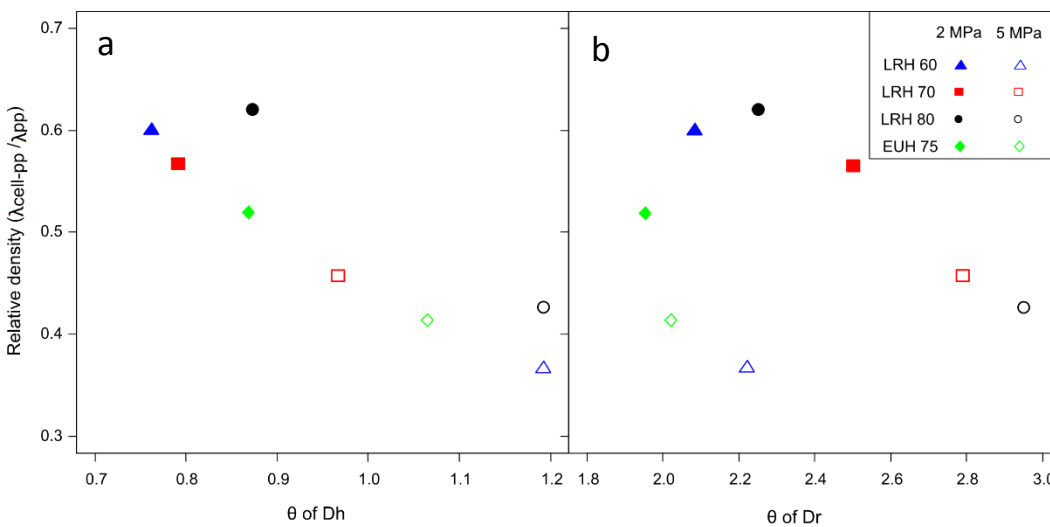


Figure 5.16 Relative density of materials over location  $\theta$  parameters of the a)  $D_h$  b) and  $D_r$  distributions for expanded materials under 2 MPa and 5 MPa of pressure.

It is inferred from figure 5.16a that there is an almost linear relation between the location  $\theta$  of the  $D_h$  distribution and the relative density of the films. The only material out of location within the graph, is the LRH 80 for both its expansions (2 MPa and 5 MPa). This might be a result of either under-estimated density or poor log normal fitting. An interpretation of this result is that the average thickness of the voids within the film increases linearly and inversely proportional to the relative density of the film.

On the other hand, figure 5.16b does not have a simple interpretation. The stiffness of the material is directly linked to the void aspect ratio of the film so that films with high aspect ratio (large  $\theta$  in figure 5.16 b) are compliant and films with low aspect ratio are stiff. Films with intermediate values of

relative density, close to 0.46, are more compliant. To sum up with reference to figure 5.16 b, samples are expected to be more compliant from left to right regarding the X axis and towards the center of Y axis (close to 0.46). So, an early prediction can be made that LRH 80 and LRH 70, expanded under 5MPa, are expected to be more compliant than the rest of the materials. The question stands on which parameter, aspect ratio or density, is going to be more influential as these results show that the mechanism of expansion is not simple.

With the expansion process, the voids grow in both width and thickness. Of the films used in this study, those with higher nominal thickness have their voids grow more in length than in thickness, as the location  $\theta$  of the Dr distributions suggest (table 5.1). This means that thinner films reach a more rounded shape of voids under lower expansion pressures. This is observed in other studies, where thinner films were used, as all voids obtained a round shape after inflation. It is also observed that a two-hour delay between pressure expansion and heat treatment, results in the film getting back to its original thickness. This is evidence that the time the air needs to diffuse in and out the material is crucial. This time is also linked with the difference in pressure between the environment and the voids. Moreover, this difference in pressure also exists when the film is under compression, with the initial state being the expanded material rather than the non-expanded one. This suggests that the time that the compression load acts needs to be considered as a parameter to the response of the material.

## **5.3 Static– Quasi static response**

### ***5.3.1 Mechanical response***

Before exploring the piezoelectric properties of these materials, their mechanical responses were obtained. Within this section, the mechanical response is tested under almost static conditions, in order to minimize the effect of stress rate and initial load. The samples were tested under step static and low constant dynamic compression with the DMA Perkin Elmer 800. Equation 5.13 shows the form of the mechanical excitation.

$$F = S + A \sin(\omega t) \quad (5.13)$$

The compressive displacement over time as well as the total displacement over compressive stress are shown in figure 5.17a and 5.17b respectively.

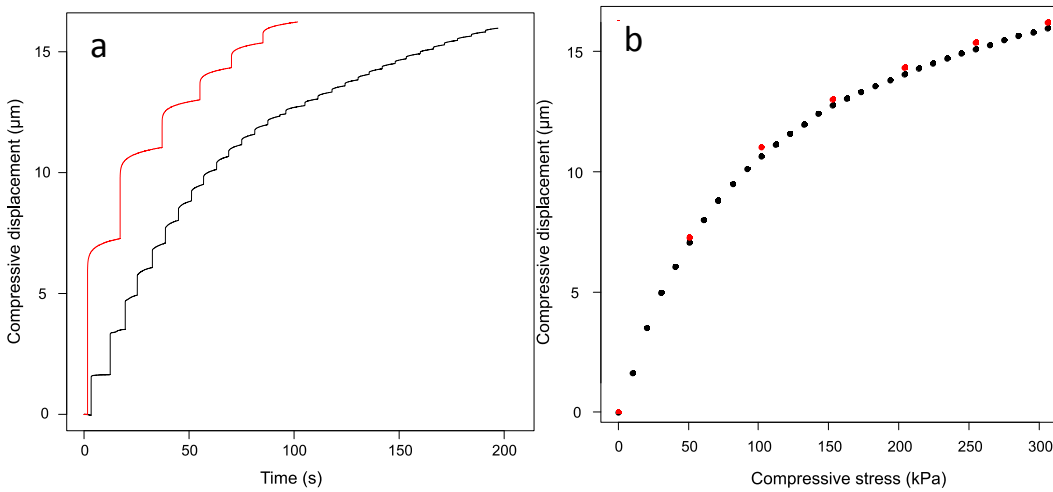


Figure 5.17. a) Compressive displacement over time and b) total displacement (including creep) over compressive stress, for static stress step increments of 10 kPa and 51 kPa. The dynamic load is 5 kPa in every case. The sample used was EUH 75 expanded under 2 MPa. Single run data

There is viscoelastic behavior observed in figure 5.17a. Creep displacement can be seen after each stress step increment for both 10 kPa and 51 kPa responses. Despite the viscoelastic response, the final obtained displacement for both responses is the same. This is shown clearly in figure 5.17b, where the total displacement for each step increment, is plotted over stress. It can be concluded that the final displacement is not influenced by the amplitude of the input steps, given that the sample is permitted to relax to equilibrium after the stress has been applied.

For every stress increment, the new thickness is calculated based on the displacement measured by the capacitive sensor. The true strain is then given as:

$$\varepsilon_t = \int_{l_0}^l \frac{dl}{l} = \ln\left(\frac{l}{l_0}\right) \quad (5.14)$$

All expanded samples were tested under a compressive step increment of 10 kPa. Based on the equilibrium displacement (after creep) the strain of the material can be calculated. In order to investigate the differences, both the engineering strain and the true strain are calculated and presented in figure 5.18.

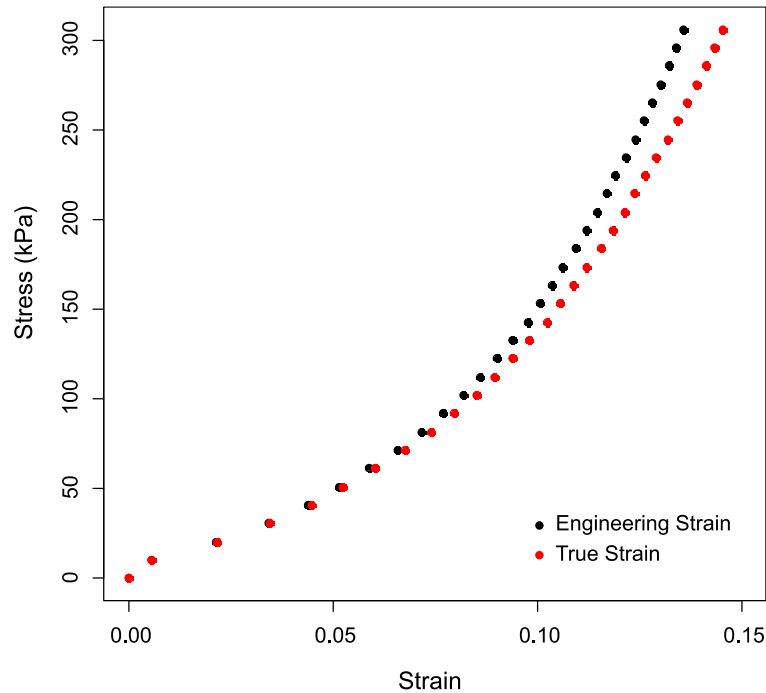


Figure 5.18. Stress over true and engineering strain, for EUH 75 expanded under 5 MPa. Single run data.

The true strain is used in most of the graphs, as we are interested in the displacement that an increment of stress caused, over the pre-strained material. The mechanical response of all the materials is described in figure 5.19.

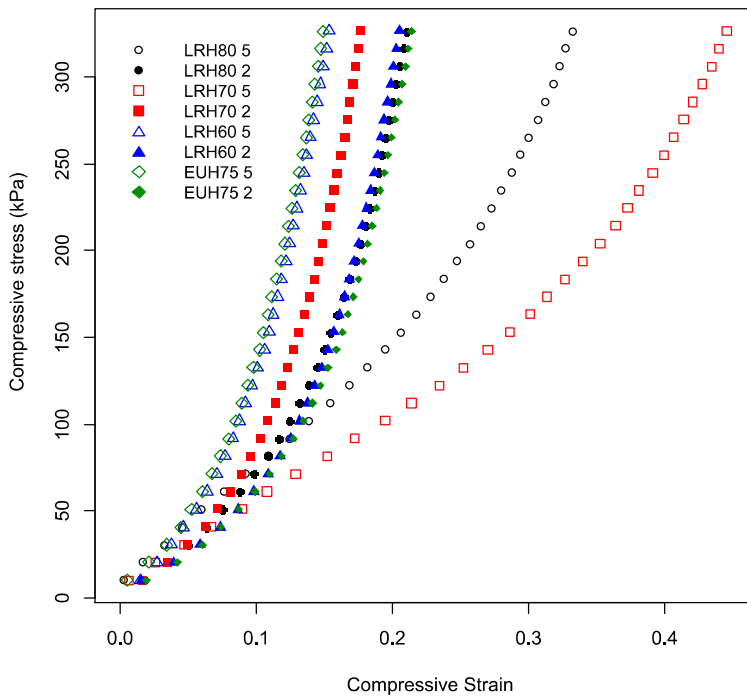


Figure 5.19 Stress over true compressive strain response of all samples. The second part of the names indicate the expansion pressure (5 MPa hollow symbols, 2 MPa filled symbols). The stress increment is 10kPa. A stress of 10 kPa acts as a preload. Single run data.

The data obtained reveal that LRH 70 and LRH 80 expanded under 5 MPa are notably more compliant than the rest of the materials. This applies even for the same material samples, expanded under 2 MPa. Considering the break point of relative density  $\lambda_{Cell-PP} / \lambda_{PP}$  around 0.46, this might mean that LRH 70 and LRH 80, expanded under 5 MPa of pressure, are still on the right-hand side of the break point, while EUH 75 and LRH 60, expanded under 5 MPa of pressure, passed the break point and are placed on the left-hand side of it. The change of Dr location ( $\theta$ ) and scale ( $\delta$ ) (table 5.1), in combination with the results in figure 5.19, are also in agreement with the calculations of E. Tuncer (Tuncer, Wegener & Gerhard-Mulhaupt, 2005), as materials with low aspect ratios are stiffer compared to those with higher aspect ratios.

Exponential relationships of the form  $y=a \exp (bx)$ , were fitted to the compressive stress (y) over true strain (x) data of figure 5.19. The rate of change of stress with strain, captured by the constant (b) of

the exponent, decreases linearly with the median of the aspect ratio distribution (figure 5.20). LRH70 and LRH80 differ from LRH60 and EUH75 in both the median void aspect ratio (high values for the former group) and the rate of compressive stress change to true strain (lower b for the former group) It should be noted here that the exponential fit of both LRH 70 and LRH 80 expanded under 5 MPa, is not as good as for the rest of the materials. The materials inflated at 2 MPa showed intermediate values for both properties with rather small differences among different materials (filled symbols in figure 5.20).

SAMPLE	Parameters						
	a	Sig.	b	Sig.	c	Sig.	R <sup>2</sup>
LRH60@2	-7.8e4	ns	14.3	***	-3.7e-6	ns	0.98
LRH70@2	2.6e5	*	13.7	***	4.6e-6	ns	0.99
LRH80@2	2.2e5	*	10.3	***	6.2e-6	ns	0.98
EUH75@2	3.9e4	*	13.9	***	8.0e-8	ns	0.98
LRH60@5	1.9e5	ns	18.3	***	-1.9e-5	***	0.97
LRH70@5	4.7e5	***	-1.8	**	1.6e-5	***	0.95
LRH80@5	7.1e5	***	-2.6	***	2.1e-5	***	0.97
EUH75@5	2.2e5	ns	19.1	***	-1.4e-05	*	0.98

Table 5.3 Parameters of the quadratic polynomials ( $c_{33}=a + b\sigma + c\sigma^2$ ),  $\sigma$ =pressure (Pa), fitted to the data presented in figure 5.21. The second part of the sample name indicate the expansion pressure  
 Sig.=significance level, ns = no significant difference from zero, \* significant difference,  $p<0.05$  \*\* significant difference  $p<0.01$  and \*\*\* significant difference  $p<0.001$ .

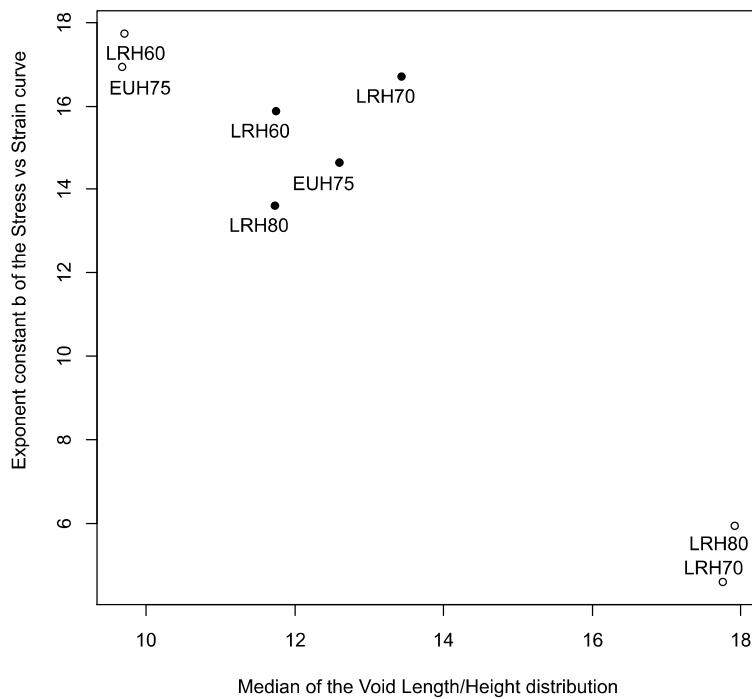


Figure 5.20 Relationship between the Median of the  $D_r$  distribution and the constant  $b$  (table 5.3). Open dots: expansion at 5MPa, solid dots: expansion at 2MPa.

A similar pattern of the materials inflated at 5 MPa is shown in figure 5.21, where stiffness  $c_{33}$  is plotted against compressive stress. For LRH 70 and LRH 80 expanded under 5 MPa,  $c_{33}$  increases slowly; the increase is accelerating but  $c_{33}$  remains at low levels up to 350 kPa of compressive stress. For LRH 60 and EUH75 expanded under 5 MPa the  $c_{33}$  increases sharply and decelerates with increasing compressive stress. In all cases the response is quadratic (table 5.3) with positive quadratic terms for the former group and negative for the latter. For materials inflated at 2 MPa the response is linear (the quadratic term is not significantly different from zero) and the rate of increase is slightly lower than that of the LRH60 and EUH 75 inflated at 5 MPa.

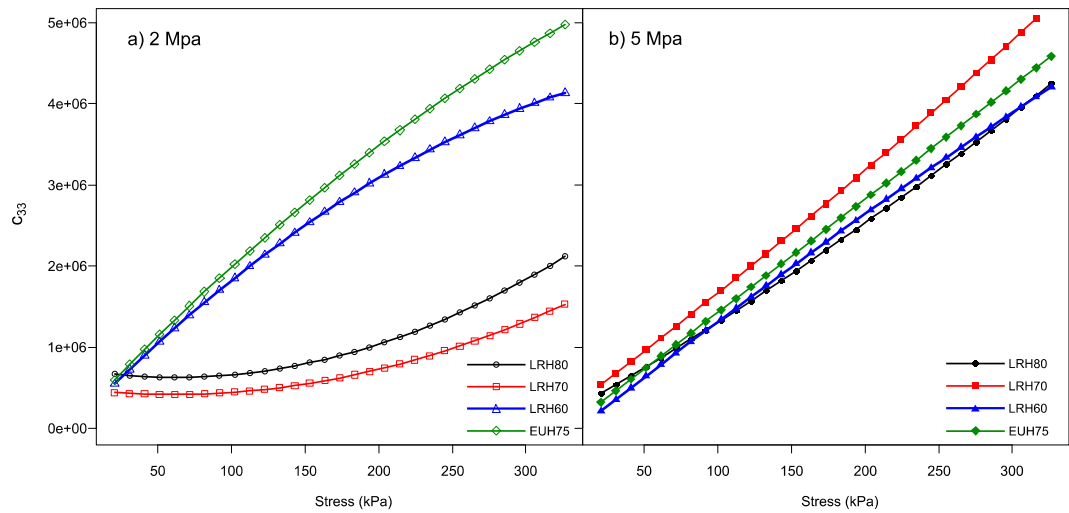


Figure 5.21 Quadratic polynomial fits (lines) of stiffness  $c_{33}$  depending on pressure for the four materials at expansions a) 2 MPa and b) 5 MPa. The stress increment is 10kPa. The parameters for each curve are given in table 5.3.

There are uncertainties occurring due to the method of measuring the total thickness of the films and the thickness of the external layers. At high inflations, measurements of the film thickness induce high uncertainties as the films have rough surfaces due to the expanded voids. Despite that, for the range of interest the difference between LRH 70 and LRH 80 in terms of their response remains statistically significant. On the contrary, the thickness of LRH 60 at 5MPa could not be measured with equal accuracy. There is an uncertainty of 5% affecting the thickness making the strain responses of LRH 60 and EUH 75 undistinguishable at a 90% confidence interval.

The stiffness of the low inflated materials is determined by their void thickness distribution. This is inferred by comparing the  $D_h$  distribution  $\theta$  and  $\delta$  (table 5.1) and the resultant stiffness (figure 5.21) of LRH 70 and LRH 60 expanded under 2 MPa, compared to the rest of the materials expanded under the same pressure. As these two films have the thinner voids, they collapse more easily, soon leading to compression of the bulk material. At higher inflations however, the void thickness distribution and as a result the relative density do not necessarily decrease stiffness. As an example, LRH 60 and LRH 80 expanded under 5 MPa with densities of 0.31 and 0.40 respectively share similar  $D_h$  distributions but their

mechanical responses differ. The major difference among these two samples is the  $D_r$  distribution. The findings are in agreement with Wegener et al. (Tuncer & Wegener, 2004) suggesting that the link between the stiffness of a material and its morphology is the aspect ratio of the voids but also with (Wegener *et al.*, 2006) suggesting that there is a break point in stiffness and piezoelectric response of the materials once their relative density passes 0.46 with GDE.

Films with high void aspect ratio have a weak structure, as the angle formed between the void polymeric supports are relatively low. As a consequence, the majority of the voids with low thickness collapse under moderate stress levels resulting in a high stiffness value attributed to the mechanical properties of the bulk material. Another possible contributor to the increment of stiffness is the high gas pressure arising in them due to compression. On the other hand, when the aspect ratio becomes lower, voids obtain more of a round shape and the structure gets stronger (higher angle is formed between the polymer supports of the voids). High stiffness in this case can be attributed to the morphological characteristics of the structure exhibiting truss-like mechanical performance.

The same principle applies when the film is under different levels of compression in the sense that the applied stress modifies the morphology and hence the stiffness of the material. For low inflated materials and for the given range of stress, voids of successively larger thickness collapse progressively, leading to a linear increase of stiffness. This does not hold for highly inflated materials at 5MPa. The rate of change of stiffness  $c_{33}$  increases for LRH 70 and LRH 80 which share a high aspect ratio (table 5.1). On the contrary, there is a decrease in the rate of change of stiffness for LRH 60 and EUH 75 which share a narrow  $D_r$  distribution (see Figure 5.15). This suggests that the aspect ratio gets higher during compression, making the structure weaker.

A hypothesis can be made, that the GDE procedure can be reversed, via means of compression. Assumptions need to be made that all of the materials are made out of polypropylene with density of  $946 \text{ kg m}^{-3}$ , the Poissons ratio  $\nu_{31}$  and  $\nu_{32}$  of the material are equal to zero, so that no

deformation occurs within the length/width direction and finally that the initial stiffness calculated for each material, falls within the linear region.

Previous data from figures 5.21 and 5.12 are re-elaborated to compare the stiffness of the films to the relative density. For this analysis, we are interested in the stiffness of each expanded material compared to the non-expanded one. Therefore, the stiffness of the film is calculated based on the engineering strain rather than the true strain. After finding the relative densities of the expanded materials based on equation 5.6, the relative density of the compressed material can be found by equation.

$$\lambda_{ad} = \frac{\frac{\Delta l}{l_{exp}} \lambda_{exp}}{\lambda_{PP}} \quad (5.15)$$

Where  $\Delta l$  is the compressive displacement.

The stiffness obtained under a preload stress of 10 kPa, is considered as the initial stiffness and plotted against the relative density, for each expanded and non-expanded material. The stiffness and relative density after each compressive step is calculated based on equations 5.5 and 5.6 and plotted within the same graph (figure 5.22)

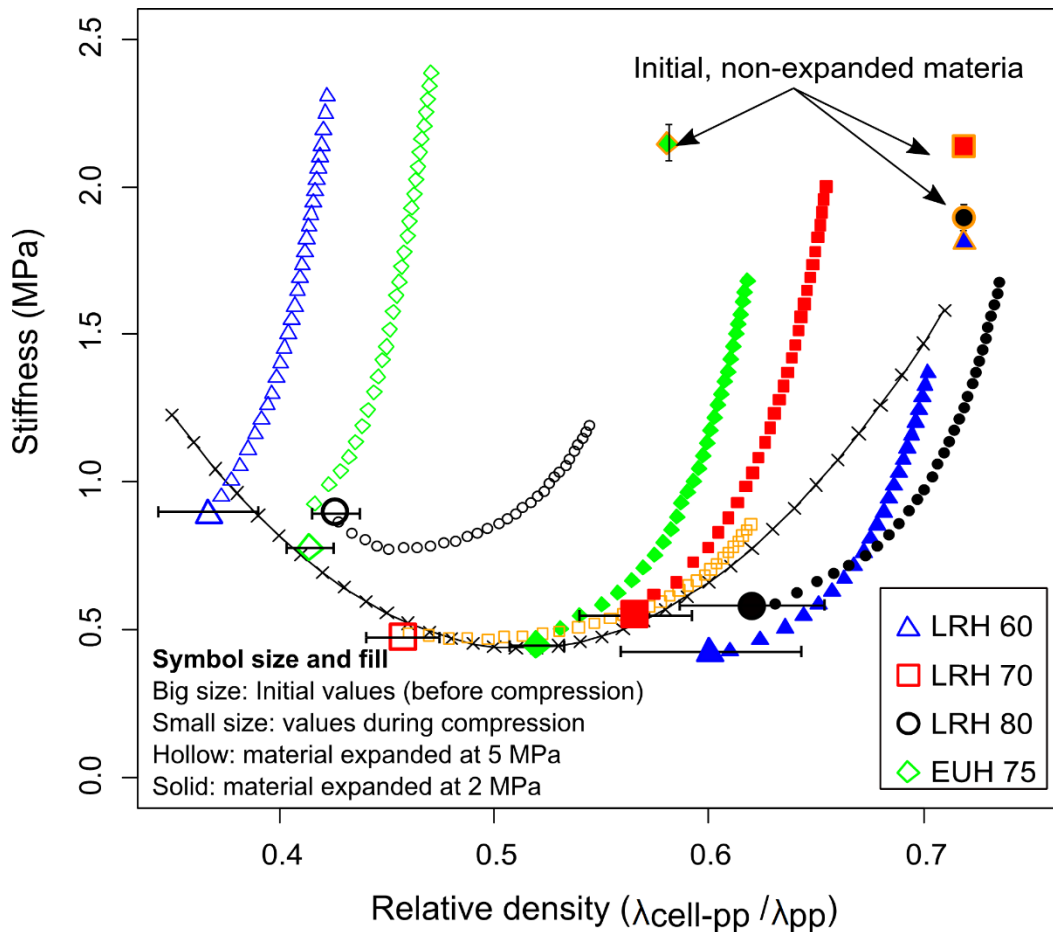


Figure 5.22 Stiffness  $c_{33}$  over calculated relative density for the expanded and non-expanded materials. Big symbols: Initial values before compression, small symbols: values during compression. Hollow symbols: materials expanded under 5 MPa, solid symbols: materials expanded under 2 MPa, Multi-color symbols: Initial values for non-expanded materials. Relative density obtained from figure 5.12. Stiffness calculated based on the engineering strain obtained from the compressive tests in figure 5.21. Error bars represent the standard deviation in initial material thickness.

The highest density uncertainty among the materials is that of LRH 60 expanded under 2 MPa of pressure which is 7%. This uncertainty though, changes the curves in both X and Y axis. For clarity, the range that the final value can take after compression is given in table 5.4.

Material	Deviation X	Deviation Y (MPa)
LRH60_2	0.05	0.1
LRH60_5	0.026	0.14
LRH70_2	0.03	0.09
LRH70_5	0.021	0.021
LRH80_2	0.04	0.09
LRH80_5	0.014	0.03
EUH75_2	0.015	0.04
EUH75_5	0.012	0.07

Table 5.4 Maximum deviation for relative density (X axis) and stiffness (Y axis) at the end of the compression.

It should be stated that the initial position of each point is not the only parameter affected by the uncertainty in the initial thickness. Higher initial thickness results in steeper slopes and higher estimation of stiffness, as the strain obtained for each step displacement is smaller. On the contrary, lower thickness has the exact opposite effect.

The “U” shape observed by (Wegener *et al.*, 2006) can be seen in figure 5.22. Guideline for the eyes is provided by a second order polynomial fit to the initial values. It is inferred from figure 5.22 that even though EUH 75, LRH 60 and LRH 80 expanded under 5 MPa have all crossed the 0.46 breakpoint of relative density, their mechanical responses differ, as the stiffness of LRH 80 is lower than LRH 60 and EUH 75 within the non-linear region. This might mean that even though the initial stiffness of the materials complies with the 0.46 break point, in practice the morphology of the voids (specifically aspect ratio) is a crucial parameter that defines the material’s behavior within the non-linear region.

A hypothesis can be made that the GDE procedure can be reversed via means of compression. For example, by compressing the 5 MPa expanded LRH 80 down to its previous 2 MPa expanded thickness, the same mechanical properties can be obtained. The same applies for the 2

MPa materials, if they are compressed down to the non-expanded thickness. However, the materials with relative density higher than or close to 0.46, do not seem to follow that rule. A probable explanation is that the bulk morphology has changed irreversibly due to the excessive deformation the walls of the voids experienced. Another possible explanation is that the stress applied within this scope is not enough for the expanded material to reach its previous and initial non-expanded state. This, would require the stiffness of the material to drop again under higher stresses.

The above response might be a beneficial feature for EH, as the films can be over-expanded, charged under high fields to gain high charge density and then compressed down so that the stiffness of the material increases. That way, the material might produce high charges with high stiffness (high  $k^2_{33}$ ).

### 5.3.2 Direct piezoelectric response

An LRH 80 sample expanded under 5 MPa was contact charged under a voltage of 6 kV. The repeatability of measurement of the direct piezoelectric effect is tested under a variety of static stresses. The results are shown in figure 5.23.

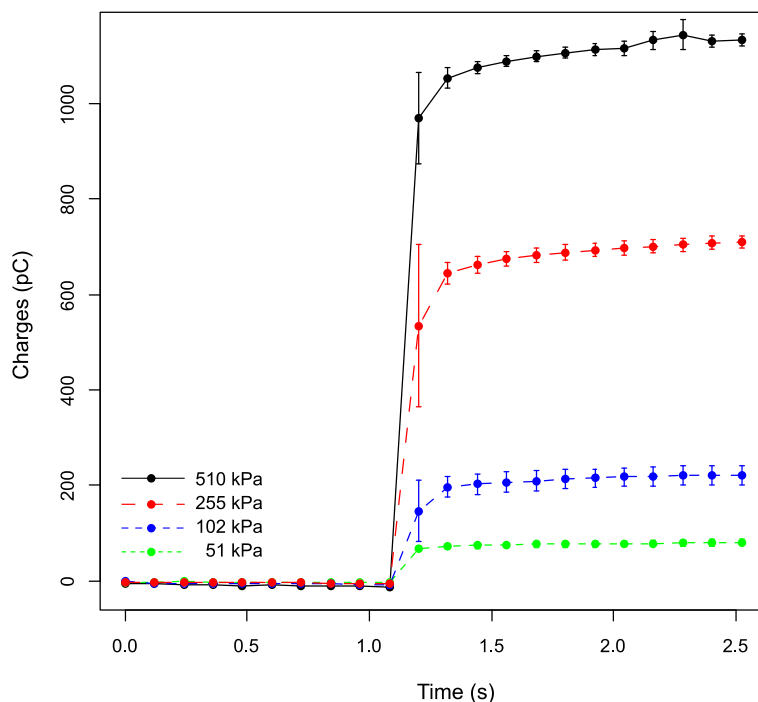


Figure 5.23 Charges over time at the application of a selection of static stress levels. Each stress was tested 4 times. The sample was dismantled from the clamps and let to relax before each test. Error bars represent the standard deviation.

It appears that the charges continue to accumulate long after the stress is applied. This is an effect of creep, as observed in the previous section and is more profound when higher stresses are applied. The average obtained piezoelectric coefficient  $d_{33}$  for the instantaneous and the equilibrium response is given in figure 5.24.

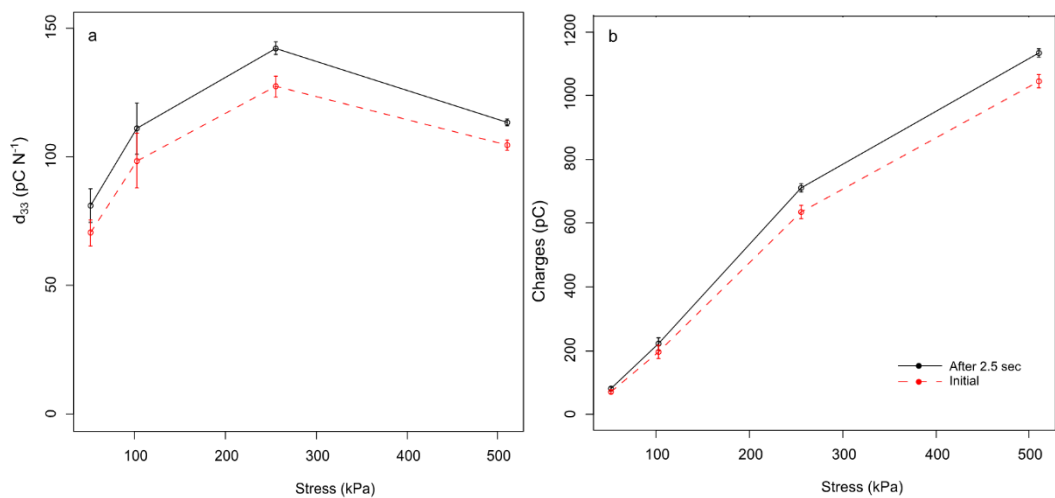


Figure 5.24 a) Calculated  $d_{33}$  emerged from a) Instantaneous and total charges produced after 2.5 seconds plotted over stress. Each data point is an average of 4 compressive runs. Error bars represent the standard deviation.

Looking at the standard deviations, it appears that the testing procedure is less accurate for lower stresses, as the signals are smaller. Furthermore, a small uncertainty in the charges creates a large deviation in the piezoelectric response  $d_{33}$ , especially under low stresses. It can also be seen that the difference between the long term and the instantaneous response is about 10%. The response of the  $d_{33}$  is not linear over stress, as there is a decrement of the charge production under high stresses ( $d_{33}$  decrement).

A continuous medium should be applied on the external layers of the polymer sample, in order to extract the total amount of charges produced on the external layers during compression. Silver epoxy has been reported

to reduce the measured piezoelectric properties as well as the dielectric properties of a PZT-polymer material by 25% and 40% respectively (Sherrit *et al.*, 1991). This is attributed to air gaps existing between the epoxy and the surface of the material, leading to unsatisfactory mechanical and electrical contact. Two different media, conductive silicone pads and an extra layer of silver paint, are compared here. In our case, it is found that conductive silicone pads or an extra thin layer of silver paint between the sample and the metal plates is enough to provide a gap-free media and better load distribution (figure 5.25). Both of them are also capable of providing a strong friction support to avoid misalignments between the plates and the sample during testing. The static piezoelectric response and the corresponding piezoelectric coefficient  $d_{33}$  of the sample, under a variety of static stresses and different media are shown in figure 5.25

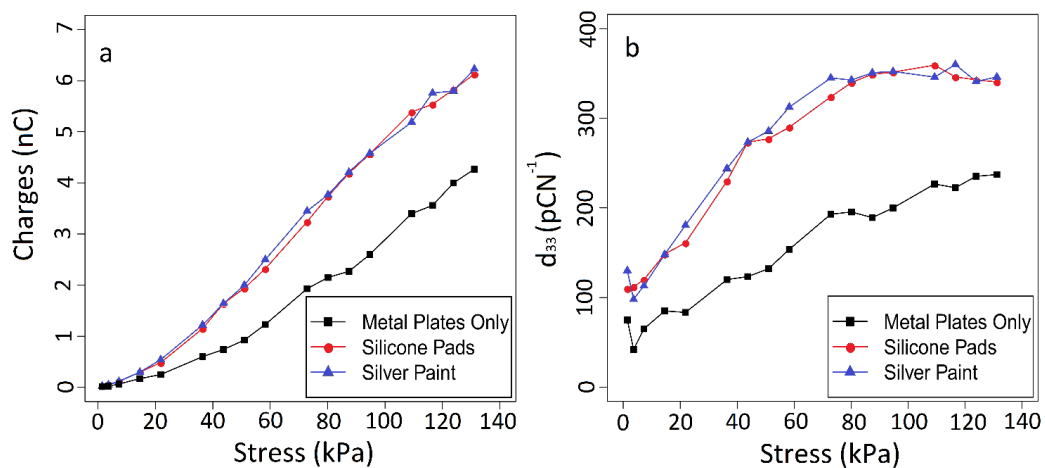


Figure 5.25 a) Charges and b) piezoelectric constant  $d_{33}$  over static stress for different media. Each data point represents the average of five measurements

In the absence of media, the obtained piezoelectric activity was reduced by more than 35% (figure 5.25). There is a slight increment in the slope of the charge production for stresses higher than 20 kPa (figure 5.25a) indicating the non-linearity of the response. The non-linear part of the response can be seen more clearly in figure 5.25b, where the piezoelectric constant  $d_{33}$  is plotted over stress. The piezoelectric coefficient  $d_{33}$

increases until a stress of about 80 kPa is reached, whereupon it is almost constant, yielding a region of linear piezoelectric response.

The EUH 75 is the only material in this work that has a glossy side.

Charging tests were held under the same charging parameters ( $d_{cg}$ ,  $d_g$ ,  $V_c$ ), for two EUH 75 samples in order to explore the effect of the glossy and the non-glossy side being exposed to the charges. The procedure was repeated for another sample in order to test the repeatability of the corona charging procedure. The results are given in figure 5.26.

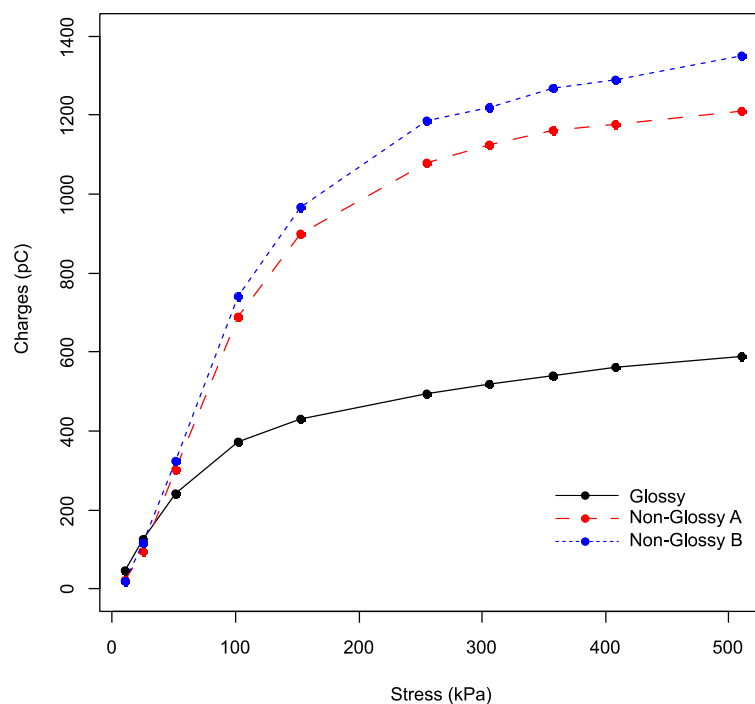


Figure 5.26 Charges over applied stress, for the EUH 75 expanded under 2 MPa charged on its glossy and non-glossy side. Before the application of each new stress level, the film was left to relax for roughly 60 seconds. Single run data.

It seems that by charging the glossy side, lower charge density is obtained. The charge production is almost half for the final 510 kPa stress (figure 5.26). The charging procedure is well controlled. There is a 10 % difference between the 2 non-glossy side charged materials.

Another parameter for investigation is the field uniformity of the charging procedure. An EUH 75 sample was tested and then cut down to smaller surface areas and tested again for its charge production. The aim is to investigate if the field is uniform closer to the edges of the sample. In case

it is not, smaller areas towards the middle of the sample will produce more charges/stress value. The piezoelectric response for concentric circles obtained from the same sample progressively cut by a circular punch plier, are given in figure 5.27.

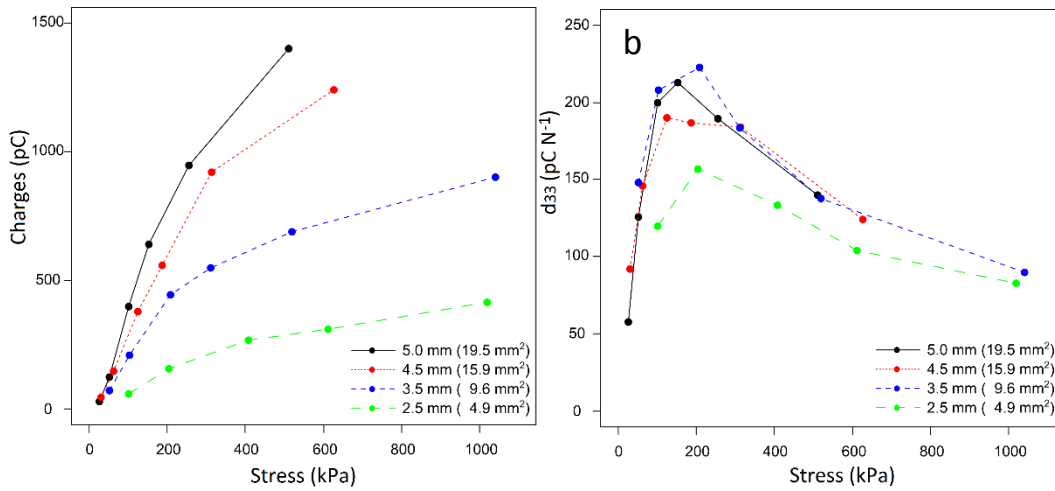


Figure 5.27 a) Charges over stress and b)  $d_{33}$  over stress, for different sample sizes. The sample was cut down with circular punch plier. Single run results.

Comparing the 19.6 mm<sup>2</sup> sample with the 9.6 mm<sup>2</sup> sample, the charges produced for the half-sized sample are exactly half. This is an indication that the charging procedure was done uniformly. As expected, the  $d_{33}$  remained the same for almost all the sample areas, with an exception of the 4.9 mm<sup>2</sup> area, that seems to have reduced piezoelectric activity compared to the larger area samples. A possible explanation is that the film is damaged at the edge during cutting. Such effect becomes more important for smaller samples for scaling laws.

Each material was left at room temperature to age for 17 days after the charging procedure. The instantaneous static response (without creep) of each material was obtained within the non-linear region. Figure 5.28 shows the piezoelectric coefficient  $d_{33}$  over applied static stress.

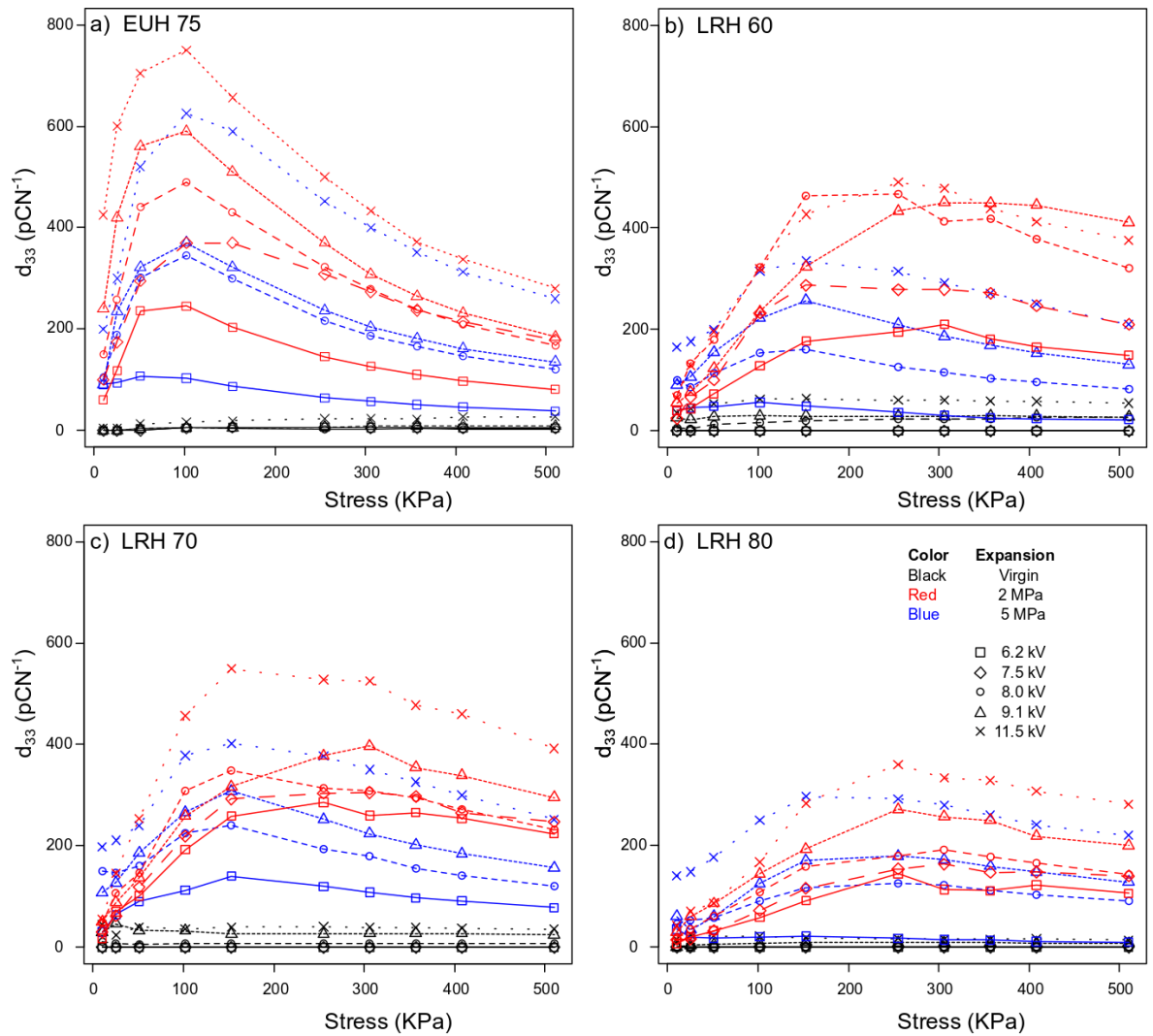


Figure 5.28 Piezoelectric coefficient  $d_{33}$  over applied static stress for all materials. Different colors designate different expansions while different symbols designate different functionalization voltage.

By comparing the two charging methods (figure 5.28d to figure 5.24b page 127) it seems that contact charging and corona charging under the same potential ( $V_g=6.2$  in corona charging compared to 6 kV potential of the plates in contact charging) has the same effect to the piezoelectric response of the film. However, the maximum potential that could be applied during contact charging was 9 kV compared to 11.5 kV potential of the grid, for the same material. This allows the thickest materials to be

charged under 22% higher potentials with corona, without a destructive discharge occurrence. There is a strong correlation between the functionalization voltage and the obtained piezoelectric coefficient  $d_{33}$  of the film (see figure 5.28). The piezoelectric response is obviously not linear with applied stress. The coefficient  $d_{33}$  increases in accordance to stress, under low stresses, and then decreases under high stresses for all materials. In most cases, for materials expanded under 2 MPa of pressure, there is a break point where  $d_{33}$  peaks. This peak changes among different materials for higher inflations. Except EUH 75, whose peak occurs at around 100 kPa for both 2 MPa and 5 MPa inflations, the rest of the materials peak around 153 kPa and 255 kPa for 2 MPa and 5 MPa of inflations respectively. The shape of the  $d_{33}$  response does not change significantly with the functionalization voltage. The curve only shifts up when higher functionalization voltages are applied. It is thus evident that the shape of the piezoelectric response within the non-linear region is influenced by the stiffness of the material, as it defines the relative displacement of the dipoles within the voids.

LRH 60, LRH 70 and LRH 80 have similar, broad responses of  $d_{33}$  over stress, while EUH 75 has a pronounced peak around 102 kPa, for both expansion inflations of 2 MPa and 5 MPa, providing also the highest piezoelectric coefficient among the materials. Analyzing the response of EUH 75, it can be seen that the first derivative of charges over stress is close to zero for stresses higher than 300 kPa in most cases (figure 5.29). This means that few charges are being produced for stresses over 300 kPa, resulting to the  $1/\sigma$  dependent decrement of  $d_{33}$  over stress seen in figure 5.28. On the other hand, referring to figure 5.19, the strain still increases for stresses higher than 300 kPa.

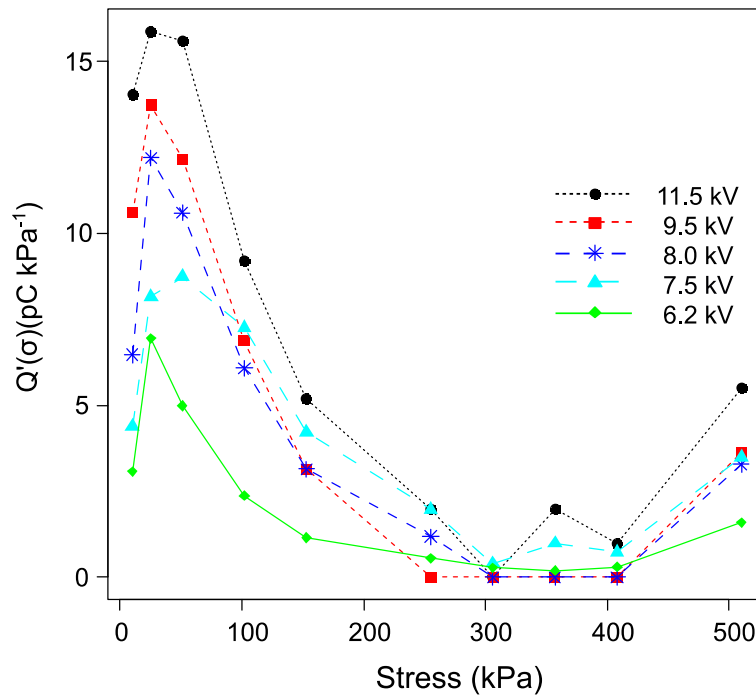


Figure 5.29 First derivative of charges plotted over stress for the EUH 75 expanded under 5 MPa. Lines are guides to the eye.

Figure 5.29 also suggests that charge production resumes for stresses higher than 500 kPa. This might be an outcome of the transition from stiff material to more compliant material, as the morphology of the voids change during compression. Further evidence of this transition can be seen in figure 5.21a where the slope of stiffness changes significantly during compression.

So far, the EUH 75 and LRH 60 seems to have the highest piezoelectric coefficient  $d_{33}$  (see figure 5.28 a) in combination with the highest stiffness  $c_{33}$  (see figure 5.21), within the non-linear region and specifically around 100 kPa of stress.

As the functionalization field depends on the voltage of the grid over the thickness of the material, which is not constant, it is more meaningful to investigate all the materials under the same field. The charges over the applied step stress as well as the obtained  $d_{33}$  over stress is given in figure 5.30. The field chosen is  $85 \text{ MVm}^{-1}$ , which is the maximum field that can be applied to the thickest material (LRH 80).

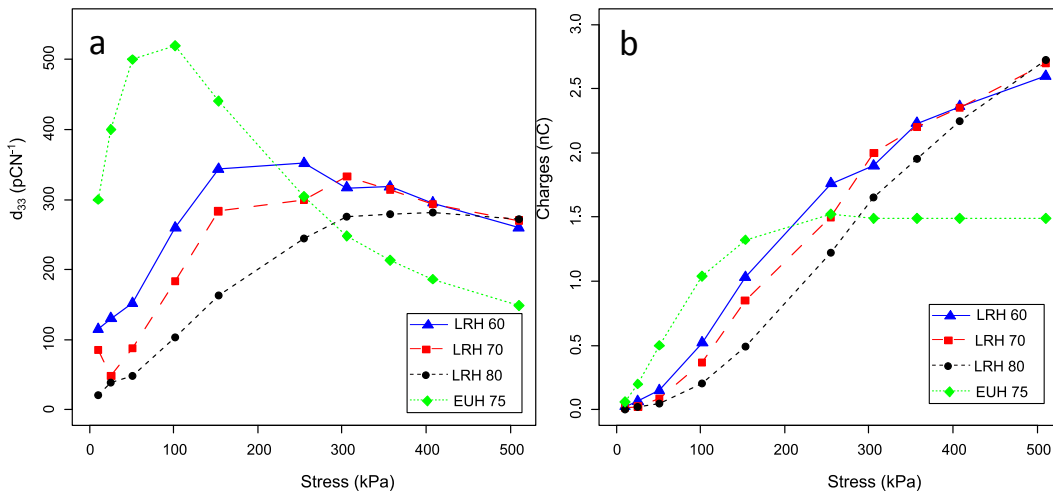


Figure 5.30 a) obtained  $d_{33}$  and b) Charges over compressive stress. Materials expanded under 5 MPa and charged under  $85 \text{ MVm}^{-1}$ . Single run results.

Even though EUH 75 (rhombs) does not produce any more charges for pressures over 255 kPa it has the highest  $d_{33}$ , as it produced high charges under low stress. It can also be seen that the rest of the materials have not reached the maximum charges they can produce, even for stresses close to 500 kPa (figure 5.30). The piezoelectric response is also plotted over relative density for both expanded and non-expanded materials charged under 11.5 kV potential (figure 5.31). The relative density is obtained from the data of figure 5.12 whereas the  $d_{33}$  value from those in figure 5.28, measured under a static stress of 255 kPa.

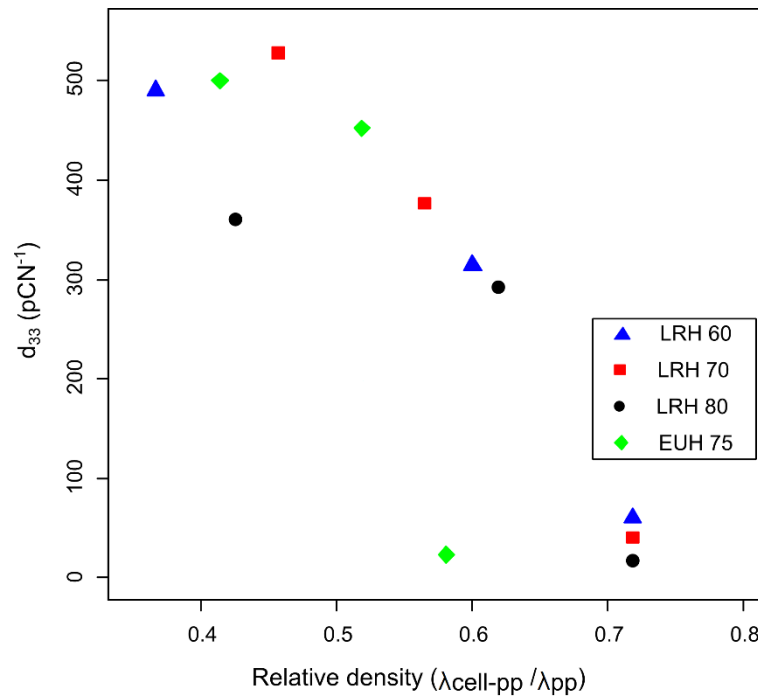


Figure 5.31 Piezoelectric response  $d_{33}$  over relative density for expanded and non-expanded materials.

It seems that the  $d_{33}$  shows the inverse response to that of figure 5.22 (stiffness over relative density). The break point of 0.46 relative density remains the same. It can also be seen that there are differences among materials. As an example, LRH 80 shows lower  $d_{33}$  than the rest of the materials.

In section 5.3.1 a hypothesis was made that the piezoelectric response of the expanded materials should match that of the lower expanded and non-expanded materials, when compressed down to their “original” thickness. On the contrary, there cannot be direct comparison of the piezoelectric coefficient  $d_{33}$ , while it is defined as charges over force (C N<sup>-1</sup>).

In order to test if the hypothesis applies to the piezoelectric response, the mechanical response and relative density data (shown in figure 5.22) and the obtained charges (shown in figure 5.28) were used.

The hypothesis is easily confirmed for LRH 70 expanded under 5 MPa of inflation (see figure 5.22). Consecutive points in figure 5.22 are separated by 10.2 kPa. The LRH 70 expanded under 5 kPa of pressure reaches the same level of stiffness and relative density with the LRH 70 expanded under 2 MPa of pressure after 15 points (153 kPa of stress). By resetting

the 5 MPa sample's charges at 153 kPa and the 2 MPa material's at 10.2 kPa charges to zero, an agreement between the 5 MPa and the 2 MPa materials is found. The results are shown in figure 5.32.

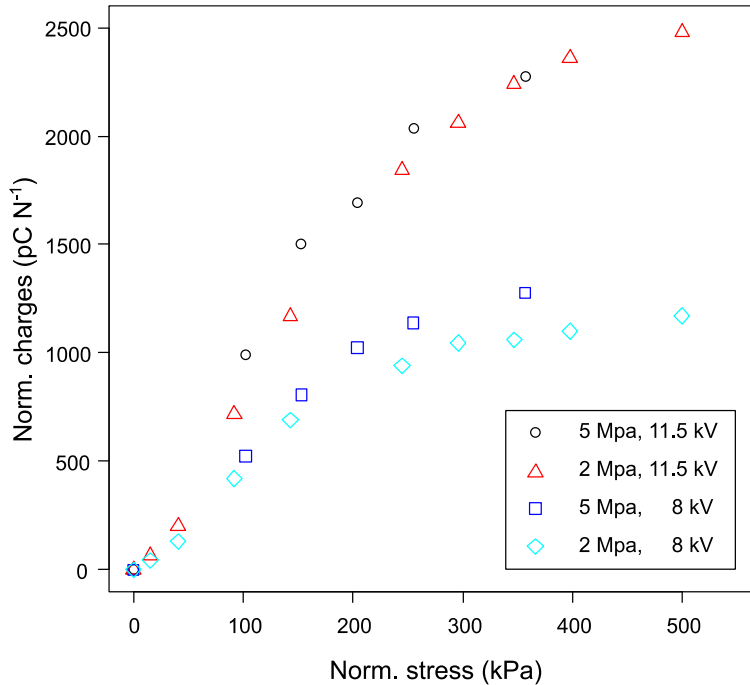


Figure 5.32 Comparison of piezoelectric response between 5 MPa and 2 MPa LRH 70 sample over stress. The charges of the 5 MPa sample and the 2 MPa sample were reset to zero at 153 kPa and 10.2 kPa respectively.

The same piezoelectric response between the two materials can be clearly seen. Similar agreement can be observed between the 2 MPa and the non-expanded materials, within the experimental uncertainties.

It should be stated here that two types of uncertainties exist within the charges. The first is the uncertainty emerged from repeatable measurements of the same material which is typically 2% for measured charges higher than 10 pC. The second uncertainty emerges from the charging procedure, which is close to 12%. Overall, the combined uncertainty is calculated as:

$$\sqrt{Uncertainty1^2 + Uncertainty2^2} \quad (5.15)$$

Based on equation 5.15, the uncertainty of the charges is 12.2%. This means that the piezoelectric response can be changed from highly

expanded material states to previous states (lower expansions) via means of compression. If this is valid, the extra charge density gained by the high expanded film due to their thicker voids, is compensated by the higher field applied on the low expanded film, provided that the voltage applied on both is the same (In this case a potential of 11.5 kV). In other words, the higher piezoelectric activity observed by the high inflated material during compression emerged from the extra charge density the material gained by having thicker voids. The same limitation applies, as discussed previously, for the over expanded materials (compressed materials with relative density lower than 0.46 cannot be brought down to lower expansions via compression) as their morphology changed significantly. Another limitation exists here, as high expanded and low expanded materials charged under low  $V_g$  do not seem to follow the hypothesis. In conclusion, it can be said that the GDE can be reversed from high expanded material B to lower expanded material A as long as their difference in relative density is not too high. Furthermore, material B shares the same piezoelectric response with material A after compression, as long as the potential they are both charged at is comparable.

### **5.3.3 Static $k^2_{33}$**

In order to investigate the role of stiffness to the electromechanical coupling coefficient  $k^2_{33}$ , the  $c_{33}$  and the  $d_{33}$  values were obtained from figures 5.21 and 5.28 respectively. The relative permittivity of the material is assumed to be  $\kappa_{33}=2.2$  based on the literature review (Mellinger, 2011). The obtained electromechanical coupling coefficient for the inflated materials is given in figure 5.33.

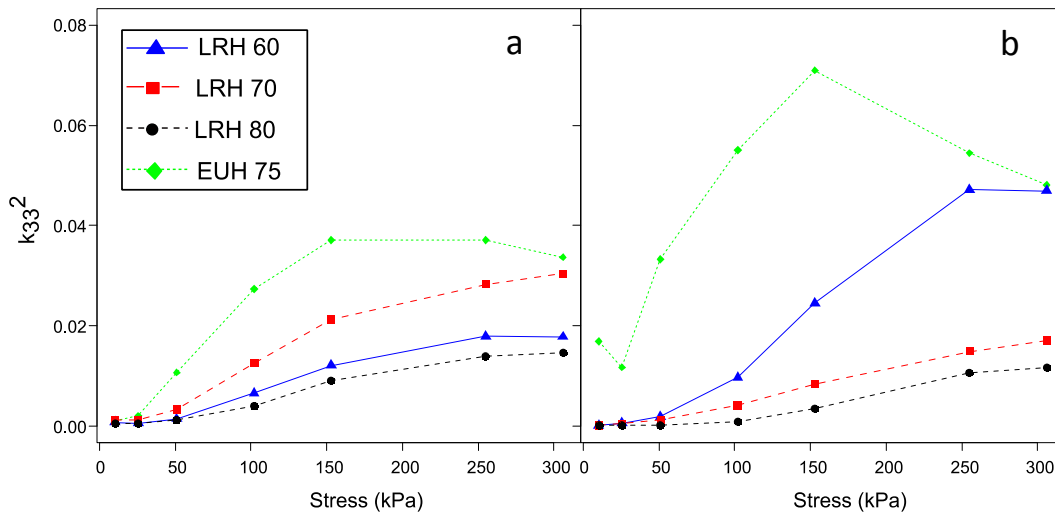


Figure 5.33 Electromechanical coupling coefficient over static step stress, for all materials charged under  $V_g=11.5$  kV and expanded under a) 2 MPa and b) 5 MPa of pressure. Data taken from figures 5.21 and 5.28.

It is inferred that  $k^2_{33}$  initially increases with pressure, up to 153 kPa, for all materials as both  $c_{33}$  and  $d_{33}$  increases.

Materials expanded under 5 MPa (figure 5.33b), do not always show larger  $k^2_{33}$  compared to 2 MPa (figure 5.33a). Comparing the values obtained from the two expansion pressures, the coefficient  $k^2_{33}$  decreases for LRH 70 and LRH 80. This is expected as these materials showed a decrement in  $c_{33}$ , despite their increment in  $d_{33}$  after expansion, within the non-linear region. On the other hand, the coefficient  $k^2_{33}$  increases for the EUH 75 and LRH 60 that showed increment in both  $c_{33}$  and  $d_{33}$ , as expected. By comparing the breakpoints of the  $d_{33}$  and  $k^2_{33}$  curvatures (figure 5.28 and 5.33 respectively), it can be seen that stiffness increment compensates for  $d_{33}$  decrement, in their contribution to the electromechanical coupling coefficient  $k^2_{33}$ . EUH 75 shows a plateau between 153 kPa and 255 kPa (figure 5.33 a). Further analysis for the EUH 75 sample show that a 18% increment in  $c_{33}$  compensates for a 23% decrement of  $d_{33}$  so that  $k^2_{33}$  remains almost constant. On the basis of the above, it can be concluded that the stiffness of the material has a key role to the  $k^2_{33}$  and thus to efficient mechanical to electrical energy conversion. The data presented above are just an approximation; refined calculations

which consider the non-linearities exhibited by the material will be presented in the following sections

#### ***5.3.4 Creep under static conditions***

As the material exhibits viscoelasticity, there is a range of displacements produced from the moment the stress is applied until the displacement reaches the final equilibrium value. The sample used in section 5.3.2 (figure 5.25) is used for this section. The creep response is tested in order to link each stress value to an equilibrium strain. The sample's engineering strain, the stress as well as the charges, given as a function of time, are presented in figure 5.34. For clarity, only a selection of the stresses applied are shown. The strain presented is in form of engineering strain.

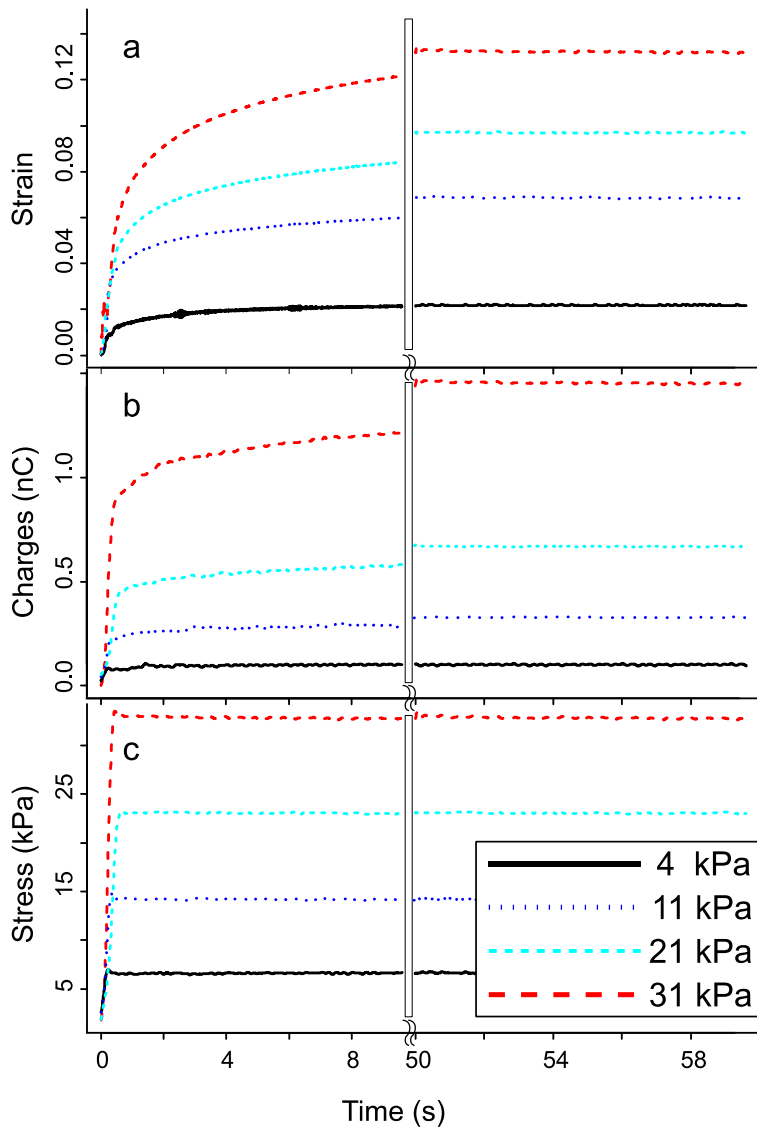


Fig 5.34 Step response of the sample to various compressive loads. The figure shows the compressive strain (a) and the charges (b) that the stress (c) produced. Single run results plotted. A 3 kPa preload ensures contact at all times.

As shown, each curve obtained is constituted of two main regions. The first region starts at  $t=0$ , when the step load is applied, and finishes when the stress reaches its maximum. As the stress is applied in a step manner, this first region is very brief, lasting from 0.2 s to 1 s for higher stresses. After  $t=1$  s stress is constant and a creep-like response is observed in the charges and the strain, that can last for 1 s to 150 s depending on the static stress applied. From the data shown in figure 5.34, it is evident that charges are being produced during creep (after the stress reaches its

maximum). This is expected due to the mechanism by which the charges are produced.

The same sample was tested under various static loads of compression. For a selection of applied stress values, figure 5.35 presents the instantaneous strains (typically attained within 10 sec of stress application) and equilibrium strains (typically after 300 sec). The fit on the equilibrium strain will be used for the next experiments, in order to define the strain produced by a static stress, when there is no way of measuring it

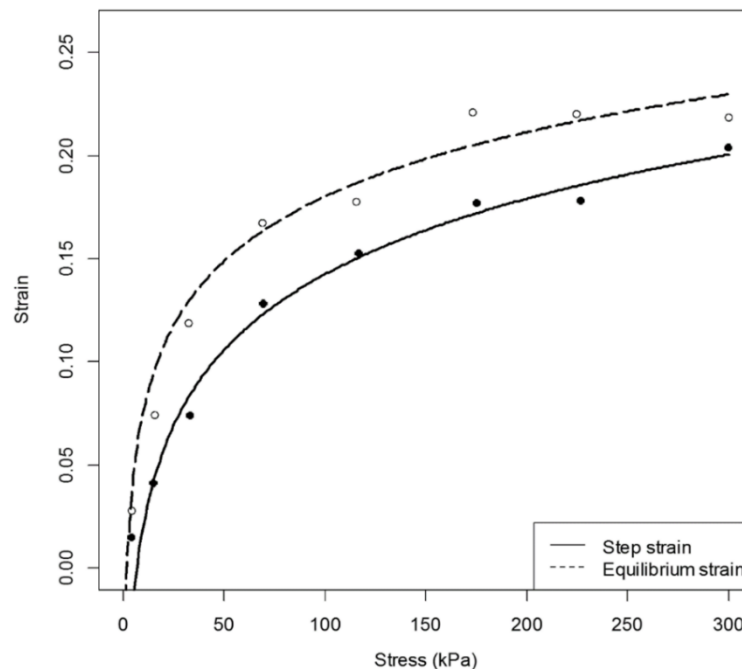


Figure 5.35 Observations and fitted lines of the instantaneous strains (filled symbols - solid line) and equilibrium strains, (hollow symbols - dashed line), plotted over static stress.

For low stress, the difference between step and equilibrium strain is smaller. This difference gets bigger for higher stresses and reaches an almost constant value for a stress higher than 150 kPa. The values of this experiment are used in later sections, where there is need of knowing the equilibrium strain that a static stress implies.

### 5.3.5 Inverse piezoelectric response

The linear region occurs under small displacements, so it can either be tested by the use of small stresses, or by the inverse piezoelectric effect that induces small strains. The inverse piezoelectric response of the same material used in the previous section is tested under low electric potentials (fields of no more than  $2 \text{ MV m}^{-1}$ ). This is 95% lower than the critical field  $E_s$  of the film. This is the minimum poling field under which the film gains piezoelectric properties defined as the critical field of the thickest void within the polymer. The engineering strain and the obtained  $d_{33}$  are presented in figure 5.36 a, b respectively. Similar to the previous 2 experiments, the engineering strain instead of the true strain is given for this test, as we are interested in the change of thickness compared to the initial thickness of the film.

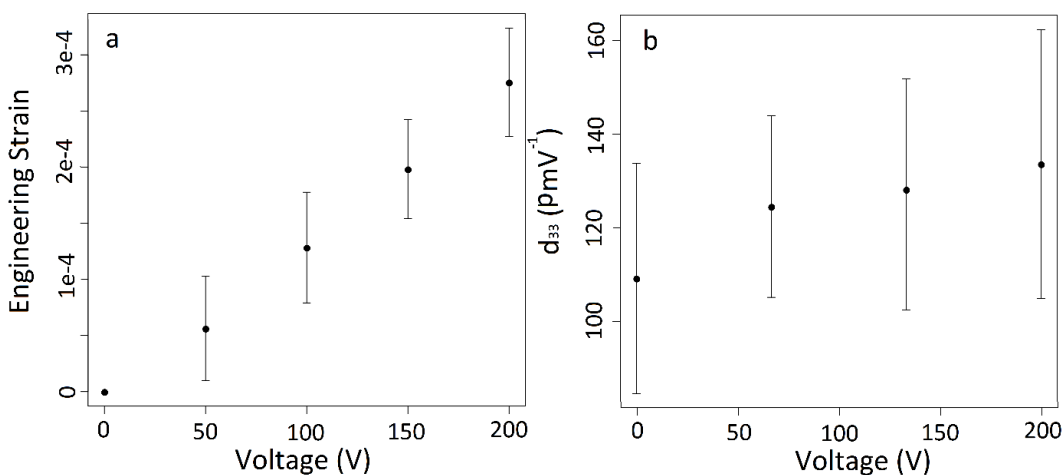


Fig 5.36 a) Strain and b) calculated  $d_{33}$  for inverse piezoelectric effect. A stress of 1.16 kPa acts as a preload to ensure reliable electrical and mechanical contacts. The result is an average of 3 runs. Error bars represent the standard deviation.

The piezoelectric coefficient (figure 5.36b) seems to be almost constant (around  $130 \text{ pmV}^{-1}$ ). The highest strain obtained by the application of the external field is rather small, indicating that the film is still within the linear region of operation.

Based on the hypothesis of section 5.3.1 the application of compressive stress on a Cell-PP film could potentially initiate a process similar and inverse to GDE (leads to increment of relative density, following the U

shape response discussed in (Wegener *et al.*, 2006)). Assuming the validity of this hypothesis, the application of a voltage potential across the sample can either increase or decrease the density of the film, depending on the relative polarity of the potential to the sample. In that sense, for this test, a polarity opposite to that of the charged material was applied on the film, as contraction in that sense is equivalent to compression.

To test the inverse piezoelectric effect within the non-linear range, various static compressive stresses were applied on the film, to induce large strains. Without these preloads, the electric field needed to obtain the full range of strains would be high enough to simply re-charge the film.

Figure 5.37 shows the static inverse piezoelectric response of the film, when pre-stressed under a variety of static stresses.

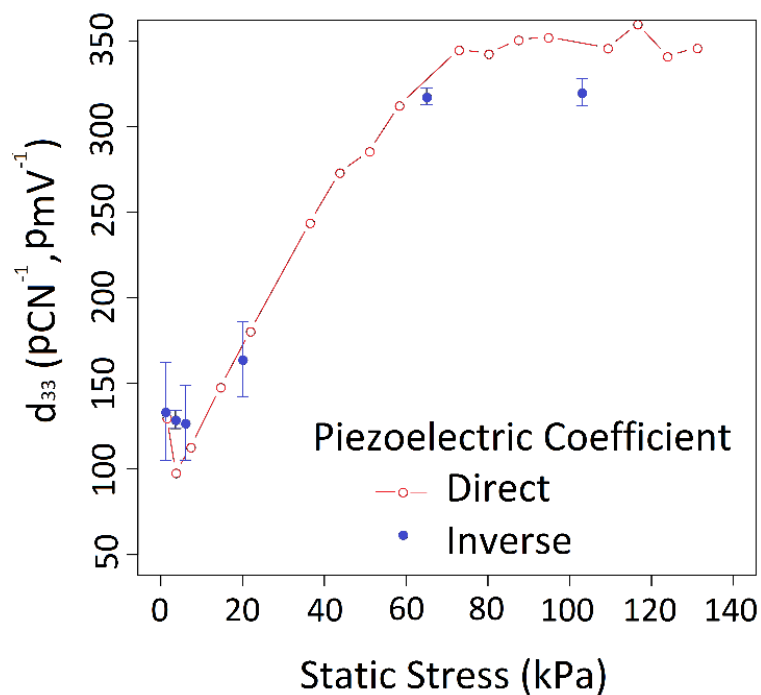


Fig 5.37 Comparison between the direct static  $d_{33}$  (data taken from figure 5.25) and inverse piezoelectric response while compressed under various static stresses. Each data point of the inverse piezoelectric effect is an average of 5 runs. Error bars represent the standard deviation.

The low stress linear region of the film is more pronounced when investigated under the inverse piezoelectric response. This region seems to be rather small compared to the full range of stress applied on the film

in previous sections, as it roughly expands up to stresses of 10 kPa. As the sample behaves non-linearly, the direct and inverse piezoelectric effects need to be tested under the same conditions (eg. large fields), so that agreement between them can be verified.

Extra care needs to be taken when characterizing non-homogeneous polymers. Under low strain, the films piezoelectric coefficient and stiffness are constant, giving linear mechanical and piezoelectric response (figure 5.37). The extent of this linearity depends on the morphology of the material's inner structure and thus the initial stiffness of the film (see figures 5.15, 5.22).

On the contrary, when under higher strains, these films exhibit non linearities (see figures 5.21, 5.28). This phenomenon can be attributed to the heterogeneous bulk of the material. For an individual void, its stiffness depends on its morphology (aspect ratio) and the charge density obtained depends on the void thickness and its functionalization parameters (eg. charging field). The different charge density and stiffness attained by two morphologically dissimilar voids results in different contributions to the final piezoelectric response of the film, under the same stress. In other words, morphologically different voids attain different charge densities by the end of the charging procedure and produce most of their charges under different stress levels, as their stiffness varies. As there is a broad distribution of morphologically different voids in the film, the charges produced (and the resulting  $d_{33}$ ) vary in accordance to the compressive stress applied on the film, yielding a smooth response (see figure 5.28).

On the other hand, having lab-made voids of the same morphology, results in the sharp drop of piezoelectric activity (Dreyfus & Lewiner, 1976), possibly because the voids are quickly engaged at low stress levels. In addition, these lab-made films usually have significantly larger voids, leading to this drop happening under low stress levels.

### **5.3.6 Ageing**

It is observed that the piezoelectric performance of the films was reduced by two factors that can be considered as ageing. The first, explored within

this section, is ageing due to charge density decay that takes place after the charging procedure. A set of samples was tested for their piezoelectric response directly after charging, for stresses up to 125 kPa. The samples were then left to age at room temperature for a period of 30 days. The piezoelectric performance was measured several times during this period, and the results are shown in figure 5.38.

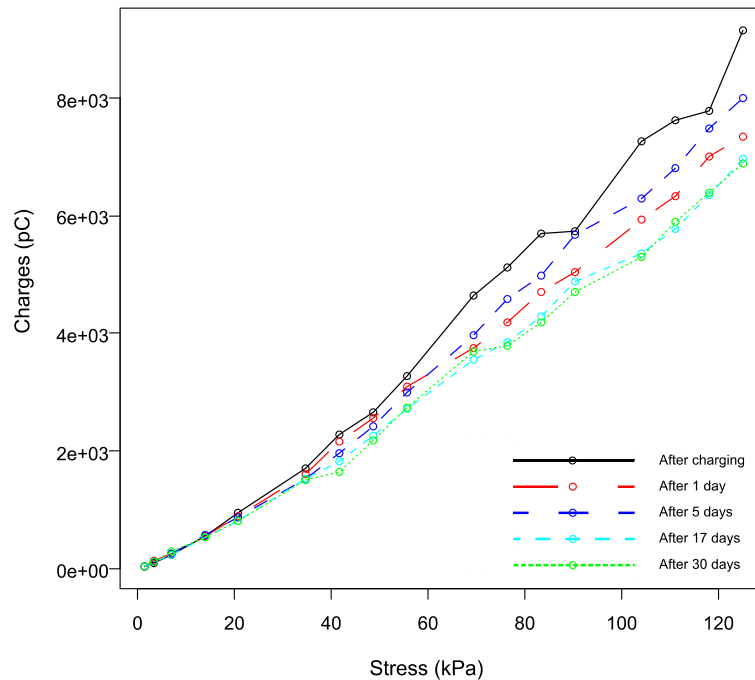


Figure 5.38 Piezoelectric performance versus compressive stress, measured over a period of 30 days. Sample used is an EUH 75 expanded under 5 MPa of pressure.

The piezoelectric performance is decreased after 1 day, to increase again after 5 days. A similar phenomenon was also observed by (Zhang, Sessler & Hillenbrand, 2007). Comparing the 17 days response with the 30 days, reveals that the piezoelectric performance has reached equilibrium, and thus further decay was below measurable. A similar response holds for the rest of the materials, expanded both under 2 MPa and 5 MPa of pressure. By numerical integration of each of the above curves, the charge production over the 125 kPa stress can be calculated. The fraction of the remaining charges over the initial charges (measured right after poling) result to the retained piezoelectric activity. The percentage of retained charges for each day, of all available samples expanded under both 2 MPa and 5 MPa pressure, are shown in figure 5.39.

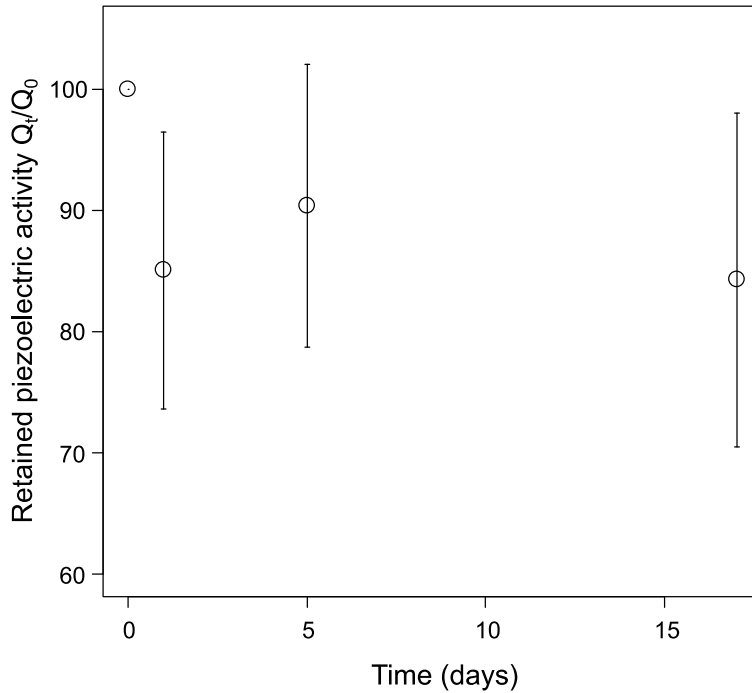


Figure 5.39 Retained piezoelectric activity over time in days, due to ageing under room temperature. Samples expanded under 5 MPa of pressure. Each data point is an average of 15 samples. Error bars represent the standard deviation.

Despite the large deviation, the remaining charges seem to be increased after 5 days compared to those after the first day. For some samples, the comparison between the initial charges (charges measured after charging) and the charges measured after 5 days yield no difference. The charge decay is not only influenced by time. The material as well as the charging field are also parameters that influence this reduced activity. Figure 5.40 shows the influence of the charging voltage to the obtained charges after equilibrium reached (17 days).

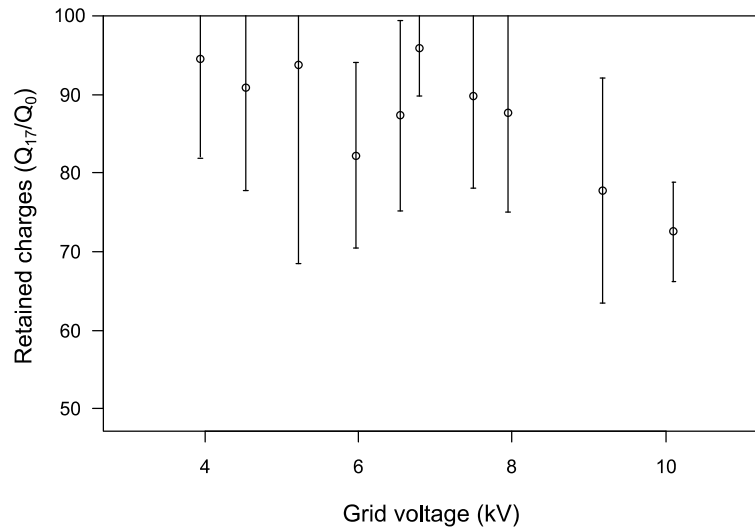


Figure 5.40 Average charge reduction measured after 17 days over charging voltage. Materials expanded under 5 MPa of pressure. Each data point is an average of the 4 materials charged under the same voltage. Error bars represent the standard deviation.

It can be concluded that a higher reduction of charges occurs when the film is charged under higher voltages. Charging the materials under low potentials, the remaining charges do not fall below 80% of the initial charges. When the charging potential is increased, the remaining charges can reduce down to 74% in the worst-case scenario.

The high deviations are due to different materials being tested all together. The charge reduction is investigated for all 4 materials, charged under the same field (see figure 5.30). Figure 5.41 shows the relation between charge reduction and thickness of the film for films expanded under 2 MPa and 5 MPa of pressure.

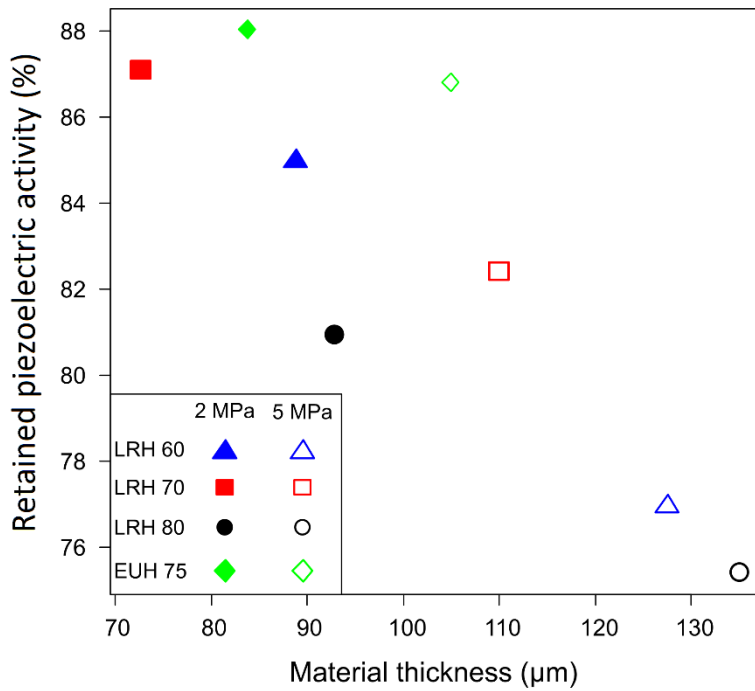


Figure 5.41 Remaining charges over material thickness. All films charges under 90 MV field. Single run data

The film thickness has a significant role to the ageing process. Thicker films tend to show higher reduction of piezoelectric response compared to thinner films. The charge decay yielded a reduction of charges up to 26 % of the initial charges for the worst-case scenario (thick films charged under high fields). There also seems to be a correlation between charge reduction and void morphology. This correlation can only be seen for materials within the same family. Figure 5.42 shows the charge reduction of the LRH family.

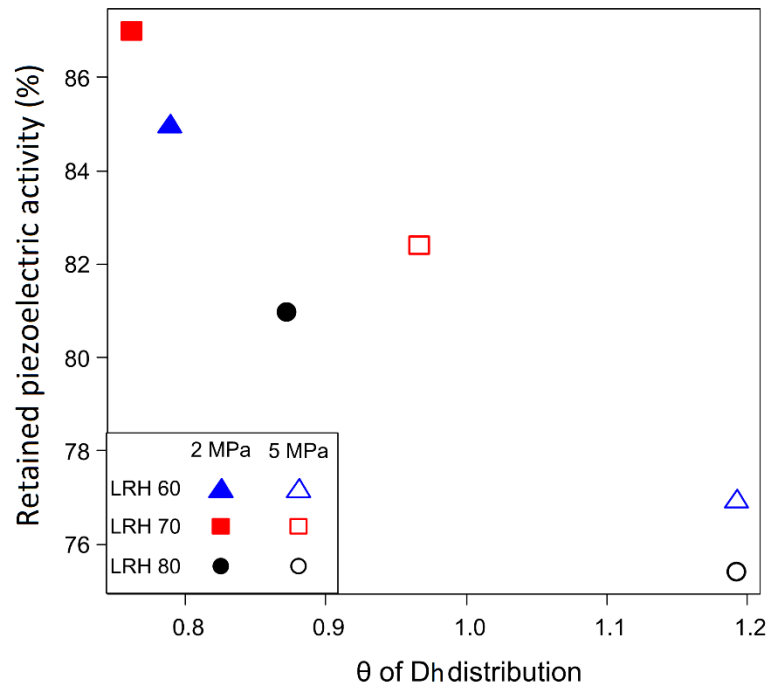


Figure 5.42 Remaining charges in percentage over the location parameter  $\theta$  of the void Dh distribution. Single run data.

The equilibrium charges reduce proportional to the location parameter of the Dh distribution (table 5.1) for the LRH family (LRH 60, LRH 70, LRH 80). According to (Mellinger, 2011) the thickest voids experience back discharges right after the removal of the external poling field. There is a possibility that this reduction continues over time, but to a lesser extent and thus observed as ageing over several days. In general, the highest charge reduction does not exceed 26%. Room temperature stored films, reveal no further reduction of charges even after 9 months.

### 5.3.7 Charge reduction due to overstress

Apart from charge reduction due to time, another factor that decreases the piezoelectric performance of the samples is the application of excessive stress. The samples used for these tests were formerly aged for 17 days to stabilize their piezoelectric response. After an initial piezoelectric performance test, the films were maintained under a compressive load of 510 kPa for three hours. Once the load was removed, the film was permitted to relax for another 30 minutes. The piezoelectric performance was measured again and compared to the initial piezoelectric performance (see Figure 5.43).

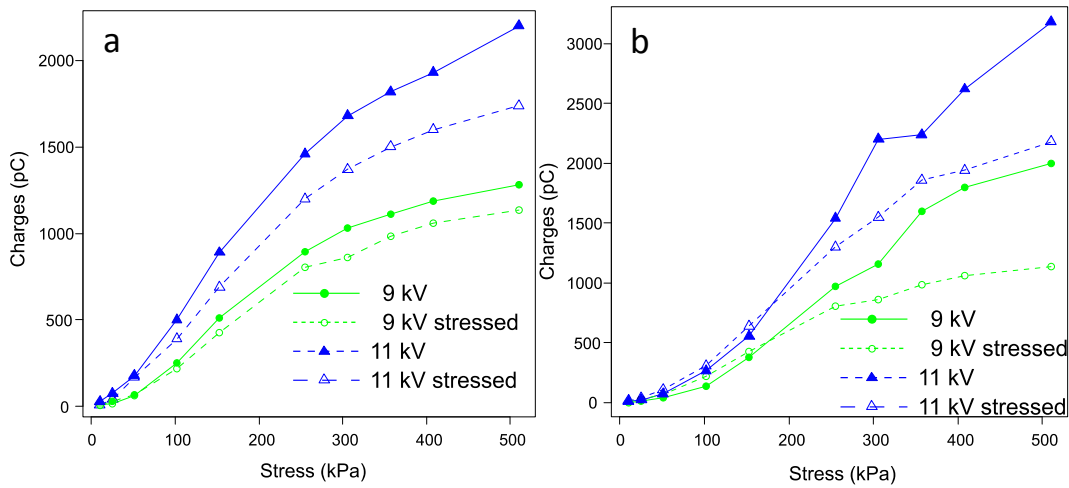


Figure 5.43 Effect of stress ageing on piezoelectric performance, for LRH 80 films expanded under 2 MPa (left) and 5 MPa (right) and charged under 9 kV and 11 kV. Each data point represents an average of 5 runs. Error bars represent the standard deviation.

The charging voltage has a significant role to the charge reduction due to stress. Table 5.5 summarizes the total charge reduction per material after ageing and over stressing.

Material	2 MPa		5 MPa	
	9 kV	11 kV	9 kV	11 kV
LRH 60	21.9%	25%	26.3%	43%
LRH 70	15.4%	23%	19%	46.4%
LRH 80	11.2%	20.9%	13.5%	31.4%
EUH 75	11.1%	27.3%	13.4%	54.2%

Table 5.5 Average charge reduction in percentage, after ageing and excessive stress, for all materials expanded under 2 MPa and 5 MPa of pressure and charged under 9 and 11 kV of potential.

The obtained charges, after ageing and overstressing, for the films expanded under 2 MPa of pressure decrease by an average of 15% and 25% when charged under 9 kV and 11 kV respectively. Films expanded under 5 MPa of pressure, have their piezoelectric activity reduced by 18% and 44% when charged under 9 kV and 11 kV respectively.

It is inferred that charge reduction due to ageing is directly linked to film's thickness and void thickness distribution. On the other hand, charge reduction due to overstressing does not show any connection with the material morphology. It seems that LRH 80 retains most of its charges after the compression test compared to the rest of the films.

## **5.4 Dynamic Response**

### ***5.4.1 Stress relaxation and creep***

To test the dynamic response, an extra layer of silver paint was preferred over the silicone pads as an interface layer between the metal plates and the sample. The silicone pads are not suitable because they are on average 5 times thicker than the Cell-PP (500  $\mu\text{m}$ ) and have comparable stiffness (1.5 MPa), which would introduce large uncertainties in measuring the strain of the sample. For this section, the material used is an EUH 75 sample expanded under 5 MPa of pressure.

It has been observed previously (section 5.3.4) that the relationship between produced charges and stress is not linear. It has also been observed that the charges produced by the material under a compressive stress, correlate to the strain rather than the stress (see figure 5.34). Further analysis reveals that the relationship between the produced charges and engineering strain is not linear either. For example, as the 20 kPa static load is applied, the strain is close to 0.05 and the obtained charges are 0.5 nC (figure 5.34). In comparison with the charge production of the 30 kPa (0.8 nC for 0.06 strain) it can be inferred that more charges were produced per unit of strain for higher stresses.

Further investigation of this non-linearity is done by applying stress ramps to the sample, while logging the charges and the strain. Figure 5.44, shows the charges, plotted against the engineering strain and stress respectively.

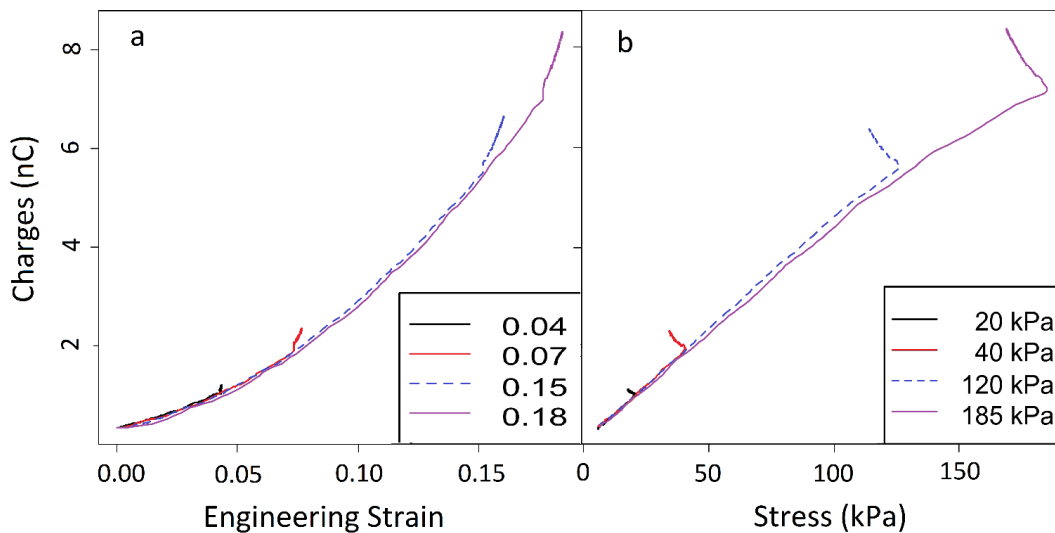


Figure 5.44 a) Charges over engineering strain and b) charges over stress, for maximum engineering strains of 0.04, 0.07 0.15 and 0.18. Graph shows stress relaxation response at the end of each ramp. The result is an average of 2 runs. The preload for this test is 6 kPa.

This test is neither stress nor strain controlled. The testing machine is commanded to perform a compression by moving the crosshead and the position is then held while  $\sigma$ ,  $\epsilon$  (via capacitive sensor) and  $Q$  are monitored. There is both stress relaxation and creep taking place in the end of each displacement ramp. As figure 5.44 suggests, charges are being produced in accordance to the creep / stress relaxation. At the end of each ramp charges are still positively correlated with the strain (albeit at a different rate), whereas they are inversely correlated to the stress. Even ignoring the relaxation region, the response is not linear, as more charges are being produced under higher strains. Moreover, it is observed that more charges are being produced per unit strain during the creep / stress relaxation period compared to the charges produced during the stress ramp. This phenomenon is more obvious for lower strains. For example, the 0.18 ramp curve slope (figure 5.44 purple solid line) is comparable to the creep / stress relaxation slope for high engineering strains (end of ramp). Even though the rate of produced charges during the stress ramp is changing with strain, the rate of charges produced during creep / stress relaxation remains constant irrespective of the stress – strain applied on the film. That means that the slope of the charges produced during the creep / stress relaxation are not influenced by the amplitude of the final

stress and the resultant strain. The change in charge production rate between the creep and the elastic response is an outcome of the different shape changes that the two phenomenon (mechanical strain and creep) induce. The first one (mechanical strain) induces a vertical change in shape of the void mostly on the maximum thickness of the void, while the latter one (creep strain) produces a change in the thickness across the total surface area of the void, thus, more charges are produced per strain.

Due to the mechanism of charge production, discussed for example by Gaal and Lewiner (Gaal ... Kreuzbruck, 2016), there is strong correlation between the strain and the charges (figure 5.44a). A macroscopic strain translates into a strain of the dipoles, due to a change in the relative position of the polymer-embedded charges. This movement, changes the inner polarization and hence, drives the new charges on the external electrodes. It follows that the strain is more directly correlated to the charges produced than the stress (figure 5.44). Whereas at low strains, in the linear region, both strain and stress are valid choices as state variable, at higher strain it becomes mandatory to use strain.

#### **5.4.2 Stress rate**

The different rates at which the charges are produced during ramp and relaxation, implies that there is correlation between the stress rate and the charge rate. This phenomenon can be clearly seen on the different charges over strain slope produced under creep response (stress rate=0) compared to the charges produced during the ramp (stress rate  $\neq 0$ ) (figure 5.44). To test this, the films were compressed to a final stress of 270 kPa using different stress rates while the charges are logged. Figure 5.45 clearly demonstrates that the charges being produced are related to the stress rate.

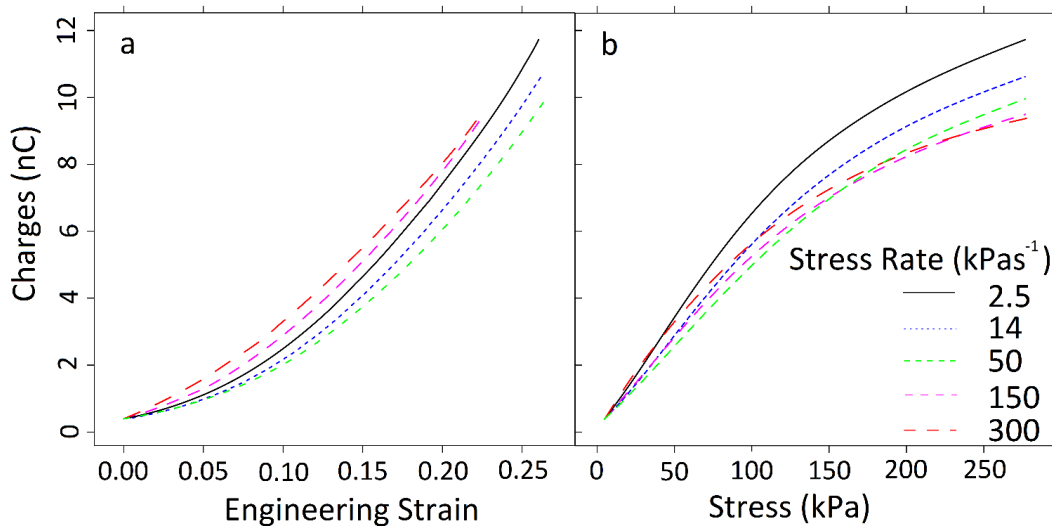


Figure 5.45 a) Charges produced over engineering strain and b) charges produced over stress, for different stress rates. The final stress for every curve is 270 kPa. The result is an average of 2 runs

As creep / stress relaxation takes place during compression, it is not surprising that the stress rate influences the strain rate and the charges (figure 5.45). For higher stress rates, creep does not have the time to develop, thus less displacement and fewer charges are observed for higher stress rates even if the same final stress is reached. Even though the final strain obtained seems to increase moderately with the stress rate (figure 5.45a, 2.5 kPa s<sup>-1</sup> to 50 kPa s<sup>-1</sup>) for low stress rates, further increment of the stress rate (150 kPa s<sup>-1</sup> and 300 kPa s<sup>-1</sup>) result in a marked decrease in the final strain. This change of behavior can be attributed to the increment of storage modulus E' of the material, when under high dynamic excitation. The general effect of stress rate is that more charges are produced at low rates. Whereas the charge production rate consistently increases with the strain state (concave curves in figure 5.45a), when considered as a function of stress, a steeper start at low stress values is followed by a progressively reduced growth (convex curves in figure 5.45b). The interpretation is that further deformation of the material makes it more electrically active by engaging more voids, albeit, at the same time, and the increased stiffness reduces the yield as a function of stress.

Similar response can be seen when the sample is tested under cyclic deformation of different amplitude. An EUH 75 sample charged under

similar conditions is used for this experiment. EUH 75 produces its highest charges per unit stress close to 100 kPa of compressive stress. For this reason, the sample is tested for harmonic compressive oscillations of 7 consecutive cycles for a variety of peak to peak stresses close to and lower than 100 kPa. For this experiment, the frequency is kept constant at 1 Hz. The results are shown in figure 5.46.

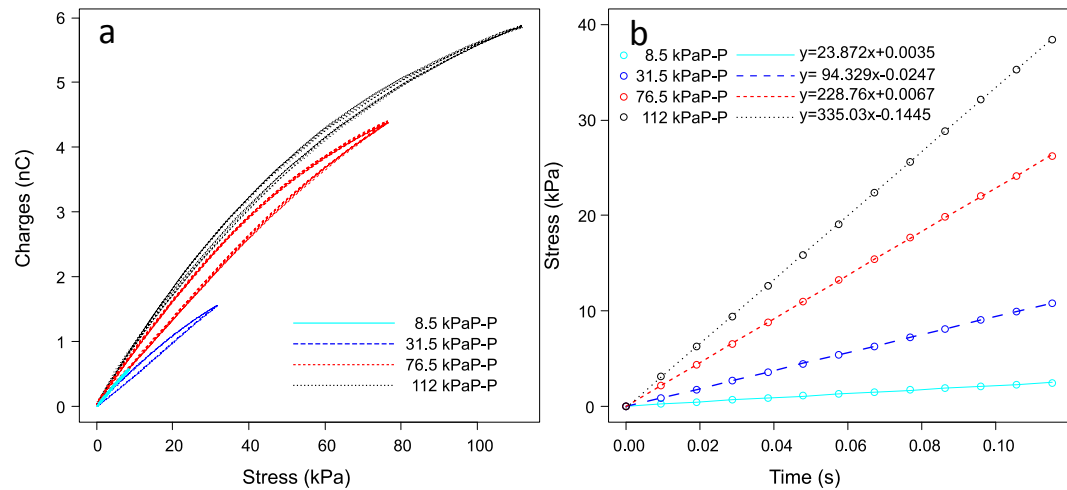


Figure 5.46 a) Charges over stress and b) stress over time for the first 0.11 rad of the loading cycle of the oscillation. Tests held for different stress amplitudes.

Less charges per unit stress are observed by the 8.5 kPa amplitude compared to the amplitude of 31.5 kPa. However, increasing the amplitude even more, leads to increased charges over stress. This is not a direct outcome of the higher amplitude of mechanical oscillation. By increasing the amplitude of the oscillation and keeping the frequency constant, the average stress rate is increased for a higher stress cycle to be obtained within the same time. A rough estimation of the applied stress rate is given by figure 5.46b, where a part of the first half period of the oscillation is shown. Linear regression is fitted to the linear part, in order to describe the stress rate. Theoretically, the stress rate of the initial linear part of the sinusoidal oscillation can be estimated based on equation 5.16.

$$\sigma' = A\omega \quad (5.16)$$

Where A is the peak amplitude of the oscillation. Equation 5.16 implies that any increment of frequency or amplitude, has the same effect on the stress rate of the linear part of oscillation. Furthermore, for each oscillation with  $A_{P-P}$  amplitude a static pre-load of  $A_P$  is applied to ensure for contact between the sample and the machine, resulting to the sample relaxing and oscillating around the strain region this preload produces.

Another observation is the different route the charges take during the decompression cycle. The decompression cycle produces more charges than the compression cycle, specifically for the lower amplitude oscillations. By integrating and subtracting the loading and the unloading curve, a comparison can be made to determine the area existing between them. It is found that the ratio of this area over the total unloading area decreases inversely proportional to the stress rate. As an example, the 31.5 kPa cycle has a ratio of 0.08 which is much higher than the ratio of the 76.5 kPa cycle at 0.03. The route becomes almost similar under higher compressive amplitudes (higher stress rates). Furthermore, as the charge rate under creep / stress relaxation does not seem to change (figure 5.44) it is expected that further increment in stress rate results to more charges being reduced during the loading cycle compared to the unloading one.

The above observations (figure 5.45 and figure 5.46) imply that the material operating under higher stress rates and / or higher stress / strain regions, becomes more elastic than viscous.

Stress / creep relaxation develops depending on the time constant of the material. When in dynamic conditions, the lag between the stress and the strain (angle  $\tau$ ) is the direct measurement of the energy dissipation of the material and thus the time constant. The storage modulus  $E'$  and the loss modulus  $E''$  are correlated to this angle as described by equations 5.17 and 5.218 respectively.

$$E' = \frac{\sigma}{\varepsilon} \cos(\delta) \quad (5.17)$$

$$E'' = \frac{\sigma}{\varepsilon} \sin(\delta) \quad (5.18)$$

Based on equations 5.17 and 5.18, the storage modulus ( $E'$ ) is maximized when the loss modulus  $E''$  is minimum.

Figure 5.47a shows the delay ( $\tau$ ) in degrees between the strain and the stress, for frequencies lower than 1 Hz and for different static preloads, with the sample being in short circuit.

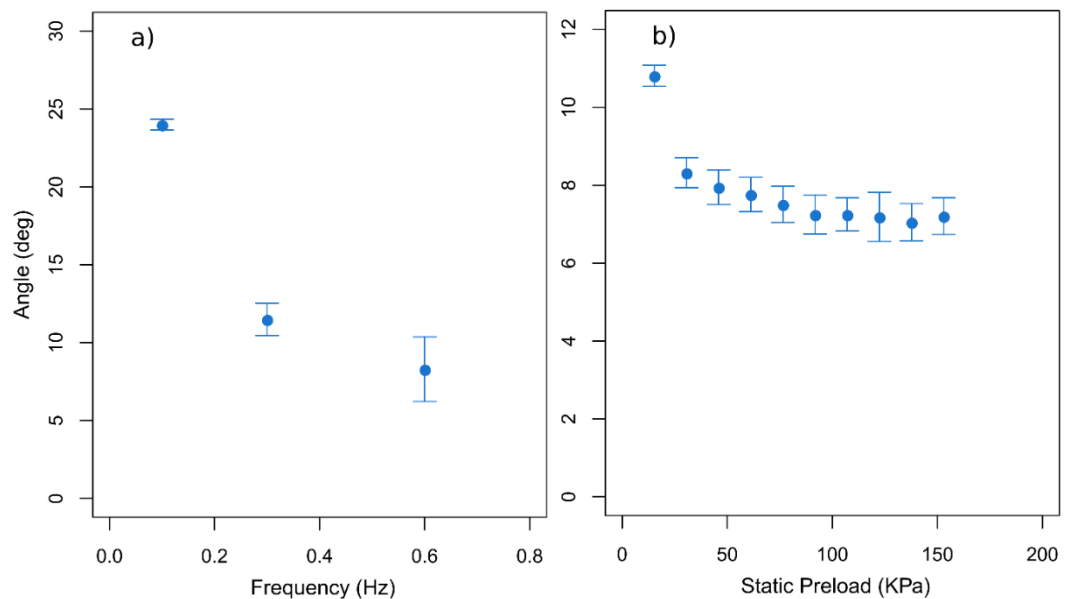


Figure 5.47 Angle  $\tau$  representing the lag between stress and strain over a) different frequencies and b) over different static stresses. Data obtained with the aid of a) Data Physics V100 shaker and 6200 Micro Epsilon and b) Perkin Elmer DMA 8000. The dynamic stress was 7 kPa for both tests. The standard deviation for figure 5.47a emerges from the uncertainty of the synchronization between the measurements. Each data point represents single run data and an average of 10 points for figures 5.47a and 5.47b respectively.

Angle  $\tau$  decreases inversely proportional to frequency. This is expected as the polymer acts like a low pass filter thus the higher the frequency, the less the phase shift. Similar decrement can be seen in figure 5.47b where the frequency remained constant and the static stress is increased. There seems to be more energy storage capability, when the material is mechanically pre-loaded (figure 5.47b).

In conclusion, when time is provided for the material to relax (low stress rate or mechanical excitation frequency), the total strain is increased followed by higher charges produced. At this point, angle  $\tau$  is high which means the loss modulus  $E''$  is high. By increasing the stress rate or the mechanical excitation frequency, less charges and strain are observed as

the material does not have time to relax hence the loss modulus is lower. Angle  $\tau$  decreases, increasing that way  $E'$  and decreasing  $E''$ . Further increment of stress rate or mechanical excitation frequency, increases  $E'$  and as a result, the material response gets closer to elastic rather than viscous, enhancing the piezoelectric properties of the material.

Based on the above, one needs to define the stress, or equilibrium strain (after creep), region of operation when measuring quantities like stiffness ( $c_{33}$ ), piezoelectric coefficient ( $d_{33}$ ), electromechanical coupling coefficient  $k^2_{33}$  etc. Clear evidence of this necessity is found in figure 5.37 (section 5.3.5), where the expected equality of  $d_{33}$  obtained from the direct and inverse piezoelectric effect is found, provided that similar strain states are investigated. In addition, when under quasi static (see figure 5.34) or dynamic compression (see figures 5.44, 5.45), where creep or stress relaxation is involved, it is obvious that the obtained charge is correlated to strain.

#### **5.4.3 Piezoelectric coefficient $d_{33}$ , stiffness $c_{33}$**

As the material behaves non-linearly in both the mechanical and electrical domain, the rate of change of  $d_{33}$  and  $c_{33}$  are expected to change under different engineering strains. For this reason, the behavior of the material is investigated in small regions of engineering strain, making linearization possible. The equations used to calculate the added stress  $\sigma_{new}$ , true strain  $\epsilon_{true}$ , stiffness  $c_{33}(\sigma)$  and piezoelectric coefficient  $d_{33}(\sigma)$ , as well as the procedure is given below.

The stress increment value, is calculated based on equation 5.19.

$$\Delta\sigma = \frac{\Delta F}{A}, \quad (5.19)$$

where  $\Delta F = F_{new} - F_{old}$  is the force increment acting upon the area  $A$  of the sample. The initial thickness  $l_0$  of the film is considered to be the voided part of the sample (excluding the two external layers). The new thickness is calculated for each stress value by subtracting the compressive displacement from the previous thickness (equation 5.20)

$$l_{new} = l_{old} - \Delta l, \quad (5.20)$$

where  $\Delta l$  is the displacement caused by the last measured increment of stress. Knowing the last compressive displacement  $\Delta l$  and the current thickness  $l_{new}$ , the true strain produced by the last stress increment can be derived as

$$\varepsilon_{true} = \frac{\Delta l}{l_{new}} = \frac{l_{old}}{l_{new}} - 1. \quad (5.21)$$

By using the true strain  $\varepsilon_{true}$  (equation 5.21) and the applied stress (equation 5.19) the stiffness of the film  $c_{33}(\sigma)$  is derived (equation 5.22).

$$c_{33}(\sigma) = \frac{\Delta\sigma}{\varepsilon_{true}} \quad (5.22)$$

Finally, the piezoelectric coefficient  $d_{33}(\sigma)$  can be calculated by dividing  $Q(\sigma)$  by  $\Delta F$  (equation 5.23).

$$d_{33}(\sigma) = \frac{Q(\sigma)}{\Delta F} \quad (5.23)$$

By making use of the above equations and for the data obtained in section, the dependence of  $d_{33}(\sigma)$  and the material stiffness  $c_{33}(\sigma)$  on engineering strain is calculated and presented in figure 5.48, for a variety of compressive stress rates. Engineering strain is chosen over true strain for X axis, as we are interested in the strain region of operation compared to the original thickness.

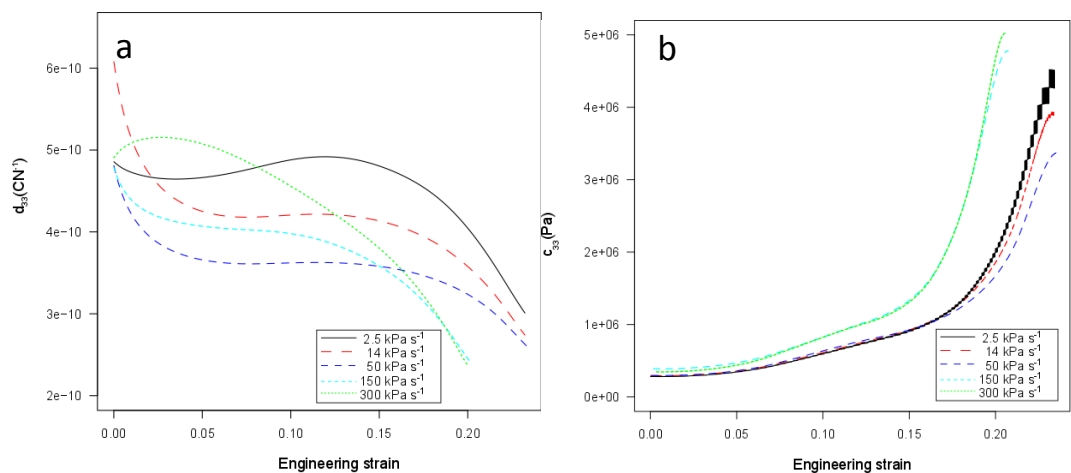


Figure 5.48 a) Piezoelectric constant  $d_{33}$  and b) material stiffness  $c_{33}$  as a function of engineering strain for a selection of compressive stress rates.

It is obvious that different stress rates give noticeably different results. For lower values of stress, small uncertainties in measuring the produced charges result to high deviations within the piezoelectric coefficient  $d_{33}$ . It can be inferred that under high stress rate,  $d_{33}$  reduces quicker after the peak point. In addition, Figure 5.48b shows that higher stress rates result in stiffer material over strain as expected, as film relaxation does not take place.

There is a region of engineering strain, where the device produces the maximum charges per compressive stress. The location of this region depends on the compressive stress rate applied on the film (Figure 5.48). When the stress rate is high, the material is providing higher charges under lower stress, resulting on the drop of  $d_{33}$  at higher strains (figure 5.48a).

Further investigation of the relation of stiffness  $c_{33}$  to engineering strain, reveals a sudden decrement on the rate of change of stiffness. This can be clearly seen by plotting the rate of change of  $c_{33}$  against engineering strain (figure 5.49). The first derivative of the polynomial fit to the produced charges are also plotted within the same figure for comparison.

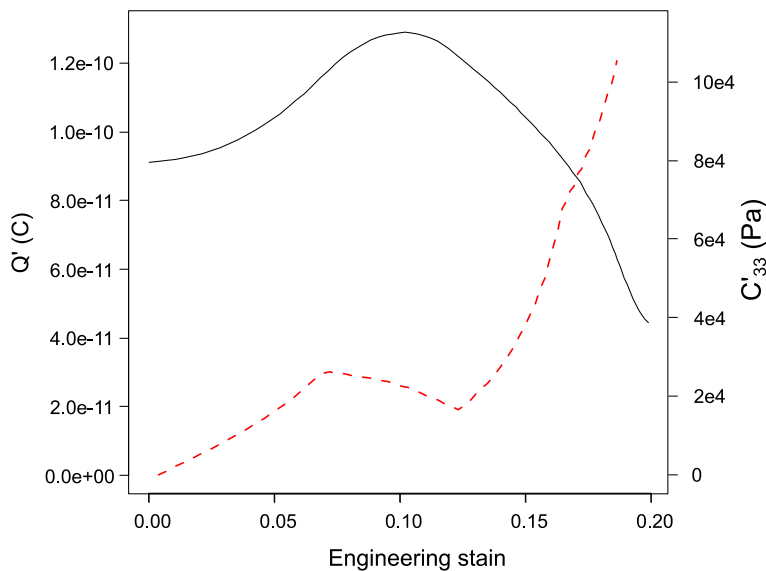


Figure 5.49 First derivative of the polynomial fits to the charges  $Q$  and stiffness  $c_{33}$  over engineering strain. Data obtained for stress rate of  $300 \text{ kPa s}^{-1}$ .

Plotting the rate of charge production against engineering strain (figure 5.49), reveals that the decrease of stiffness rate is accompanied by an increase in the rate of charge production. As seen before, the morphology of the voids inside the film change when the material is under compression. This might explain the sudden decrement of  $c'_{33}$  with increasing strain. Similar results were obtained for the same material when the stiffness of the material was plotted over compressive stress. The material and GDE treatment used were the same (Qiu, Gerhard & Mellinger, 2011).

## **5.5 Energy harvesting**

### **5.5.1 Permittivity**

The permittivity  $\kappa(\sigma)$  of the material is obtained indirectly, by measuring the capacitance of the sample. Impedance analysis equipment (Bode 100) was used to estimate the capacitance of the film when being under a variety of static stresses. Once the film stopped from relaxing, 100 measurements of the capacitance and compressive displacement were taken. Equation 5.24 was used to calculate the permittivity.

$$\kappa(\sigma) = \frac{C(\sigma) l(\sigma)}{A\kappa_0} \quad (5.24)$$

The permittivity of the material as a function of the engineering strain is shown in figure 5.50.

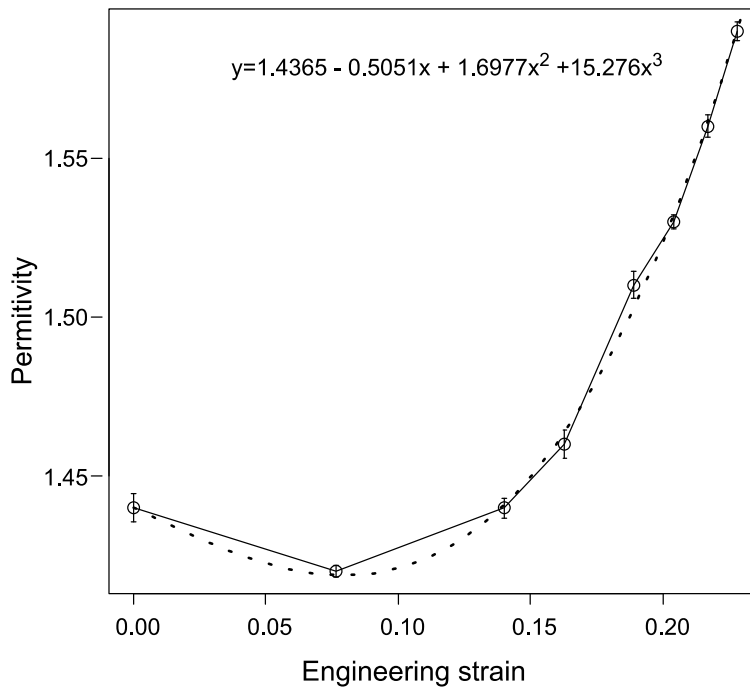


Figure 5.50 Observations and fitted line of permittivity  $\kappa$  as a function of engineering strain. Each data point is the average of  $N=100$  measurements. Error bars represent the standard deviation.

It is inferred that the permittivity is not constant throughout different regions of engineering strain. On the contrary, the permittivity seems to be reasonably constant for the 0 to 0.15 range of strain. The third order polynomial fit will be used for the calculation of  $k_{33}^2$ .

The relative permittivity of the material has both positive and negative influence on the piezoelectric properties of the material. Firstly, high permittivity values are often associated with higher piezoelectric activity. On the contrary,  $k_{33}^2$  decreases proportionally with the permittivity. The relative permittivity of the material increases dramatically for strains higher than 0.15 (figure 5.50). For strains lower than 0.15, the increment in capacitance  $C(\sigma)$  due to compressive displacement, seem to be cancelled out by the decrement of sample thickness  $l(\sigma)$  (equation 5.24).

### 5.5.2 Electromechanical coupling coefficient $k_{33}^2$

Having every parameter in hand, the electromechanical coupling coefficient can be estimated by equation 5.25. Figure 5.51 shows  $k_{33}^2(\sigma)$  for every stress rate, plotted over engineering strain.

$$k_{33}^2(\sigma) = \frac{d_{33}^2(\sigma)c_{33}(\sigma)}{\kappa_{33}(\sigma)\kappa_0} \quad (5.25)$$

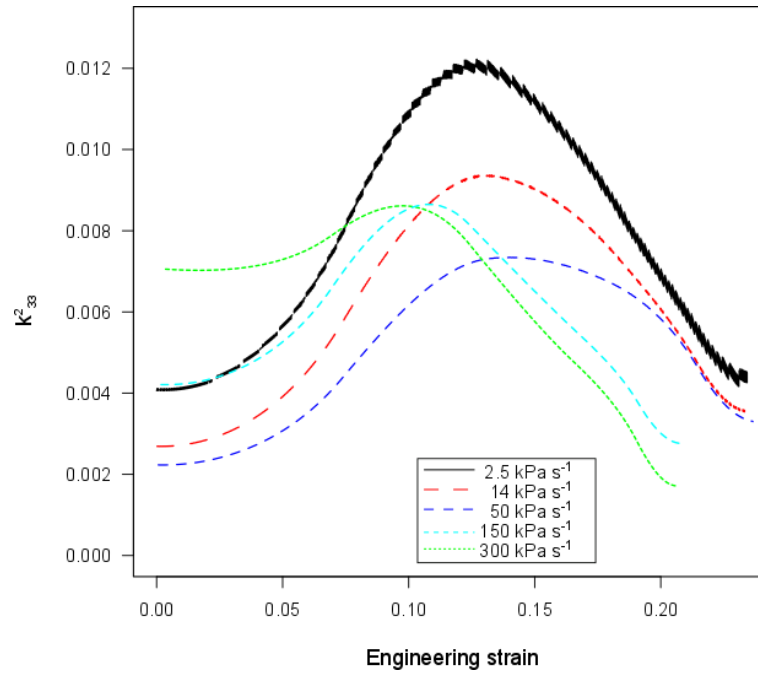


Figure 5.51 Electromechanical coupling coefficient  $k_{33}^2(\sigma)$  over engineering strain for different stress rates. Points were derived by using equation 6. Each point is an average of 2 data points.

As expected,  $k_{33}^2(\sigma)$  is not constant throughout the higher range of engineering strain. There is a region of strain less than 0.01, where the  $k_{33}^2$  seems to be constant. Furthermore, the extend of this region as well as the whole response depends strongly on the stress rate, similar to the previous observed quantities. All curves show a peak around an average strain of  $\varepsilon(\sigma) = 0.12 \pm 0.02$ , reaching an average value of  $k_{33}^2(\sigma) = 0.009 \pm 0.002$ . The peak of  $k_{33}^2$  is located close to stress of 65 kPa (9N) for the lower stress rates, while for the higher stress rates around 54 kPa (7.5N).

In order to investigate the relative benefits of the above regions to EH, the film was subjected to a mechanical 1Hz frequency sinusoidal compression with a peak to peak (P-P) amplitude of 7kPa. The static load was increased from 7 kPa to 63 kPa (F= 1 to 10 N) with 7 kPa increments. The  $k_{33}^2(\sigma)$  is derived the same way as in figure 5.51 (by using equation 5.25). The resultant  $k_{33}^2(\sigma)$  for each test is the average of all the points of 3 excitation cycles. The strain produced by the dynamic stress is not negligible, therefore, there is a large deviation on both the strain (X axis)

as well as the  $k_{33}^2(\sigma)$  value (Y axis). Before acquisition, the sample was allowed to relax under the sinusoidal oscillation until no more creep / stress relaxation was observed. Here, it is assumed that the static stress leads to a strain obtained from figure 5.35 (equilibrium strain curve). Figure 5.52 shows the resultant averages as well as their deviations, plotted as a function of engineering strain. The engineering strain for each static stress is inferred from figure 5.35 (equilibrium strain). Each point is an average of 3 cycles, with error bars showing the combination of the standard deviation of data among the 3 cycles and the data of each dynamic excitation cycle.

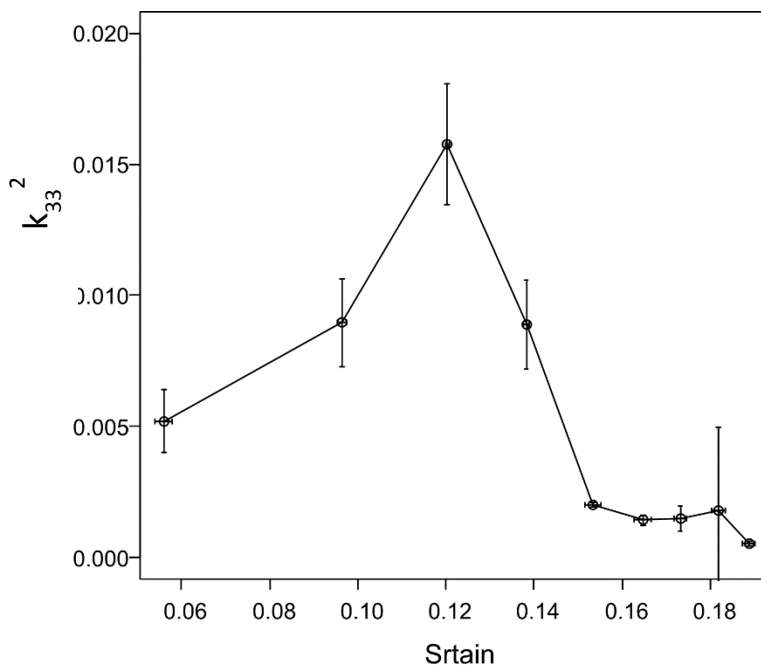


Figure 5.52 Electromechanical coupling coefficient  $k_{33}^2$  over engineering strain for static stresses of 7 kPa to 63 kPa with 7kPa increments. The sinusoidal dynamic stress has frequency of 1 Hz and amplitude of 7 kPa<sub>p</sub>. The line is a guide to the eye.

The excitation stress applied on the film is of the form shown by equation 5.13. It seems that operating in the optimum strain region yields higher values for  $k_{33}^2$  than the values obtained in figure 5.51. For instance, the highest value in figure 5.52 is 25% higher than the peak value obtained from the 2.5 kPa s<sup>-1</sup> ramp in figure 5.51. Despite that, the peak is located at a strain of 0.12, similar to the peak of the previous experiment. Thus,

harvesting in the specific region of strain maximizes the efficiency of mechanical to electrical conversion.

All of the above relationships, have an effect on the behavior of  $k^2_{33}$  with engineering strain. There is a different maximum peak location of  $k^2_{33}$  for each stress rate (see figure 5.51). At lower stress rates,  $k^2_{33}$  peaks close to a strain of 0.12, while at high stress rates peaks close to a strain of 0.1, corresponding to stresses of 65 kPa and 54 kPa respectively. On the other hand, a strain of 0.12 is achieved with a static stress of 22 kPa (figure 5.35) after full creep. The maximum  $k^2_{33}$  was obtained by dynamically exciting the sample around this strain (see figure 5.52). In conclusion, agreement between figure 5.51 and 5.52 is obtained, when  $k^2_{33}$  is given as a function of strain and not as a function of stress. This further increases the evidence of the piezoelectric properties being linked to the strain rather than stress.

As explained before (section 5.3.3) the stiffness of the material has a significant role to the obtained  $k^2_{33}$ . The LRH family materials are tested for their electromechanical coupling coefficient under sinusoidal dynamic condition with the same procedure that led to figure 5.51. The calculated values of  $k^2_{33}$  are presented in figure 5.53 for an excitation cycle.

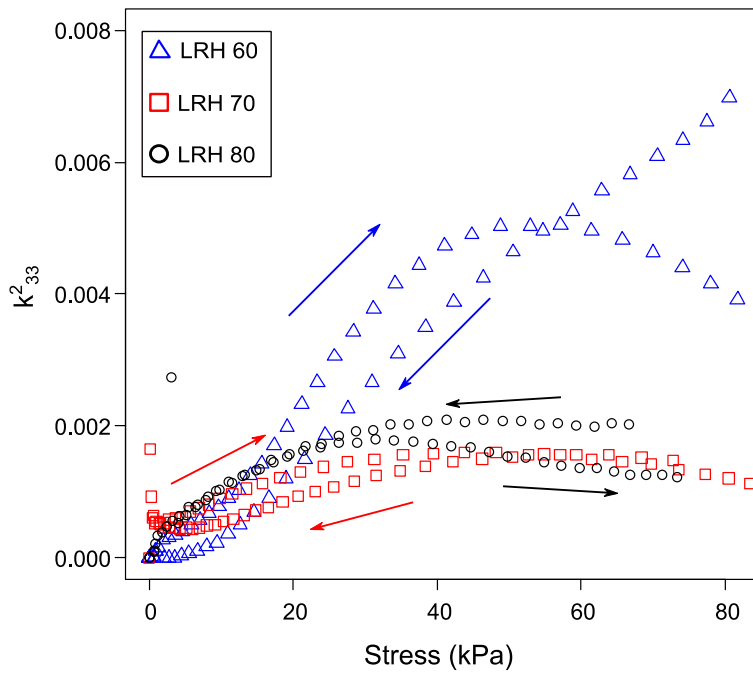


Figure 5.53 Calculated  $k^2_{33}$  values for the LRH material family over stress. The applied compressive stress is sinusoidal. Arrows designate the loading and unloading sequence.

The permittivity is calculated for each material as in figure 5.50. Despite the higher relative permittivity of LRH 60 under low stresses (2.6 and 1.7 for LRH 70 and LRH 80 respectively) the strain of LRH 70 and LRH 80 is significantly higher than LRH 60. As a result, the permittivity of LRH 70 and LRH 80 increases more quickly than that of LRH 60 under higher stresses, decreasing that way  $k^2_{33}$  (equation 5.25). Despite that, even if  $k^2_{33}$  is calculated assuming constant permittivity  $\kappa$ , LRH 60 shows higher coupling coefficient. This demonstrated the importance of stiffness for an efficient mechanical energy harvester.

### 5.5.3 Power generation

Concerning the harvesting applications, the electrical output power is of importance. Before harvesting with the film, the optimum resistance that maximizes the electrical power output is found. Figure 5.54 shows the obtained power over the load resistor. The frequency and the stress amplitude of the dynamic mechanical excitation for this experiment are 1

Hz and 7 kPa<sub>P-P</sub> respectively. The power was calculated using equation 5.26, based on the average value of the voltage output  $V_{avg}$ .

$$W_{out} = \frac{V_{avg}^2}{R_{load}} \quad (5.26)$$

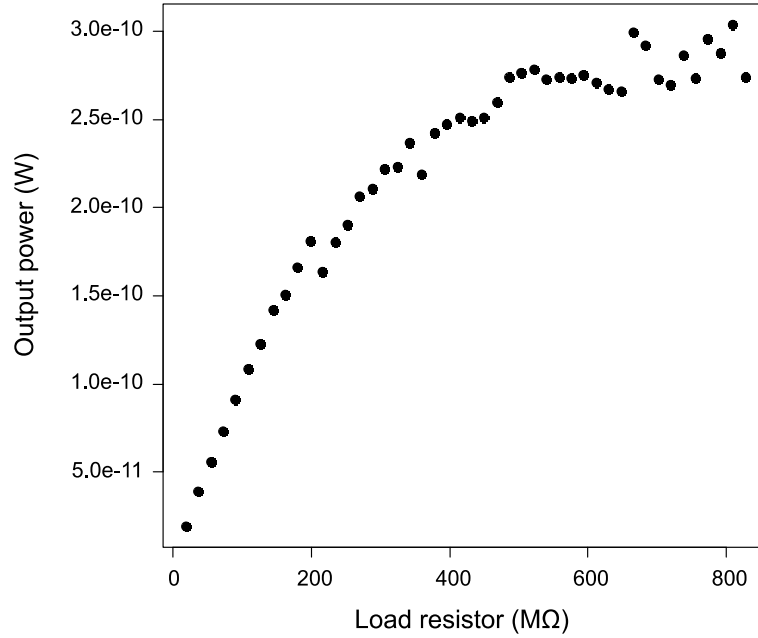


Figure 5.54 Obtained power over load resistor. The output power is derived based on equation 5.26.

An optimum resistor of 600 MΩ was used for harvesting. Firstly, the sample was tested for the maximum power it can produce. The sample was preloaded with a stress of 106 kPa. Subsequently, the amplitude of the dynamic stress was increased to approximately 208 kPa, to ensure contact with the clamp and the moving part at all times. The voltage as well as the stress against time are given in figure 5.55.

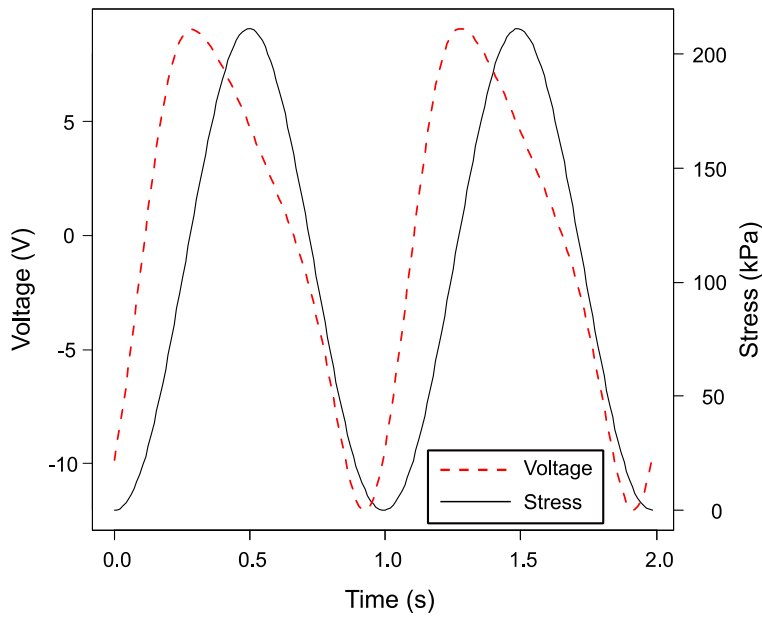


Figure 5.55 Electrical performance of the sample and mechanical input over time for harvesting with a static stress of 106 kPa and dynamic stress of 208 kPa. The load resistor is 600 M $\Omega$ .

Based on 21.2 V<sub>P-P</sub>, the sample generated a peak power of 0.75  $\mu$ W which translates to a charge density of 5.2 mW m<sup>-2</sup>. The average power is calculated based on the V<sub>avg</sub> value of the voltage and is 93 nW (0.65 mW m<sup>-2</sup>). The efficiency of the device can be calculated by use of equation 5.27

$$n = \frac{W_{out}}{W_{in}} \quad (5.27)$$

$$W_{in} = F_{avg} D_{avg} \quad (5.28)$$

Where  $W_{out}$  and  $W_{in}$  are calculated based on equations 5.26 and 5.28 respectively. The efficiency is estimated to be  $n=0.0086$ . Despite the force following a sinusoidal wave, voltage has a more irregular shape. It is evident that there is difference in the produced voltage between the loading and the unloading phase (figure 5.55). This can be clearly seen in figure 5.56, where the voltage is plotted over stress for a full cycle of harvesting.

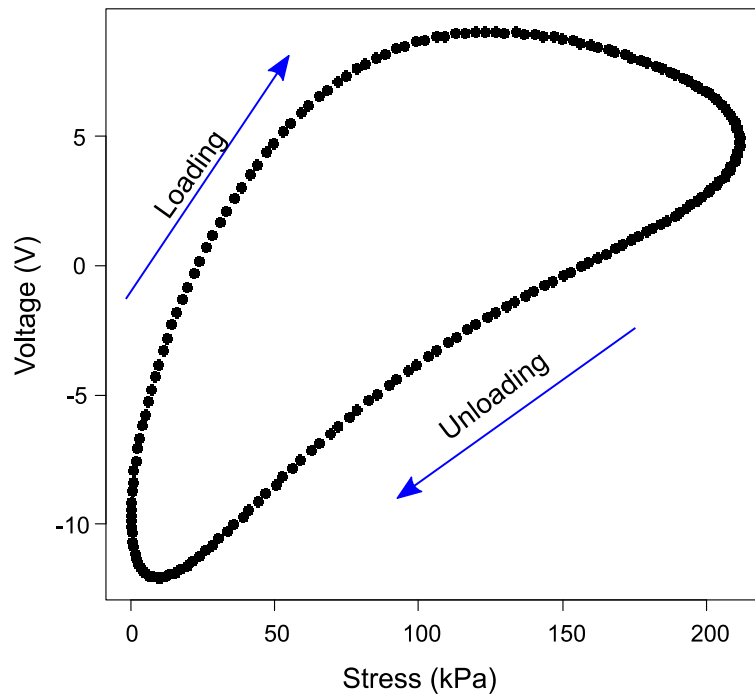


Figure 5.56 Hysteresis loop between voltage and stress. The arrows show the transition from loading to unloading phase. Data do not show the beginning of the oscillation.

The lag of the voltage can be clearly seen in figure 5.55. When the stress becomes zero after the unloading period, the voltage still decreases towards zero. There is a difference of 17% in terms of output power between the loading and unloading phase. It can be concluded here that more power is coming out of the sample when loading compared to unloading.

The lag observed in figure 5.55 has a minimum value of 0.019 sec occurring for a stress of 82 kPa and a voltage of -4 V (figure 5.55). Based on the data shown in figure 5.50 the capacitance of the sample is estimated to be close to 17 pF for lower stress. By assuming that the 600 M $\Omega$  load resistor is comparable to the impedance of the sample and thus close to the combined impedance of the sample and the resistor itself, an RC filter with a time constant of 0.01 sec is found which is comparable including the uncertainties involved. However, this lag is not constant throughout the whole cycle, as it increases with the applied stress.

Finally, the effect of preloading to the efficiency and the output power of the device is tested. The same setup that produces the data shown in

figure 5.52 is used. The resultant  $W_{out}$  as well as the efficiency of the device are given in figure 5.57.

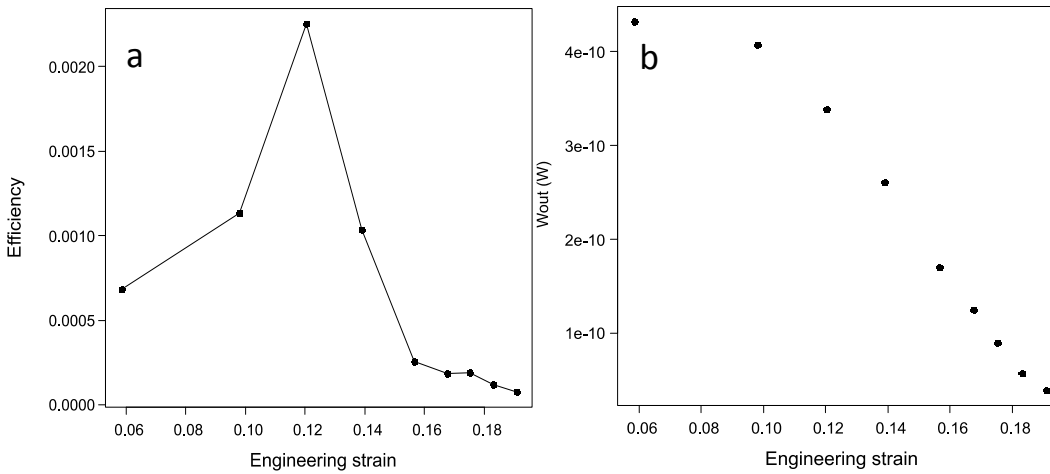


Figure 5.57 Efficiency (a) and output power (b) of the sample over engineering strain. Data were collected for a variety of static stresses. The engineering strain is calculated at the equilibrium strain shown in figure 5.35.

Figure 5.57 shows that the output power decreases with the applied static stress. It should be mentioned here that the thickness of the film is decreased upon the application of the initial static stress. On the other hand, the efficiency and the  $k^2_{33}$  (see figure 5.52) follow the same pattern as expected.

Characterizing the film as an energy harvester, the highest  $k^2_{33}$  found is 0.016 (figure 5.52) with maximum efficiency of 0.018 (figure 5.57a) and peak output power of 2.7 nW (figure 5.57b) when operating under engineering strain of 0.12. Despite that, the maximum peak output obtained when under static stress was 3.5 nW under a strain of 0.06 (figure 5.57b). This leads to the conclusion that the increment of the efficiency is an outcome of the decrement of the mechanical input power  $W_{in}$  rather than the  $W_{out}$ , which only decreases proportional to the static stress. The decrement of  $W_{in}$  is a direct result of the increment in stiffness of the material as has been shown previously.

## 5.6 Dielectric Resonance Spectroscopy (DRS)

Dielectric resonance spectroscopy method is a valid standardized method for obtaining the resonance and anti-resonance frequencies of the material. Apart from the limitation due the high mechanical losses of Cell-PP (Mellinger, 2003) another limitation is that the characterization can only be done for the linear low strain part of the material's response. This means that DRS response can only be compared with the linear part of the response obtained by the previous experiments.

An EUH 75 sample expanded under 5 MPa of pressure was electroded by gold sputtering and subsequently contact charged under 9 kV of potential. The film got attached on a metallic surface. In this case, the antiresonance frequency (the frequency where in the absence of losses the reactance is zero) is described by equation 2.37 but with the thickness multiplied by 4 in the denominator.

$$f_a = \frac{v_3}{4l_3} = \frac{1}{4l_3} \sqrt{\frac{c_{33}^D}{\lambda}} \quad (2.37)$$

Based on equation 2.37, the antiresonance frequency is found to be 100 kHz.

By using equation 5.25, an approximation of the electromechanical coupling coefficient  $k_{33}^2=0.0035$  is made for the EUH 75 sample expanded under 5 MPa and charged under 9 kV potential and for stiffness of  $c_{33}=0.78$  MPa (see figure 5.21), permittivity of  $\kappa=1.4$  (see figure 5.50), and piezoelectric coefficient of  $d_{33}=240$  pC N<sup>-1</sup> (see figure 5.28).

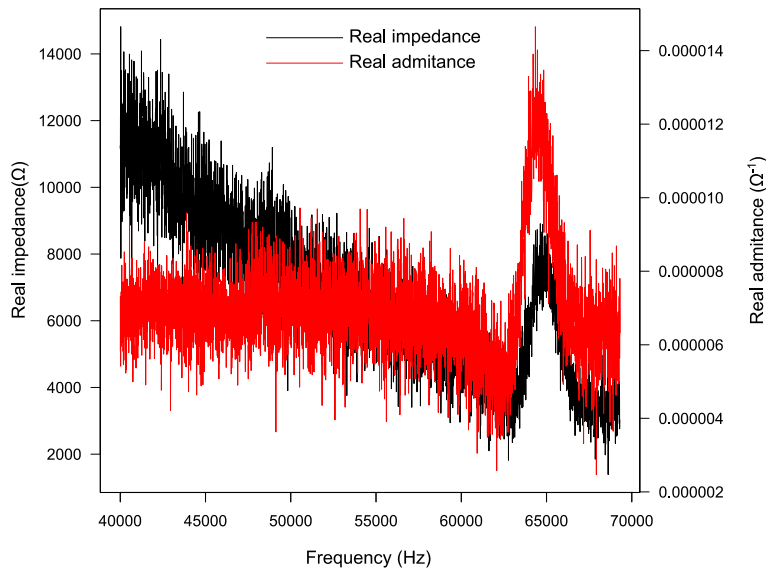


Figure 5.58 Real parts of impedance and admittance of an LRH 70 sample expanded under 5 MPa of pressure, acquired with resonance spectroscopy method.

The frequencies where the real part of the impedance and the admittance ( $f_p$  and  $f_s$ ) maximize are found to be 64.82 kHz and 64.74 kHz respectively (figure 5.58). The thickness coupling factor is calculated to be  $k_t^2=0.003$  (by equation 2.40).

The two coupling coefficients are comparable ( $k_{33}^2=0.0035$  and  $k_t^2=0.003$ ). As discussed before, these coefficients represent the efficiency of the material under small stresses. Still, the results are comparable with the previous data.

## 5.7 Mechanical model

The main objective of this model is to recreate the 3D structure of the Cell-PP samples, using as few as possible parameters, and by replicating the biaxial stretching and GDE procedures. These 3D representations are done to examine the mechanical response of the Cell-PP with different void morphology. As the morphology is obtained by cross sectional images, the main aim is to investigate if these cross sections give a good approximation of the mechanical behavior.

Only two independent parameters are used for the creation of the 3D geometry: the total thickness of the polymer part (including external layers

and excluding air) and the final Inflation in percentage. Everything else is determined by these two parameters. Since the first step is to predict the morphological parameters by simulating the biaxial stretching and the expansion procedure, the model was calibrated based on one sample. The sample chosen was the LRH80 at 5 MPa of inflation. The predictive power of the model was then tested by running it on other films. The obtained cross sections of the real material and the 3D model expanded under 2 MPa and 5 MPa are shown in figure 5.59.

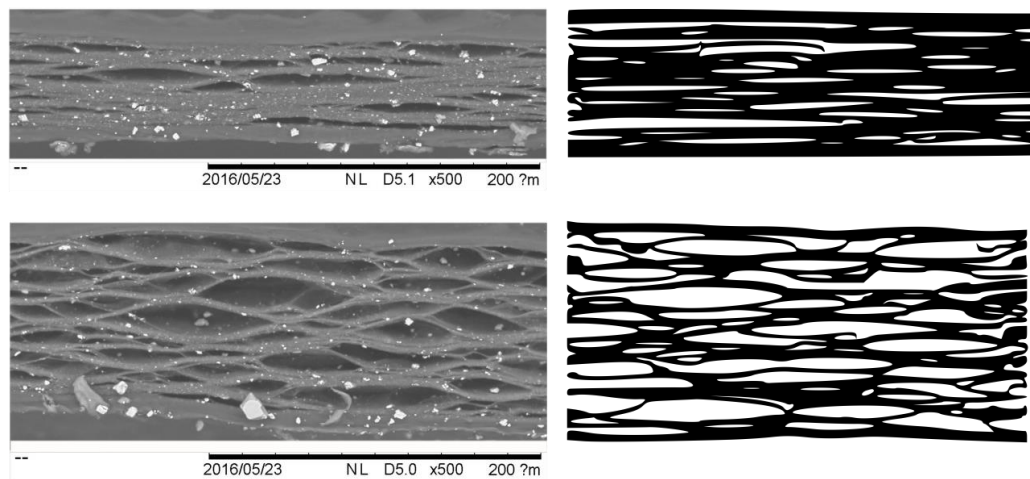


Figure 5.59 Cross sections of real (left) and modelled (right) LRH 60 film inflated at 2 MPa (top) and 5 MPa (bottom) the SEM scale applies to the modeled materials as well.

When a high aspect ratio value combines with a small thickness, as in LRH60 inflated at 2 MPa, the material exhibits a high stiffness as voids with a small thickness may collapse and eventually what is compressed under a certain force is the bulk material. This means that in order to have a compliant material with a weak structure, the void thickness should be as high as in the case of LRH 80 and LRH 70 inflated at 5 MPa. A low aspect ratio value implies a strong material structure with a relatively high stiffness. The stiffness of such materials, like LRH60 and EUH75, with more spherical voids, increases at higher inflations. This is because the average void thickness is increasing under high inflation while the structure of the material remains strong. The model describes accurately the high inflated materials but the modelled films tend to be stiffer than the real material (figure 5.60). A reason for this discrepancy may be the

difference between the distributions of morphological parameters of the 3D voids in the real material and the corresponding distributions imposed in the model, which were observed in 2D cross-sections.

To summarize both the results of the modelled and the real materials, the exponent constant  $b$  values of compressive stress to true strain relationship (section 5.3.1 table 5.3) is plotted in the morphological space of the materials defined by the location parameter  $\theta$  of the void  $D_r$  distribution (x axis) and the location parameter  $\theta$  of the void thickness distribution (y axis) (Figure 5.60). Across the x axis the increased aspect ratio implies a weaker structure of the material (i.e. elongated voids that collapse under moderate stress).

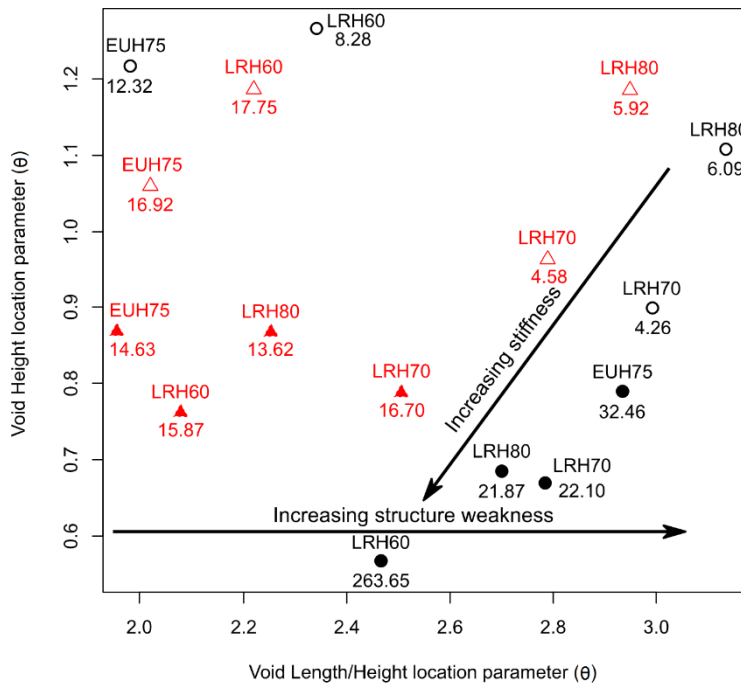


Figure 5.60 Location parameter  $\theta$  of the thickness distribution ( $D_h$ ) against the location parameter  $\theta$  of the aspect ratio distribution ( $D_r$ ). The constant ( $b$ ) of the exponent of the strain to stress relationship is noted below each point. Empirical data in triangles, model results in dots. Solid symbols are 2 MPa inflation and hollow symbols 5MPa inflation.

The FE results showed the weakness of the structure for the highly inflated materials, where the structure differences are more evident (see figure 5.15c, d). However, the model does not predict the difference, in terms of response, for most of the low inflated materials. This behavior is confirmed by experimental data: there are minimal differences among low inflated materials in terms of their morphology (see figure 5.15 a, b) and mechanical response (see figure 5.19).

A 2D cross-section can give valuable information about the material response despite the fact that the porosity of the material can be underestimated (Lopez-Sanchez & Llana-Fúnez, 2015). It is yet to be shown how the true morphology of the sample compares to the cross sections emerging from them. In any case, 2D sections can be safely used for the comparison of sample morphology. Furthermore, 2D cross-sections provide good representations of the material structure, as excellently shown by LRH80 inflated at 5MPa for which the model has been calibrated, and to a lesser extent for the other materials (where the model was extrapolated).

## **5.8 Optimum charging method**

### ***5.8.1 Correlation between independent variables***

Before performing the regression analysis, the correlation between the independent variables ( $E_s$ ,  $\Theta$ ,  $V_c$ ,  $d_{cg}$  and “sample”) is investigated. For this investigation, data are extracted from 64 experiments. Figure 5.61 shows the correlation coefficients for all pairs of variables as well as plots of their relationships.

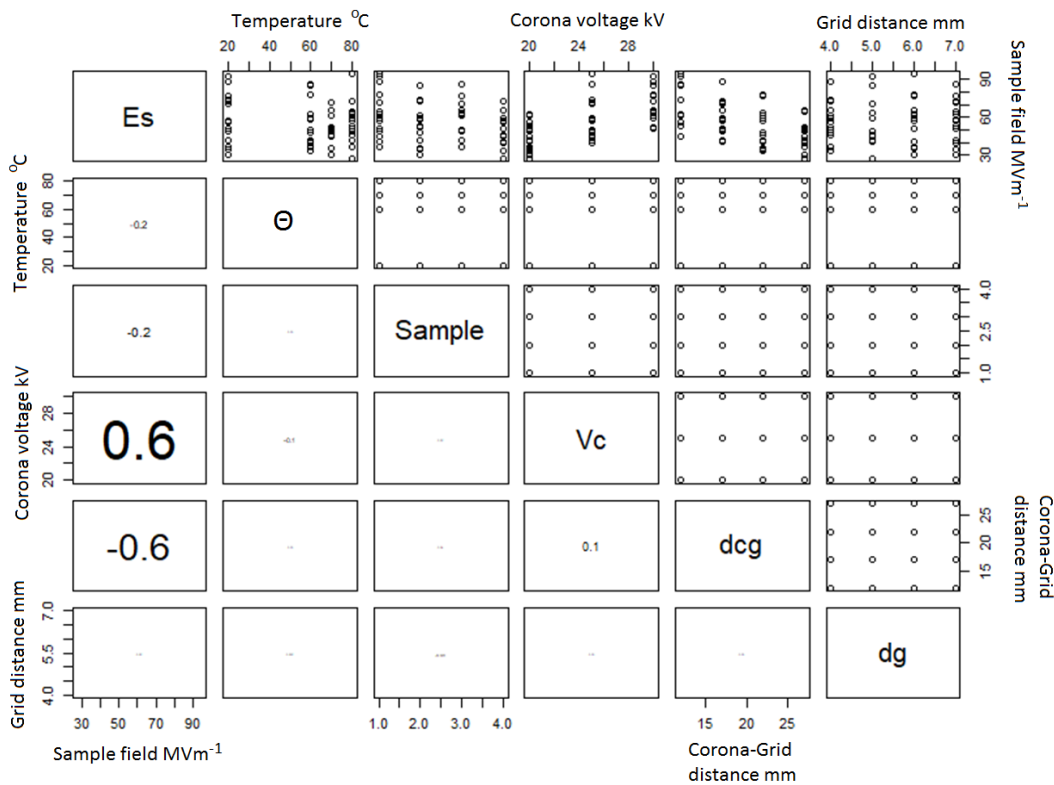


Figure 5.61 Correlation between independent variables (lower left part) and plotted data (upper right part). The font of the values increases with the correlation.

As expected,  $E_s$  correlates with the corona voltage  $V_c$  and the corona to grid distance  $d_{cg}$ . This is because both  $V_c$  and  $d_{cg}$  influence  $V_g$ , which is directly linked to  $E_s$  by equation 4.3. The negative sign in front of the correlation between  $d_{cg}$  and  $E_s$  implies that higher corona to grid distance reduces the sample field. To assess the collinearity between  $E_s$ ,  $V_c$  and  $d_{cg}$ , variance inflation factors were estimated using function `vif()` from R package “car” (Fox *et al.*, 2018), on the basis of which  $V_c$  was excluded from the regression analysis. Although  $E_s$  has a higher `vif()` than  $V_c$ , this was kept.

The crucial output variables studied here, are the  $\Theta_{TSD}$ ,  $Q_s$ ,  $I_{s-peak}$ ,  $\rho_s$  and “ageing”. The generalized linear regression model fitted to the data obtained by the 5 crucial responses, reveals the factors that significantly affect the outputs of the experiments. This information is summarized in table 5.6, where the model, the goodness of fit and the significance of parameters are presented. It is found that  $E_s$  and “sample” are significant predictors for almost all output parameters, except  $I_s$ . Additionally,

temperature is found to be significant predictor of Peak temp and Charges. To assess the relative importance of Temperature for Peak temp and charges, the model fits were repeated for these response variables without including Temperature as a predictor. By comparing the model residuals with and without Temperature, one can estimate the additional variation in the model explained by Temperature. This was done by estimating partial  $R^2$  with function `partial.R2()` of R package `asbio` (Aho, 2017). It is found that Temperature explains 18% of the variation in charges not explained by the other predictors and 42% of the variation in PeakTemp, not explained by the other predictors.

Response variable	model	$R^2$	Factor significance (Pr > Chi)				
			$E_s$	$d_{cg}$	$d_g$	$\Theta$	Sample
TSD peak temperature	$\Theta_{TSD} \sim E_s + \Theta + d_{cg} + d_g + \text{Sample}$	0.75	*			*	*
Maximum charges	$Q_s \sim E_s + \Theta + d_{cg} + d_g + \text{Sample}$	0.86	*			*	*
Log (Charge Density)	$\text{Log}(\rho_s) \sim E_s + \Theta + d_{cg} + d_g + \text{Sample}$	0.69	*				*
Log (Sample current peak)	$\text{Log}(I_{s\text{-Peak}}) \sim E_s + \Theta + d_{cg} + d_g + \text{Sample}$	0.75		*	*		*
Ageing	$\text{Ageing} \sim E_s + \Theta + d_{cg} + d_g + \text{Sample}$	0.75	*				*

Table 5.6 Results of linear regression between output variables and independent input variables. Model, goodness of fit measured by  $R^2$  and significance of independent variables at a 1% level. Rejection of the null hypothesis is designated with an asterisk. Note that  $\Theta$ ,  $V_c$ ,  $d_{cg}$  and “sample” are modelled as factors, while  $E_s$  is treated as a continuous variable.

### 5.8.2 Relationship between $\Theta_{TSD}$ , and $\Theta$

The temperature where the biggest peak occurs within the Thermally Stimulated Discharge (TSD) test is influenced by the “sample”,  $E_s$  and  $\Theta$ , while the distances  $d_g$  and  $d_{cg}$  do not play a significant role to the response. Based on the partial correlation, all of the significant parameters influence positively the highest peak occurrence, with the highest influence observed by  $E_s$  and “sample”.

In order to check the influence of  $\Theta$  to  $\Theta_{TSD}$ , a number of tests were run for the same material (EUH 75) and for different values of  $E_s$  and  $\Theta$ . Four TSD curves corresponding to different poling temperatures are plotted within the same graph (figure 5.62) along with a second TSD test run of one of the samples for comparison. The second TSD test run is expected to have a flat curve, as all charges are expected to have been released during the first run. Since  $E_s$  is a continuous variable, there are not 4 experiments within any of the material families that have the same  $E_s$ . Experiments with dispersed  $E_s$  were selected, in an attempt to cancel the effect of  $E_s$  out.

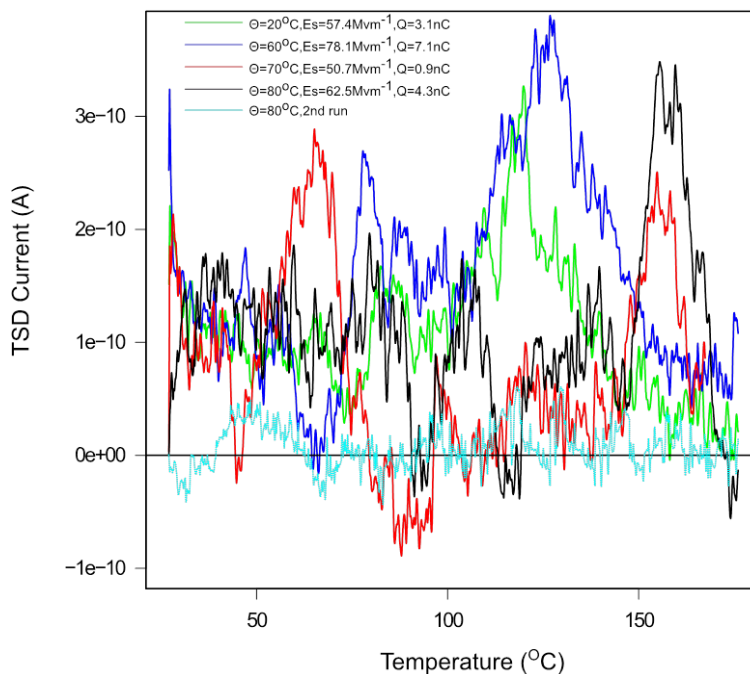


Figure 5.62 TSD curves for EUH 75 samples charged under 20, 60, 70 and 80 °C of temperature. The 80 °C sample was tested again for comparison.

Charging under higher temperatures shifts the TSD current peaks to higher peak temperatures. The highest current peaks for samples charged under 20 °C and 60 °C of temperature occur at 120 °C and 130 °C respectively, while the peaks for the 70 °C and 80 °C occur at 155 °C. This might mean that when the charging procedure is done under higher temperatures the higher mobility of the polymer allows charges to be trapped deeper within the bulk of the material. A second run of the 80 °C charged sample reveal that there are almost no charges that can be released at those temperatures. The ratio of charges obtained within each observed peak over the total amount of charges is presented in table 5.7.

Charge temperature	50 °C - 75 °C	75 °C - 95 °C	100 °C - 140 °C	145 °C - 170 °C	TOTAL
20 °C	0.12	0.11	<b>0.24</b>	0.04	0.24
60 °C	0.05	<b>0.19</b>	<b>0.36</b>	0.06	0.55
70 °C	<b>0.46</b>	0	0.07	<b>0.23</b>	0.69
80 °C	<b>0.22</b>	0.14	0.12	<b>0.25</b>	0.47

Table 5.7 Ratio of observed charges, under observed peaks, over total amount of charges found within the sample

The highest peak contains more than 20 % of the charges, for the materials charged under high temperatures. It is also evident that the 80 °C charged sample loses almost equally its charge density throughout the lower range of temperatures.

Observing the 70 °C charged sample, there is a pronounced peak located at 65 °C. As the specific material is charged under low  $E_s$ , there might be a chance that the dipole mobility due to the moderate applied field was low, leading to charges trapped closer to the surface of the voids. As a result, these surface charges escape the material under lower temperatures during TSD.

The 60 °C sample produced a more pronounced peak (at 130 °C) compared to the 20 °C sample. This might be an outcome of the higher  $E_s$

field applied to it while charging. It is known that the charge density of the material increases with the functionalization field even after the higher back discharges that occur under higher fields. The remaining charge density of the material, after ageing, can be found by integration of the TSD current curve (figure 5.63).

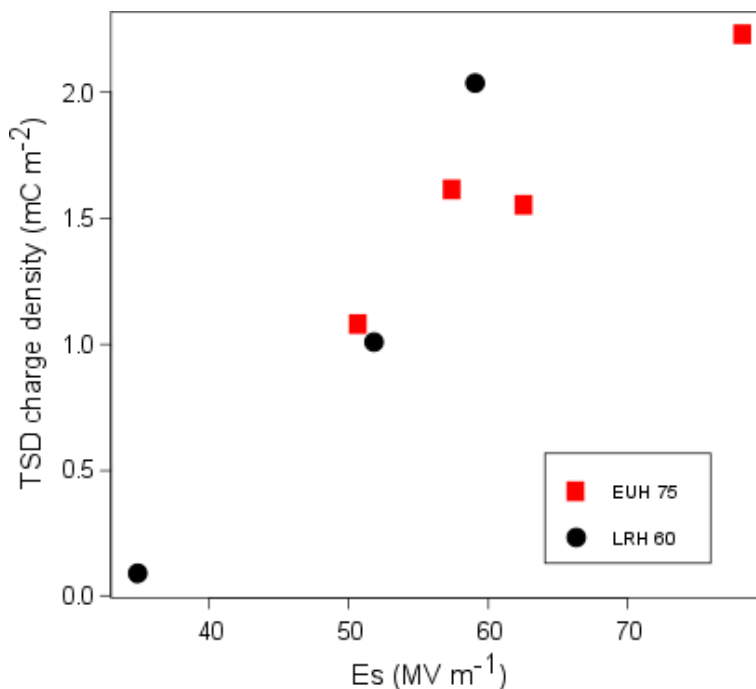


Figure 5.63 Charge density found by integration of the TSD curve over charging field  $E_s$ .

As expected, the remaining charge density within the material obtained by TSD after ageing is proportional to the functionalization field. As a summary, the charging field  $E_s$  is correlated to the final remaining charges within the material after ageing and to an extent, how deep in the material the charges will be trapped. There are no other obvious correlations revealed by the analysis.

### 5.8.3 Piezoelectric response

The piezoelectric response of the charged samples is defined by two parameters: the highest piezoelectric activity ( $d_{33\text{-Peak}}$ ) and the produced charges under 130 kPa of stress ( $Q_s$ ). The analysis showed that  $E_s$  and “sample” are significant determinants of both parameters, while the factor  $\Theta$  is significant only for the obtained charges  $Q_s$ . Again the two distances

$d_c$  and  $d_{cg}$  do not significantly influence the parameters. The relation between the square root of the maximum charges  $Q_s$  produced by the 4 different materials under a static load of 130 kPa, over the applied field  $E_s$  is given in figure 5.64.

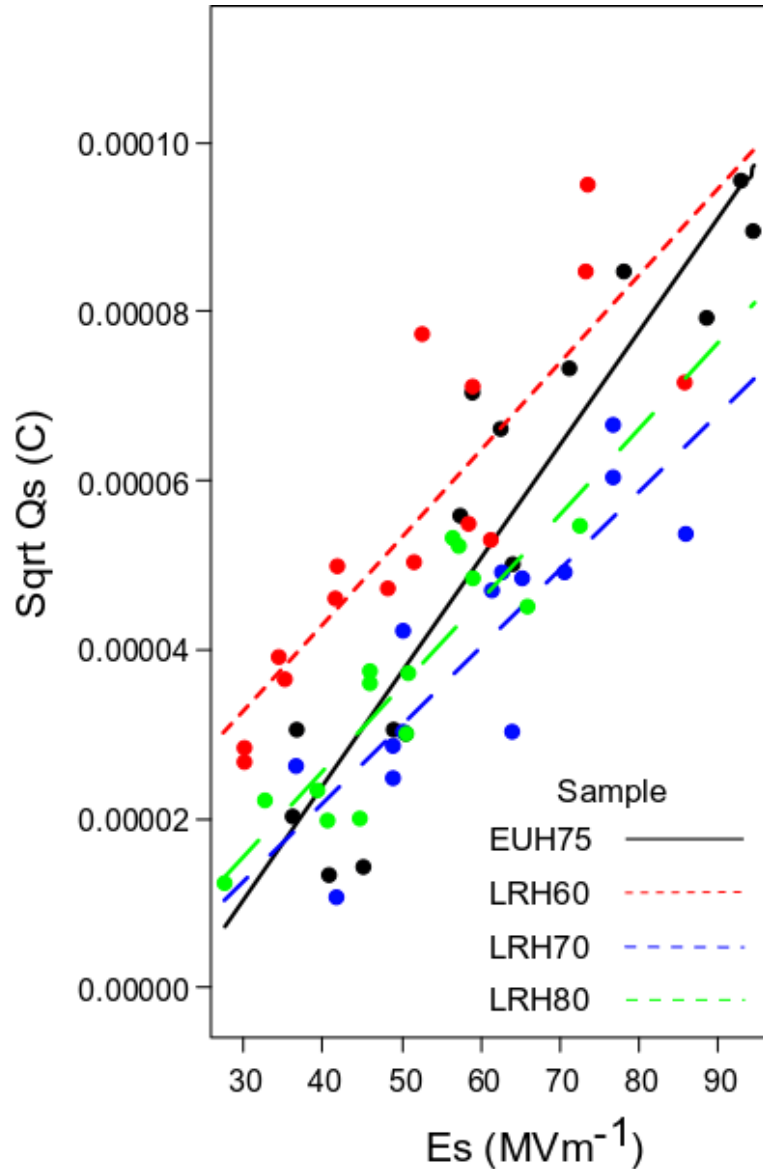


Figure 5.64 Root square of maximum charges  $Q_s$  produced by compression of the sample under 130 kPa, over the applied charging field to the film  $E_s$ . Lines represent a linear fit to the data.

It is observed that the square root of the charges grows linearly with  $E_s$ . EUH 75 gains charges more quickly than the rest of the materials over  $E_s$ . On the other hand, materials within the same family show similar charge increment over  $E_s$  with a different offset. LRH 60 shows the highest piezoelectric response among the rest of the materials of the LRH family.

This means that LRH 60 gained charge density earlier compared to the rest of the materials.

The type of the material also defines at what stress the  $d_{33}$ -Peak occurs. As discussed in section 5.4, the stiffness of the material influences the shape of the piezoelectric response. Figure 5.65 shows the obtained  $d_{33}$ -Peak over the charging field  $E_s$  for all materials. It should be mentioned here that the  $d_{33}$ -Peak was measured under 130 kPa.

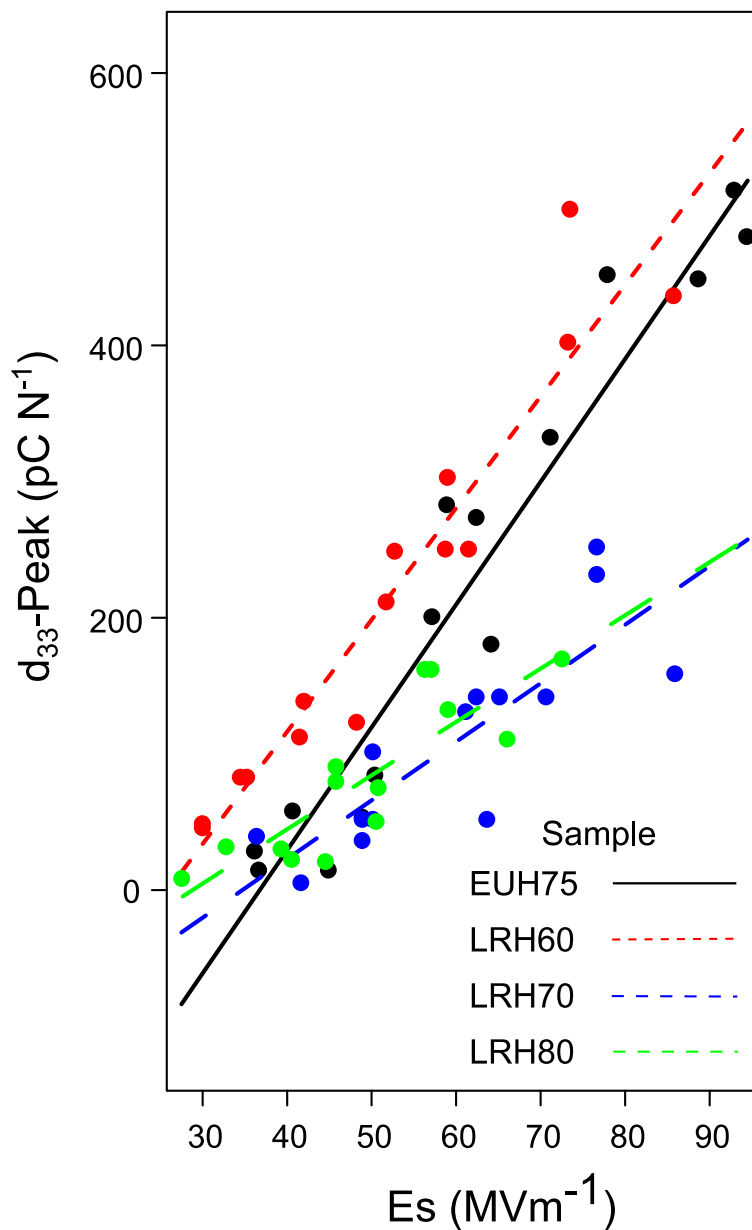


Figure 5.65 Peak  $d_{33}$  produced by compression of the materials over the charging field of the film  $E_s$ . Lines represent the linear fit to the data.

The stiffer materials EUH 75 and LRH 60, show steeper  $d_{33\text{-Peak}}$  response compared to the rest of the materials. As expected, LRH 60 shows a higher initial value for low  $E_s$ , as there is correlation between  $d_{33\text{-Peak}}$  and  $Q_s$ . Based on figure 5.28 the materials of the LRH family, have a smoother  $d_{33}$  response without showing a well-established peak. This means that the charges released are distributed over the stress. By contrast, the peak of EUH 75 is more profound, resulting in higher  $d_{33\text{-Peak}}$  values. This higher response is reflected also in figure 5.65.

Based on the literature, the final obtained charge density within each void is directly linked to the externally applied field (Mellinger, 2011). The void charge density increases linearly from the point where the externally applied field  $E_s$  is higher than the critical field  $E_b$  of the void. As a result, the critical field of the thickest void found within the film, designates the critical field under which the film gains its initial charges (Mellinger, 2011). For example, LRH 60 gained piezoelectric properties under lower  $E_s$  (lower charging field) compared to the rest of the materials. This can be seen in figure 5.65 and is the field where the fitted data cross the X axis. Similar critical values can be obtained by extrapolating the  $Q_s$  curves (see figure 5.64) towards the lower fields, revealing the critical field under which each material gained its first charges. The resultant critical fields obtained by the two figures are presented in table 5.8. On the basis of the morphology analysis done in section 5.2.2, the thickest voids found within each material are also presented in table 5.8, along with their relative abundance and the critical field based on Paschen's law, under atmospheric pressure.

It is inferred that  $d_{33\text{-Peak}}$  overall defines better the critical field of the film compared to the  $Q_s$ , especially for EUH 75. The experimentally found critical field of the film is in agreement with the theoretical critical value of the thicker voids existing within the films, despite the low relative population of the latter within each film.

Material	Thickest void ( $\mu\text{m}$ )	Relative popul. (%)	Theoretical $E_b$ ( $\text{MV m}^{-1}$ )	Extrapol. $d_{33}\text{-Peak}$ ( $\text{MV m}^{-1}$ )	Extrapol. $Q_s$ ( $\text{MV m}^{-1}$ )
LRH 60	33.5	0.3	28	26	30
LRH 70	19.9	0.6	40	35	38
LRH 80	30	0.3	30	29	29
EUH 75	21	0.8	39	37	50

Table 5.8 Thickest void within each material, its relative population as well as theoretical and obtained critical fields.

Apart from the differences among materials, another parameter for consideration is the coefficients of Paschen's law, which reduces with higher temperature. As a result, the critical field  $E_b$  of each sample is decreased. Figure 5.66 shows the estimated minimum critical field needed to charge the films under 23 °C and 80 °C. The optimized Paschen coefficients were taken from (Mellinger, 2011) as they tend to describe better the critical field for each void, within the film.

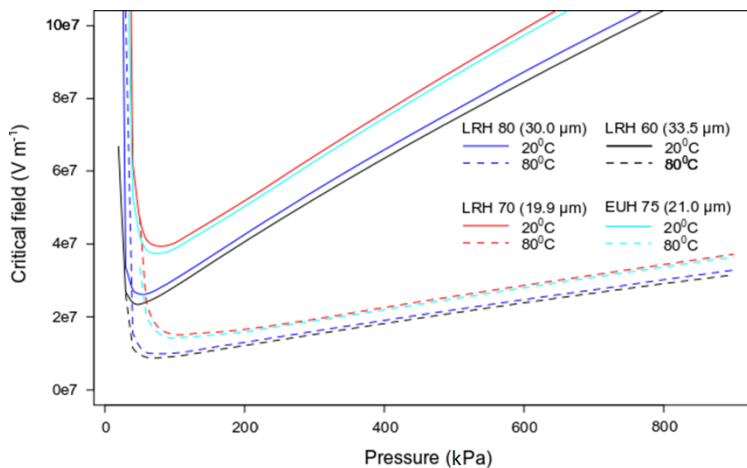


Figure 5.66 Theoretical critical field  $E_b$  over atmospheric pressure for the thickest voids found within each material. Paschen curves created with the optimized coefficients  $A=500 \text{ V m}^{-1}\text{Pa}^{-1}$  and  $C=8 \text{ m}^{-1} \text{Pa}^{-1}$  and  $A=125 \text{ V m}^{-1}\text{Pa}^{-1}$  and  $C=8 \text{ m}^{-1} \text{Pa}^{-1}$ .

Materials with thicker voids (LRH 60 and LRH 80) require lower fields for gaining piezoelectricity compared to materials with thinner voids (LRH 70 and EUH 75). What is also inferred from figure 5.66 is that there is a

specific pressure under which the critical field is the lowest for the curves obtained at 23 °C. On the other hand, under elevated temperature (80 °C), there is a broad region of pressures that minimize the critical charging field.

To investigate the contribution of temperature  $\Theta$  to  $Q_s$ , the  $Q_s$  response is plotted over  $E_s$  for every material and temperature. The data are fitted with a linear regression, as the response is still expected to be linear. As the number of experimental points is small, some of the fits are not good enough. The goodness of fit is presented in terms of  $R^2$ . The first order polynomial is solved, and the root represents the critical field of the film. Table 5.9 presents the experimental and theoretical critical fields.

Material	$\Theta=20$	$R^2$	$\Theta=60$	$R^2$	$\Theta=70$	$R^2$	$\Theta=80$	$R^2$
LRH 60	29.6	1	31.5	0.98	24.9	0.99	19.7	1
LRH 70	40.5	0.89	-17.7	0.87	39.7	0.98	9.9	0.28
LRH 80	21.9	0.58	30.5	0.88	29.1	0.62	27.4	0.71
EUH 75	33.3	1	35.8	1	44.2	0.998	25.9	0.80

Table 5.9 Critical fields found experimentally by extrapolation of  $d_{33}$ -Peak (see figure 5.65) and  $R^2$  of the fit, for all materials charged under different temperatures.

It can be concluded here that charging under higher temperatures decreases the critical field of the film, allowing for the materials to gain their initial charge density by lower fields. However, no significant increment is observed to the final piezoelectric activity due to the temperature  $\Theta$ . This might be a result of higher back discharges occurring by the end of the charging procedure, bringing that way down the effective charge density to comparable levels to materials charged under room temperatures.

#### **5.8.4 Sample current, charge density ( $I_s$ -Peak, $\rho_s$ )**

From table 5.6, it appears that the peak current flowing through the sample once the output of the high voltage power supply is enabled, is

influenced by the two distances  $d_g$  and  $d_{cg}$ . The current peak  $I_{s\text{-peak}}$  shows how quickly the potential of the sample will reach the potential of the grid and thus how quickly the charging process will finish. Figure 5.67 shows the relation between  $I_{s\text{-Peak}}$  (in log scale) and the two distances.

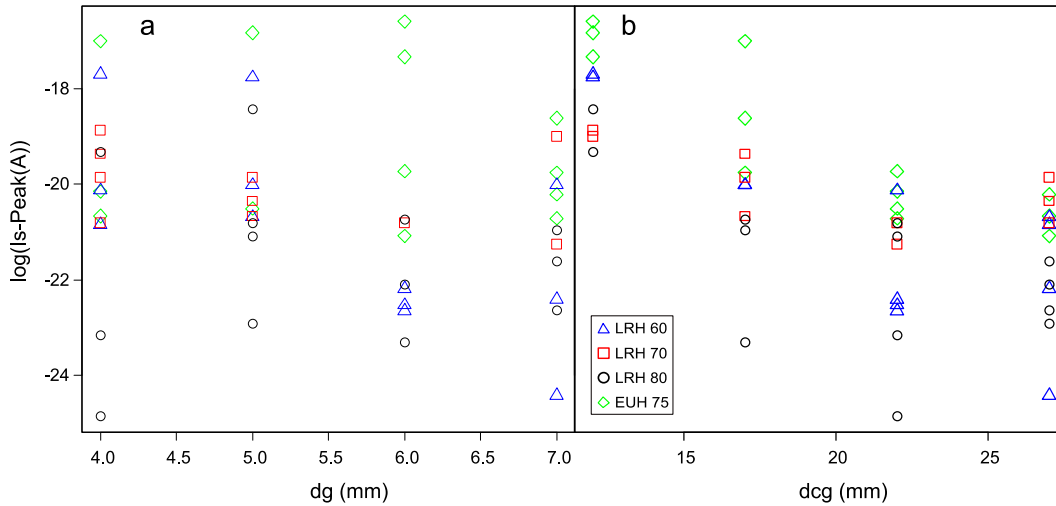


Figure 5.67 Maximum current flow through the sample  $I_{s\text{-Peak}}$  in log scale, over distance a)  $d_g$  and b)  $d_{cg}$ .

As expected, the maximum current  $I_{s\text{-Peak}}$  is higher the lower the distances of  $d_{cg}$  and  $d_g$ . LRH 80 and LRH 60 show a higher dispersion of values. It seems that  $I_{s\text{-Peak}}$  for thicker materials is not influenced only by the distances. As a result, the charging time does not change significantly with the distances.

The obtained charge density can be found by integration of the current  $I_s$  flowing through the sample  $I_s$ . Figure 5.68 shows the influence of  $E_s$  on the measured charge density after charging.

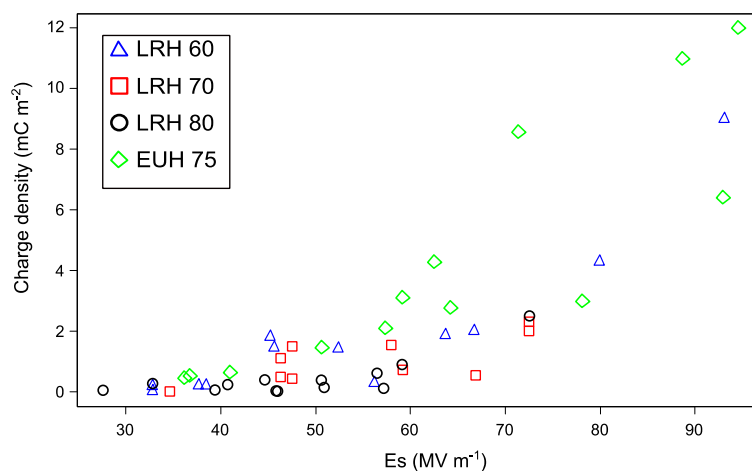


Figure 5.68 Obtained charge density over  $E_s$  measured by integration of the current flowing through the sample  $I_s$ .

EUH 75 shows higher charge density over field  $E_s$  obtained by the end of the charging procedure. It should be noted that some of the points are not presented as the charge density could not be calculated correctly. This is a result of sudden increase of current observed during charging.

The highest observed value of charge density is close to  $12 \text{ mC m}^{-2}$ . This is due to back discharges occurring within the film when the application of the charging field is over. These back discharges are able to bring the effective charge density of the film down to 25% of its initial value. This high reduction can be observed in figure 5.68 and figure 5.63, where the final charge density obtained after TSD is in order of a few  $\text{mC m}^{-2}$ .

### 5.8.5 Film ageing

Film ageing is observed on the first days after the functionalization. This can be attributed to the re-combination of the charges that were not embedded deep within the bulk of the polymer. Further evidence of the charge recombination is seen when the material is compressed under high mechanical pressure for the first time after the functionalization (see figure 5.43). Ageing of films is higher for materials charged under higher fields (see figure 5.40). For the previous experiments in section 5.3.2, higher  $E_s$  fields were obtained with smaller distance between the corona tip and the grid ( $d_{cg}$ ). Within the design of experiments, the charging field was controlled by different  $d_g$ ,  $d_{cg}$  and  $V_c$  values. From the analysis it appears

that ageing of the film is influenced by  $E_s$  and material. Despite these correlations, plotting the ageing percentage over  $E_s$  for different materials, revealed a large deviation. Furthermore, a closer look at the residuals of the model over the ageing, reveal that they follow an increase toward higher values of ageing. This might mean that the model cannot describe the ageing process fully with the given factors. Further analysis including  $V_c$  as a factor, reveals a better model for ageing. Comparison between the initial obtained charges and the charges obtained after 17 days revealed the equilibrium ageing of the films. The ageing of the films is presented in form of box plots in figure 5.69.

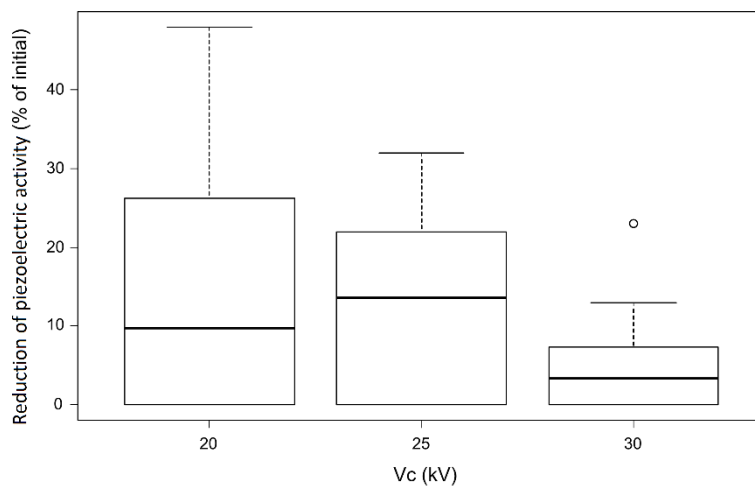


Figure 5.69 Ageing of films charged under a corona potential of  $V_c=20$  kV, 25 kV and 30 kV.

As it can be deduced from figure 5.69, films charged under high  $V_c$  showed lower reduction of charges  $Q_s$  after the equilibrium period of 17 days irrespective of the distances  $d_{cg}$  and  $d_g$ . It should be noted here that the average charging fields are almost the same regardless of the corona potential  $V_c$ .

### 5.8.6 Constant current charging

The constant current method is used to test the effect of different current rates during charging, to the final piezoelectric activity. The current  $I_s$  is logged from the moment the device is switched on, until the end of the charging procedure. Figure 5.70 shows the logged current  $I_s$ .

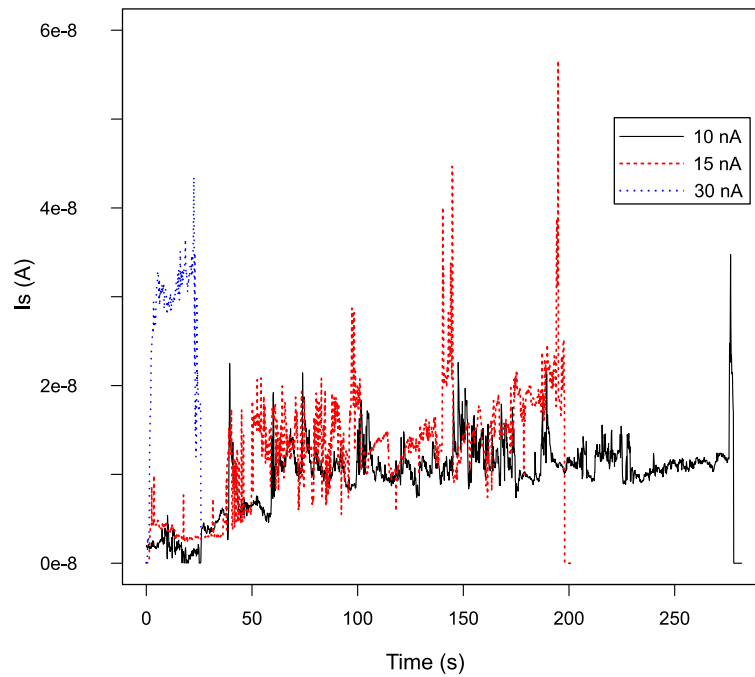


Figure 5.70 Current  $I_s$  over time for current rated of 10 nA 15 nA and 30 nA.

The end of the charging process is designated with the spontaneous rise of  $I_s$  at which point the corona device is manually switched off. The rapid increment in current is attributed to the material's dielectric strength being reached.

The materials are tested for their piezoelectric activity after 17 days to account for film ageing (figure 5.71).

It is inferred that the poling can be done under higher charging fields when the current is low. This is a result of lower potential difference between the sample surface and the grid. That way, the dielectric strength of the air gap as well as the material is harder to be breached.

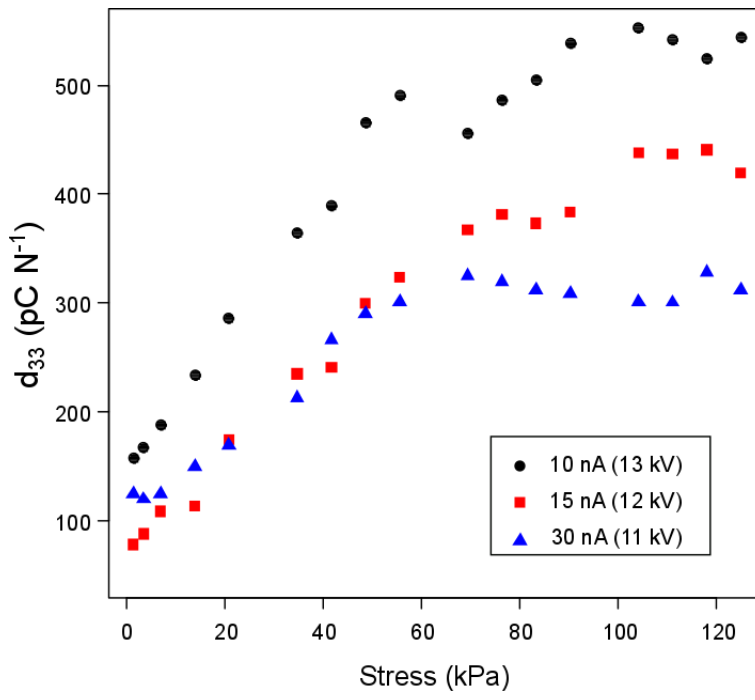


Figure 5.71 Piezoelectric coefficient  $d_{33}$  of three EUH 75 samples charged under different constant current values. The final  $V_g$  obtained before switch off is shown in brackets.

## Chapter 6. Conclusion

This work explored the potential of Cellular Polypropylene (Cell-PP) films, a flexible, cheap to produce piezoelectric harvester. The aim was to enhance the piezoelectric properties of the material with focus on low frequency energy harvesting, exploited in wearable energy applications. The main objective is to increase the electromechanical coupling coefficient  $k^2_{33}$  of the material.

Four different Cell-PP films were expanded with Gas Diffusion Expansion method (GDE) which by changing the relative density and stiffness of the materials, eventually affects their piezoelectric performance. A universal method of defining the stiffness within the non-linear region of operation is presented since, unlike in other studies, the materials used are not comparable solely on the basis of their relative densities but a more detailed description of their morphology is required. The main morphological features of the film are described by a two-parametric distribution of the voids aspect ratio ( $Dr$ ). It is shown that the median of  $Dr$  correlates significantly with the corresponding mechanical response as estimated from the slope of the stress-strain curve. This emphasizes the key role of void morphology for the mechanical response of Cell-PP within the non-linear region of operation and suggests that a 2D cross-section of the material provides valuable information for the mechanical response, despite the possible underestimation of porosity.

This was accurately shown by LRH 80 inflated at 5 MPa for which the finite element model was calibrated, and to a lesser extent for the other materials to which the model was applied. It is also proven that compressing the material has the inverse impact of GDE on both the mechanical and electrical properties of the film.

The influence of charging parameters to the electrical and mechanical response as well as the thermal stability of the film was studied, poling the Cell-PP with a negative corona triode. For the thinnest (105  $\mu\text{m}$ ) film the highest field attained by the contact charging was 77  $\text{MV m}^{-1}$ , compared to 106  $\text{MV m}^{-1}$  which can be easily applied with corona charging. This 28%

increment in corona charging field increased the final piezoelectric response, by 20% on average.

For expanded films having thick voids of 30  $\mu\text{m}$  the required minimum poling field (critical field  $E_b$ ), for the material to be rendered piezoelectric, is about 30  $\text{MV m}^{-1}$ . Still, the majority of the voids within the film have higher  $E_b$  as they are thinner, gaining no charge density by the end of the poling process.

Decrement of the critical field can be obtained by charging under elevated temperatures, but the final effective charge density does not increase. The optimum charging temperatures were between 70  $^{\circ}\text{C}$  and 80  $^{\circ}\text{C}$  which help the charges to be trapped deeper within the bulk of the material.

After a charge decay period of 17 days, at room temperature, the piezoelectric performance is reduced to 74% in the worst-case scenario, of that measured just after charging. This reduction is greater for higher charging fields as well as high film thickness. It is shown that by charging under high corona voltage ( $V_c$ ) under comparable charging fields  $E_s$  or by a constant current technique with a low sample current  $I_s$ , this reduction is significantly less.

A simple, quick way of placing electrodes on functionalized Cell-PP samples is presented. Silver paint electrodes are applied in room temperature so that thickness reduction due to high temperatures is avoided. Insertion of two media between the electrodes and the measuring equipment prevented the reduction of the charges picked up by the measuring device. In the absence of contact media the charges being picked up are 65% less.

The highest piezoelectric response, at room temperature poling, was achieved for the 105  $\mu\text{m}$  thick EUH 75 film expanded under 5 MPa pressure. Charged under a field of 109.5  $\text{MV m}^{-1}$ , this material attained a piezoelectric coefficient of 900  $\text{pC N}^{-1}$  which was reduced after ageing to 750  $\text{pC N}^{-1}$ . This response was obtained by compression within the non-linear region of the film.

Extra care is needed when using excessive compressive stress on the material, as the piezoelectric response was found to be reduced by 46% of

the initial response after charging, in the worst-case scenario. This reduction however, appears under high compressive stress typically outside of the optimal region of operation for each film.

Up to date, there is limited work done on the non-linearity of the mechanical and piezoelectric response of the Cell-PP. As flexibility is a key property for human based EH, emphasis was given on the non-linear region of response occurring when the material is operated under high strain. It is strongly supported by the experimental work, that there is an optimum region of strain where the efficiency of the material and  $k^2_{33}$  is maximized. In this optimal range, there is a threefold increase in efficiency in comparison to the efficiency obtained outside it. This increment is mostly due to the contribution of the lower input power. With the correct static stress, an increment of 3 times in  $k^2_{33}$  reaching a value of  $k^2_{33}=0.0158$ , was achieved when harvesting under strains of 0.12 compared to lower strains. However, a 30% decrement of the output electrical power is observed when harvesting outside the optimal region of strain. A peak power  $W_{out}= 5.2 \text{ mW m}^{-2}$ , corresponding to  $49 \text{ W m}^{-3}$ , was harvested under a peak stress of 208 kPa and a frequency of 1 Hz. This is obtained under the “safe range” of stress that does not induce further depolarization and under low input frequency.

Under static input, the piezoelectric parameters can be expressed either as a function of the applied static stress or the final strain (total strain after creep). On the contrary, during quasi static and dynamic input, there is creep / stress relaxation and the time dimension of the response must be considered. Hence, comparison of values of the direct and inverse piezoelectric coefficients, within the non- linear region, can only be achieved when the film is tested under similar strain conditions. As shown in this study, the produced charges correlate to the strain rather than the stress, making the strain a better quantity for defining the piezoelectric activity of Cell-PP.

Cell-PP can produce high energy density, when it comes to applications that involve high mechanical flexibility. Functionalized Cell-PP exhibits non-linear increase of generated charges in response to stress (strong charge non-linearities). So, for any given application it is important to

consider and optimize the operational region of stress and the best expansion procedure. For different applications, either sensors or actuators, differently prepared films in terms of available surface area, strain levels, stress amplitude and stress rate, are suitable. The piezoelectric coefficient  $d_{33}$  and the stiffness  $c_{33}$  doubles within the static non-linear region. Thus, it is beneficial for the Energy Harvester that requires high piezoelectric coefficient ( $d_{33}$ ) and stiffness ( $c_{33}$ ) to operate at that region. The permittivity  $\kappa$  of the Cell-PP also exhibits a non-linear response and needs to be measured throughout the compression.

Further work is needed to show how the true morphology of the sample can be reconstructed from its cross sections. A way of finding out the exact morphology of the film could be by 3D recreation of the material via means of microtome SEM. A drafting program could stack the 2D cross sections, so that the 3D image is recreated. Still, 2D sections can be safely used for the comparison of the morphology of different samples and provide good representations of the material structure.

It is shown that stiffness is a key parameter for energy conversion, returning higher electromechanical coupling coefficient. Highly expanded materials have high stiffness, but it is still not known how they behave within their non-linear region. It is yet to be shown if high expansions can provide more efficient energy conversion by compressing them to the optimal region.

The increased piezoelectric response of the material can be triggered with the GDE procedure. The GDE procedure, however, cannot be easily implemented during manufacturing of the material (roll to roll basis) leading to an extra cost, as this procedure has to be done separately. To overcome this problem, cheap polymer materials can be created by 3D printing. That way, the thickness of the voids can be controlled leading to optimization of the mechanical and electrical properties by selecting the type of the resin and the shape of the voids.

## REFERENCES

- A.H. Meitzler, A. W. Warner, H. F. Tiersten & D. Berlincourt (1987) An American National Standard IEEE Standard on Piezoelectricity. *ANSI/IEEE Std 176-1987*. [Online] (Std 176-1987), 74. Available from: doi:10.1109/T-SU.1984.31464.
- Aho, K. (2017) *asbio: A Collection of Statistical Tools for Biologists*. [Online]. Available from: <https://CRAN.R-project.org/package=asbio> [Accessed: 25 April 2018].
- Altafim, R.A.C., Altafim, R.A.P., Basso, H.C., Qiu, X., et al. (2009a) *Dielectric barrier discharges in multi-layer polymer ferroelectrets*. In: [Online]. August 2009 IEEE. pp. 142–145. Available from: doi:10.1109/CEIDP.2009.5377827 [Accessed: 4 April 2018].
- Altafim, R.A.P., Basso, H.C., Altafim, R.A.C., Wirges, W., et al. (2010) *Dielectric resonance spectroscopy of piezoelectrets with tubular channels: Channel dimensions control resonances*. In: [Online]. July 2010 IEEE. pp. 1–4. Available from: doi:10.1109/ICSD.2010.5568034 [Accessed: 4 April 2018].
- Altafim, R.A.P., Qiu, X., Wirges, W., Gerhard, R., et al. (2009b) Template-based fluoroethylenepropylene piezoelectrets with tubular channels for transducer applications. *Journal of Applied Physics*. [Online] 106 (1), 014106. Available from: doi:10.1063/1.3159039.
- An, Z., Zhao, M., Yao, J., Zhang, Y., et al. (2009) Improved piezoelectric properties of cellular polypropylene ferroelectrets by chemical modification. *Applied Physics A*. [Online] 95 (3), 801–806. Available from: doi:10.1007/s00339-009-5074-9.
- Anton, S., Farinholt, K. & Erturk, A. (2014) Piezoelectret foam–based vibration energy harvesting. *Journal of Intelligent Material Systems and Structures*. [Online] 25 (14), 1681–1692. Available from: doi:10.1177/1045389X14541501.
- Arlt, G., Hennings, D. & de With, G. (1985) Dielectric properties of fine-grained barium titanate ceramics. *Journal of Applied Physics*. [Online] 58 (4), 1619–1625. Available from: doi:10.1063/1.336051.
- Bechmann, R. (1956) Elastic, Piezoelectric, and Dielectric Constants of Polarized Barium Titanate Ceramics and Some Applications of the Piezoelectric Equations. *The Journal of the Acoustical Society of America*. [Online] 28 (3), 347–350. Available from: doi:10.1121/1.1908324.
- Belhora, F., Cottinet, P.-J., Guyomar, D., Petit, L., et al. (2013) Optimization of energy harvesting conversion using the hybridization of electrostrictive polymers and electrets. *Sensors and Actuators A: Physical*. [Online] 189, 390–398. Available from: doi:10.1016/j.sna.2012.10.032.
- Bouteffaha, A., Bendaoud, A., Tilmatine, A., Medles, K., et al. (2013) *Experimental and Numerical Characterization of Corona Discharge Generated by a Triode Electrode System*. 6.
- Braña, G.O., Segovia, P.L., Magraner, F. & Quijano, A. (2011) Influence of corona charging in cellular polyethylene film. *Journal of Physics: Conference Series*. [Online] 301, 012054. Available from: doi:10.1088/1742-6596/301/1/012054.

- Campos, J.S.C., Giacometti, J.A. & Oliveira, O.N. (1992) *Electrical characteristics of point to plate corona systems with a biased cylinder*. In: [Online]. 1992 IEEE. pp. 421–426. Available from: doi:10.1109/CEIDP.1992.283215 [Accessed: 4 April 2018].
- Cao, H., Schmidt, V.H., Zhang, R., Cao, W., et al. (2004) Elastic, piezoelectric, and dielectric properties of 0.58Pb(Mg<sub>1/3</sub>Nb<sub>2/3</sub>)O<sub>3</sub>-0.42PbTiO<sub>3</sub> single crystal. *Journal of Applied Physics*. [Online] 96 (1), 549–554. Available from: doi:10.1063/1.1712020.
- Chang, W.-Y., Chung, C.-C., Yuan, Z., Chang, C.-H., et al. (2018) Patterned nano-domains in PMN-PT single crystals. *Acta Materialia*. [Online] 143, 166–173. Available from: doi:10.1016/j.actamat.2017.10.016.
- Chao-Nan Xu, Akiyama, M., Nonaka, K. & Watanabe, T. (1998) Electrical power generation characteristics of PZT piezoelectric ceramics. *IEEE Transactions on Ultrasonics, Ferroelectrics and Frequency Control*. [Online] 45 (4), 1065–1070. Available from: doi:10.1109/58.710589.
- Cho, J., Anderson, M., Richards, R., Bahr, D., et al. (2005) Optimization of electromechanical coupling for a thin-film PZT membrane: I. Modeling. *Journal of Micromechanics and Microengineering*. [Online] 15 (10), 1797–1803. Available from: doi:10.1088/0960-1317/15/10/002.
- Choi, C.-H., Seo, I.-T., Song, D., Jang, M.-S., et al. (2013) Relation between piezoelectric properties of ceramics and output power density of energy harvester. *Journal of the European Ceramic Society*. [Online] 33 (7), 1343–1347. Available from: doi:10.1016/j.jeurceramsoc.2012.12.011.
- Cornogolub, A., Cottinet, P.-J. & Petit, L. (2016) Hybrid energy harvesting systems, using piezoelectric elements and dielectric polymers. *Smart Materials and Structures*. [Online] 25 (9), 095048. Available from: doi:10.1088/0964-1726/25/9/095048.
- Cronin, D.S. & Ouellet, S. (2016) Low density polyethylene, expanded polystyrene and expanded polypropylene: Strain rate and size effects on mechanical properties. *Polymer Testing*. [Online] 53, 40–50. Available from: doi:10.1016/j.polymertesting.2016.04.018.
- Cury Basso, H., Monteiro, J.R.B. de A., Baladelli Mazulquim, D., Teixeira de Paula, G., et al. (2013) Alternating current-generated plasma discharges for the controlled direct current charging of ferroelectrets. *Journal of Applied Physics*. [Online] 114 (10), 104101. Available from: doi:10.1063/1.4821113.
- Daosheng Pan, Zhang, X., Xuwen Wang, Gongxun Cao, et al. (2009) *Piezoelectricity of cross-linked polypropylene films treated by hot-stretching*. In: [Online]. July 2009 IEEE. pp. 1166–1169. Available from: doi:10.1109/ICPADM.2009.5252281 [Accessed: 4 April 2018].
- De Cicco, G., Morten, B., Dalmonago, D. & Prudenziati, M. (1999) Pyroelectricity of PZT-based thick-films. *Sensors and Actuators A: Physical*. [Online] 76 (1–3), 409–415. Available from: doi:10.1016/S0924-4247(99)00056-4.
- Delignette-Muller, M.-L., Dutang, C., Pouillot, R., Denis, J.-B., et al. (2017) *fitdistrplus: Help to Fit of a Parametric Distribution to Non-Censored or Censored Data*.

[Online]. Available from: <https://CRAN.R-project.org/package=fitdistrplus>  
[Accessed: 26 April 2018].

- Deng, X. & Adamiak, K. (1997) *The Electric Corona Discharge in the Triode System*. 6.
- Dias, C.J., Marat-Mendes, J.N. & Giacometti, J.A. (1989) Effects of a corona discharge on the charge stability of Teflon FEP negative electrets. *Journal of Physics D: Applied Physics*. [Online] 22 (5), 663–669. Available from: doi:10.1088/0022-3727/22/5/014.
- Dreyfus, G. & Lewiner, J. (1976) Free energy of electrets. *Physical Review B*. [Online] 14 (12), 5451–5457. Available from: doi:10.1103/PhysRevB.14.5451.
- Eddiai, A., Meddad, M., Guyomar, D., Hajjaji, A., et al. (2012) Enhancement of electrostrictive polymer efficiency for energy harvesting with cellular polypropylene electrets. *Synthetic Metals*. [Online] 162 (21–22), 1948–1953. Available from: doi:10.1016/j.synthmet.2012.08.012.
- Edwards, M.E., Batra, A.K., Chilvery, A.K., Guggilla, P., et al. (2012) Pyroelectric Properties of PVDF:MWCNT Nanocomposite Film for Uncooled Infrared Detectors. *Materials Sciences and Applications*. [Online] 03 (12), 851–855. Available from: doi:10.4236/msa.2012.312124.
- Esterly, D.M. (2002) *Manufacturing of Poly(vinylidene fluoride) and Evaluation of its Mechanical Properties*. 71.
- Fang, H., Li, Q., Yang, Z., Luo, N., et al. (2015) Effects of pre-polarization on the dielectric and piezoelectric properties of 0–3 type PIN–PMN–PT/PVDF composites. *Journal of Materials Science: Materials in Electronics*. [Online] 26 (9), 6427–6433. Available from: doi:10.1007/s10854-015-3232-8.
- Featherstone, R. & Teh, Y.H. (2006) Improving the Speed of Shape Memory Alloy Actuators by Faster Electrical Heating. In: Marcelo H. Ang & Oussama Khatib (eds.). *Experimental Robotics IX*. [Online]. Berlin, Heidelberg, Springer Berlin Heidelberg. pp. 67–76. Available from: doi:10.1007/11552246\_7 [Accessed: 4 April 2018].
- Feng, Y., Hagiwara, K., Iguchi, Y. & Suzuki, Y. (2012) Trench-filled cellular parylene electret for piezoelectric transducer. *Applied Physics Letters*. [Online] 100 (26), 262901. Available from: doi:10.1063/1.4730952.
- Feng, Y. & Suzuki, Y. (2013) *All-polymer soft-X-ray-charged piezoelectret with embedded PEDOT electrode*. In: [Online]. January 2013 IEEE. pp. 865–868. Available from: doi:10.1109/MEMSYS.2013.6474380 [Accessed: 4 April 2018].
- Fox, J., Weisberg, S., Price, B., Adler, D., et al. (2018) *car: Companion to Applied Regression*. [Online]. Available from: <https://CRAN.R-project.org/package=car> [Accessed: 25 April 2018].
- França, E.L.T., dos Santos, A.O., Coelho, A.A. & da Silva, L.M. (2016) Magnetocaloric effect of the ternary Dy, Ho and Er platinum gallides. *Journal of Magnetism and Magnetic Materials*. [Online] 401, 1088–1092. Available from: doi:10.1016/j.jmmm.2015.10.138.

- Fritze, H., Schulz, M. & Richter, D. (2014) *Stability and Applications of High-Temperature Piezoelectric Crystals*. 2.
- Fu, Y., Ouyang, H. & Davis, R.B. (2019) Triboelectric energy harvesting from the vibro-impact of three cantilevered beams. *Mechanical Systems and Signal Processing*. [Online] 121, 509–531. Available from: doi:10.1016/j.ymssp.2018.11.043.
- Gaal, M., Bovtun, V., Stark, W., Erhard, A., et al. (2016) Viscoelastic properties of cellular polypropylene ferroelectrets. *Journal of Applied Physics*. [Online] 119 (12), 125101. Available from: doi:10.1063/1.4944798.
- Giacometti, J.A. (1987) Radial current-density distributions and sample charge uniformity in a corona triode. *Journal of Physics D: Applied Physics*. [Online] 20 (6), 675–682. Available from: doi:10.1088/0022-3727/20/6/001.
- Giacometti, J.A. & DeReggi, A.S. (1993) Thermal pulse study of the polarization distributions produced in polyvinylidene fluoride by corona poling at constant current. *Journal of Applied Physics*. [Online] 74 (5), 3357–3365. Available from: doi:10.1063/1.354561.
- Giacometti, J.A., Fedosov, S. & Costa, M.M. (1999) Corona charging of polymers: recent advances on constant current charging. *Brazilian Journal of Physics*. [Online] 29 (2), 269–279. Available from: doi:10.1590/S0103-97331999000200009.
- Giacometti, J.A. & Sinézio Carvalho Campos, J. (1990) Constant current corona triode with grid voltage control. Application to polymer foil charging. *Review of Scientific Instruments*. [Online] 61 (3), 1143–1150. Available from: doi:10.1063/1.1141438.
- Gilbert-Tremblay, H., Mighri, F. & Rodrigue, D. (2012) Morphology development of polypropylene cellular films for piezoelectric applications. *Journal of Cellular Plastics*. [Online] 48 (4), 341–354. Available from: doi:10.1177/0021955X12443687.
- Giurgiutiu, V. (2000) Review of Smart-Materials Actuation Solutions for Aeroelastic and Vibration Control. *Journal of Intelligent Material Systems and Structures*. [Online] 11 (7), 525–544. Available from: doi:10.1106/HYTV-NC7R-BCMM-W3CH.
- Glickman, Y., Winebrand, E., Arie, A. & Rosenman, G. (2006) Electron-beam-induced domain poling in LiNbO<sub>3</sub> for two-dimensional nonlinear frequency conversion. *Applied Physics Letters*. [Online] 88 (1), 011103. Available from: doi:10.1063/1.2159089.
- Granstrom, J., Feenstra, J., Sodano, H.A. & Farinholt, K. (2007) Energy harvesting from a backpack instrumented with piezoelectric shoulder straps. *Smart Materials and Structures*. [Online] 16 (5), 1810–1820. Available from: doi:10.1088/0964-1726/16/5/036.
- Gross, B., Gerhard-Multhaupt, R., Berraissoul, A. & Sessler, G.M. (1987) Electron-beam poling of piezoelectric polymer electrets. *Journal of Applied Physics*. [Online] 62 (4), 1429–1432. Available from: doi:10.1063/1.339648.
- Gutnik, Y., Altafim, R.A.P., Veronese, P.R., Resende, J.F., et al. (2012) *Piezoelectret sensors detect geometry-related modifications of the acoustical signatures from*

- partial discharges in an electrical equipment chamber*. In: [Online]. October 2012 IEEE. pp. 108–111. Available from: doi:10.1109/CEIDP.2012.6378734 [Accessed: 4 April 2018].
- Haberman, M.R. & Berthelot, Y.H. (2007) A differential effective medium model for piezoelectret foams. *Journal of Applied Physics*. [Online] 102 (12), 124903. Available from: doi:10.1063/1.2822451.
- Harris, S. & Mellinger, A. (2012) Pressure dependence of space charge deposition in piezoelectric polymer foams: simulations and experimental verification. *Applied Physics A*. [Online] 107 (3), 553–558. Available from: doi:10.1007/s00339-012-6835-4.
- Harris, S. & Mellinger, A. (2014) Towards a better understanding of dielectric barrier discharges in ferroelectrets: Paschen breakdown fields in micrometer sized voids. *Journal of Applied Physics*. [Online] 115 (16), 163302. Available from: doi:10.1063/1.4871678.
- HARRISON, J.S. & OUNAIES, Z. (2001) *PIEZOELECTRIC POLYMERS*. 27.
- Herous, L., Nemamcha, M., Remadnia, M. & Dascalescu, L. (2009) Factors that influence the surface potential decay on a thin film of polyethylene terephthalate (PET). *Journal of Electrostatics*. [Online] 67 (2–3), 198–202. Available from: doi:10.1016/j.elstat.2009.01.028.
- Hill, R.A., Knoesen, A. & Mortazavi, M.A. (1994) Corona poling of nonlinear polymer thin films for electro-optic modulators. *Applied Physics Letters*. [Online] 65 (14), 1733–1735. Available from: doi:10.1063/1.112899.
- Hillenbrand, J. & Sessler, G.M. (2000) *Piezoelectricity in Cellular Electret Films*. 7 (4), 6.
- Hillenbrand, J., Sessler, G.M. & Zhang, X. (2005) Verification of a model for the piezoelectric d33 coefficient of cellular electret films. *Journal of Applied Physics*. [Online] 98 (6), 064105. Available from: doi:10.1063/1.2058185.
- Hillenbrand', J., Xia, Z., Zhang, X. & Sessler', G.M. (2002) *PIEZOELECTRICITY OF CELLULAR AND POROUS POLYMER ELECTRETS*. 4.
- Hillenbrand, J., Zhang, X., Zhang, Y. & Sessler, G.M. (2003) *Pressure-treated cellular polypropylene with large piezoelectric coefficients*. In: [Online]. 2003 IEEE. pp. 40–43. Available from: doi:10.1109/CEIDP.2003.1254789 [Accessed: 4 April 2018].
- Hu, Z. & von Seggern, H. (2006) Breakdown-induced polarization buildup in porous fluoropolymer sandwiches: a thermally stable piezoelectret. *Journal of Applied Physics*. [Online] 99 (2), 024102. Available from: doi:10.1063/1.2161825.
- Intra, P. & Tippayawong, N. (2009) Progress in unipolar corona discharger designs for airborne particle charging: A literature review. *Journal of Electrostatics*. [Online] 67 (4), 605–615. Available from: doi:10.1016/j.elstat.2008.12.018.
- Jain, A., K. J., P., Sharma, A.K., Jain, A., et al. (2015) Dielectric and piezoelectric properties of PVDF/PZT composites: A review. *Polymer Engineering & Science*. [Online] 55 (7), 1589–1616. Available from: doi:10.1002/pen.24088.

- Jin, W., Wang, Z., Huang, H., Hu, X., et al. (2018) High-performance piezoelectric energy harvesting of vertically aligned Pb(Zr,Ti)O<sub>3</sub> nanorod arrays. *RSC Advances*. [Online] 8 (14), 7422–7427. Available from: doi:10.1039/C7RA13506H.
- Kepler, R.G. & Anderson, R.A. (1978) Piezoelectricity and pyroelectricity in polyvinylidene fluoride. *Journal of Applied Physics*. [Online] 49 (8), 4490–4494. Available from: doi:10.1063/1.325454.
- Kim, H.S., Kim, J.-H. & Kim, J. (2011) A review of piezoelectric energy harvesting based on vibration. *International Journal of Precision Engineering and Manufacturing*. [Online] 12 (6), 1129–1141. Available from: doi:10.1007/s12541-011-0151-3.
- Kim, K.-B., Hsu, D.K., Ahn, B., Kim, Y.-G., et al. (2010) Fabrication and comparison of PMN-PT single crystal, PZT and PZT-based 1-3 composite ultrasonic transducers for NDE applications. *Ultrasonics*. [Online] 50 (8), 790–797. Available from: doi:10.1016/j.ultras.2010.04.001.
- Korge, H., Laan, M. & Paris, P. (1993) On the formation of negative coronas. *Journal of Physics D: Applied Physics*. [Online] 26 (2), 231–236. Available from: doi:10.1088/0022-3727/26/2/010.
- Kressmann, R. (2001) Linear and nonlinear piezoelectric response of charged cellular polypropylene. *Journal of Applied Physics*. [Online] 90 (7), 3489–3496. Available from: doi:10.1063/1.1398597.
- Kumara, S., Serdyuk, Y. & Gubanski, S. (2009) Charging of Polymeric Surfaces by Positive Impulse Corona. *IEEE Transactions on Dielectrics and Electrical Insulation*. [Online] 16 (3), 726–733. Available from: doi:10.1109/TDEI.2009.5128512.
- Lee, H.J. & Zhang, S. (2012) Perovskite Lead-Free Piezoelectric Ceramics. In: Shashank Priya & Sahn Nahm (eds.). *Lead-Free Piezoelectrics*. [Online]. New York, NY, Springer New York. pp. 291–309. Available from: doi:10.1007/978-1-4419-9598-8\_9 [Accessed: 4 April 2018].
- Li, J. (2004) The effective pyroelectric and thermal expansion coefficients of ferroelectric ceramics. *Mechanics of Materials*. [Online] 36 (10), 949–958. Available from: doi:10.1016/j.mechmat.2003.05.005.
- Li, X., Ma, T., Tian, J., Han, P., et al. (2014) Micromachined PIN-PMN-PT crystal composite transducer for high-frequency intravascular ultrasound (IVUS) imaging. *IEEE Transactions on Ultrasonics, Ferroelectrics, and Frequency Control*. [Online] 61 (7), 1171–1178. Available from: doi:10.1109/TUFFC.2014.3016.
- Lindner, M., Bauer-Gogonea, S., Bauer, S., Paajanen, M., et al. (2002) Dielectric barrier microdischarges: Mechanism for the charging of cellular piezoelectric polymers. *Journal of Applied Physics*. [Online] 91 (8), 5283–5287. Available from: doi:10.1063/1.1459751.
- Liu, G., Zhang, S., Jiang, W. & Cao, W. (2015) Losses in ferroelectric materials. *Materials Science and Engineering: R: Reports*. [Online] 89, 1–48. Available from: doi:10.1016/j.mser.2015.01.002.
- Liu, W. & Ren, X. (2009) Large Piezoelectric Effect in Pb-Free Ceramics. *Physical Review Letters*. [Online] 103 (25). Available from: doi:10.1103/PhysRevLett.103.257602 [Accessed: 4 April 2018].

- Lopez-Sanchez, M.A. & Llana-Fúnez, S. (2015) An evaluation of different measures of dynamically recrystallized grain size for paleopiezometry or paleowattometry studies. *Solid Earth*. [Online] 6 (2), 475–495. Available from: doi:<https://doi.org/10.5194/se-6-475-2015>.
- Lou, K., Zhang, X. & Xia, Z. (2012) Piezoelectric performance of fluor polymer sandwiches with different void structures. *Applied Physics A*. [Online] 107 (3), 613–620. Available from: doi:[10.1007/s00339-012-6839-0](https://doi.org/10.1007/s00339-012-6839-0).
- Luo, Z., Zhu, D. & Beeby, S.P. (2015) Multilayer ferroelectret-based energy harvesting insole. *Journal of Physics: Conference Series*. [Online] 660 (1), 012118. Available from: doi:[10.1088/1742-6596/660/1/012118](https://doi.org/10.1088/1742-6596/660/1/012118).
- Luo, Z., Zhu, D., Shi, J., Beeby, S., et al. (2015) Energy harvesting study on single and multilayer ferroelectret foams under compressive force. *IEEE Transactions on Dielectrics and Electrical Insulation*. [Online] 22 (3), 1360–1368. Available from: doi:[10.1109/TDEI.2015.7116323](https://doi.org/10.1109/TDEI.2015.7116323).
- Maharjan, P., Cho, H., Rasel, M.S., Salauddin, M., et al. (2018) A fully enclosed, 3D printed, hybridized nanogenerator with flexible flux concentrator for harvesting diverse human biomechanical energy. *Nano Energy*. [Online] 53, 213–224. Available from: doi:[10.1016/j.nanoen.2018.08.034](https://doi.org/10.1016/j.nanoen.2018.08.034).
- Malič, B., Koruza, J., Hreščak, J., Bernard, J., et al. (2015) Sintering of Lead-Free Piezoelectric Sodium Potassium Niobate Ceramics. *Materials*. [Online] 8 (12), 8117–8146. Available from: doi:[10.3390/ma8125449](https://doi.org/10.3390/ma8125449).
- Mateu, L. & Moll, F. (2006) Appropriate charge control of the storage capacitor in a piezoelectric energy harvesting device for discontinuous load operation. *Sensors and Actuators A: Physical*. [Online] 132 (1), 302–310. Available from: doi:[10.1016/j.sna.2006.06.061](https://doi.org/10.1016/j.sna.2006.06.061).
- Mellinger, A. (2011) *Breakdown Threshold of Dielectric Barrier Discharges in Ferroelectrets: Where Paschen's Law Fails*. 18 (1), 6.
- Mellinger, A. (2003) Dielectric resonance spectroscopy: a versatile tool in the quest for better piezoelectric polymers. *IEEE Transactions on Dielectrics and Electrical Insulation*. [Online] 10 (5), 842–861. Available from: doi:[10.1109/TDEI.2003.1237333](https://doi.org/10.1109/TDEI.2003.1237333).
- Mellinger, A. (2002) *Piezoelectric Resonances in the Dielectric Spectrum of Polymer Films*. 8.
- Mellinger, A., Wegener, M., Wirges, W., Mallepally, R.R., et al. (2006) Thermal and Temporal Stability of Ferroelectret Films Made from Cellular Polypropylene/Air Composites. *Ferroelectrics*. [Online] 331 (1), 189–199. Available from: doi:[10.1080/00150190600737933](https://doi.org/10.1080/00150190600737933).
- Mohd Jani, J., Leary, M., Subic, A. & Gibson, M.A. (2014) A review of shape memory alloy research, applications and opportunities. *Materials & Design (1980-2015)*. [Online] 56, 1078–1113. Available from: doi:[10.1016/j.matdes.2013.11.084](https://doi.org/10.1016/j.matdes.2013.11.084).
- Molinié, P. (1999) Charge injection in corona-charged polymeric films: potential decay and current measurements. *Journal of Electrostatics*. [Online] 45 (4), 265–273. Available from: doi:[10.1016/S0304-3886\(98\)00053-9](https://doi.org/10.1016/S0304-3886(98)00053-9).

- Moon, J.-D., Chung, S.-H. & Lee, K.-T. (1994) Control of corona characteristics with third electrode and bias voltage. *IEEE Transactions on Dielectrics and Electrical Insulation*. [Online] 1 (4), 569–577. Available from: doi:10.1109/94.311699.
- Neugschwandtner, G.S., Schwödauer, R., Vieytes, M., Bauer-Gogonea, S., et al. (2000) Large and broadband piezoelectricity in smart polymer-foam space-charge electrets. *Applied Physics Letters*. [Online] 77 (23), 3827–3829. Available from: doi:10.1063/1.1331348.
- O'Brien, R.C., Ambrosi, R.M., Bannister, N.P., Howe, S.D., et al. (2008) Safe radioisotope thermoelectric generators and heat sources for space applications. *Journal of Nuclear Materials*. [Online] 377 (3), 506–521. Available from: doi:10.1016/j.jnucmat.2008.04.009.
- Olsen, M., Zhang, R., Örtengren, J., Andersson, H., et al. (2019) Frequency and voltage response of a wind-driven fluttering triboelectric nanogenerator. *Scientific Reports*. [Online] 9 (1). Available from: doi:10.1038/s41598-019-42128-7 [Accessed: 21 April 2019].
- Ono, R., Nakazawa, M. & Oda, T. (2004) Charge Storage in Corona-Charged Polypropylene Films Analyzed by LIPP and TSC Methods. *IEEE Transactions on Industry Applications*. [Online] 40 (6), 1482–1488. Available from: doi:10.1109/TIA.2004.836131.
- Oubla, M., Lamire, M., Boutahar, A., Lassri, H., et al. (2016) Structural, magnetic and magnetocaloric properties of layered perovskite La<sub>1.1</sub>Bi<sub>0.3</sub>Sr<sub>1.6</sub>Mn<sub>2</sub>O<sub>7</sub>. *Journal of Magnetism and Magnetic Materials*. [Online] 403, 114–117. Available from: doi:10.1016/j.jmmm.2015.11.076.
- Paajanen, M., Lekkala, J. & Valimäki, H. (2001) Electromechanical modeling and properties of the electret film EMFI. *IEEE Transactions on Dielectrics and Electrical Insulation*. [Online] 8 (4), 629–636. Available from: doi:10.1109/94.946715.
- Paajanen, M. & Va, H. (2000) Modelling the electromechanical "Im (EMFi). *Journal of Electrostatics*. 12.
- Paajanen, M., Wegener, M. & Gerhard-Multhaupt, R. (2001a) Understanding the role of the gas in the voids during corona charging of cellular electret films - a way to enhance their piezoelectricity. *Journal of Physics D: Applied Physics*. [Online] 34 (16), 2482–2488. Available from: doi:10.1088/0022-3727/34/16/313.
- Paajanen, M., Wegener, M. & Gerhard-Multhaupt, R. (2001b) Understanding the role of the gas in the voids during corona charging of cellular electret films - a way to enhance their piezoelectricity. *Journal of Physics D: Applied Physics*. [Online] 34 (16), 2482–2488. Available from: doi:10.1088/0022-3727/34/16/313.
- Panda, P.K. & Sahoo, B. (2015) PZT to Lead Free Piezo Ceramics: A Review. *Ferroelectrics*. [Online] 474 (1), 128–143. Available from: doi:10.1080/00150193.2015.997146.
- Pecharsky, V., Gschneidner, K., Pecharsky, A. & Tishin, A. (2001) Thermodynamics of the magnetocaloric effect. *Physical Review B*. [Online] 64 (14). Available from: doi:10.1103/PhysRevB.64.144406 [Accessed: 4 April 2018].

- Pekárek, S. (2009) *Effect of polarity on ozone production of DC corona discharge with and without photocatalyst*. 4.
- Pengfeng Zhang, Zhongfu Xia, Xunlin Qiu, FeiPeng Wang, et al. (2005) *Influence of Charging Parameters on Piezoelectricity for Cellular Polypropylene Film Electrets*. In: [Online]. 2005 IEEE. pp. 39–42. Available from: doi:10.1109/ISE.2005.1612313 [Accessed: 4 April 2018].
- Pisani Altafim, R., Rychkov, D., Wirges, W., Gerhard, R., et al. (2012a) Laminated tubular-channel ferroelectret systems from low-density polyethylene films and from fluoroethylene-propylene copolymer films - A comparison. *IEEE Transactions on Dielectrics and Electrical Insulation*. [Online] 19 (4), 1116–1123. Available from: doi:10.1109/TDEI.2012.6259978.
- Pisani Altafim, R.A., Corrêa Altafim, R.A., Qiu, X., Raabe, S., et al. (2012b) Fluoropolymer piezoelectrets with tubular channels: resonance behavior controlled by channel geometry. *Applied Physics A*. [Online] 107 (4), 965–970. Available from: doi:10.1007/s00339-012-6848-z.
- Pondrom, P., Hillenbrand, J., Sessler, G.M., Bös, J., et al. (2014) Vibration-based energy harvesting with stacked piezoelectrets. *Applied Physics Letters*. [Online] 104 (17), 172901. Available from: doi:10.1063/1.4874305.
- Pozzi, M. (2016) Magnetic plucking of piezoelectric bimorphs for a wearable energy harvester. *Smart Materials and Structures*. [Online] 25 (4), 045008. Available from: doi:10.1088/0964-1726/25/4/045008.
- Pozzi, M., Aung, M.S.H., Zhu, M., Jones, R.K., et al. (2012) The pizzicato knee-joint energy harvester: characterization with biomechanical data and the effect of backpack load. *Smart Materials and Structures*. [Online] 21 (7), 075023. Available from: doi:10.1088/0964-1726/21/7/075023.
- Prashanthi, K., Miriyala, N., Gaikwad, R.D., Moussa, W., et al. (2013) Vibrational energy harvesting using photo-patternable piezoelectric nanocomposite cantilevers. *Nano Energy*. [Online] 2 (5), 923–932. Available from: doi:10.1016/j.nanoen.2013.03.013.
- Qaiss, A., Saidi, H., Fassi-Fehri, O. & Bousmina, M. (2013) Theoretical modeling and experiments on the piezoelectric coefficient in cellular polymer films. *Polymer Engineering & Science*. [Online] 53 (1), 105–111. Available from: doi:10.1002/pen.23234.
- Qi, L., Petersson, L. & Liu, T. (2014) Review of Recent Activities on Dielectric Films for Capacitor Applications. *Journal of International Council on Electrical Engineering*. [Online] 4 (1), 1–6. Available from: doi:10.5370/JICEE.2014.4.1.001.
- Qiu, X. (2010) Patterned piezo-, pyro-, and ferroelectricity of poled polymer electrets. *Journal of Applied Physics*. [Online] 108 (1), 011101. Available from: doi:10.1063/1.3457141.
- Qiu, X., Gerhard, R. & Mellinger, A. (2011) Turning polymer foams or polymer-film systems into ferroelectrets: dielectric barrier discharges in voids. *IEEE Transactions on Dielectrics and Electrical Insulation*. [Online] 18 (1), 34–42. Available from: doi:10.1109/TDEI.2011.5704490.

- Qiu, X., Mellinger, A. & Gerhard, R. (2008) Influence of gas pressure in the voids during charging on the piezoelectricity of ferroelectrets. *Applied Physics Letters*. [Online] 92 (5), 052901. Available from: doi:10.1063/1.2841037.
- Qiu, X., Mellinger, A., Wegener, M., Wirges, W., et al. (2007a) Barrier discharges in cellular polypropylene ferroelectrets: How do they influence the electromechanical properties? *Journal of Applied Physics*. [Online] 101 (10), 104112. Available from: doi:10.1063/1.2735410.
- Qiu, X., Mellinger, A., Wirges, W. & Gerhard, R. (2007b) Spectroscopic study of dielectric barrier discharges in cellular polypropylene ferroelectrets. *Applied Physics Letters*. [Online] 91 (13), 132905. Available from: doi:10.1063/1.2786597.
- Ramadan, K.S., Sameoto, D. & Evoy, S. (2014) A review of piezoelectric polymers as functional materials for electromechanical transducers. *Smart Materials and Structures*. [Online] 23 (3), 033001. Available from: doi:10.1088/0964-1726/23/3/033001.
- Rao, Y.J. (1999) Recent progress in applications of in-plane Bragg grating sensors. *Optics and Lasers in Engineering*. 28.
- Raukola, J.I. (1998) *A new technology to manufacture polypropylene foam sheet and biaxially oriented foam film*. VTT publications 361. Espoo, Technical Research Centre of Finland.
- Romero Gómez, J., Ferreiro Garcia, R., De Miguel Catoira, A. & Romero Gómez, M. (2013) Magnetocaloric effect: A review of the thermodynamic cycles in magnetic refrigeration. *Renewable and Sustainable Energy Reviews*. [Online] 17, 74–82. Available from: doi:10.1016/j.rser.2012.09.027.
- Rubio-Marcos, F., López-Juárez, R., Rojas-Hernandez, R.E., del Campo, A., et al. (2015) Lead-Free Piezoceramics: Revealing the Role of the Rhombohedral–Tetragonal Phase Coexistence in Enhancement of the Piezoelectric Properties. *ACS Applied Materials & Interfaces*. [Online] 7 (41), 23080–23088. Available from: doi:10.1021/acsami.5b06747.
- Saarimäki, E., Paajanen, M., Savijärvi, A.-M., Minkkinen, H., et al. (2006) *Novel Heat Durable Electromechanical Film: Processing for Electromechanical and Electret Applications*. 13 (5), 10.
- Sahli, S., Bellel, A., Ziari, Z., Kahlouche, A., et al. (2003) Measure and analysis of potential decay in polypropylene films after negative corona charge deposition. *Journal of Electrostatics*. 13.
- Sborikas, M., Qiu, X., Wirges, W., Gerhard, R., et al. (2014) Screen printing for producing ferroelectret systems with polymer-electret films and well-defined cavities. *Applied Physics A*. [Online] 114 (2), 515–520. Available from: doi:10.1007/s00339-013-7998-3.
- Sborikas, M. & Wegener, M. (2013) Cellular-foam polypropylene ferroelectrets with increased film thickness and reduced resonance frequency. *Applied Physics Letters*. [Online] 103 (25), 252901. Available from: doi:10.1063/1.4850523.
- Schwodiauer, R., Graz, I. & Bauer, S. (2004) *Charging and switching of ferroelectrets. how much can ferroelectrets behave like ferroelectrics?* In: [Online]. 2004 IEEE.

- pp. 134–137. Available from: doi:10.1109/ISAF.2004.1418355 [Accessed: 4 April 2018].
- von Seggern, H. (1981) Isothermal and thermally stimulated current studies of positively corona charged polyfluoroethylene propylene (Teflon FEP). *Journal of Applied Physics*. [Online] 52 (6), 4081–4085. Available from: doi:10.1063/1.329257.
- Seiner, H., Stoklasová, P., Sedlák, P., Ševčík, M., et al. (2016) Evolution of soft-phonon modes in Fe–Pd shape memory alloy under large elastic-like strains. *Acta Materialia*. [Online] 105, 182–188. Available from: doi:10.1016/j.actamat.2015.12.025.
- Sessler, G.M. (1999) *Electromechanical Response of Cellular Electret Films*. 4.
- Sessler, G.M., Alquié, C. & Lewiner, J. (1992) Charge distribution in Teflon FEP (fluoroethylene propylene) negatively corona-charged to high potentials. *Journal of Applied Physics*. [Online] 71 (5), 2280–2284. Available from: doi:10.1063/1.351127.
- Sgardelis, P. & Pozzi, M. (2017) *An FE model of a cellular polypropylene: exploring mechanical properties*. In: Luis Fonseca, Mika Prunnila, & Erwin Peiner (eds.). [Online]. 31 May 2017 p. 1024609. Available from: doi:10.1117/12.2266265 [Accessed: 19 April 2018].
- Shenck, N.S. & Paradiso, J.A. (2001) Energy scavenging with shoe-mounted piezoelectrics. *IEEE Micro*. [Online] 21 (3), 30–42. Available from: doi:10.1109/40.928763.
- Sherrit, S. (2007) *Characterization of Piezoelectric Materials for Transducers*. 45.
- Sherrit, S., Gauthier, N., Wiedrick, H.D., Mukherjee, B.K., et al. (1991) *The Effect of Electrode Materials on Measured Piezoelectric Properties of Ceramics and Ceramic-Polymer Composites*. 4.
- Shimizu, S., Shiogai, J., Takemori, N., Sakai, S., et al. (2019) Giant thermoelectric power factor in ultrathin FeSe superconductor. *Nature Communications*. [Online] 10 (1). Available from: doi:10.1038/s41467-019-08784-z [Accessed: 21 April 2019].
- Shinekumar, K. & Dutta, S. (2015) High-Temperature Piezoelectrics with Large Piezoelectric Coefficients. *Journal of Electronic Materials*. [Online] 44 (2), 613–622. Available from: doi:10.1007/s11664-014-3534-2.
- Shrout, T.R. & Zhang, S.J. (2007) Lead-free piezoelectric ceramics: Alternatives for PZT? *Journal of Electroceramics*. [Online] 19 (1), 113–126. Available from: doi:10.1007/s10832-007-9047-0.
- SHUR, M.S., BYKHOVSKI, A.D. & GASKA, R. (1998) *PYROELECTRIC AND PIEZOELECTRIC PROPERTIES OF GAN-BASED MATERIALS*. 12.
- Silva, L.B.M. (2014) *Quartz and GaPO<sub>4</sub> pressure transducers for high resolution applications in high temperature: a simulation approach*. 4.
- Smith, W.A. (1989) *The role of piezocomposites in ultrasonic transducers*. In: [Online]. 1989 IEEE. pp. 755–766. Available from: doi:10.1109/ULTSYM.1989.67088 [Accessed: 4 April 2018].

- Tan, Y., Zhang, J., Wu, Y., Wang, C., et al. (2015) Unfolding grain size effects in barium titanate ferroelectric ceramics. *Scientific Reports*. [Online] 5, 9953. Available from: doi:10.1038/srep09953.
- Thakur, O.P., Singh, J.P., Prakash, C. & Kishan, P. (2007) Modified Lead-zirconate-titanate for Pyroelectric Sensors. *Defence Science Journal*. [Online] 57 (3), 233–239. Available from: doi:10.14429/dsj.57.1764.
- Tuncer, E. (2005) Numerical calculations of effective elastic properties of two cellular structures. *Journal of Physics D: Applied Physics*. [Online] 38 (3), 497–503. Available from: doi:10.1088/0022-3727/38/3/023.
- Tuncer, E. & Wegener, M. (2013) *Elastic properties of cellular polypropylene films: Finite element simulations and their comparison with experiments*. 23.
- Tuncer, E. & Wegener, M. (2004) Elastic properties of highly anisotropic thin poly(propylene) foams. *Materials Letters*. [Online] 58 (22–23), 2815–2818. Available from: doi:10.1016/j.matlet.2004.05.002.
- Tuncer, E., Wegener, M. & Gerhard-Multhaupt, R. (2005) Modeling electro-mechanical properties of layered electrets: application of the finite-element method. *Journal of Electrostatics*. [Online] 63 (1), 21–35. Available from: doi:10.1016/j.elstat.2004.06.002.
- Uchino, K. (2015) Glory of piezoelectric perovskites. *Science and Technology of Advanced Materials*. [Online] 16 (4), 046001. Available from: doi:10.1088/1468-6996/16/4/046001.
- Uwiragiye, E., Farooq, M.U., Moon, S.-H., Pham, T.L., et al. (2017) High performance lead-free piezoelectric  $0.96(\text{K} 0.48 \text{Na} 0.52) \text{NbO}_3 - 0.03[\text{Bi} 0.5 (\text{Na} 0.7 \text{K} 0.2 \text{Li} 0.1) 0.5] \text{ZrO}_3 - 0.01(\text{Bi} 0.5 \text{Na} 0.5) \text{TiO}_3$  single crystals grown by solid state crystal growth and their phase relations. *Journal of the European Ceramic Society*. [Online] 37 (15), 4597–4607. Available from: doi:10.1016/j.jeurceramsoc.2017.06.015.
- Waller, D., Iqbal, T. & Safari, A. (1989) Poling of Lead Zirconate Titanate Ceramics and Flexible Piezoelectric Composites by the Corona Discharge Technique. *Journal of the American Ceramic Society*. [Online] 72 (2), 322–324. Available from: doi:10.1111/j.1151-2916.1989.tb06125.x.
- Wang, J.-J., Hsu, T.-H., Yeh, C.-N., Tsai, J.-W., et al. (2012) Piezoelectric polydimethylsiloxane films for MEMS transducers. *Journal of Micromechanics and Microengineering*. [Online] 22 (1), 015013. Available from: doi:10.1088/0960-1317/22/1/015013.
- Wang, P., Li, Y. & Lu, Y. (2011) Enhanced piezoelectric properties of  $(\text{Ba}_{0.85}\text{Ca}_{0.15})(\text{Ti}_{0.9}\text{Zr}_{0.1})\text{O}_3$  lead-free ceramics by optimizing calcination and sintering temperature. *Journal of the European Ceramic Society*. [Online] 31 (11), 2005–2012. Available from: doi:10.1016/j.jeurceramsoc.2011.04.023.
- Wang, Q., Bowen, C.R., Lewis, R., Chen, J., et al. (2019) Hexagonal boron nitride nanosheets doped pyroelectric ceramic composite for high-performance thermal energy harvesting. *Nano Energy*. [Online] 60, 144–152. Available from: doi:10.1016/j.nanoen.2019.03.037.

- Wegener, M., Tuncer, E., Gerhard-Mulhaupt, R. & Bauer, S. (2006) *Elastic properties and electromechanical coupling factor of inflated polypropylene ferroelectrets*. In: [Online]. October 2006 IEEE. pp. 752–755. Available from: doi:10.1109/CEIDP.2006.312041 [Accessed: 4 April 2018].
- Wegener, M., Tuncer, E., Wirges, W., Gerhard-Mulhaupt, R., et al. (2004a) *Ferroelectrets: highly anisotropic electrically charged polymer foams for electromechanical transducer applications*. In: [Online]. 2004 IEEE. pp. 1138–1141. Available from: doi:10.1109/ULTSYM.2004.1417981 [Accessed: 4 April 2018].
- Wegener, M., Wirges, W., Fohlmeister, J., Tiersch, B., et al. (2004b) Two-step inflation of cellular polypropylene films: void-thickness increase and enhanced electromechanical properties. *Journal of Physics D: Applied Physics*. [Online] 37 (4), 623–627. Available from: doi:10.1088/0022-3727/37/4/013.
- Wegener, M., Wirges, W., Gerhard-Mulhaupt, R., Dansachmüller, M., et al. (2004c) Controlled inflation of voids in cellular polymer ferroelectrets: Optimizing electromechanical transducer properties. *Applied Physics Letters*. [Online] 84 (3), 392–394. Available from: doi:10.1063/1.1641171.
- Wheeler, B. (2014) *AlgDesign: Algorithmic Experimental Design*. [Online]. Available from: <https://CRAN.R-project.org/package=AlgDesign> [Accessed: 26 April 2018].
- Wood, R.J., Steltz, E. & Fearing, R.S. (2005) Optimal energy density piezoelectric bending actuators. *Sensors and Actuators A: Physical*. [Online] 119 (2), 476–488. Available from: doi:10.1016/j.sna.2004.10.024.
- Wu, N., Cheng, X., Zhong, Q., Zhong, J., et al. (2015) Cellular Polypropylene Piezoelectret for Human Body Energy Harvesting and Health Monitoring. *Advanced Functional Materials*. [Online] 25 (30), 4788–4794. Available from: doi:10.1002/adfm.201501695.
- Xunlin Qiu, Mellinger, A., Wirges, W. & Gerhard, R. (2007) *Dielectric barrier discharges during the generation of ferroelectrets: Optical spectroscopy for process monitoring*. In: [Online]. 2007 IEEE. pp. 828–831. Available from: doi:10.1109/CEIDP.2007.4451487 [Accessed: 4 April 2018].
- Yamamoto, N., Yamashita, Y., Hosono, Y. & Itsumi, K. (2013) Electrical and physical properties of reoped PMN–PT single-crystal sliver transducer. *Sensors and Actuators A: Physical*. [Online] 200, 16–20. Available from: doi:10.1016/j.sna.2012.10.002.
- Ye, H.-J., Yang, L., Shao, W.-Z., Sun, S.-B., et al. (2013) Effect of electroactive phase transformation on electron structure and dielectric properties of uniaxial stretching poly(vinylidene fluoride) films. *RSC Advances*. [Online] 3 (45), 23730. Available from: doi:10.1039/c3ra43966f.
- Yovcheva, T.A., Mekishev, G.A. & Marinov, A.T. (2004) A percolation theory analysis of surface potential decay related to corona charged polypropylene (PP) electrets. *Journal of Physics: Condensed Matter*. [Online] 16 (3), 455–464. Available from: doi:10.1088/0953-8984/16/3/021.

- Zhang, J.W., Lebrun, L., Guiffard, B., Cottinet, P.-J., et al. (2012a) Influence of corona poling on the electrostrictive behavior of cellular polypropylene films. *Sensors and Actuators A: Physical*. [Online] 175, 87–93. Available from: doi:10.1016/j.sna.2011.11.038.
- Zhang, S., Xia, R., Shrout, T.R., Zang, G., et al. (2006) Piezoelectric properties in perovskite  $0.948(\text{K}0.5\text{Na}0.5)\text{NbO}_3\text{--}0.052\text{LiSbO}_3$  lead-free ceramics. *Journal of Applied Physics*. [Online] 100 (10), 104108. Available from: doi:10.1063/1.2382348.
- Zhang, X., Hillenbrand, J. & Sessler, G.M. (2004a) Improvement of piezoelectric activity of cellular polymers using a double-expansion process. *Journal of Physics D: Applied Physics*. [Online] 37 (15), 2146–2150. Available from: doi:10.1088/0022-3727/37/15/015.
- Zhang, X., Hillenbrand, J. & Sessler, G.M. (2004b) Improvement of piezoelectric activity of cellular polymers using a double-expansion process. *Journal of Physics D: Applied Physics*. [Online] 37 (15), 2146. Available from: doi:10.1088/0022-3727/37/15/015.
- Zhang, X., Hillenbrand, J. & Sessler, G.M. (2004c) Piezoelectric  $d_{33}$  coefficient of cellular polypropylene subjected to expansion by pressure treatment. *Applied Physics Letters*. [Online] 85 (7), 1226–1228. Available from: doi:10.1063/1.1781388.
- Zhang, X., Hillenbrand, J., Sessler, G.M., Haberzettl, S., et al. (2012b) Fluoroethylenpropylene ferroelectrets with patterned microstructure and high, thermally stable piezoelectricity. *Applied Physics A*. [Online] 107 (3), 621–629. Available from: doi:10.1007/s00339-012-6840-7.
- Zhang, X., Huang, J., Chen, J., Wan, Z., et al. (2007) Piezoelectric properties of irradiation-crosslinked polypropylene ferroelectrets. *Applied Physics Letters*. [Online] 91 (18), 182901. Available from: doi:10.1063/1.2803316.
- Zhang, X., Huang, J., Wang, X. & Xia, Z. (2010) *Piezoelectricity and Dynamic Characteristics of Laminated Fluorocarbon Films*. 17 (4), 7.
- Zhang, X., Sessler, G.M. & Hillenbrand, J. (2007) Improvement of piezoelectric coefficient of cellular polypropylene films by repeated expansions. *Journal of Electrostatics*. [Online] 65 (2), 94–100. Available from: doi:10.1016/j.elstat.2006.07.006.
- Zhang, X., Sessler, G.M. & Wang, Y. (2014) Fluoroethylenpropylene ferroelectret films with cross-tunnel structure for piezoelectric transducers and micro energy harvesters. *Journal of Applied Physics*. [Online] 116 (7), 074109. Available from: doi:10.1063/1.4893367.
- Zhang, Y., Wang, S., Liu, D., Zhang, Q., et al. (2011) Fabrication of angle beam two-element ultrasonic transducers with PMN–PT single crystal and PMN–PT/epoxy 1–3 composite for NDE applications. *Sensors and Actuators A: Physical*. [Online] 168 (1), 223–228. Available from: doi:10.1016/j.sna.2011.04.004.
- Zhu, M. & Worthington, E. (2009) *Design and testing of piezoelectric energy harvesting devices for generation of higher electric power for wireless sensor networks*. In: [Online]. October 2009 IEEE. pp. 699–702. Available from: doi:10.1109/ICSENS.2009.5398559 [Accessed: 4 April 2018].

Zhukov, S. & von Seggern, H. (2007a) Breakdown-induced light emission and poling dynamics of porous fluoropolymers. *Journal of Applied Physics*. [Online] 101 (8), 084106. Available from: doi:10.1063/1.2716872.

Zhukov, S. & von Seggern, H. (2007b) Polarization hysteresis and piezoelectricity in open-porous fluoropolymer sandwiches. *Journal of Applied Physics*. [Online] 102 (4), 044109. Available from: doi:10.1063/1.2764024.